Olaf Wiest
Yundong Wu *Editors*

Computational Organometallic Chemistry

Springer

Computational Organometallic Chemistry

Olaf Wiest • Yundong Wu
Editors

Computational Organometallic Chemistry

Springer

Editors

Prof. Olaf Wiest
University of Notre Dame
Department of Chemistry and
Biochemistry
Notre Dame Indiana
USA
owiest@nd.edu

Prof. Yundong Wu
Peking University
Shenzhen Graduate School
Key Lab of Chemical Genomics Peking
China
People's Republic
chydwu@ust.hk

ISBN 978-3-642-25257-0 e-ISBN 978-3-642-25258-7
DOI 10.1007/978-3-642-25258-7
Springer Heidelberg Dordrecht London New York

Library of Congress Control Number: 2012931237

Printed on acid-free paper

Springer is part of Springer Science+Business Media (www.springer.com)

Preface

The use of computational methods has become an indispensible tool for elucidating the mechanism of organometallic reactions, including the mechanisms involved in catalysis by transition metals. The rapid increase in computer speed and the development of new computational methods and algorithmic improvements allow the study of the frequently complex reaction mechanisms in the important processes. As shown in this volume, the new developments in the field allow not only the study of systems such as clusters, which were previously out of reach for high-level calculations, but also see a shift from the rationalization of the mechanism towards more predictive models. We expect that this shift, which took place for purely organic molecules several years ago, will lead to an even stronger interest in the use of computational methods.

This volume contains a snapshot of the state of the art of computational studies of organometallic reactions, a field that has grown significantly and no single volume can attempt to provide a comprehensive overview. We therefore selected contributions in selected fields from authors in Asia, Europe, and the USA. The volume opens with a contribution by Yuxue Li on zirconium catalysis, a particularly timely topic in light of the award of the 2010 Nobel prize in Chemistry to Prof. Negishi, a pioneer in the synthetic application of these reactions. Marcus Meuwley reviews the use of force field methods in organometallic chemistry, which is a new and increasingly important method for the rapid studies of mechanism and selectivity in organometallic chemistry. The hydrogenation of π-systems is discussed in two contributions. Shuhua Li provides a broad overview of different mechanisms for the activation of molecular hydrogen. Forbes et al. discuss the rhodium, ruthenium, and iridium catalysis of this transformation, which is used in a number of large-scale production processes. Two further contributions discuss the oxidative functionalization of unactivated C–H bonds and of olefins. Xin Xu and coworkers provide an overview of the intensely studied field of alkane functionalization. The widely used osmylation reaction, for which computational methods played a crucial role in the determination of the now widely accepted reaction mechanism, is the topic of the contribution by Thomas Strassner and coworkers.

The use of molecular oxygen, a green oxidant, for oxidations through the use of transition metal clusters, is outlined by Zexing Cao. Clusters are also the topic of the contribution by Matthias Beller and Haijun Jiao, which demonstrates the interplay between experimental and computational methods that has been the hallmark of many studies in the field.

The breadth and depth of the contributions not only demonstrate the crucial role that computational methods play in the study of a wide range of organometallic reactions, but also attest to the robust health of the field that continues to benefit from, as well as inspire, novel experimental studies.

Notre Dame, IN, USA — Olaf Weist
Peking, People's Republic of China — Yundong Wu

Contents

DFT Studies on Zirconium-Mediated Reactions

Yuxue Li

Abstract Organozirconium compounds are attractive intermediates in an impressive array of synthetic methodology and have received much attention in recent years. The structure of the intermediates, the reaction pathways, and the origin of the selectivity for several reactions involving organozirconium compounds were studied here using high level DFT methods.

1 Determine the Intermediate Structure via NMR Calculations

1.1 Experimental Background

In recent years, transition-metal-mediated inter- or intramolecular cyclodimerization of alkynes has received lots of attention [1, 2]. During the study of the mechanism of zirconium-mediated cyclodimerization of heteroaryl-substituted alkynes [1], the zirconium intermediate **10** was successfully isolated (Scheme 1). However, in the ^{13}C NMR spectral data, there was no resonance in the region of 70–100 ppm, which is typical for the cyclobutadiene carbons in a cyclobutadiene–metal complex [3, 4]. Further NMR experiments (DEPT, COSY, HMQC, and HMBC) show that its structure may be zirconacyclopentadiene **10n** or the allenyl structure **10n′**. The large difference in the ^{13}C NMR chemical shifts of the two sp^2 carbon atoms bonded to Zr (Scheme 1, C6 and C9, 159.1 vs. 207.4) also supports the allenyl structure **10n′**. The ^{1}H chemical shifts of the *ortho* protons adjacent to N atom show that there exist two different types of pyridine rings in **10**.

Y. Li (✉)
State Key Laboratory of Organometallic Chemistry, Shanghai Institute of Organic Chemistry, Chinese Academy of Sciences, 354 Fenglin Lu, Shanghai 200032, People's Republic of China
e-mail: liyuxue@sioc.ac.cn

O. Wiest and Y. Wu (eds.), *Computational Organometallic Chemistry*,
DOI 10.1007/978-3-642-25258-7_1,

Scheme 1 Possible structures of the zirconium intermediate **10**. **10n**: zirconacyclopentadiene; **10n′**: allenyl structure

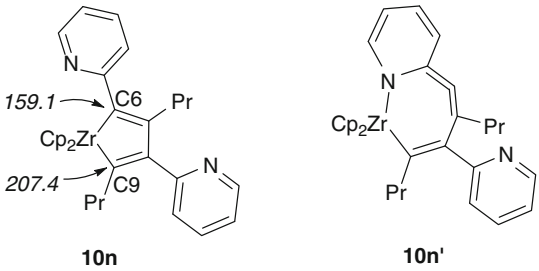

To better understand the structure of intermediate **10**, density functional theory (DFT) [5, 6] studies have been performed with the GAUSSIAN03 program [7] using the B3LYP [8, 9] method. In this calculation, for C, H, and N, the 6-311+G** basis set was used; for Zr, the Lanl2DZ basis set with effective core potential (ECP) [10] was used.

1.2 Results and Discussion

First, the allenyl structure **10n′** was explored (Scheme 1). In this model, methyl groups were used instead of propyl groups. The results indicate that this structure is not a minimum and always converged to a structure in which C6 coordinated with the Zr atom (Fig. 1), i.e., the structure **10n** in Scheme 1. Harmonic vibration frequency calculation was carried out, and this structure is shown to be a minimum (has no imaginary frequencies). With this model, atomic charges were calculated by NBO natural bonding analysis [11], and ^{13}C and ^{1}H chemical shifts were computed by the gauge including atomic orbital (GIAO) method [12]. Selected results are shown in Fig. 1.

The calculated NMR shifts are in good agreement with the experimental values. The most interesting thing is the large difference in the ^{13}C chemical shifts of C6 (159.1) and C9 (207.4), which seem to be the same type of carbon. The calculated NBO atomic charge of C6 is −0.433, much larger than that of C9 (−0.246), indicating that the shielding effect of the large electron density on C6 causes the chemical shift to move upfield.

In the optimized structure, Py1 coordinated with the Zr atom; consequently, it is coplanar with Zr, C6, and C7, and the dihedral angle N1–C5–C6–Zr is only −3.3°. This indicates that Py1 can be conjugated with C6. The C5–C6 bond has some double bond characteristics (1.434 Å). Py2 is rotated off this plane, and the dihedral angle N2–C20–C8–C7 is −67.0°. The C6–Zr bond length is 2.273 Å, even stronger than the C9–Zr bond (2.379 Å). The coordination of Py1 with the Zr center indicates that the 2-pyridyl group on the alkyne may be important to the reductive elimination of the zirconacyclopentadienes [1, 2].

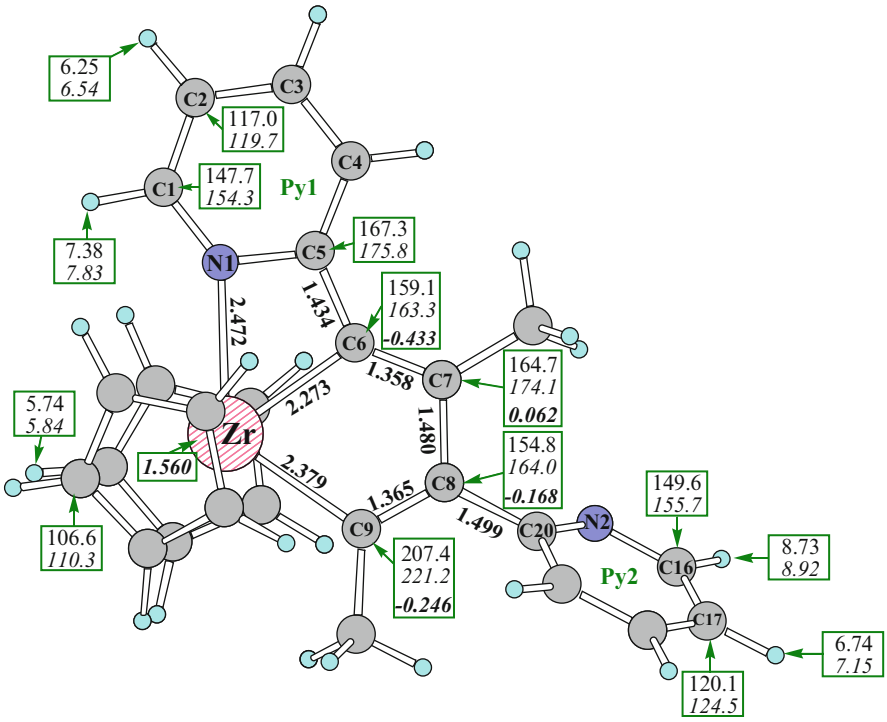

Fig. 1 Optimized structure of **10n** (in this model, methyl groups were used instead of propyl groups), selected ^{13}C and ^{1}H chemical shifts (normal for experimental values, italic for calculated results), NBO atomic charges (*bold italic*), and bond lengths (*bold*). Both the geometry optimization and the NMR studies were calculated at the B3LYP/6-311+G**/Lanl2DZ level

To find out the origin of the large electron density on C6, the three models in Fig. 2 were studied. In model **A**, the coordination effect of Py1 can be excluded. This model is nonplanar, but the two pyridines are conjugated to some extent with the two double bonds. The NBO charge distribution shows that C6 has larger negative charges than C9. This apparently can be explained by resonance electronic effects of the two pyridine rings and the hyperconjugation effect of the two methyl groups. In model **B**, the positions of Py1 and Py2 are equivalent, but Py1 is twisted with C6 and C7 and Py2 is coplanar with C9 and C8 (dihedral angle N1–C11–C6–C7 is $-149.4°$, dihedral angle N2–C10–C9–C8 is $0.8°$). Consequently, C9 has larger negative charges than C6. This result indicates that good conjugation will increase resonance electronic effects. In model **C**, Py1 is rotated to $-67.0°$ (the same as that of Py2 in Fig. 1) with the Zr–C6–C7 plane. The conjugation effect of Py1 with C6–C7–C8–C9 is reduced. As a result, the difference of the negative charges on C6 and C9 decreased from 0.187 (see Figs. 1 and 2) to 0.079. So the resonance electron effects and the coordination of Py1 should mainly account for the larger negative charges on C6.

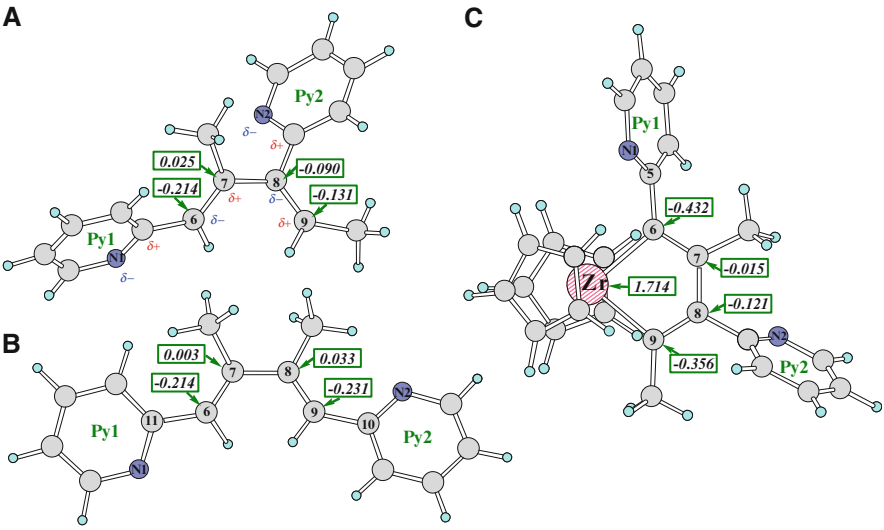

Fig. 2 The optimized structures of models **A**, **B**, and **C** with selected NBO atomic charges, calculated at the B3LYP/6-311+G**/Lanl2DZ level

2 The Origin of the Stereoselectivity in the Synthesis of β-Hydroxyallenes

2.1 Experimental Background

The development of new methods to synthesize molecules with multiple stereogenic centers in one flask is very important in organic synthesis [13]. Functionalized allenes are of great interest since they serve as versatile synthetic intermediates in many asymmetric syntheses. Under mild conditions, stereoselective synthesis of β-hydroxyallenes was obtained via aldehyde addition to α-alkenyl-substituted zirconacyclopentenes (Scheme 2). The product **5** has two contiguous stereogenic centers and an adjacent axial chirality.

To understand the stereoselectivity of this reaction, DFT [5, 6] studies have been performed with GAUSSIAN03 program [7] using B3LYP [8, 9] method. For C, H, O, 6-311+G** basis set was used; for Zr, Lanl2DZ basis set with ECP [10] was used. Harmonic vibration frequency calculation was carried out and the optimized structures are all shown to be transition states with one imaginary frequency. In the calculation models, R^1 = Me, R^2 and R^3 = Ph. The results are shown in Fig. 3.

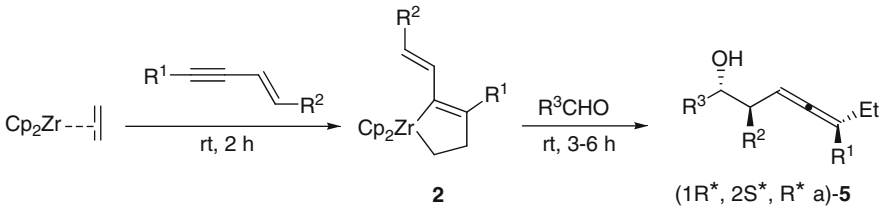

Scheme 2 Stereoselective formation of β-hydroxyallenes with multiple stereogenic centers

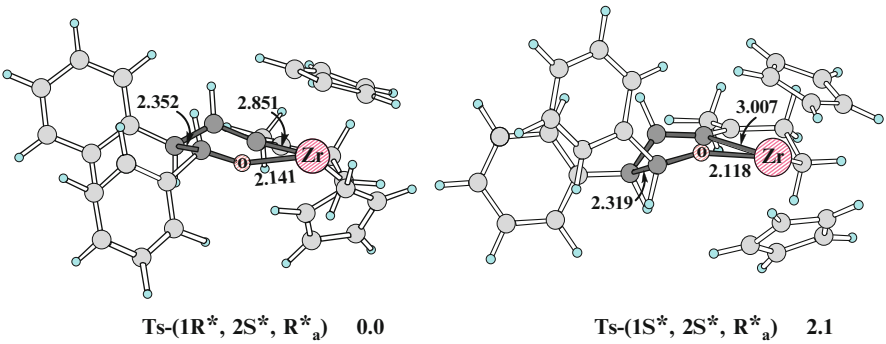

Fig. 3 The optimized six-membered transition structures with selected bond lengths (in angstroms). Their relative Gibbs free energies are in kcal/mol. Calculated at the B3LYP/6-311+G**/Lanl2DZ level

2.2 Results and Discussion

The results show that the configuarion of the favorable transition states of *E*-enyne product (**Ts-(1R*, 2S*, R*$_a$)**) is consistent with the experimental products. In this transition state, the C4–O–Zr six-membered ring is in a stable *chair* conformation, whereas in **Ts-(1S*, 2S*, R*$_a$),** the C4–O–Zr six-memberd ring is in an unstable *boat* conformation. The relative stabilities of **Ts-(1R*, 2S*, R*$_a$)** and **Ts-(1S*, 2S*, R*$_a$)** may be understood this way: if the position of the phenyl group and the hydrogen atom of the aldehyde are exchanged in **Ts-(1R*, 2S*, R*$_a$)**, we get **Ts-(1S*, 2S*, R*$_a$)**. Obviously, if the C4–O–Zr six-memberd ring still keeps its *chair* conformation, the phenyl group of the aldehyde will eclipse with the Cp ring. Therefore, the C4–O–Zr six-membered ring must be deformed to avoid this large steric effect. Therefore, the stereoselectivity of this reaction originates from the steric effect of the phenyl group of the aldehyde and the Cp ring.

3 Mechanistic Study on the Generation of Allenic/Propargylic Zirconium Complexes

3.1 Experimental Background

Organozirconium compounds are attractive intermediates in an impressive array of synthetic methodology and have received much attention in recent years [14]. Among various possibilities for the generation of organozirconium reagents, low-valent zirconium-induced β-alkoxide elimination reaction is a particularly attractive protocol.

Allenic/propargylic zirconium species can be conveniently prepared by treatment of propargylic ethers with dibutylzirconocene complex (Scheme 3). In principle, both allenic **3** and propargylic zirconium species **4** could be formed under the reaction conditions, and there exists an equilibrium between the two species. The intermediate **3/4** will lead to allenes and/or alkynes after hydrolysis. The R^1 group of the propargyl ethers is crucial to the product type: aryl-substituted propargylic ethers favor the allene products (**1g**), while TMS-substituted propargylic ethers afford alkynes (**1m**, **1n**). However, the in situ NMR of the reaction with TMS-substituted propargylic ethers **1n** shows that the allenic zirconium species

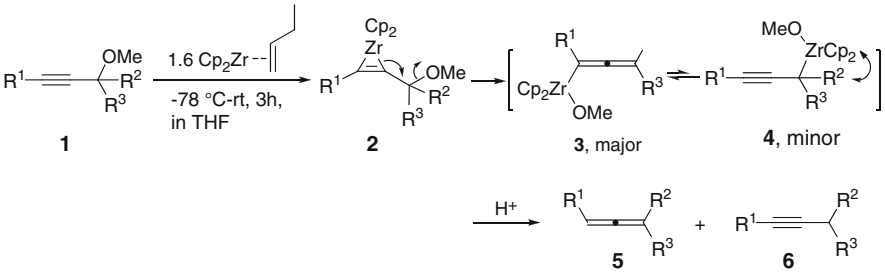

Selected results:

Propargyl ether	Product(**5**)	Yield(%)	Product(**6**)	Yield(%)
1g	**5g**	64	-	
1m	-		**6m**	60
1n	-		**6n**	55

Scheme 3 Formation of allenes and/or alkynes by the reaction of Cp2ZrBu2 with propargyl ethers

3n (R^1 = TMS, R^2, R^3 = $-(CH_2)_5-$) was formed as a major zirconium species (90% NMR yield) according to ^1H and ^{13}C NMR spectra.

3.2 Results and Discussion

*The equilibrium of intermediates **3** and **4**.* To better understand the structure of intermediates **3** and **4**, DFT [5, 6] studies have been performed with the GAUSSIAN03 program [7] using the B3LYP [8, 9] method. For C, H, O, Cl, and Si, the 6-311+G** basis set was used; for Zr, the Lanl2DZ basis set with ECP [10] was used. The optimized structures were all checked with harmonic vibration frequency calculations. The structures of allenic zirconium species **3g** (R^1= Ph, R^2= R^3 = Me), propargylic zirconium species **4g**, and the transition states for their rearrangement **TS–3g–4g** have been fully optimized with complete models (Fig. 4). For the TMS-substituted propargylic ether **1m**, the simplified model **3m′** with R^2 = R^3 = Me was used. To find out the effect of the R^2 and R^3 groups, the model **3g′** with R^1 = Ph and R^2 = R^3 = H was also studied.

The results indicate that the allenic structure **3g** is more stable than the propargylic structure **4g** by about 11.4 kcal/mol. Therefore, the allenic structure **3g** should be dominant under room temperature. The barrier of the rearrangement from **3g** to **4g** (**TS–3g–4g**) is 23.3 kcal/mol. For **3m′**, the situation is similar. Therefore, R^1 has a small effect on the equilibrium of **3** and **4**. The barriers of the rearrangement are over 23 kcal/mol, which indicates a reaction being completed within hours. Since the hydrolysis of **3g** and **3m** by 3 N HCl can be completed within minutes, the hydrolysis via the propargylic pathway can be excluded safely. Interestingly, the propargylic structure **4g′** is more stable than the allenic structure **3g′** by 1.5 kcal/mol, and the rearrangement barrier (**TS–3g′–4g′**) is also dropped to 12.7 kcal/mol, indicating that R^2 and R^3 have a great effect on the relative stabilities of **3** and **4**. The C–Zr bond lengths in **4g** (2.437 Å) and **4m′** (2.434 Å) are much longer than that in **4g′** (2.364 Å), **3g** (2.347 Å), and **3m′** (2.327 Å). This indicates that the large repulsion between the R^2/R^3 and the Cp rings decreases the interaction of the carbanion and the metal center. Consequently, the energies of the propargylic structures are increased [15, 16].

To further confirm that the allenic structure **3** is dominant under room temperature, the ^{13}C chemical shifts of **3n** were calculated by the GIAO method [12]. The selected results are shown in Fig. 5. The calculated NMR shifts are in good agreement with the experimental values.[1]

The origin of the regioselectivity in the hydrolysis reaction. The mechanisms of the hydrolysis of **3g** and **3m′** by 3 N HCl have been studied with the models shown in Fig. 6. In these models, both the proton H^+ and the Cl^- ion were solvated by an

[1] The experimental NMR shift of C6 might be overlapped with Cp impurities in the range of 110.3–114.1 ppm.

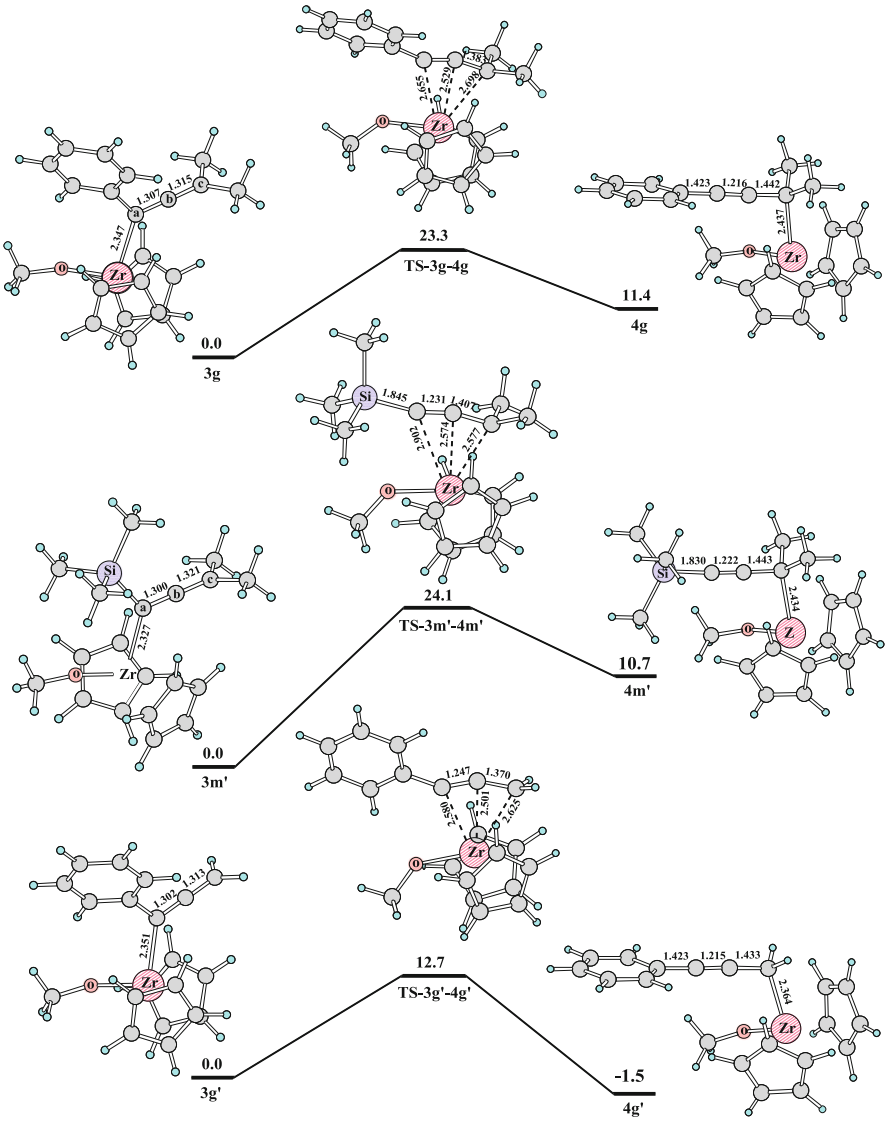

Fig. 4 Optimized allenic structures **3g** (R^1 = Ph, R^2 = R^3 = Me), **3m′** (R^1 = TMS, R^2 = R^3 = Me), and **3g′** (R^1 = Ph, R^2 = R^3 = H); the propargylic structures **4g**, **4m′**, and **4g′**; and the rearrangement transition states **TS-3g-4g**, **TS-3m′-4m′** and **TS-3g′-4g′**. The selected bond lengths are in angstroms, and the relative free energies Δ*G* are in kcal/mol. Calculated at the B3LYP/6-311+G**/Lanl2DZ level

explicit water molecule. The long-range solvent effect was estimated with IEFPCM [17, 18] (UAHF atomic radii) method in water (ε = 78.39) using the gas-phase optimized structures. The atomic charges were calculated by NBO natural bonding analysis [11]. As shown in Fig. 6, in transition states **TS–3g–alkyne** and

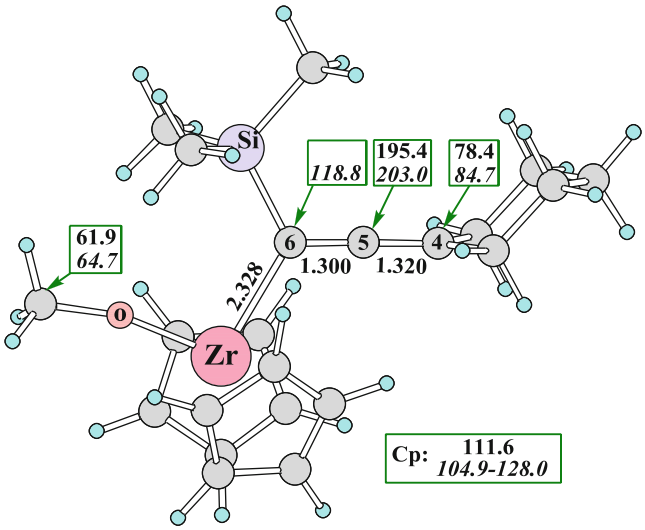

Fig. 5 Optimized structure of **3n**, the selected ^{13}C chemical shifts (regular font for experimental values, and italic for calculated results), and bond lengths (in angstroms). Both the geometry optimization and the NMR studies were calculated at the B3LYP/6-311+G**/Lanl2DZ level

TS–3m′–alkyne, the protons attack C_c and lead to alkyne products, whereas in transition states **TS–3g–allene** and **TS–3m′–allene**, the protons attack C_a and lead to allene products. **TS–3g–allene** is 6.8 kcal/mol lower in energy than **TS–3g–alkyne**; however, **TS–3m′–allene** is 4.7 kcal/mol higher in energy than **TS–3m′–alkyne**, which is well consistent with the experimental observations: **3g** favors the allenic product, whereas **3m′** favors the alkyne product.

Generally, in the allenic zirconium complexes **3g** and **3m′**, the carbon atom that is connected with the Zr center (C_a) possesses a greater negative charge. In **3g**, the NBO charges on C_a and C_c are −0.465 and −0.158, respectively; in **3m′**, the NBO charges on C_a and C_c are −0.901 and −0.198, respectively. Consequently, C_a is more easily attacked by the proton. This is the case for **3g**. However, the situation may be changed by the steric effect of R^1, R^2, and R^3. Obviously, in **TS–3g–allene**, the flat phenyl group causes small steric energy on the attack of the proton, whereas in **TS–3m′–allene**, the bulky TMS group will cause large steric repulsion. **3g** or **3m′** will be distorted on the attack of the proton. This distortion is to some extent caused by the steric effect of R^1, R^2, R^3 and the Cp rings. Therefore, the steric energies in the four transition states were estimated by the distortion energy (**DE**) [19]. **DE** was calculated by this way: for the four transition states shown in Fig. 6, the HCl and the two H_2O molecules were deleted with the rest part unchanged, and then the single-point energies were calculated. Using the undistorted **3g** and **3m′** as the zero-point references, the relative distortion energies for the four transition states were obtained. As shown in Fig. 6, the **DE** of **TS–3m′–allene** is 3.3 kcal/mol higher than that of **TS–3m′–alkyne**, whereas the **DE** of **TS–3g–allene** is nearly the same as that of **TS–3g–alkyne**. Thus, the steric effect is one of the important factors to determine the selectivity.

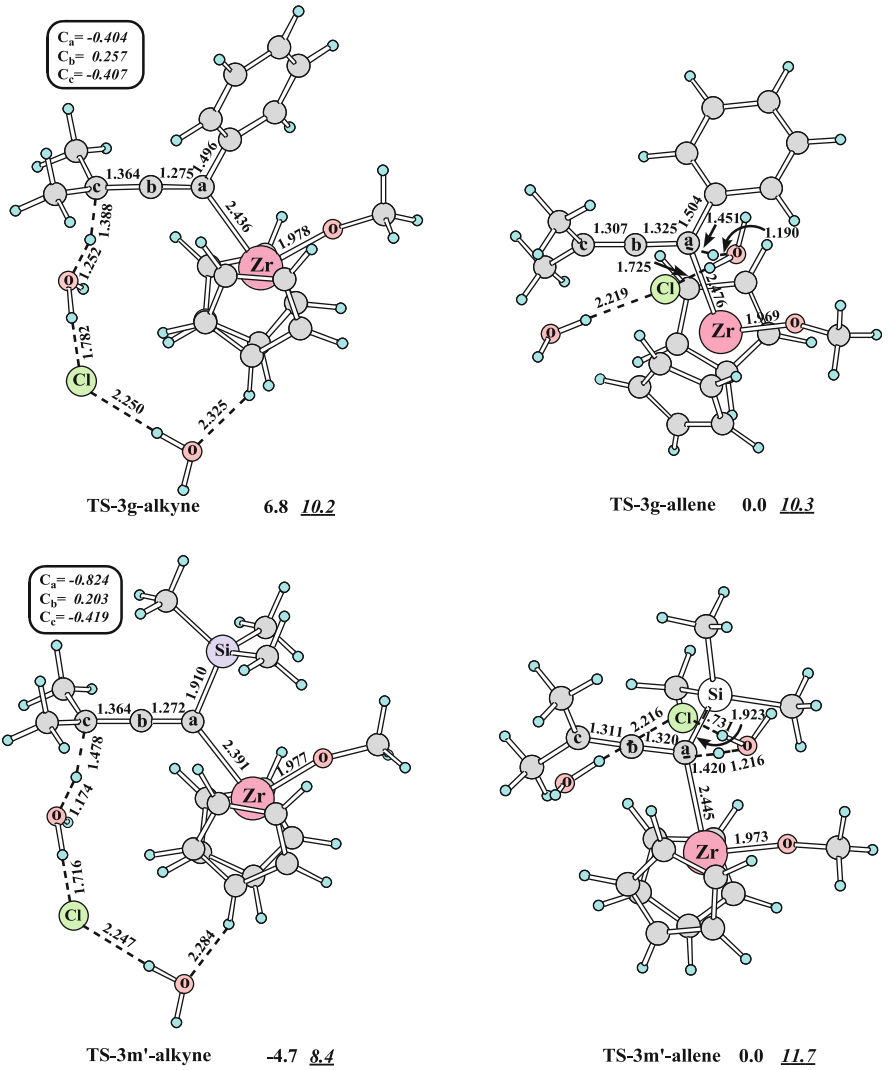

Fig. 6 Optimized transition states for the hydrolysis reaction. The selected NBO charges for C_a, C_b and C_c are given in the *box*. The selected bond lengths (*bold*) are in angstroms, and the relative free energies including solvent effect ΔG_{sol} (*bold*) and the relative distortion energies (**DE**, *italic underlined*) are in kcal/mol. Calculated at the B3LYP/6-311+G**/Lanl2DZ level

On the contrary, for the transition states to form alkyne products, the attack of the proton on C_c will arouse positive charges on C_b. The calculated NBO atomic charge of C_b in **TS–3m′–alkyne** is 0.203. It is smaller than that of C_b in **TS–3g–alkyne** (0.257), indicating that TMS group can stabilize the positive charges on C_b. This can be explained by the well-known β-effect [20] of the TMS group, i.e., the hyperconjugation of the C_a–Si σ bond with the partially

positive charged *p* orbital on the β position (C_b). Thus both the large steric effect and the β-effect of the TMS group favor the alkyne product, reversing the selectivity.

4 Mechanistic Study on Aldehyde Addition to 1,3-Butadiyne-Derived Zirconacyclocumulenes: Stereoselective Synthesis of *cis*-[3]Cumulenols

4.1 Experimental Background

Zirconacycles have attracted a lot of attention due to their versatile utility in organometallic and organic synthesis (for reviews, see [21–31]). The successful isolation of highly reactive metal species well accelerated the development in this area. It was demonstrated that zirconacycles with a cumulenic structure could be formed during the coupling process (for reviews, see [32–41]). The direct addition of aldehydes to zirconacyclocumulenes affords an efficient access to synthetically useful [3]cumulenols with high regio- and stereoselectivity [42].

The reaction of zirconacyclocumulenes **2/3** with aldehydes affords *cis*-[3]cumulenol **5** smoothly (Scheme 4). This reaction occurred exclusively at the cumulenic zirconium moiety.

To understand the high regioselectivity in the reaction of zirconacycle **2/3** (R^1 = Ph) with aldehyde, DFT [5, 6] studies have been performed with the GAUSSIAN03 program [7] using the B3LYP [8, 9] method. For C, H, O, the 6-311+G** basis set was used; for Zr, the Lanl2DZ basis set with ECP [10] was used. For each optimized structure, harmonic vibrational frequency calculation was carried out and thermal corrections were made. All structures were shown to be either transition states (with one imaginary frequency) or local minima (with no

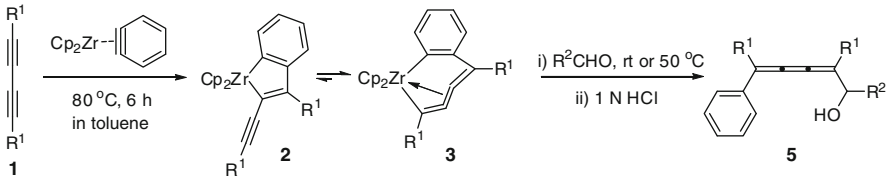

Selected result:

butadiyne	aldehyde	product		yield(%)[a]
Ph—≡—≡—Ph (**1a**)	CHO	Ph, Ph, Ph, Ph, HO	**5a**	83

Scheme 4 Formation of *cis*-[3]Cumulenols via the reaction with aldehydes

imaginary frequency). The solvent effect was estimated with IEFPCM [17, 18] (UAHF atomic radii) method in toluene ($\varepsilon = 2.379$) using the gas-phase optimized structures.

4.2 Results and Discussion

The structure of ***2a*** *and* ***3a***. First, two possible isomers of the zirconacycle intermediates **2a** and **3a** have been fully optimized (Fig. 7). The results indicate that the seven-membered structure **3a** is −1.7 kcal/mol more stable than the five-membered structure **2a**. Therefore, **3a** should be dominant under room temperature. The transition state of the isomerization from **2a** to **3a** has also been located (**TS–2a–3a**). The isomerization barrier is only 4.1 kcal/mol. The low barrier of this isomerization indicates that the seven-membered zirconacyclocumulene may be formed via the five-membered zirconacyclic intermediate [43, 44].

Both experimental and theoretical studies of the seven-membered zirconacyclocumulenes have been reported [43, 45, 46]. The stability of the seven-membered zirconacyclocumulene has been ascribed to the interaction between one of the Zr *d* orbital with one terminal σ orbital and the in-plane π orbital of the cumulene, forming σ type covalent bonding interaction [46]. The molecule orbital analysis shown in Fig. 8 is consistent with this conclusion (Fig. 8, HOMO-2). In HOMO-4, the Zr d_z^2 orbital overlaps with the sp^2 hybridized orbital of C1, forming the Zr–C1σ covalent bond.

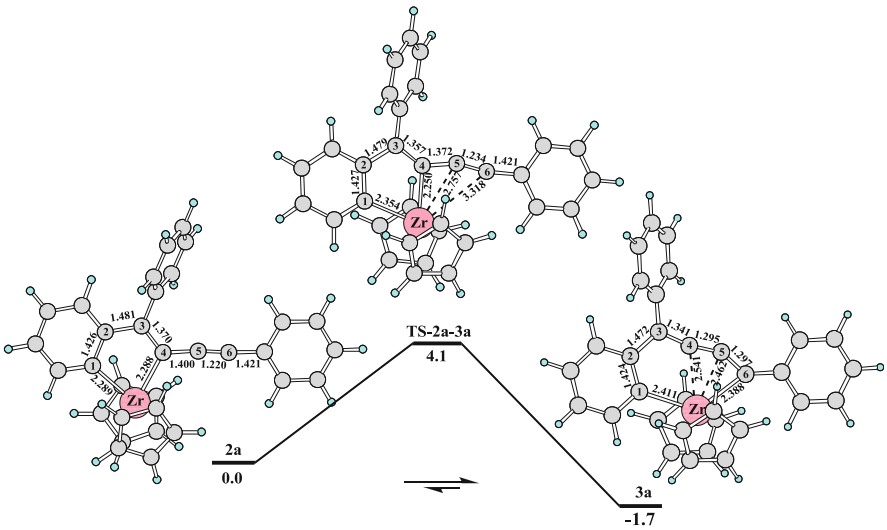

Fig. 7 The optimized five-membered structure **2a**, the seven-membered structure **3a**, and their isomerization transition state **TS-2a-3a**. The relative free energies including solvent effect ΔG_{sol}(298 K) are in kcal/mol (calculated at the B3LYP/6-311+G** level)

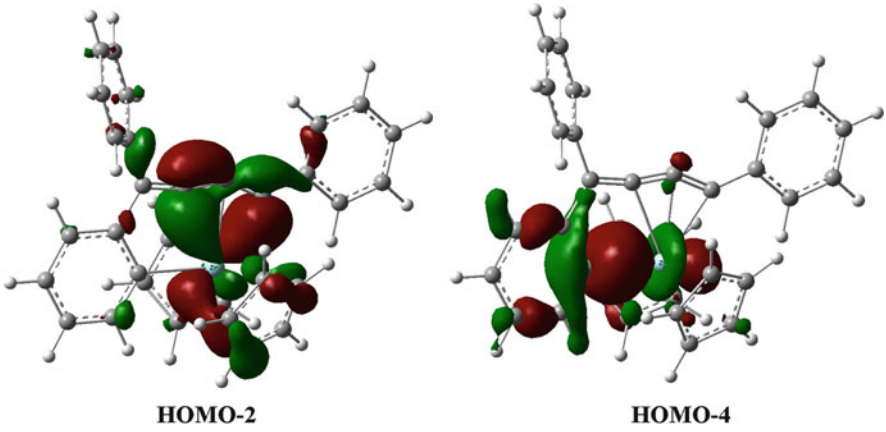

Fig. 8 The HOMO-2 and HOMO-4 molecule orbitals of **3a** (depicted using isodensity at 0.04 au). HOMO-2 is involved in the interaction of C4, C6, and the Zr center. HOMO-4 shows that the C1-Zr σ bond is formed by the overlap of the Zr d_z^2 orbital with the C1 sp^2 hybridized orbital

In a previous study of the α-alkynylzirconacyclopentenes [47], a similar five-membered/seven-membered ring equilibrium has been found (Fig. 9). Actually, according to NMR analysis of the zirconium intermediate, it was suggested that the structure of the major zirconium intermediate might be best described as the seven-membered zirconacycle. Theoretical calculations show that the zirconacyclocumulenes are thermodynamically more stable than the isomeric zirconacyclopentenes, and the calculated NMR shifts of the zirconacyclocumulene structures are in good agreement with the experimental values.

The origin of regioselectivity. The transition states for the insertion of aldehyde into the zirconacycle have been explored first with the seven-membered structure **3a**, since it is more stable than **2a**. In the calculation, as the aldehyde becomes close to C6, the seven-membered ring **3a** will convert to five-membered ring **2a** before reaching the insertion transition state. This result is also confirmed by the relaxed potential energy surface (PES) scan along the Zr–O and C7–C6 bonds (Fig. 10).

In **3a**, the Zr center is buried deeply, and C1 and C6 are shielded more tightly. Therefore, the attack of the aldehyde will encounter large steric hindrance. Thus, the five-membered ring is less stable and has higher reactivity. The former calculation shows that seven-membered ring and five-membered ring are easy to convert to each other. Therefore, as shown in Fig. 11, the insertion reaction was studied based on the complex of the five-membered structure **2a** and the aldehyde PhCHO (**R**).

The calculation results show that **Path 2** is more favorable; its activation barrier is lower than that of **Path 1** by 11.9 kcal/mol. This result is consistent with the experimental observations. Apparently, if the aldehyde inserts into the Zr–C4 bond, a large steric interaction will be encountered with the alkynyl group. We propose that the steric factor is important to the preference of **TS2**. As shown in Fig. 11, the alkynyl group is sticking out, and the attack of C7 to C6 only causes little steric energy. In contrast, in **TS1**, the aldehyde pushes the Cp rings aside since the Zr–C1

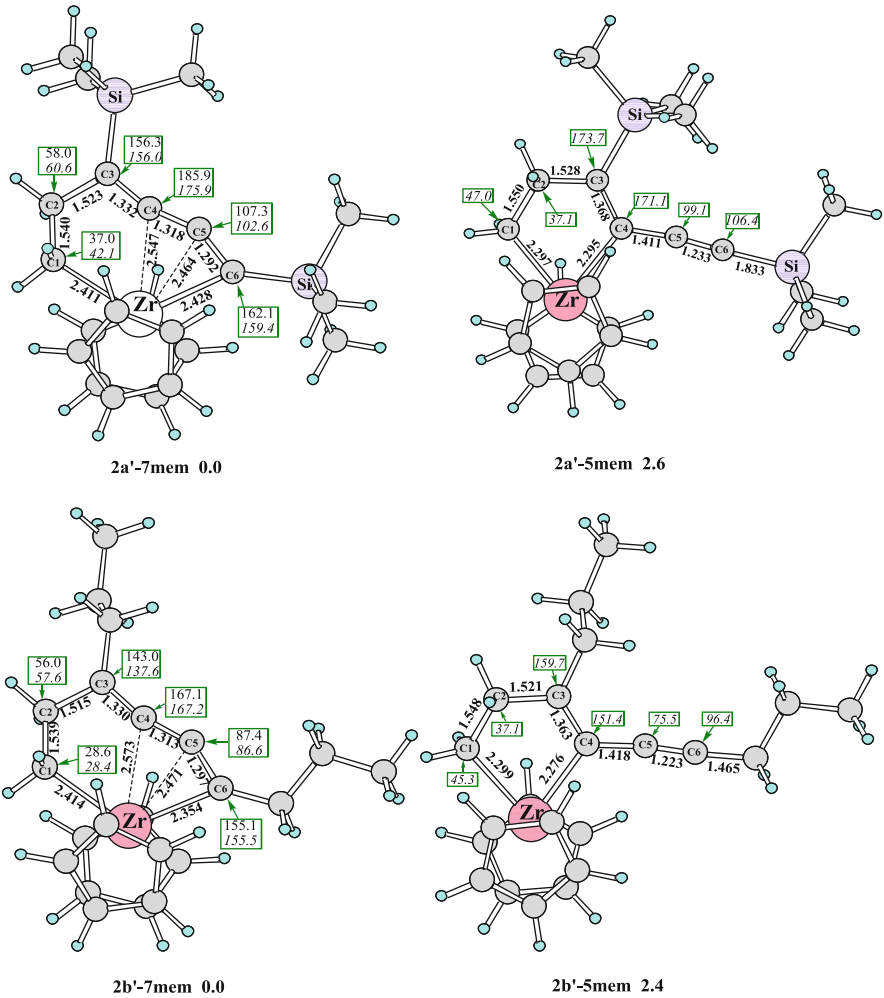

Fig. 9 The optimized isomers of **2a**′ and **2b**′, the selected ^{13}C chemical shifts (normal for experimental values, italic for calculated results, the assignment of the chemical shifts of C1–C6 for experimental values is based on the 2D NMR results), and the bond lengths (*bold*, in angstroms). The relative energies are in kcal/mol. Both the geometry optimization and the NMR studies were calculated at the B3LYP/6-31 + G*/Lanl2DZ level

bond is partially shielded by the two Cp rings. In addition, compared with **TS1**, the oxygen atom in **TS2** coordinated with the Zr center with a shorter distance (2.182 vs. 2.272 Å) and a better angle (the lone pair of the O atom pointing to the Zr center). Product **P1**, which is not obtained in the experiment, is much stable than product **P2**, so this reaction is kinetic controlled. The structure of **TS2** indicates that to form a *trans* product is impossible; therefore, the *cis* product should be dominant.

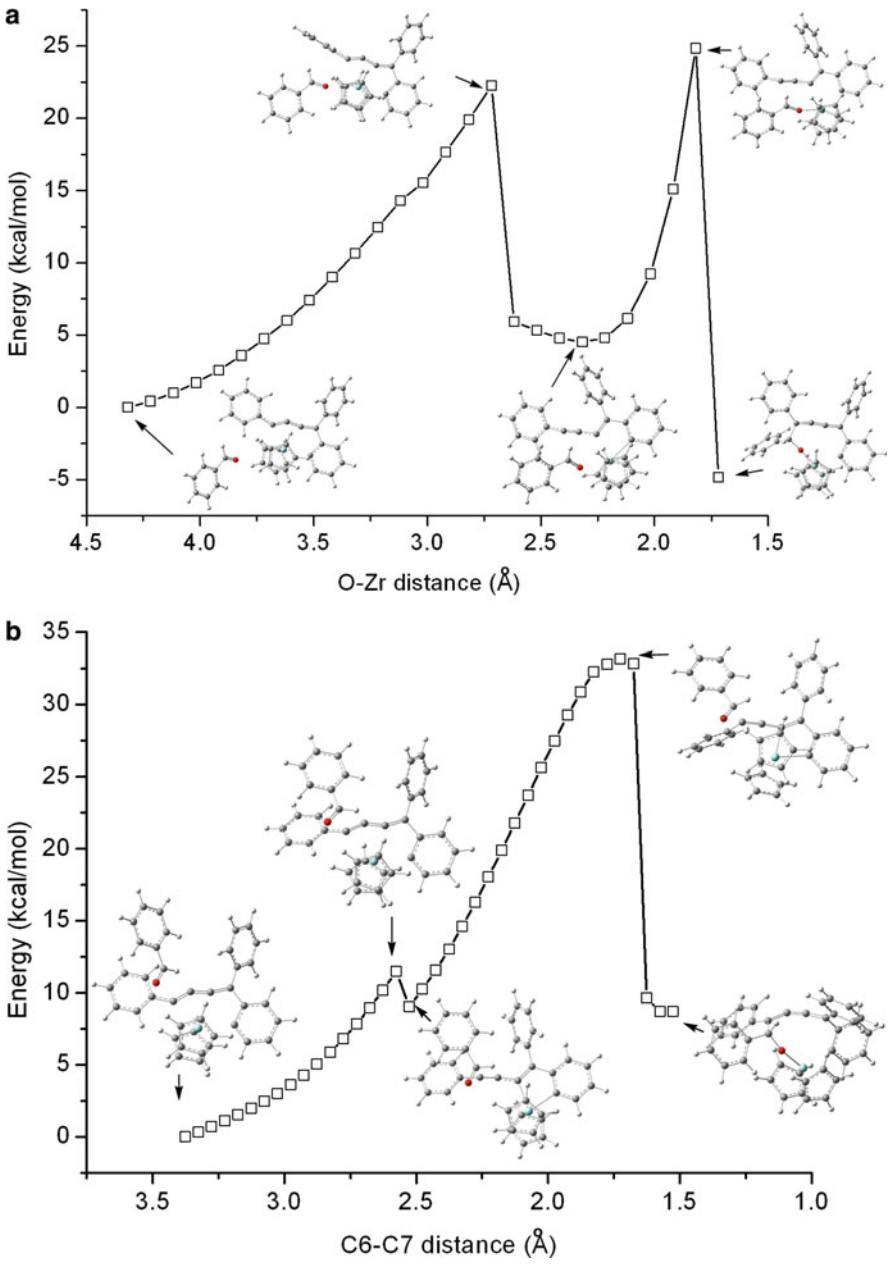

Fig. 10 (**a**) Scan along the O–Zr direction. The results show that **2a** transformed to **3a** before reaching the insertion transition state. (**b**) Scan along the C6–C7 direction. The results show that **2a** transformed to **3a** before the C6–C7 bond formation

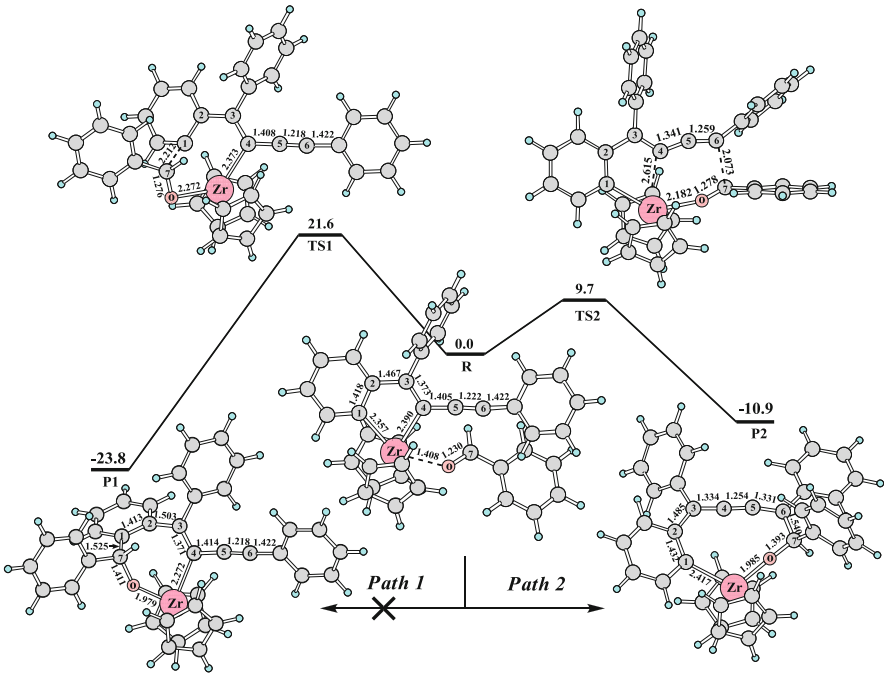

Fig. 11 The insertion of aldehyde from the *left side* (**Path 1**) and the *right side* (**Path 2**) of the zirconacycle **2a**. **TS1** and **TS2**: The optimized transition states for the insertion reaction. The relative free energies including solvent effect ΔG_{sol} (298 K) are in kcal/mol (calculated at the B3LYP/6-311+G**/Lanl2DZ level)

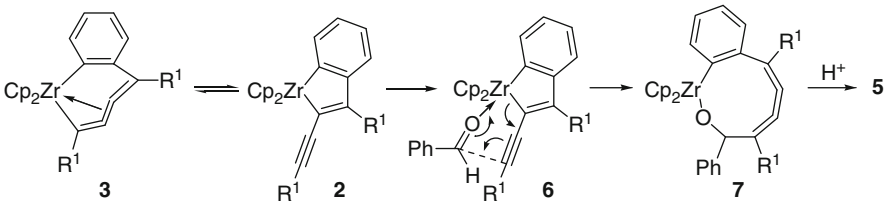

Scheme 5 Possible reaction mechanism for the synthesis of cumulenols

Considering the experimental data and DFT calculations disclosed above, a possible reaction mechanism for the synthesis of cumulenols is outlined in Scheme 5: First of all, a fast equilibrium between seven-membered zirconacycle **3** and five-membered zirconacycle **2** exists in the reaction mixture, in which **3** is more stable, whereas **2** is more reactive. The addition of carbonyl group to the propargyl zirconium moiety in **2** proceeds to generate a nine-membered oxazirconacycle **7** via a cyclic S_E2' process, and hydrolysis of **7** affords the cumulenol **5**.

References

1. Song Z, Li Y, Liu M, Cong L, Liu Y (2006) Organometallics 25:5035
2. Liu Y, Liu M, Song Z (2005) J Am Chem Soc 127:3662
3. Harrison RM, Brotin T, Noll BC, Michl J (1997) Organometallics 16:3401
4. Yamamoto Y, Arakawa T, Itoh K (2004) Organometallics 23:3610
5. Hohenberg P, Kohn W (1964) Phys Rev 136:B864
6. Kohn W, Sham L (1965) J Phys Rev 140:A1133
7. Frisch MJ, Trucks GW, Schlegel HB, Scuseria GE, Robb MA, Cheeseman JR, Montgomery JA Jr, Vreven T, Kudin KN, Burant JC, Millam JM, Iyengar SS, Tomasi J, Barone V, Mennucci B, Cossi M, Scalmani G, Rega N, Petersson GA, Nakatsuji H, Hada M, Ehara M, Toyota K, Fukuda R, Hasegawa J, Ishida M, Nakajima T, Honda Y, Kitao O, Frisch MJ, Nakai H, Klene M, Li X, Knox JE, Hratchian HP, Cross JB, Adamo C, Jaramillo J, Gomperts R, Stratmann RE, Yazyev O, Austin AJ, Cammi R, Pomelli C, Ochterski JW, Ayala PY, Morokuma K, Voth GA, Salvador P, Dannengerg JJ, Zakrzewski VG, Dapprich S, Daniels AD, Strain MC, Farkas O, Malick DK, Rabuck AD, Raghavachari K, Foresman JB, Ortiz JV, Cui Q, Baboul AG, Clifford S, Cioslowski J, Stefanov BB, Liu G, Liashenko A, Piskorz P, Komaromi I, Martin RL, Fox DJ, Keith T, Al-Laham MA, Peng CY, Nanayakkara A, Challacombe M, Gill PMW, Johnson B, Chen W, Wong MW, Gonzalez C, Pople JA (2004) Gaussian 03, Revision C.02. Gaussian Inc, Wallingford, CT, USA
8. Becke AD (1993) J Chem Phys 98:5648
9. Lee C, Yang W, Parr RG (1988) Phys Rev B37:785
10. Wadt WR, Hay PJ (1985) J Chem Phys 82:284
11. Reed AE, Curtiss LA, Weinhold F (1988) Chem Rev 88:899–926
12. Ditchfield R (1974) Mol Phys 27:789–807
13. Zhou Y, Chen J, Zhao C, Wang E, Liu Y (2009) J Org Chem 74:5326–5330
14. Zhang H, Fu X, Chen J, Wang E, Liu Y (2009) J Org Chem 74:9351–9358
15. Ito H, Nakamura T, Taguchi T, Hanzawa Y (1995) Tetrahedron 51:4507
16. Ito H, Nakamura T, Taguchi T, Hanzawa Y (1992) Tetrahedron Lett 33:3769
17. Cances E, Mennucci B, Tomasi J (1997) J Chem Phys 107:3032
18. Cossi M, Barone V, Mennucci B, Tomasi J (1998) Chem Phys Lett 286:253
19. Legault CY, Garcia Y, Merlic CA, Houk KN (2007) J Am Chem Soc 129:12664–12665
20. Lambert JB (1990) Tetrahedron 46:2677
21. Hu Q, Lu J, Wang C, Wang C, Xi Z (2007) Tetrahedron 63:6614
22. Marek I (Ed) (2002) Titanium and Zirconium in organic synthesis. Wiley-VCH, Weinheim
23. Negishi E, Takahashi T (2003) Organometallic Complexes of Zirconium and Hafnium. In: Imamoto T (Ed) Science of synthesis (Houben-Weyl Methods of Molecular Transformations). Georg Thieme, Germany, pp 681–848
24. Takahashi T, Xi Z, Hara R (1997) Trends Organomet Chem 2:117
25. Rosenthal U, Burlakov VV, Arndt P, Baumann W, Spannenberg A (2005) Organometallics 24:456
26. Xi Z, Li Z (2004) Top Organomet Chem 8:27
27. Buchwald SL (1993) Science 261:1696
28. Kotora M, Xi Z, Takahashi TJ (1997) Synth Org Chem Jpn 55:958
29. Negishi E, Takahashi T (1998) Bull Chem Soc Jpn 71:755
30. Takahashi T, Xi Z, Kotora M (1998) Pure Appl Chem 2:515
31. Takahashi T, Kotora M, Hara R, Xi Z (1999) Bull Chem Soc Jpn 72:2591
32. Rosenthal U, Burlakov VV, Arndt P, Baumann W, Spannenberg A (2005) Organometallics 24:456 and the references therein
33. Rosenthal U, Burlakov VV, Arndt P, Baumann W, Spannenberg A (2003) Organometallics 22:884
34. Rosenthal U (2003) Angew Chem 115:1838
35. Rosenthal U (2003) Angew Chem Int Ed 42:1794

36. Rosenthal U (2004) Angew Chem 116:3972
37. Rosenthal U (2004) Angew Chem Int Ed 43:3882
38. Rosenthal U, Arndt P, Baumann W, Burlakov VV, Spannenberg AJ (2003) Organomet Chem 670:84
39. Rosenthal U (2004) In: Diederich F, Stang PJ, Tykwinski RR (eds) Modern acetylene chemistry II–Chemistry, biology, and material science, Chap 4. Wiley-VCH, Weinheim, p 139
40. Rosenthal U, Pellny P, Kirchbauer FG, Burlakov VV (2000) Acc Chem Res 33:119
41. Hsu DP, Davis WM, Buchwald SL (1993) J Am Chem Soc 115:10394
42. Fu X, Liu Y, Li Y (2010) Organometallics 29:3012
43. Pellny P-M, Kirchbauer FG, Burlakov VV, Baumann W, Spannenberg A, Rosenthal U (1999) J Am Chem Soc 121:8313
44. Bredeau S, Ortega E, Delmas G, Richard P, Fröhlich R, Donnadieu B, Kehr G, Pirio N, Erker G, Meunier P (2009) Organometallics 28:181
45. Hsu DP, Davis WM, Buchwald SL (1993) J Am Chem Soc 115:10394
46. Bredeau S, Delmas G, Pirio N, Richard P, Donnadieu B, Meunier P (2000) Organometallics 19:4463
47. Chen J, Li Y, Gao H, Liu Y (2008) Organometallics 27:5619

Computational Organometallic Chemistry with Force Fields

Jing Huang, Michael Devereux, Franziska Hofmann, and Markus Meuwly

Abstract This chapter discusses molecular mechanics (MM)-based approaches to investigate organometallic complexes. In particular, ligand field MM (LFMM), "Sum of Interactions Between Fragments *Ab Initio*" (SIBFA), and VALBOND with its extension to VALBOND-TRANS are presented in some detail. Two particular applications of VALBOND-TRANS to an Ir(III) and a Pt(II) complex are presented. Possible future extensions, including the study of chemical reactions and polarization effects, are briefly discussed at the end.

1 Introduction

Theoretical and computational methods can be very helpful for understanding and predicting structure and reactivity in organometallic chemistry. Over the past decade, quantum chemical methods—in particular density functional theory (DFT)—have made steady progress in addressing questions of practical relevance for increasingly complex systems. Especially hybrid functionals including B3LYP [1, 2] have been found to provide good accuracy for a range of properties at moderate computational cost. However, despite the continuing effort in devising

J. Huang • F. Hofmann
Department of Chemistry, University of Basel, Klingelbergstr 80, Basel CH 4056, Switzerland

M. Devereux
Department of Chemistry, University of Basel, Klingelbergstr 80, Basel CH 4056, Switzerland

IFR Laboratoire de Chimie et Biochimie Pharmacologique et Toxique, Université Paris Descartes, Paris, France

M. Meuwly (✉)
Department of Chemistry, University of Basel, Klingelbergstr 80, Basel CH 4056, Switzerland

Department of Chemistry, Brown University, Providence, RI, USA
e-mail: m.meuwly@unibas.ch

O. Wiest and Y. Wu (eds.), *Computational Organometallic Chemistry*,
DOI 10.1007/978-3-642-25258-7_2,

more general and more accurate functionals, all quantum methods invariably reach a point where they become computationally too demanding. In most cases, DFT calculations are limited to geometry optimizations of gas-phase structures or to model systems with smaller and sometimes unrealistic ligands. Dynamics simulations and calculations over large libraries of compounds are often impractical, and including the effect of solvent beyond implicit models is typically impossible. Therefore, having faster, even if approximate methods is desirable. Molecular mechanics (MM) force fields such as AMBER [3], CHARMM [4], or OPLS [5] have become standard methods in biomolecular chemistry and are routinely used for molecular dynamics simulations of systems with up to one million atoms. However, the development of general force fields for transition metal complexes has been relatively limited because of the unique difficulties presented by these types of compounds [6–8]: metals can have a variety of coordination numbers, π-binding ligands can bind in various ways, and electronic effects such as Jahn–Teller distortion or the trans influence need to be addressed.

The realization that the electronic Schrödinger equation can only be solved for small systems led to the development of important alternative approaches to study chemical reactivity. They date back to London's work on the $H+H_2$ reaction for which he used a 2×2 valence bond treatment [9]. Building on this, refined and extended approaches led to the London–Eyring–Polanyi (LEP) [10] and the London–Eyring–Polanyi–Sato (LEPS) surfaces [11, 12]. A development that continued the efforts to use valence bond theory to describe multistate chemical systems is the diatomics-in-molecules (DIM) theory [13]. Following a slightly different perspective, Pauling profoundly influenced the theoretical description of chemical reactivity through his work on molecular structure and the nature of the chemical bond [14, 15]. Significant relations, such as the one between bond length and bond order, later became foundations to empirical descriptions of reactivity [16, 17].

Explicit exclusion of all electronic effects leads to empirical force fields (FF). They were developed with the emphasis to carry out studies of the structure and dynamics of macromolecules, including peptides and proteins [3, 5, 18–23]. Thus, their primary application area was sampling and characterizing conformations of extensive molecular structures. The mathematical form of a generic FF is $V_{\mathrm{tot}} = V_{\mathrm{bond}} + V_{\mathrm{valence}} + V_{\mathrm{dihe}} + V_{\mathrm{elstat}} + V_{\mathrm{vdW}}$, where each of the terms is separately parametrized

$$
\begin{aligned}
V_{\mathrm{bond}} &= \sum K_{\mathrm{b}}(r - r_{\mathrm{e}})^2, \\
V_{\mathrm{valence}} &= \sum K_{\theta}(\theta - \theta_{\mathrm{e}})^2, \\
V_{\mathrm{dihe}} &= \sum K_{\phi}(1 + \cos(n\phi - \delta)), \\
V_{\mathrm{elstat}} &= \frac{1}{4\pi\varepsilon_0} \sum \frac{q_i q_j}{r_{ij}}, \\
V_{\mathrm{vdw}} &= \sum \varepsilon_{ij} \left[\left(\frac{R_{\mathrm{min},ij}}{r_{ij}} \right)^{12} - \left(\frac{R_{\mathrm{min},ij}}{r_{ij}} \right)^{6} \right].
\end{aligned}
\tag{1}
$$

The first three terms comprise "bonded" interactions, while the latter two describe the "nonbonded" ones. In these expressions, K represents the force constants associated with the particular type of interaction, r_e and θ_e are equilibrium values, n is the periodicity of the dihedral, and δ is the phase which determines the location of the maximum. The sums for the bonded terms are carried out over all atoms involved. Nonbonded interactions include electrostatic and van der Waals terms where the sums include all nonbonded atom pairs. q_i and q_j are the partial charges of the atoms i and j involved and ε_0 is the vacuum dielectric constant. For the van der Waals terms, the potential energy is expressed as a Lennard-Jones potential with well depth $\varepsilon_{ij} = \sqrt{\varepsilon_i \varepsilon_j}$ and range $R_{\min,ij} = (R_{\min,i} + R_{\min,j})/2$ at the Lennard-Jones minimum. This interaction captures long-range dispersion ($\propto -r^{-6}$) and exchange repulsion ($\propto r^{-12}$) where the power of the latter is chosen for convenience. The set of expressions in (1) constitutes a minimal model for a force field which might be extended by using explicit terms for hydrogen bonds or for metal-containing systems [24].

Building on the success of FFs for "simple" chemical and biological systems, attempts were made to not only retain their functional simplicity but also encode additional functionality to treat metal-containing systems. In the following, we describe several attempts to do this and discuss particular applications relevant to our own work. The chapter ends with an outlook.

2 Conceptual Approaches

In the following section, different techniques to investigate the energetics and dynamics of organometallic systems based on extensions of force field concepts are discussed.

2.1 Ligand Field Molecular Mechanics

Ligand field theory (LFT) can be considered as a combination of crystal field theory (CFT) and molecular orbital (MO) theory [25]. Unlike in CFT where interactions between ligands and center metal atoms are described with electronic interactions, LFT takes into account the overlap between atomic orbitals as ligands approach a metal center. Thus in LFT, the metal–ligand bonding is by its very nature partially covalent.

LFT is very successful in explaining magnetic and spectral properties of many transition metal complexes. In its framework, the perturbation Hamiltonian for separate ligands interacting with the metal center is assumed to be independent and additive. Thus, LFT can in principle be introduced into a MM force field. The first successful combination was made by Burton et al. [26]. Afterwards, Deeth and coworkers [24, 27–32] developed the approach gradually into a force field called

Ligand Field Molecular Mechanics (LFMM). Thus, LFMM is based on a combination of a conventional force field with terms explicitly capturing electronic effects, which takes the following functional form:

$$E_{\text{tot}} = E_{\text{bonds}} + E_{\text{angles}} + E_{\text{dihedrals}} + E_{\text{nonbonded}} + \text{LFSE}. \tag{2}$$

The essential part in (2) is the ligand field stabilization energy (LFSE). In LFMM, such an energy is obtained by diagonalizing a 5 × 5 ligand field potential matrix, with elements

$$\langle d_i | V_{\text{LF}} | d_j \rangle = \sum_{l}^{N} \sum_{k}^{3} F_{i,k}^{l} F_{k,j}^{l} e_k^l. \tag{3}$$

The first summation (l) is over all N metal–ligand interactions, while the second summation runs over three symmetry modes ($k = \sigma, \pi_x, \pi_y$). Whether certain symmetry modes are included or not depends on the ligand type. For example, only one term e_σ is required for saturated amines because they cannot interact with the metal through π-bonding [26].

In (3), the radial and angular parts of the M–L interactions are separated. The general form of a radial contribution e_λ is given by

$$e_\lambda = a_0 + a_1 r + a_2 r^{-2} + a_3 r^{-3} + a_4 r^{-4} + a_5 r^{-5} + a_6 r^{-6}, \tag{4}$$

where r is the metal–ligand bond length. In practice, most coefficients a_i zero and only one or two terms in (4) take effect, which decreases the number of force field parameters that need to be fitted.

All the angular dependence is encoded in the F factors as defined in the angular overlap model (AOM) [33, 34]. These angular overlap factors characterize the angular dependence of overlap integrals between atomic orbitals of the center atom and the ligand atom. A detailed expression of F functions in the ligand's angular coordinates (θ, φ, ψ) has been worked out by Schaeffer [35] and can be found in Table 1 in [34]. For instance, considering an octahedral complex with O_h symmetry, the six ligands have the following angular coordinates with respect to the metal center:

	1	2	3	4	5	6
θ	0	$\frac{\pi}{2}$	$\frac{\pi}{2}$	$\frac{\pi}{2}$	$\frac{\pi}{2}$	π
ϕ	0	0	$\frac{\pi}{2}$	π	$\frac{3\pi}{2}$	0

and if the ligand is unidentate, ψ may take an arbitrary value, e.g., 0. Then for the first ligand,

$$\begin{aligned} F^1_{z^2,\sigma} &= (1 + 3\cos 2\theta)/4 = 1, \\ F^1_{yz,\pi^y} &= \cos\phi\cos\theta\cos\psi - \cos\phi\cos 2\theta\sin\psi = 1, \\ F^1_{zx,\pi^x} &= -\sin\phi\cos\theta\sin\psi + \cos\phi\cos 2\theta\cos\psi = 1, \end{aligned} \tag{5}$$

and all the other F values equal zero. Similarly, all the non-zero F values for the fifth ligand are

$$\begin{aligned} F^5_{z^2,\sigma} &= (1 + 3\cos 2\theta)/4 = -\frac{1}{2}, \\ F^5_{x^3-y^2,\sigma} &= \frac{\sqrt{3}}{4}\cos 2\phi(1 - \cos 2\theta) = -\frac{\sqrt{3}}{2}, \\ F^5_{xy,\pi^y} &= \cos 2\phi \sin\theta \cos\psi - \frac{1}{2}\sin 2\phi \sin 2\theta \sin\psi = -1, \\ F^5_{yz,\pi^x} &= \cos\phi \cos\theta \sin\psi + \sin\phi \cos 2\theta \cos\psi = 1. \end{aligned} \tag{6}$$

Two additional energy terms e_{ds} and e_{pair} are then introduced to the LFSE for completeness, and they also take the functional form (4). The d–s mixing term, e_{ds}, characterizes the mixing between valence s orbital and d orbitals of the metal atom with matching symmetry. For example, in a planar D_{4h} $[CuCl_4]^{2-}$ system, such a configuration interaction between Cu 4s orbital with $3d_{z^2}$ need to be included to obtain the correct relative energies. The interelectronic repulsion term, e_{pair}, captures the effect of the two-electron d–d electrostatic interactions and is important for predicting the actual spin state.

The total LFMM energy is, therefore, calculated from an electronic term (LFSE) and additional terms that can be obtained from a conventional force field, such as AMBER [3], CHARMM [4], or the more complex MMFF [36]. Caution is needed when handling the energy terms involving metal atoms, such as the explicit metal–ligand bond energy $E_{\mathrm{M-L}}$. The functional forms may need to be adjusted and parameters refitted to lead to correct coordination geometries. For example, $E_{\mathrm{M-L}}$ is better described by a Morse function

$$E_{\mathrm{M-L}} = D_{\mathrm{e}}\{1 - \exp[\beta(r - r_0)]\}^2 - D_{\mathrm{e}} \tag{7}$$

with three parameters D_{e}, β, and r_0. Besides, the explicit L1–M–L2 angle bend term should be replaced by a simple ligand–ligand repulsive term to avoid double counting of energy.

The complete LFMM force field has been implemented in the molecular operating environment (MOE) as an extension named DommiMOE (d orbital molecular mechanics in MOE) [28]. LFMM has been applied extensively to copper complexes, from simple Cu(II) amines [29] to copper enzymes [32], and a variety of force field parameters for copper complexes are available. The parametrization is done by fitting the parameters in (4) to the crystallographic structure data provided by the Cambridge Structural Database [29, 30], while DFT calculation results are sometimes also involved in the fitting [32].

LFMM parameters for other transition metal complexes, such as manganese-, nickel-, and zinc-containing complexes, are also provided by Deeth and coworkers following a similar parametrization protocol [26, 30, 31]. The majority of applications of LFMM force fields concerns "first-low" transition metal complexes,

since the LFT is based on the assumption that the d shell of the metal center is weakly affected by the ligand environment. Applications to organometallic compounds are possible [27], but a valence bond approach based on hybridization schemes might be more feasible.

2.2 SIBFA

An alternative approach to modeling organometallic complexes within a classical molecular mechanics framework is the "Sum of Interactions Between Fragments Ab Initio" (SIBFA) method. Development of this force field began in the 1980s, with contributions from Claverie, Gresh, and Piquemal, among others [37–40]. SIBFA is a fragment-based approach employing a detailed force field that has been widely applied to organometallic systems, from small complexes to metalloproteins [41–44]. The force field explicitly accounts for anisotropic fragment polarization, repulsion and charge transfer, and incorporates distributed multipole moments centered at both nuclear positions and bond barycenters to describe electrostatics. The additional detail afforded by these energetic terms makes SIBFA more computationally expensive than less detailed force fields such as CHARMM [4] and AMBER [3], but as a consequence, SIBFA can yield molecular structures and energies that are in close agreement with ab initio data while maintaining a much lower computational overhead than would be required for a full ab initio computation. While the standard, most widely applied version of SIBFA affords close agreement in calculated interaction energies with ab initio reference data for a wide range of organic compounds and closed-shell organometallic systems (metals including Mg(II), Ca(II), Zn(II), and Cd(II)), a recent extension "SIBFA-LF" including ligand field effects via the AOM has extended the range of application to metal ions such as Cu(II) with partially filled d-shells. Both SIBFA and SIBFA-LF will be described in more detail in the following sections with examples of successful application of the method.

The basic premise of SIBFA is to build a force field that can account for each of the terms of an energy decomposition of the ab initio intermolecular interaction energy, as defined within the Restricted Variational Space Approximation (RVS) of Stevens and Fink [45]. Within the RVS scheme, the total interaction energy is broken down into first-order Coulomb (E_c) and exchange-repulsion (E_e) energies, and second-order polarization (E_{pol}) and charge transfer (E_{ct}). Agreement with correlated post-Hartree–Fock methodologies is achieved by inclusion of an additional dispersion energy term [46]. Faithful reproduction of these terms within the force field, including ligand dependence, radial dependence, and anisotropy, allows SIBFA to account for the total ab initio interaction energy for any conformation of an arbitrary complex as long as general parameters for the metal center and the fragments required to build up the ligands exist. In addition, short-range energetic corrections allow SIBFA to describe the formation of ligand–metal complexes without resorting to separate bonded and nonbonded parameters to describe the

bound and unbound states. A single, consistent parameter set is used to explore the binding, dissociation, and the relative energies of different tautomers and conformers. One limitation of the SIBFA approach is that parameters are only fitted for minimum energy conformers of each fragment used to build a molecule or complex. Individual fragment geometries are therefore kept frozen. This allows only torsional degrees of freedom within a molecule about fragment connection points, a limitation that is currently being addressed along with implementation of analytical gradients to allow the future application of SIBFA to molecular dynamics simulations.

Electrostatic Interaction Energy: Multipole moments used in SIBFA are derived from the ab initio charge density according to the procedure of Vigne-Maeder and Claverie [47]. E_{mtp} is truncated at quadrupole–quadrupole interactions. The sharing of multipoles between both atom and bond centers ensures improved short-range convergence of E_{mtp}. A recently extended formulation [42] also includes a penetration contribution to account for the overlap of molecular charge densities. Penetration becomes important at short range where significant overlap of the electron density of separate atoms or molecules takes place, and a standard multipolar expansion breaks down. Explicitly accounting for overlap is, therefore, necessary to achieve good agreement in the Coulomb energy with RVS results, and thereby with the total ab initio interaction energy. The multipolar interaction energy E_{mtp} between all atoms in fragment $\mathcal{A}$ and those in $\mathcal{B}$ without penetration is expressed using spherical tensor formalism as [48, 49]

$$E_{\mathrm{mtp}}(\mathcal{A},\mathcal{B}) = \frac{1}{2}\sum_{A\in\mathcal{A}}\sum_{B\in\mathcal{B}} E_{\mathrm{mtp}}(\mathbf{A},\mathbf{B}), \tag{8}$$

$$E_{\mathrm{mtp}}(\mathbf{A},\mathbf{B}) = \sum_{l_A l_B k_A k_B} T_{l_A l_B k_A k_B}(\mathbf{r}_{AB})\, Q_{l_A k_A} Q_{l_B k_B}. \tag{9}$$

The sum in (8) runs over all multipolar centers (nuclei and bond barycenters) of fragments $\mathcal{A}$ and $\mathcal{B}$. The interaction energy E_{mtp} between the multipoles on two sites with position vectors $\mathbf{A}$ and $\mathbf{B}$ is calculated by summing the product of a geometrical tensor T and each multipole moment Q. Multipole moments are expressed using spherical harmonics with rank l, k, where $l = 0, 1, 2$. T is used to relate the local axis systems of the multipolar sites A and B separated by vector $\mathbf{r}_{AB}$.

The modified electrostatic interaction energy, including penetration, includes an additional energetic dependence of the monopole–monopole and monopole–dipole terms on the number of valence electrons present in each overlapping site. Only the monopole–monopole and monopole–dipole terms are currently corrected as they dominate the total electrostatic energy in most situations. The monopole–monopole term for atoms A and B with monopoles q_A and q_B and number of valence electrons Z_A and Z_B separated by distance r is then defined as

$$E_{\text{mono-mono}} = [Z_A Z_B - \{Z_A(Z_B - q_B)(1 - \exp(-a_B r_{AB})) - Z_B(Z_A - q_A)(1 - \exp(-a_A r_{AB}))\} + (Z_A - q_A)(Z_B - q_B)(1 - \exp(-b_A r_{AB}))\,(1 - \exp(-b_B r_{AB}))](1/r_{AB}). \quad (10)$$

For monopoles centered on bonds, Z is equal to zero. In the limit of large separation r_{AB}, this expression converges toward the familiar Coulomb charge–charge interaction energy. The parameters a_A and b_A are obtained from $a_A = \gamma/R_{\text{w}A}$ and $b_A = \delta/R_{\text{w}A}$, where γ and δ are two unitless constants that have been calibrated as 4.42 and 4.12, respectively [40]. $R_{\text{w}A}$ is the van der Waals radius of the atom, or where bond multipoles are concerned, the averaged radius over the two atoms involved in the bond. The modified charge–dipole term is then obtained from the scalar product

$$E_{\text{mono-dip}} = -\mu_B \times \xi_A^*(\mathbf{B}). \quad (11)$$

μ is the dipole moment of site B. In the uncorrected multipolar interaction energy, $\xi_A^*(\mathbf{B})$ represents the electric field created by monopole A at point B with position vector $\mathbf{B}$, $\xi_A(\mathbf{B}) = q_A \mathbf{r}_{AB}/r_{AB}^3$, where $\mathbf{r}_{AB}$ is the vector running from site A to site B. The corrected monopole–dipole term including an overlap contribution is

$$\xi_A^*(\mathbf{B}) = \{Z_A - (Z_A - q_A)(1 - \exp(-\eta r_{AB}))\}\mathbf{r}_{AB}/r_{AB}^3 \quad (12)$$

$$\eta = \chi/((R_{\text{w}A} + R_{\text{w}B})/2), \quad (13)$$

where χ is a unitless constant equal to 2.4. While this penetration correction clearly adds complexity to the evaluation of an electrostatic interaction, the complexity is easily justifiable in the case of metal complexes where metal and ligand atoms approach particularly close to one another, and charged metal ion centers produce a strong short-range electrostatic interaction energy. The ability to evaluate short-range interactions then avoids the need for separate "bonded" and "nonbonded" terms between the metal ion and complexed ligands.

Short-Range Repulsion: Strong short-range Pauli repulsion between same-spin electrons is modeled in SIBFA using a sum of bond–bond, bond–lone pair, and lone pair–lone pair interactions. Bond sites are again located at the barycenters between bonded atoms inside a fragment. Simpler, isotropic repulsion terms do not account for orientational dependence of the repulsion energy. The relative orientation of bound complexes is, therefore, determined not only by the anisotropic electrostatic interaction, but at close range also by anisotropic electron pair repulsion. While valence electron pairs are involved in bond formation and are hence found between bonded atoms, additional nonbonded valence lone pairs must also be taken into account for atom types such as oxygen and nitrogen. The positions of these electron lone pairs must be defined, and one means of achieving this is the electron localization function (ELF) originally proposed by Becke and Edgecombe [50]. Once the centroids of localized orbitals have been located using ELF in ab initio calculations, then their coordinates can be stored in SIBFA in the fragment's local axis system.

The distance between two interacting centroids r_{ij} on separate fragments can then be used to approximate the degree of overlap of the electron pairs S, and hence used to estimate the repulsion energy in SIBFA according to [42]

$$\mathrm{rep}(i,j) = N_{\mathrm{occ}}(i)N_{\mathrm{occ}}(j)\left[c_1 S^2(i,j)\Big/ r_{ij} + c_2 S^2(i,j)\Big/ r_{ij}^2\right]. \tag{14}$$

$N_{\mathrm{occ}}(i)$ is the occupation number of orbital i (equal to 2 for doubly occupied bonds and lone pairs, 1 for π-type lone pairs), c_1 and c_2 are multiplicative constants that are to be fitted for an atom type using the ab initio energies of a series of reference complexes in different geometries. Note that the r_{ij}^2 correction has recently been added in accord with the original proposal of Murrell and Teixeras-Dias [51]. The total repulsion between atoms is evaluated between all lone pair and bond combinations so that the repulsion between atom A involved in bonds b_A with lone pairs L_A and atom B involved in bonds b_B with lone pairs L_B is the sum of all pair–pair interactions [52]

$$\begin{aligned} E_{\mathrm{rep}} = c_1 \Bigg(& \sum_{b_A}\sum_{b_B} rep\,(b_A, b_B) + \sum_{b_A}\sum_{L_B} rep\,(b_A, L_B) \\ & + \sum_{L_A}\sum_{b_B} rep\,(L_A, b_B) + \sum_{L_A}\sum_{L_B} rep\,(L_A, L_B) \Bigg). \end{aligned} \tag{15}$$

The remaining orbital overlap term S is approximated using tabulated orbital coefficients and effective atomic radii for the atom in the fragment of interest. Further details are to be found in [52].

Charge Transfer: Charge transfer becomes important where metal–ligand bonds exhibit some degree of covalent character. Electron density from the bound ligands can be transferred to the central metal cation M, and back donation to or from the d-orbitals of transition metals can provide an additional energetic contribution. Charge transfer in SIBFA is based on the expression [53–55]

$$E_{\mathrm{ct}} = -2c_{\mathrm{M}} \sum_{a \in L_A} N_{\mathrm{occ},a}\left((I_{a,\mathrm{M}^*})^2 \Big/ \Delta E_{a,\mathrm{M}^*} \right). \tag{16}$$

The summation runs over all electron pairs L belonging to the electron donor-atom A of fragment $\mathcal{A}$. The constant c is characteristic of the metal cation M, the occupation number of the electron pair N_{occ} is multiplied by an integral I describing overlap of the donor lone pair and acceptor cation, and by $\Delta E_{a,\mathrm{M}*}$, the difference between the lone pair ionization potential and the acceptor atom electron affinity. This integral has been approximated within a classical molecular mechanics framework using the distance and angles between orbital centroids containing electron lone pairs. The positions of these orbital centroids in the fragment's local axis system are identified in the same way as for the repulsion term E_{rep}. The form of the

expression and the derivation from the full overlap integral are given in detail in [39, 53, 56, 57]. In addition, as the charge transfer energy in certain divalent cation complexes represents a significant contribution to the total interaction energy, a series of corrections have been made to increase its accuracy. In these corrections, metal and ligand properties such as atomic radius and electron affinity are allowed to alter as a function of the electric field that they encounter. Full details of these modifications are found in [39].

Polarization: Electron polarization makes the final major contribution to the total interaction energy in the standard SIBFA force field. A second-order correction to the electrostatic interaction energy, polarization affects primarily the outer valence electrons of an atom. As such, polarizable sites in SIBFA are located at the same bond barycenter and electron lone pair sites used to calculate the Pauli repulsion energy E_{rep}. The polarization energy takes the form of an interaction between an induced dipole and the electric field generated by surrounding moieties, and an induced quadrupole with the field gradient (induced quadrupoles are applied to metal cations only). The magnitude of the induced dipole is [42]

$$\mu_{i,p}^{\text{ind}} = \alpha_{ij,p}\, \xi_j(\mathbf{p}). \tag{17}$$

$\alpha_{ij,p}$ represents an element i, j of the 3×3 polarizability tensor of polarizable site p acting on component i (x, y or z) of the induced dipole moment $\mu_{i,p}^{\text{ind}}$ as a result of component j of the electric field ξ at $\mathbf{p}$. The total electric field at $\mathbf{p}$, the position vector of site p belonging to fragment $\mathcal{A}$, is obtained using

$$\xi_j(\mathbf{p}) = \sum_{\mathcal{B}\neq\mathcal{A}} \sum_{m\in\mathcal{B}} \xi_{j,m}(\mathbf{p}). \tag{18}$$

The first sum is over each fragment $\mathcal{B}$ interacting with $\mathcal{A}$, and the second sum is over all multipolar sites m of fragment $\mathcal{B}$ that give rise to an electric field. Note that sites within the same fragment do not interact, and certain terms are removed from the interaction between atoms at the connection points of two fragments that are covalently bonded in a larger molecule. Central metal atoms and coordinated ligands are, however, not treated as covalently bonded fragments and are allowed to interact fully. Partial covalent character is then encapsulated by charge transfer and short-range contributions such as penetration. A screening term intervenes in the polarization energy at very close range to prevent close contact between charge-carrying sites of one moiety and polarizable sites of another, giving rise to non-physical polarization energies. A Gaussian function g screens the electric field ξ arising from multipolar site m at polarizable site p according to

$$\xi_m(\mathbf{p}) = (1 - g(r_{pm}))\xi_m^0(\mathbf{p}), \tag{19}$$

$$g(r_{pm}) = q_m K_1 \exp[-K_2(r_{pm}^2/(R_{1\text{w}p} + R_{1\text{w}m}))], \tag{20}$$

where r_{pm} is the distance between polarizable site p and multipolar site m with monopole moment q_m, R_{1wp} is the effective radius of the atom containing site p, and R_{1wm} is the effective radius of the atom containing multipolar site m. For sites located on a barycenter, the effective radius used is the average of the two atoms that make up the bond. K_1 and K_2 are parameters fitted for the moiety of interest [39]. The total polarization energy of p is then

$$E_{\mathrm{pol},p} = -0.5 \sum_i \xi_i^0(\mathbf{p}) \sum_j \alpha_{ij,p}\, \xi_j(\mathbf{p}) \tag{21}$$

with $\xi_i^0(\mathbf{p})$ as component i of the electric field at $\mathbf{p}$ due to the permanent multipoles of all interacting sites. $\xi_j(\mathbf{p})$ is component j of the electric field due to the sum of the permanent and induced multipoles. As the electric field involves the induced multipoles of surrounding moieties, an iterative, self-consistent procedure is used. The quadrupolar polarizability is implemented in a similar fashion, describing the second-order correction to the quadrupole moment of each site m arising from interaction with the electric field gradient [42].

Ligand Field Effects: In order to extend the range of application of the SIBFA force field to metals with partially filled d-shells such as Cu(II) with clear biological importance, a LFSE based on the same AOM introduced in the LFMM approach was recently added [38]. The total interaction energy of a metal–ligand complex (including a dispersion term E_{disp} for improved agreement with correlated ab initio methods) [46] in SIBFA-LF is defined, therefore, as

$$E_{\mathrm{int}} = E_{\mathrm{mtp}} + E_{\mathrm{rep}} + E_{\mathrm{pol}} + E_{\mathrm{ct}} + E_{\mathrm{disp}} + E_{\mathrm{LFSE}}. \tag{22}$$

The first four terms are the Coulomb, repulsion, polarization, and charge transfer energies, respectively. As previously described, the LFSE E_{LFSE} arises from the interaction of metal d-orbitals with surrounding ligands. The degree of overlap of a d-orbital with a given ligand again depends on the distance and relative orientation, as can be ascertained from an overlap integral. The AOM overlap integral for SIBFA is also divided into angular and radial contributions. The radial component of the overlap is approximated using an exponential decay [58] $e_\lambda = a + b \exp(-cr_{\mathrm{ML}})$, where a, b, and c are parameters specific to the metal–ligand pair and r_{ML} is the metal–ligand separation. The angular component of the overlap is then described using second-order ($l = 2$) spherical harmonics to describe d-orbital shapes. The spherical harmonics give rise to angular coefficients D that describe the degree of overlap between a ligand σ-orbital and a metal d-orbital i as a function of the polar coordinates θ and φ between them [38] (Table 1).

The coefficients are combined with the radial term e_λ to construct a simplified Hamiltonian describing the d-orbital energies. Note that e_λ represents a radial correction due to LFSE only, and that the primary contribution to the radial dependence of the ligand–metal interaction energy comes from the standard

Table 1 Angular coefficients between metal d-orbitals and ligand σ bonding orbitals

i	$D_i(\theta, \phi)$
z^2	$1/2(3\cos^2\theta - 1)$
yz	$1/2(\sqrt{3}\sin 2\theta \sin\phi)$
xz	$1/2(\sqrt{3}\sin 2\theta \sin\phi)$
xy	$1/4(\sqrt{3}(1-\cos 2\theta)\sin 2\phi)$
$x^2 - y^2$	$1/4(\sqrt{3}(1-\cos 2\theta)\cos 2\phi)$

energetic terms listed in (22). Each element of the Hamiltonian matrix represents a sum of the overlap with every ligand l

$$\mathcal{H}_{dd'} = \sum_l e_\lambda^l \langle d|l\rangle\langle l|d'\rangle. \tag{23}$$

The final relative energy ε of each of the i d-orbitals is then obtained from the Hamiltonian matrix by diagonalization. Note that only bonds to ligand orbitals with σ symmetry are presently included in SIBFA-LF; an extension to π symmetry analogous to that of the LFMM force field described earlier remains to be implemented. E_{LFSE} of a d^n system is calculated from the orbital energies ε according to

$$E_{\mathrm{LFSE}} = -2\sum_{i=1}^{5}\varepsilon_i + \sum_{i=1}^{n}\rho_i\varepsilon_i + E_{\mathrm{wall}}, \tag{24}$$

where ρ_i is the occupation number of orbital i. The repulsive term E_{wall} is necessary to allow geometry optimization of a complex as the LFSE can become nonphysically large at very short range, leading to collapse. E_{wall} takes the form of an exponential with parameters c_{mul} and γ to be fitted for a given metal–ligand pair

$$E_{\mathrm{wall}} = \sum_l c_{\mathrm{mul}} \exp\left(-\gamma r_{\mathrm{ML}}\right). \tag{25}$$

While some of the terms included in the components of the SIBFA interaction energy are observable or can be obtained directly from ab initio calculations, others are parameters that must be fitted to ab initio reference data. Parametrization of metal–ligand complexes typically takes place in a mono-ligated complex involving the metal center and different types of ligand. Varying the M–L distance and performing RVS energy decomposition at each point allow the parametrization of the corresponding SIBFA energy terms as a function of distance. Validation can then take place by comparison with larger complexes and complexes involving different types of ligand. The large number of parameters to be fitted to account accurately for each term of the RVS decomposition means that parametrization of new metals or fragments can require a significant initial investment of time. Once parameters are available, however, they are generally more transferable than those

of simpler force fields and so are less likely to require refitting. For example, the polarization term of each fragment ensures that a single set of multipole moments in a methylene fragment is equally valid when used to build methanol and ethane.

2.3 VALBOND and VALBOND-TRANS

VALBOND, developed by Landis and coworkers [59–63], is based on valence bond theory, where hybrid orbital strength functions are used for the molecular mechanics. Following foundations laid by Pauling [64, 65] who examined chemical bonding from the perspective of valence bond theory, VALBOND aimed at correctly capturing bending potentials over a wide range of angular distortions which primarily determine the shape of molecules. VALBOND can describe both non-hypervalent and hypervalent molecules (not following the octet rule) [60] and transition metal complexes [62, 63] because the functional form for valence-angle distortions L1–M–L2 is suitable to also describe very large angular distortions. The formulation is based on generalized hybrid orbital strength functions. Given two equivalent sp^3 hybrid orbitals $\phi_1 = \frac{1}{2}\left(|1s\rangle + \sqrt{3}\,|p_z\rangle\right)$ and $\phi_2 = \frac{1}{2}[|1s\rangle + \sqrt{3}(\cos\,\alpha\,|p_z\rangle + \sin\alpha|p_x\rangle)]$, where the maximum value of φ_1 is along the z-axis and that of φ_2 is in the xz-plane and forms an angle α with φ_1, their strength S is given by the angular part which is $S = 2$ in both cases. The overlap between these two orbitals is $\Delta = \frac{1}{4}\left(1 + \sqrt{3}\,\cos\,\alpha\right)$. Pauling established that the decrease in S between two orbitals can be related to the overlap. Consequently, S represents a concentration of electron density in the bond-forming region, and S of hybrid orbitals has been interpreted as the bond-forming power of the orbitals. However, it was found that the correlation of S with bond dissociation energies is poor [14].

Nevertheless, the geometry-based hybrid orbital strength functions turned out to be useful to capture the angular parts of force fields. Therefore, VALBOND is used in conjunction with a conventional force field such as CHARMM, where the typical harmonic bending terms are replaced with a new parametrization. In fact, VALBOND was developed together with CHARMM [59]. The additional energy term is of the form

$$E_i = k_i\left(S_i^{\max} - S_i(\alpha_{ij})\right), \tag{26}$$

which arises for every ligand i. Here, k_i is an empirical scaling factor, $S_i^{\max}$ is the maximum strength for a particular hybrid orbital ($S^{\max} = 2$ for a sp^3 hybrid), and $S(\alpha_{ij})$ is the reduction in maximal strength due to the particular angular arrangement of the two hybrid orbitals involved (see above) on two different ligands i and j.

For two $sp^m d^n$ hybrid orbitals at an angle α, the expression for $S^{\max}$ is

$$S^{\max} = \sqrt{\frac{1}{1+m+n}}\left(1 + \sqrt{3m} + \sqrt{5n}\right) \tag{27}$$

and $S(\alpha)$ is in general given by

$$S(\alpha) = S^{\max}\sqrt{1 - \frac{1 - \sqrt{1 - \Delta^2}}{2}}. \tag{28}$$

The overlap Δ for two $sp^m d^n$ hybrid orbitals is

$$\Delta = \frac{1}{1 + m + n}\left(|1s\rangle + m\cos\alpha|p_z\rangle + \frac{n}{2}\left(3\cos^2\alpha - 1\right)|d_{z^2}\rangle\right). \tag{29}$$

Combining (26)–(29) constitutes the core of VALBOND.

For hypervalent molecules, one has to take into account that there are several resonance structures, each described by a weighting factor c_j, which depends on the geometry. For a 3-center/4-electron bond (such as in ClF_3), the total energy of the structure is the sum of three (formally equivalent) resonance structures, each of which are mixed ionic-covalent Lewis structures. Assigning a bond order of 1 to one particular CF bond with the two other CF bonds having bond order 1/2 (and cyclic permutation), the total energy of CF_3 is given by $E_{\text{tot}} = \sum_{j=1}^{3} c_j E_j$, where c_j are mixing coefficients which depend on the molecular geometry. One choice for these mixing coefficients is [60]

$$c_j = \frac{\prod_{i=1}^{hype}\cos^2\alpha_i}{\sum_{j=1}^{config}\prod_{i=1}^{hype}\cos^2\alpha_i}, \tag{30}$$

where the products run over all hypervalent angles i, and config stands for the number of resonance configurations. In general, the total energy is then given by

$$E_{\text{tot}} = \sum_j c_j E_j, \tag{31}$$

where the sum is over all resonance configurations j. For the energy expression E_j of a particular resonance configuration, the following form was suggested

$$E(\alpha) = \text{BOF} \times k_\alpha\left(1 - \Delta\,(\alpha + \pi)^2\right). \tag{32}$$

Here, BOF is the bond order factor, k_α is the VALBOND parameter (k for non-hypervalent bonds), Δ is given in (29) (for $sp^m d^n$ hybrid orbitals), and α is the bond angle. The BOF is the product of the formal bond orders of the two bonds described by the hybrid orbitals and standing at an angle α.

Despite these extensions, additional ingredients are necessary to capture electronic effects, such as the trans influence. One such generalization is VALBOND-TRANS [66]. The purpose of this additional development is to capture electronic effects related to the structural trans effect. Quadratic planar complexes, especially

Pt(II) metal complexes, are known to exhibit a structural trans effect. In octahedral complexes, trans effects can also occur, even if these effects are less pronounced [67]. The trans effect is attributed to electronic effects and is defined as "the effect of a coordinated group on rate of substitution reactions of ligands trans to itself" [68]. One can distinguish between an energetic (or kinetic) trans effect and a structural trans effect in an arrangement L1–M–L2. Here, L1 is trans to L2. The energetic trans effect (not considered in VT) refers to a bond weakening of the M–L2 bond depending on the chemical identity of ligand L1. Contrary to this, the structural trans effect (or influence) reports on bond length changes in M–L2 depending on L1 [69].

The key equation in VALBOND for hypervalent compounds is (32). For a 3-center/4-electron bond, it describes the bending energy as the overlap between one orbital and another orbital shifted by 180°. This term favors linear geometries in hypervalent bonds because it is at a minimum for $\alpha = 180°$. Because the trans influence also acts along hypervalent bonds and is expected to be maximal at linear geometries, a natural place to include additional electronic effects is the term $\Delta(\alpha + \pi) = 1$. This is done by reweighting the energy depending on the chemical identity of ligands L1 and L2 trans to each other in the motif L1–M–L2

$$E_{\text{trans}} = \sum_{\text{trans}} p_{\text{AB}} \left(\Delta(\alpha + \pi)^2 \right). \tag{33}$$

Here, A and B stand for the chemical identity of the atoms of L1 and L2, respectively, bonding to the metal M; p_{AB} is a parameter for the structural trans effect, which depends on the atom types involved and the metal; and α is the L1–M–L2 angle [66]. For a perfect octahedron, this expression is simplified to

$$E_{\text{trans}} = \sum_{\text{trans}} p_{\text{AB}}. \tag{34}$$

To consider the structural trans influence, one has to determine the bond lengths

$$r_{\text{A(B)}} = r_{\text{A}}^0 (1 + s_{\text{A}} \times i_{\text{B}}/100), \tag{35}$$

where $r_{\text{A(B)}}$ is the equilibrium bond length A–M which has atom B trans to it. r_{A}^0 is the unperturbed bond length A–M, i_{B} is the bond lengthening intensity of atom type B, and S_{A} is the bond lengthening sensitivity of atom type A. The trans influence and, therefore, the relative change in the bond length $r_{\text{A(B)}}$ are captured in VALBOND-TRANS as [66]

$$r_{\text{A(B)}} = r_{\text{A}}^0 \left(1 + s_{\text{A}} \times \Delta(\alpha + \pi)^2 \cdot \ i_{\text{B}}/100 \right). \tag{36}$$

2.4 Combination of VALBOND-TRANS with MMPT

One advantage of force field methods is their extensibility. To model a chemically complicated compound, different and separately developed force field methods can be combined. A more familiar example might be the combined quantum mechanics/molecular mechanics (QM/MM) approach [70], which treats a localized region (usually where the chemical reactions occur) by QM methods and the rest of the system by MM force fields. Similarly, we can combine VALBOND with another force field developed in our group, molecular mechanics with proton transfer (MMPT) [71, 72], to study the transition metal complexes whose ligands interact via strong hydrogen bonds. The system can be partitioned into regions treated by VALBOND or MMPT or conventional CHARMM force field, as we will discuss in detail in the application section. Dealing with the interactions across the boundary of different MM regions is relatively simple since force field is additive, while in QM/MM methods the correct description of the boundary region still remains a technical challenge [73].

A detailed account of MMPT has been given in [72]. Briefly, MMPT uses parametrized three-dimensional potential energy surfaces (PES) $V(R, \rho, \theta)$ fitted to high-level ab initio calculations (MP2/6-311++G(d,p)) of prototype proton transfer systems (H_3N–H^+···NH_3, H_2O–H^+···OH_2 and H_3N–H^+···OH_2) to describe the interactions within a general DH–A motif, where D is the donor, H is the hydrogen, and A is the acceptor atom. R is the distance between the donor and the acceptor, ρ is the relative position of H for a particular value of R, and θ is the angle between vectors $\overrightarrow{DA}$ and $\overrightarrow{DH}$. The relationship between ρ and the D–H distance r is given by

$$\rho = (r - r_{\min})/(R - 2r_{\min}), \tag{37}$$

where $r_{\min} = 0.8$ Å is in principle arbitrary but should be sufficiently small to cover the shortest D–A separations. Depending on the position of the transferring H-atom (DH–A or D–HA), bonded interactions on the donor and acceptor side are switched on and off. And by PES morphing [74] through coordinate transformations, MMPT is capable of describing topologically similar but energetically different hydrogen-bonding motifs in an accurate and concise way. VALBOND and MMPT have both been implemented into CHARMM [75]. The implementation has been made in such a way that VALBOND is by default applied to all the atoms and MMPT is applied only to predefined atoms.

3 Applications

3.1 *Refining Force Field Parameters in VALBOND TRANS: Application to an Octahedral Iridium-PHOX Catalyst*

DFT has, over the past decade, emerged as a convenient and versatile computational method. It has been used successfully to obtain a wide range of data such as thermochemistry, molecular structures, force field parameters, vibrational frequencies, nuclear magnetic resonance and electron spin resonance characteristics, UV spectra, dipole moments, transition-state structures, and activation barriers [76]. DFT is also used to provide reference values for the VALBOND-TRANS force field. In this work, DFT calculations were carried out using the B3LYP functional [1, 2] with the all-electron 6-31G(d,p) basis set for C, H, N, O, and P atoms, and a LANL2DZ ECP [77] for Ir, Pt, and Cl atoms. All electronic structure calculations were carried out using the Gaussian03 suite of programs [78] with the grid=ultrafine option.

In the following, the VALBOND-TRANS force field is parametrized for model octahedral complexes of Ir, with the aim to best capture relative energies calculated from DFT for different diastereomers. The (re-)parametrization of VALBOND-TRANS is important for successful use in further atomistic simulations. The fitting procedure can be conveniently carried out by using a recent combination of CHARMM and the I-NoLLS fitting environment [79, 80]. This parameter optimization environment can carry out interactive nonlinear least-square fittings to determine model parameters for a wide variety of applications.

Here, a first optimization of the van der Waals parameters of an octahedral iridium(III)-PHOX catalyst with a triphenylposphate coordinated group (see Fig. 1) is described in some more detail. Starting from standard vdW parameters $R_{\min,i}$ and ε_i and nuclear charges q_i, several optimization cycles are carried out to better reproduce the relative energetics of 20 diastereomers of the test compound. The relative energies from B3LYP/6-31G(d,p) calculations span a range of 21 kcal/mol. Using these energies as the target data, the vdW parameters are iteratively improved. Figure 2 compares the initial RMSD between the reference data (DFT) and VALBOND-TRANS without (green squares) and with optimized vdW parameters (blue circles). It decreases from 7.37 to 3.74 kcal/mol, which is an improvement of 50%. A linear regression gives a correlation coefficient of 0.87 and 0.92, respectively. The most significant change concerns ε_i for the phosphorus atom, which decreases from −0.585 to −1.378 kcal/mol. Noticeable changes also occur for the vdW radii of N (from 1.85 to 1.06 Å), Ir (from 1.91 to 2.75 Å), and P (from 2.15 to 1.53 Å).

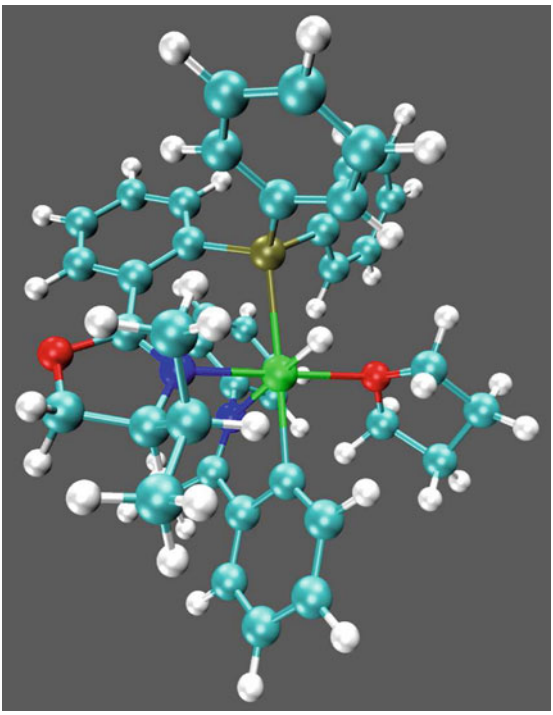

Fig. 1 One diastereomer of the octahedral Ir(III)–metal complex. Color codes are as follows: *light green*: Ir, *light blue*: C, *dark green*: P, *red*: N, *dark blue*: O, *white*: H

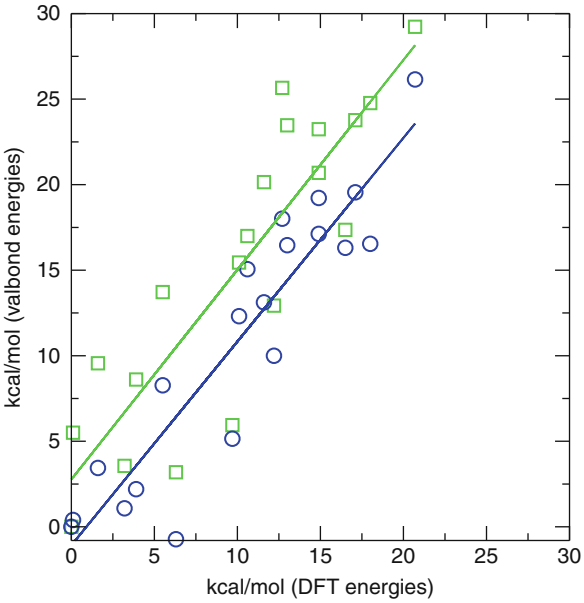

Fig. 2 Energies of all diastereomers of the Ir(III)–metal complex, using unoptimized Lennard-Jones parameters (*green squares*) and fitted Lennard-Jones parameters (*blue cycles*), both with unoptimized Mulliken charges. All energies (kcal/mol) are relative to that of complex 3

3.2 *Energetics and Dynamics of a Hydrogen-Bonded Bidentate Catalyst*

Bidentate ligands are important for controlling selectivity in homogeneous catalysis, but their synthesis is difficult and rational design is usually impossible. In 2003, Breit et al. proposed a new approach for generating bidentate ligands by self-assembly of monodentate ligands via complementary hydrogen-bonding interactions [81]. For example, the self-assembly of 6-diphenylhposphanyl-pyridone (6-DPPon) in the presence of a transition metal such as platinum(II) or rhodium(I) can provide high activity and regioselectivity in the hydroformylation of terminal alkenes [81–83]. In this subsection, we study the energetics and dynamics of *cis*-Pt[Cl_2(6-DPPon)$_2$] [81], a hydrogen-bonded catalyst, with an MM force field.

The Force Field: As illustrated in Fig. 3, the force field for Pt[Cl_2(6-DPPon)$_2$] is decomposed into three parts: the metal center Pt and the ligand atoms P and Cl that are treated with VALBOND; the double proton transfer (DPT) motifs N–H–N and O–H–O which are described by MMPT potentials; and the remainder of the molecule for which the conventional CHARMM force field is used.

The parameters for VALBOND are directly taken from the literature [59, 62] and the corresponding supplementary materials. Force field parameters for MMPT are based on our previous study of 2-pyridone·2-hydroxypyridine (2PY2HP) dimer [72]. Since the DPT motif in the two systems is topologically similar, the MMPT PESs of 2PY2HP are regarded as the zeroth-order potentials, and the following PES morphing [74] is applied

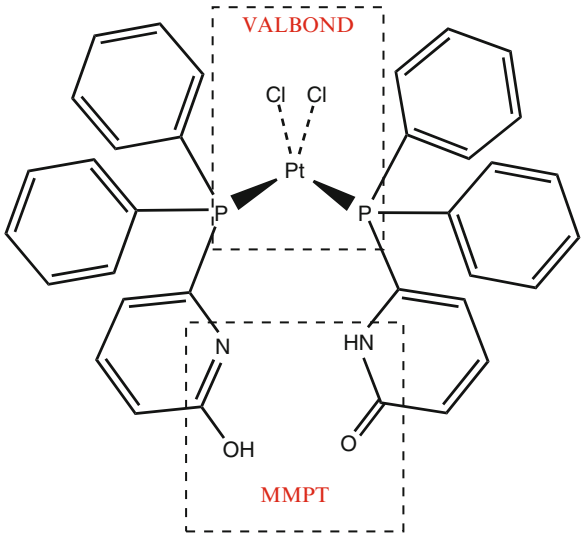

Fig. 3 Pt[Cl_2(6-DPPon)$_2$], and the force field decomposition

$$V^{\mathrm{NHN}}(R',\,\rho',\,\theta') = 0.75 \times V_0^{\mathrm{NHN}}(R - 0.08,\,\rho + 0.235, 0.85\theta)$$
$$V^{\mathrm{OHO}}(R',\,\rho',\,\theta') = 0.75 \times V_0^{\mathrm{OHO}}(R + 0.03,\,\rho - 0.210, 0.70\theta) \quad (38)$$

to generate the PES—and thus the corresponding MMPT parameters—for the Pt complex in this study. The CHARMM22 parameter set [4] is used for all other force field terms required. When CHARMM parameters were missing, those from analogous CHARMM atom types are used, as was done in the previous work [66]. The Lennard-Jones parameters for Pt and Cl atoms are taken from [84], and all the atomic partial charges are determined from natural population analysis (NPA) [85].

The efficiency of force field approaches allows also to perform calculations in explicit solvent. To demonstrate this, we have solvated the Pt[Cl_2(6-DPPon)$_2$] complex in deuterochloroform and carried out MD simulations. The force field parameters for $CDCl_3$ are determined by combining ab initio calculation results at the MP2/6-311++G** level and suggested values from the literature [86, 87].

Validation of the Force Field: As a validation of the MM force field, equilibrium structures of *cis*-Pt[Cl_2(6-DPPPon)$_2$] are determined by different methods and compared in Fig. 4. Starting from the experimental X-ray structure [81], conjugate gradient minimization with CHARMM is used to further relax it, and the DFT structure is generated by full optimization at the B3LYP/6-31G**/LANL2DZ level. The three structures overlap with each other very well (see bond lengths and angles in Table 2). The distances between the platinum center and ligand atoms (P and Cl) are well reproduced by the MM force field, while the P–Pt–P angle in the MM structure differs by 10° and 18° with the X-ray and DFT structures, respectively. This is related to the predefined hybridization of the Pt atom in VALBOND force field, and can be optimized by manually assigning a different sp^{m}d^n hybridization.

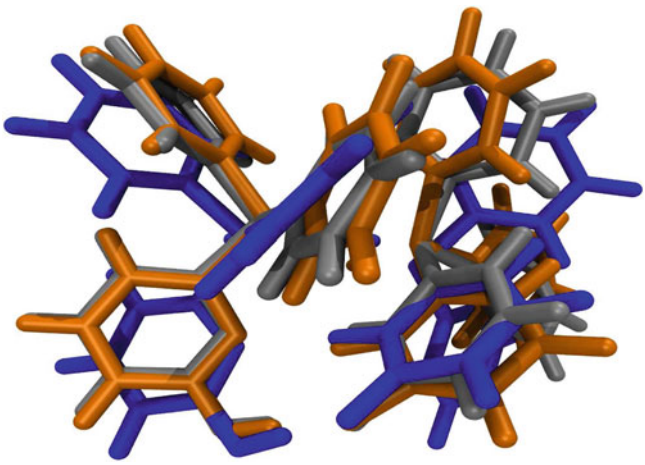

Fig. 4 Superposition of the X-ray structure (*silver*), DFT equilibrium structure (*blue*), and MM structure (*orange*) of *cis*-Pt[Cl_2(6-DPPon)$_2$]

Table 2 Comparison of selected bond lengths and angles from structures determined by X-ray crystallography [81], MM force field optimization, and DFT optimization

Geometry	X-ray	DFT	MM
N–N	3.070	2.966	2.967
N–H	0.84	1.033	1.033
∠N–H–N	136.9	156.3	155.5
O–O	2.684	2.631	2.632
O–H	0.86	1.003	1.004
∠O–H–O	164.3	173.3	177.7
Pt–P[a]	2.247	2.310	2.312
∠P–Pt–P	97.6	105.5	87.6
Pt–Cl[a]	2.338	2.462	2.438
P–C[a]	1.825	1.841	1.872

[a]Average values

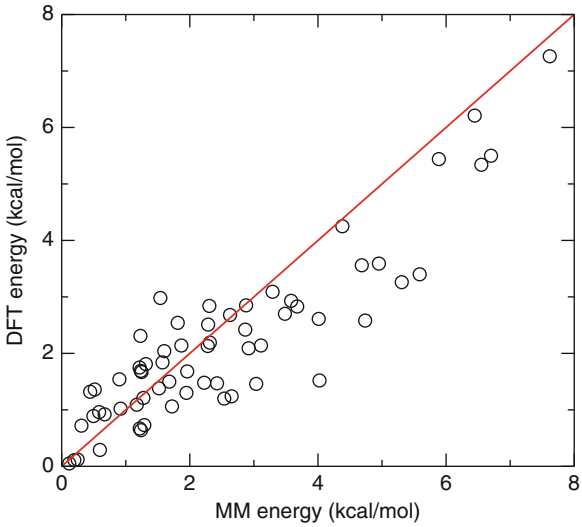

Fig. 5 Comparison of energies calculated by MM force field and DFT method

Besides the equilibrium structure, energies at different hydrogen-bonding situations are also compared. DFT energy calculations are performed by fixing the N–N distance R_{NN}, the O–O distance R_{OO}, the N–H bond length r_{NH}, and the O–H bond length r_{OH} while fully relaxing other degrees of freedom. Such computations have been carried out on a regular grid, giving 63 single-point DFT energies in total. The same constrained minimizations were done with the MM force field. These two sets of energies are compared in Fig. 5. The correlation coefficient between the MM and DFT energies is 0.90, and the mean absolute error (MAE) equals 0.68 kcal/mol. Considering the error of DFT energy calculations which is ≈0.5 kcal/mol, the performance of MM force field is acceptable.

It is worth pointing out that no fitting procedure is performed in this work. The MMPT force field parameters are generated by mapping those of a previously

studied system 2PY2HP to new ones. The PES morphing presented here is heuristic, and a more sophisticated morphing strategy is currently under investigation. Fitting with a CHARMM/I-Nolls interface [80] is also a possible if sufficient experimental data or high-level ab initio calculation results are available.

Molecular Dynamics Simulations: With rapid evaluation of energies and gradients, molecular dynamics (MD) simulations can be carried out. For MD simulations in the gas phase, the complex was first heated to 300 K by 6,000 steps and equilibrated at that temperature for 100 ps. Then, a 5-ns NVE trajectory was generated by free dynamics. The time step was 0.1 fs to follow the fast proton motions. For simulations in explicit solvent, a 46.0 Å × 46.0 Å × 40.9 Å box of $CDCl_3$ was first generated with a density of 1.50 g/cm^3. The Pt[Cl_2(6-DPPon)$_2$] complex was then solvated and periodic boundary conditions were applied. A cutoff of 12 Å was applied to the shifted electrostatic and switched van der Waals interactions. Before 1-ns free dynamics simulations, the system was heated to 300 K and then equilibrated for 10^5 time steps.

One of the essential issues in using nonstandard force fields is whether MD simulations carried out with them conserve total energy. The energy fluctuations $\Delta E(t) = E(t) - \langle E \rangle$ along the 5-ns MD trajectory are shown in Fig. 6. The probability histogram of ΔE is near-Gaussian, with a full width at half maximum (FWHM) of 0.005 kcal/mol. For the 1-ns MD simulation in $CDCl_3$ solvation, the fluctuation of total energies is also small and the FWHM equals 0.02 kcal/mol. Thus, the total energies in NVE simulations are conserved on the nanosecond timescale, which ensures that forces are calculated correctly and that further analysis of the MD trajectories yields meaningful results.

It will be interesting to use this parametrization to further investigate infrared and NMR spectra. These applications will require conformational sampling of the metal complex at finite temperature, which will provide useful starting points for more detailed investigations at the DFT level. For example, an accurate assessment of the temperature-dependent ^{1}H-NMR spectrum of Pt[Cl_2(6-DPPon)$_2$] can only be achieved by combining our MM force field and DFT calculations. Such a study is currently in progress.

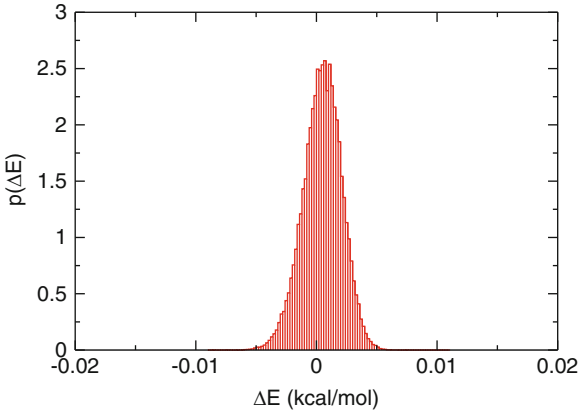

Fig. 6 The fluctuations of total energy ($\Delta E = E - \langle E \rangle$) sampled from a 5-ns molecular dynamics trajectory for *cis*-Pt [Cl_2(6-DPPon)$_2$] in gas phase at 300 K

4 Outlook

This outlook summarizes some new and expected future developments in investigating organometallic chemistry using force field-based techniques.

For the particular case of VALBOND-TRANS, a more comprehensive fitting of an integrated force field is an obvious next step. Until now it was demonstrated that inclusion of electronic effects such as the trans-influence is possible and leads to quantitatively meaningful results when compared with reference DFT calculations. However, for a dedicated force field, all terms (including the bonded ones) need to be fitted. An important question will be how transferable the resulting FF parameters are for the standard chemical atom types (H, C, N, O) between complexes with different transition metals, or whether independent parametrizations are required for different metals and different oxidation states.

The combination of largely independent but mutually beneficial techniques such as VALBOND-TRANS and MMPT as shown in Sect. 3.2 will open up new possibilities in organometallic chemistry. Such extensions can also be envisaged between VALBOND-TRANS and adiabatic reactive MD (ARMD) [88], which will allow reactions involving TMs to be followed explicitly. A prerequisite for such applications is to more routinely adjust force field parameters for particular chemistries.

Approaches discussed in this chapter address the problem of describing TM complexes from two largely different perspectives. Either one starts from a force field and seeks to suitably extend its range of applicability by adding (or integrating) new terms which can describe electronic degrees of freedom (LFMM, VALBOND). Alternatively, one can start from an energy expression and decompose it into terms that can be parametrized. Ultimately, one will be interested not only in carrying out energy evaluations but also in sampling configurational space using such an energy expression. Thus, either Monte Carlo or MD simulations should be possible with such a force field. For VALBOND-TRANS dynamics, the possibility to carry out MD simulations has been demonstrated here, and LFMM has recently been applied to study the dynamics of tyrosinase (a copper-containing protein) [89]. As analytical derivatives for the different terms of the SIBFA interaction energy are not yet fully implemented, the application of SIBFA over recent years has primarily been to the energetic analysis of interactions in biomolecules that are too large to be examined with full ab initio calculations [43, 44, 90, 91]. The envisaged extension of SIBFA to molecular dynamics simulations would allow exploration of an accurate and detailed free energy surface, and remains an important goal. The ability to model metal ion centers accurately in enzyme active sites in energy minimizations and single-point calculations, however, makes SIBFA a useful tool where meaningful analysis of protein–ligand-binding interactions using a classical, nonpolarizable force field is challenging, and where the number of atoms is too large to successfully employ ab initio techniques. The polarization energy in systems with charged metal ions in particular contributes strongly to the total interaction energy [44]. Some recent applications include

modeling of binding energies of different low-energy ligand conformations in protein-active sites in docking studies [90, 91], examining the role of polarizable water molecules in ligand binding [43], and modeling of the formation of complexes that comprise ligand field effects [38].

A major issue remains to incorporate polarization effects in conventional force fields. Polarization can be divided into two important contributions. *Intramolecular polarization*, the response of a molecule's electron density to changes in molecular conformation, can be important in calculating certain sensitive dynamic properties. Modeling of bond vibrational responses to local electric fields in MD simulations provides one such example [92–94]. This form of polarization is currently missing in many force fields and is only partially present even in detailed potentials such as SIBFA, which have focused on an accurate representation of the second, *intermolecular polarization*. Intermolecular polarization describes the response of the electron density of one molecule to the electric field generated by its nonbonded neighbors. As the intermolecular polarization energy is a function of the external electric field, which originates from multipole moments of surrounding moieties which are themselves polarizable, a self-consistent procedure is necessary to achieve very accurate results. Successful incorporation of both inter- and intramolecular polarization within a single force field would allow fully polarizable molecular dynamics simulations, which may offer an important increase in accuracy for detailed applications in charged or polar environments.

Acknowledgments This work is supported by the Schweizerischer Nationalfonds. The authors acknowledge stimulating discussions with Profs. N. Gresh and J.-P. Piquemal.

References

1. Lee C, Yang R, Parr WG (1988) Development of the Colle-Salvetti correlation-energy formula into a functional of the electron density. Phys Rev B 37:785
2. Becke AD (1993) Density-functional thermochemistry. III. The role of exact exchange. J Chem Phys 98:5648
3. Weiner SJ, Kollman PA, Case DA, Singh U, Ghio C, Alagona G, Profeta S Jr, Weiner P (1984) A new force-field for molecular mechanical simulation of nucleic-acids and proteins. J Am Chem Soc 106:765
4. MacKerell JAD, Bashford D, Bellott M, Dunbrack JRL, Evanseck JD, Field MJ, Fischer S, Gao J, Guo H, Ha S, Joseph-McCarthy D, Kuchnir L, Kuczera K, Lau FTK, Mattos C, Michnick S, Ngo T, Nguyen DT, Prodhom B, Reiher I, Roux B, Schlenkrich M, Smith JC, Stote R, Straub J, Watanabe M, Wiorkiewicz-Kuczera J, Yin D, Karplus M (1998) All atom empirical potential for molecular modeling and dynamics studies of proteins. J Phys Chem B 102:3586
5. Jorgensen WL, Tirado-Rives J (1657) The OPLS potential functions for proteins–energy minimizations for crystals of cyclic-peptides and crambin. J Am Chem Soc 110
6. Comba P (1993) The relation between ligand structures, coordination stereochemistry, and electronic and thermodynamic properties. Coord Chem Rev 123:1
7. Landis CR, Root DM, Cleveland T (1995) Reviews in computational chemistry. Rev Comput Chem 6:73

8. Zimmer M (1995) Bioinorganic molecular mechanics. Chem Rev 95:2629
9. London F (1929) Quantum mechanical interpretation of the process of activation. Z Elektrochem 35:552
10. Eyring H, Polanyi M (1931) Concerning simple gas reactions. Z Phys Chem Abt B 12:279
11. Sato S (1955) On a new method of drawing the potential energy surface. J Chem Phys 23:592
12. Sato S (1955) Potential energy surface of the system of three atoms. J Chem Phys 23:2465
13. Ellison FO (1963) A method of diatomics in molecules. 1. General theory and application to H2O. J Am Chem Soc 85:3540
14. Pauling L (1960) The nature of the chemical bond. Cornell University Press, Ithaca, NY
15. Pauling L (1932) The nature of the chemical bond. IV. The energy of single bonds and the relative electronegativity of atoms. J Am Chem Soc 54:3570
16. Johnston HS, Parr C (1963) Activation energies from bond energies. I. Hydrogen transfer reactions. J Am Chem Soc 85:2544
17. van Duin ACT, Dasgupta S, Lorant F, Goddard WA III (2001) ReaxFF: a reactive force field for hydrocarbons. J Phys Chem A 105:9396
18. Lifson S, Warshel A (1968) Consistent force field fpr calculations of conformations vibrational spectra and enthalpies of cycloalkane and n-alkane molecules. J Chem Phys 49:5116
19. Levitt M, Lifson S (1969) Refinement of protein conformations using a macromolecular energy minimization procedure. J Mol Biol 46:269
20. Hwang MJ, Stockfisch TP, Hagler AT (1994) Derivation of class II force fields: 2. Derivation and characterization of a class II force field, CFF93, for the alkyl functional group and alkane molecules. J Am Chem Soc 116:2515
21. Maple JR, Hwang MJ, Stockfisch TP, Dinur U, Waldman M, Ewig CS, Hagler AT (1994) Derivation of class-II force-fields: 1. Methodology and quantum force-field for the alkyl functional-group and alkane molecules. J Comput Chem 15:162
22. Brooks B, Bruccoleri R, Olafson B, States D, Swaminathan S, Karplus M (1983) CHARMM: A program for macromolecular energy, minimization, and dynamics calculations. J Comput Chem 4:18
23. Hermans J, Berendsen HJC, van Gunsteren WF, Postma JPM (1984) A consistent empirical potential for water-protein interactions. Biopolymers 23:1513
24. Deeth R, Anastasi A, Diedrich C, Randell K (2009) Molecular modelling for transition metal complexes: dealing with d-electron effects. Coord Chem Rev 253:795
25. Figgis BN, Hitchman MA (2000) Ligand field theory and its applications. Wiley-VCH, New York
26. Burton VJ, Deeth RJ, Kemp CM, Gilbert PJ (1995) Molecular mechanics for coordination complexes: the impact of adding d-electron stabilization energies. J Am Chem Soc 117:8407
27. Deeth RJ, Fey N, Deeth RJ, Fey N (2004) A molecular mechanics study of copper(II)-catalyzed asymmetric Diels-Alder reactions. Organometallics 23:1042
28. Deeth RJ, Fey N, Williams-Hubbard B (2005) DommiMOE: an implementation of ligand field molecular mechanics in the molecular operating environment. J Comput Chem 26:123
29. Deeth RJ, Hearnshaw LJA (2005) Molecular modelling for coordination compounds: Cu(II)-amine complexes. Dalton Trans 22:3638–3645
30. Deeth RJ (2008) General molecular mechanics method for transition metal carboxylates and its application to the multiple coordination modes in mono- and dinuclear Mn(II) complexes. Inorg Chem 47:6711
31. Deeth RJ, Randell K (2008) Ligand field stabilization and activation energies revisited: molecular modeling of the thermodynamic and kinetic properties of divalent, first-row aqua complexes. Inorg Chem 47:7377
32. Deeth RJ (2007) Comprehensive molecular mechanics model for oxidized type I copper proteins: active site structures, strain energies, and entatic bulging. Inorg Chem 46:4492
33. Schaeffer CE, Jorgensen CK (1965) The angular overlap model, an attempt to revive the ligand field approaches. Mol Phys 9:401

34. Larsen E, Mar GNL (1974) The angular overlap model. How to use it and why. J Chem Educ 51:633
35. Schaeffer CE (1968) A perturbation representation of weak covalent bonding. Struct Bond 5:68
36. Halgren TA (1998) Merck molecular force field. I. Basis, form, scope, parameterization, and performance of MMFF94. J Comput Chem 17:490
37. Gresh N, Claverie P, Pullman A (1984) Theoretical studies of molecular conformation. Derivation of an additive procedure for the computation of intramolecular interaction energies. Comparison with ab initio SCF computations. Theor Chim Acta 66:1
38. Piquemal J-P, Williams-Hubbard B, Fey N, Deeth RJ, Gresh N, Giessner-Prettre C (2003) Inclusion of the ligand field contribution in a polarizable molecular mechanics: SIBFA-LF. J Comput Chem 24:1963
39. Gresh N (1995) Energetics of Zn binding to a series of biologically relevant ligands: a molecular mechanics investigation grounded on ab initio self-consistent field supermolecule calculations. J Comput Chem 16:856
40. Piquemal J-P, Gresh N, Giessner-Prettre C (2003) Improved formulas for the calculation of the electrostatic contribution to the intermolecular interaction energy from multipolar expansion of the electronic distribution. J Phys Chem A 107:10353
41. Gresh N, Policar C, Giessner-Prettre C (2002) Modeling copper(I) complexes: SIBFA molecular mechanics versus *ab initio* energetics and geometrical arrangements. J Phys Chem A 106:5660
42. Gresh N, Piquemal J-P, Krauss M (2005) Representation of Zn(II) complexes in polarizable molecular mechanics. Further refinements of the electrostatic and short-range contributions. Comparison with ab initio computations. J Comput Chem 26:1113
43. de Courcy B, Piquemal J-P, Garbay C, Gresh N (2010) Polarizable water molecules in ligand-macromolecule recognition. Impact on the relative affinities of competing pyrrolopyrimidine inhibitors for FAK kinase. J Am Chem Soc 132:3312
44. de Courcy B, Piquemal J-P, Gresh N (2008) Energy analysis of Zn polycoordination in a metalloprotein environment and of the role of a neighboring aromatic residue. What is the impact of polarization? J Chem Theor Comput 4:1659
45. Stevens WJ, Fink W, Stevens WJ, Fink W (1987) Frozen fragment reduced variational space analysis of hydrogen-bonding interactions—application to the water dimer. Chem Phys Lett 139:15
46. Piquemal J-P, Chevreau H, Gresh N (2007) Toward a separate reproduction of the contributions to the Hartree-Fock and DFT intermolecular interaction energies by polarizable molecular mechanics with the SIBFA potential. J Chem Theor Comput 3:824
47. Vigne-Maeder F, Claverie P (1988) The exact multipolar part of a molecular charge-distribution and its simplified representations. J Chem Phys 88:4934
48. Popelier PLA (2000) Atoms in molecules: an introduction. Pearson Education, London
49. Stone AJ (1996) The theory of intermolecular forces. Clarendon, Oxford
50. Becke AD, Edgecombe KE (1990) A simple measure of electron localization in atomic and molecular systems. J Chem Phys 92:5397
51. Murrell JN, Teixeiras-Dias JJN (1970) The dependence of exchange on orbital overlap. Mol Phys 19:521
52. Gresh N (1997) Model, multiply hydrogen-bonded water oligomers (N=3-20). How closely can a separable, ab initio-grounded molecular mechanics procedure reproduce the results of supermolecule quantum chemical computations? J Phys Chem A 101:8680
53. Gresh N, Claverie P, Pullman A (1986) Intermolecular interactions: elaboration on an additive procedure including an explicit charge-transfer contribution. Int J Quant Chem 29:101
54. Gresh N (1995) Energetics of Zn^{2+} binding to a series of biologically relevant ligands: a molecular mechanics investigation grounded on ab initio self-consistent field supermolecular computations. J Comput Chem 16:856

55. Murrell JN, Randic M, Williams DR (1965) The theory of intermolecular forces in the region of small orbital overlap. Proc R Soc Lond 284:566
56. Gresh N, Claverie P, Pullman A (1985) Cation-ligand interactions: reproduction of extended basis set *ab initio* SCF computations by the SIBFA 2 additive procedure. Int J Quant Chem 28:757
57. Gresh N, Claverie P, Pullman A (1982) Computations of intermolecular interactions: expansion of a charge-transfer energy contribution in the framework of an additive procedure. Applications to hydrogen-bonded systems. Int J Quant Chem 22:199
58. Woodley SM, Battle PD, Catlow CRA, Gale JD (2001) Development of a new interatomic potential for the modeling of ligand field effects. J Phys Chem B 105:6824
59. Root DM, Landis CR, Cleveland T (1993) Valence bond concepts applied to the molecular mechanics description of molecular shapes. 1. Application to nonhypervalent molecules of the p-block. J Am Chem Soc 115:4201
60. Cleveland T, Landis CG (1996) Valence bond concepts applied to the molecular mechanics description of molecular shapes. 2. applications to hypervalent molecules of the p-block. J Am Chem Soc 118:6020
61. Landis CR, Firman TK, Root DM, Cleveland T (1998) A valence bond perspective on the molecular shapes of simple metal alkyls and hydrides. J Am Chem Soc 120:1842
62. Landis CR, Cleveland T, Firman TK (1998) Valence bond concepts applied to the molecular mechanics description of molecular shapes. 3. Applications to transition metal alkyls and hydrides. J Am Chem Soc 120:2641
63. Firman TK, Landis CR (2001) Valence bond concepts applied to the molecular mechanics description of molecular shapes. 4. Transition metals with pi-bonds. J Am Chem Soc 123:11728
64. Pauling L (1928) The shared-electron chemical bond. Proc Natl Acad Sci USA 14:359
65. Pauling L (1931) The nature of the chemical bond. Application of results obtained from the quantum mechanics and from a theory of paramagnetic susceptibility to the structure of molecules. J Am Chem Soc 53:1367
66. Tubert-Brohman I, Schmid M, Meuwly M (2009) A molecular mechanics force field for octahedral organometallic compounds with inclusion of the trans influence. J Chem Theor Comput 5:530
67. Quagliano JV, Schubert L (1952) The trans effect in complex inorganic compounds. Chem Rev 50:201
68. Coe BJ, Glenwright SJ (2000) Trans-effects in octahedral transition metal complexes. Coord Chem Rev 203:5
69. Anderson KM, Orpen AG (2001) On the relative magnitudes of cis and trans influences in metal complexes. Chem Commun 2682–2683
70. Warshel A, Levitt M (1976) Theoretical studies of enzymic reactions: dielectric, electrostatic and steric stabilization of the carbonium ion in the reaction of lysozyme. J Mol Biol 103:227
71. Lammers S, Meuwly M (2007) On the relationship between infrared spectra of shared protons in different chemical environments: a comparison of protonated diglyme and protonated water dimer. J Phys Chem A 111:1638
72. Lammers S, Lutz S, Meuwly M (2008) Reactive force fields for proton transfer dynamics. J Comput Chem 29:1048
73. Lin H, Truhlar DG (2007) QM/MM: what have we learned, where are we, and where do we go from here? Theor Chim Acta 117:185
74. Meuwly M, Hutson J (1999) Morphing ab initio potentials: a systematic study of Ne-HF. J Chem Phys 110:8338
75. Brooks BR, Bruccoleri RE, Olafson BD, States DJ, Swaminathan S, Karplus M (1983) CHARMM: a program for macromolecular energy, minimization and dynamics calculations. J Comput Chem 4:187
76. Ziegler T (1991) Approximate density functional theory as a practical tool in molecular energetics and dynamics. Chem Rev 91:651

77. Hay PJ, Wadt WR (1985) Ab initio effective core potential for molecular calculation. J Chem Phys 82:270
78. Frisch MJ, Trucks GW, Schlegel HB, Scuseria GE, Robb MA, Cheeseman JR, Montgomery JJA, Vreven T, Kudin KN, Burant JC, Millam JM, Iyengar SS, Tomasi J, Barone V, Mennucci B, Cossi M, Scalmani G, Rega N, Petersson GA, Nakatsuji H, Hada M, Ehara M, Toyota K, Fukuda R, Hasegawa J, Ishida M, Nakajima T, Honda Y, Kitao O, Nakai H, Klene M, Li X, Knox JE, Hratchian HP, Cross JB, Bakken V, Adamo C, Jaramillo J, Gomperts R, Stratmann RE, Yazyev O, Austin AJ, Cammi R, Pomelli C, Ochterski JW, Ayala PY, Morokuma K, Voth GA, Salvador P, Dannenberg JJ, Zakrzewski VG, Dapprich S, Daniels AD, Strain MC, Farkas O, Malick DK, Rabuck AD, Raghavachari K, Foresman JB, Ortiz JV, Cui Q, Baboul AG, Clifford S, Cioslowski J, Stefanov BB, Liu G, Liashenko A, Piskorz P, Komaromi I, Martin RL, Fox DJ, Keith T, Al-Laham MA, Peng CY, Nanayakkara A, Challacombe M, Gill PMW, Johnson B, Chen W, Wong MW, Gonzalez C, Pople JA (2004) Gaussian 03, Revision C.02. Gaussian Inc, Wallingford, CT
79. Law MM, Hutson JM (1997) I-NoLLS: a program for interactive nonlinear least-square fitting of the parameters of physical models. Comp Phys Commun 102:252
80. Devereux M, Meuwly M (2010) Force field optimization using dynamics and ensemble-averaged data: vibrational spectra and relaxation in bound MbCO. J Chem Inf Model 50:349
81. Breit B, Seiche W (2003) Hydrogen bonding as a construction element for bidentate donor ligands in homogeneous catalysis: regioselective hydroformylation of terminal alkenes. J Am Chem Soc 125:6608
82. Seiche W, Schuschkowski A, Breit B (2005) Bidentate ligands by self-assembly through hydrogen bonding: a general room temperature/ambient pressure regioselective hydroformylation of terminal alkenes. Adv Synth Catal 347:1488
83. Chevallier F, Breit B (2006) Self-assembled bidentate ligands for Ru-catalyzed anti-Markovnikov hydration of terminal alkynes. Angew Chem Int 45:1599
84. Lienke A, Klatt G, Robinson DJ, Koch KR, Naidoo KJ (2001) Modeling platinum group metal complexes in aqueous solution. Inorg Chem 40:2352
85. Glendening ED, Reed AE, Carpenter JE, Weinhold F NBO Version 3.1
86. Fox T, Kollman PA (1998) Application of the RESP methodology in the parametrization of organic solvents. J Phys Chem B 102:8070
87. Kab G, Schroder C, Schwarzer D (2002) Intramolecular vibrational redistribution and energy relaxation in solution: a molecular dynamics approach. PCCP 4:271
88. Danielsson J, Meuwly M (2008) Atomistic simulation of adiabatic reactive processes based on multi-state potential energy surfaces. J Chem Theor Comput 4:1083
89. Deeth RJ, Diedrich C (2010) Structural and mechanistic insights into the oxy form of tyrosinase from molecular dynamics simulations. J Biol Inorg Chem 15:117
90. Gresh N, Audiffren N, Piquemal JP, de Ruyck J, Ledecq M, Wouters J (2010) Analysis of the interactions taking place in the recognition site of a bimetallic Mg(II)-Zn(II) enzyme, isopentenyl diphosphate isomerase. A parallel quantum-chemical and polarizable molecular mechanics study. J Phys Chem B 114:4884
91. Miller Jenkins LM, Hara T, Durell SR, Hayashi R, Inman JK, Piquemal JP, Gresh N, Appella E (2007) Specificity of acyl transfer from 2-mercaptobenzamide thioesters to the HIV-1 nucleocapsid protein. J Am Chem Soc 129:11067
92. Plattner N, Meuwly M (2008) The role of higher CO-multipole moments in understanding the dynamics of photodissociated carbonmonoxide in myoglobin. Biophys J 94:2505
93. Plattner N, Bandi T, Doll J, Freeman DL, Meuwly M (2008) MD simulations using distributed multipole electrostatics: structural and spectroscopic properties of CO- and methane-containing clathrates. Mol Phys 106:1675
94. Devereux M, Plattner N, Meuwly M (2009) Application of multipolar charge models and molecular dynamics simulations to study stark shifts in inhomogeneous electric fields. J Phys Chem A 113:13199

New Insights into the Molecular Mechanism of H_2 Activation

Guixiang Zeng, Yong Guo, and Shuhua Li

Abstract Mechanistic studies of H_2 activation by the newly developed frustrated Lewis acid–Lewis base pairs, main-group metal complexes, transition-metal thiolate complexes, and transition-metal-based pincer ligand catalysts have been reviewed in this chapter. The reaction of H_2 with frustrated Lewis acid–Lewis base pairs and main-group metal complexes is found to proceed via an unprecedented concerted Lewis acid–Lewis base mechanism. The molecular mechanism of H_2 with transition metal thiolate complexes depends on the transition metals. The iridium thiolate complex splits the H–H bond through the oxidation addition step, while the rhodium thiolate complex heterolytically cleaves the H–H bond with a nonclassical dihydrogen complex as the intermediate. In the reaction of H_2 with the transition-metal-based pincer ligand complex, the metal center and the pincer ligand work cooperatively through the dearomatization/aromatization process of the pincer ligand.

1 Introduction

Dihydrogen activation has attracted extensive attention for decades due to their vital applications in hydrogenation reactions [1–10], biological related processes [11–17], and the hydrogen economy [18–22]. Since the H−H bond is one of the strongest single bonds with the bond energy of 104 kcal/mol, its splitting into two hydrogen atoms (or a hydride and a proton) requires the assistance of efficient catalysts. The homogeneous catalysts for H_2 activation can be divided into two categories: metal-based catalysts (especially transition-metal-based catalysts) and

G. Zeng • Y. Guo • S. Li (✉)
Key Laboratory of Mesoscopic Chemistry of Ministry of Education, School of Chemistry and Chemical Engineering, Institute of Theoretical and Computational Chemistry, Nanjing University, Nanjing 210093, People's Republic of China
e-mail: shuhua@nju.edu.cn

O. Wiest and Y. Wu (eds.), *Computational Organometallic Chemistry*,
DOI 10.1007/978-3-642-25258-7_3,

metal-free catalysts. In recent years, a great deal of progress has been achieved in developing environment-friendly and efficient catalysts, especially metal-free catalysts.

The pioneering work on the synthesis of metal-free catalysts for H_2 activation was contributed by Stephen et al. in 2006 [23]. They reported that a phosphine-borane species, $(C_6H_2Me_3)_2P(C_6F_4)B(C_6F_5)_2$, could split the H−H bond at 25°C to yield a salt species, $(C_6H_2Me_3)_2PH(C_6F_4)BH(C_6F_5)_2$, which could liberate H_2 at temperatures above 100°C (Scheme 1). Then, they also found that a combination of a sterically demanding Lewis base, PR_3 (R=^{t}Bu, $C_6H_2Me_3$), and a Lewis acid B $(C_6F_5)_3$ could also heterolytically cleave the H–H bond under ambient temperature [24]. This combination of a Lewis base and a Lewis acid, which cannot interact directly due to steric hindrance, was described as a "frustrated Lewis pair" (FLP). Subsequently, a series of other FLPs (Scheme 2) [25–29] have been reported, which are capable of heterolytically cleaving H_2 under mild conditions. The concept of FLPs opens a new direction for developing metal-free catalysts for activating small molecules, such as H_2 and CO_2 [30].

In addition to various FLPs, other metal-free catalysts for H_2 activation found recently include singlet carbenes [31–37], digermyne [38–46], and distannyle compounds [47]. Theoretical calculations [35] revealed that a singlet carbene has a vacant *p* orbital and a lone pair in a nonbonding orbital, similar to a transition

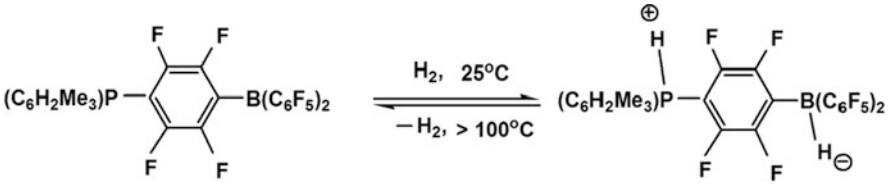

Scheme 1 Reversible H_2 activation by the phosphine-borane species

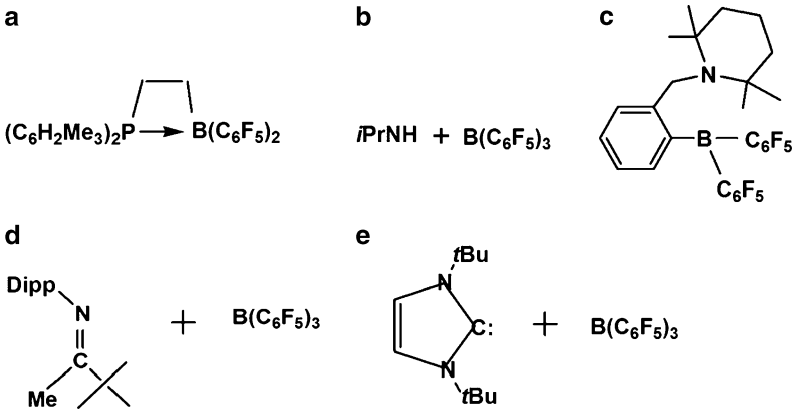

Scheme 2 Some FLPs that can heterolytically split H_2 under mild conditions

metal that has empty *d* orbitals and occupied *d* orbitals. Thus, the interaction picture between a singlet carbene and H_2 should be similar to that between a transition metal and H_2. Also, the reactive nature of digermyne or distannyle compounds toward H_2 is possibly due to the singlet diradical character of the Ge≡Ge (or Sn≡Sn) bond [48].

The H_2 activation by transition metal compounds has been extensively studied experimentally and theoretically. The interaction picture between a transition metal and H_2 is schematically shown in Scheme 3. According to this picture, H_2 donates a pair of electrons on the σ bonding orbital to the empty *d* orbital of the metal atom and the metal atom back-donates nonbonding d electrons to the antibonding orbital (σ*) of H_2, weakening the H–H bond [49–51].

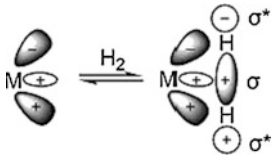

Scheme 3 Orbital presentation for H_2 activation by transition-metal catalysts

The cleavage of H_2 at transition metal centers usually occurs via two mechanisms, homolytic or heterolytic. The homolytic cleavage involves oxidative additions at electron–rich transition metals, leading to two hydrides; whereas the heterolytic cleavage usually involves a dihydrogen complex as an intermediate, producing a proton and a hydride. Since the heterolytic H–H cleavage is a key step in the function of hydrogenases [52–56], designing and synthesizing structural model complexes to unravel the catalytic behaviors of hydrogenases have been an active field. Since an M–S bond was suggested to play a key role in the H−H activation of [NiFe] hydrogenase, a number of structural models with metal thiolate sites for [NiFe] hydrogenase have been reported [57–62]. Nevertheless, the metal thiolate complexes that could cleave the H−H bond under mild conditions are rarely known. In 2008, Tatsumi and his coworkers made an important progress toward this direction. They reported two transition metal thiolate complexes, [Cp*M(PMe_3)(SDmp)]($BArF_4$) (M = Ir, Rh), which can split the H−H bond under mild conditions (Scheme 4) [63].

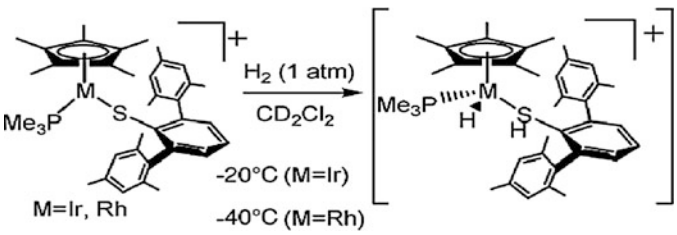

Scheme 4 The reaction of H_2 with the iridium (or rhodium) thiolate complex

Another direction in designing transition metal catalysts for H_2 activation is to develop metal–ligand bifunctional catalysts. Milsten's group has demonstrated that pincer ligand catalysts can react with H_2 under mild conditions [64, 65]. For example, the (PNP)Ir(C_6H_5) complex can react with one equiv of H_2 in benzene at room temperature, producing the *trans*-dihydride complex, (PNP)Ir$(H)_2(C_6H_5)$, exclusively (Eq. 3) [65]. The cooperation between the transition metal and the PNP ligand was suggested to be essential for the activation of the H−H bond.

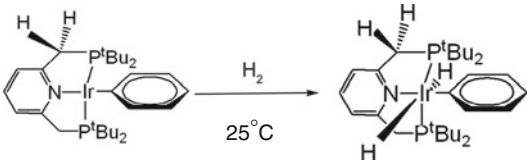

In contrast to the transition-metal-based catalysts, main-group metal catalysts for activating H_2 are still rare. In 2002, the main-group metal catalyst KO^{t}Bu was found by Müller et al. to catalyze the hydrogenation reaction of ketones through the heterolysis of H_2 [66, 67].

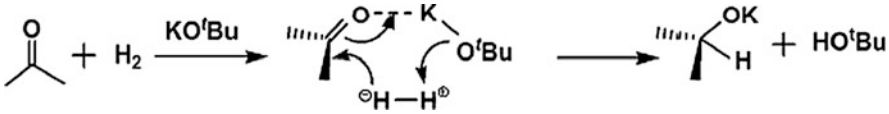

In 2008, several main-group metal catalysts, such as the following organo-calcium catalyst, were found to readily cleave the H−H bond during the hydrogenation reactions of conjugated alkenes [68].

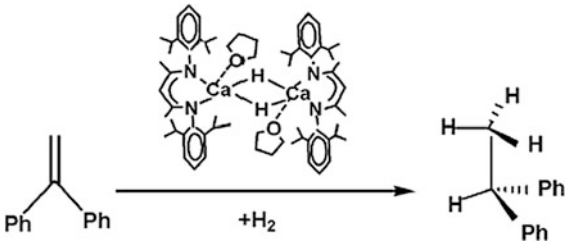

It is well known that computational quantum chemistry can nowadays make significant contribution to the understanding of various chemical reactions. Especially, density functional theory (DFT) methods [69, 70] have been demonstrated to provide quite accurate energies and structures for a wide range of chemical systems. In recent years, we have undertaken a systematic investigation on the molecular mechanisms of some novel reactions involving dihydrogen activation. The reactions of H_2 with the phosphine-borane species, transition-metal thiolate complexes, metal–ligand bifunctional catalysts, and main-group metal catalysts have been studied. The mechanistic details we obtained for these reactions not only reasonably account for the observed experimental facts, but also provide valuable guideline for

devising more efficient catalysts for the H_2 activation. In this chapter, we will try to summarize some important insights on the reaction mechanisms of dihyhdrogen activation by several recently developed systems.

1.1 H_2 Activation by Frustrated Lewis Pairs

The reaction mechanism of H_2 with the phosphonium-borate compound, $(C_6H_2Me_3)_2P(C_6F_4)B(C_6F_5)_2$, revealed from our study [71], is somewhat beyond the experimentalist's expectation. Before our theoretical study, Stephen et al. suggested that the reaction may proceed via two reaction pathways, as shown in Scheme 5. However, our calculations showed that the free energy barriers for these two reaction pathways are very high, inconsistent with the experimental observation. Thus, we turned to search for other energetically favorable pathways. It turns out that the pathway shown in Scheme 6 is thermodynamically and kinetically more favorable

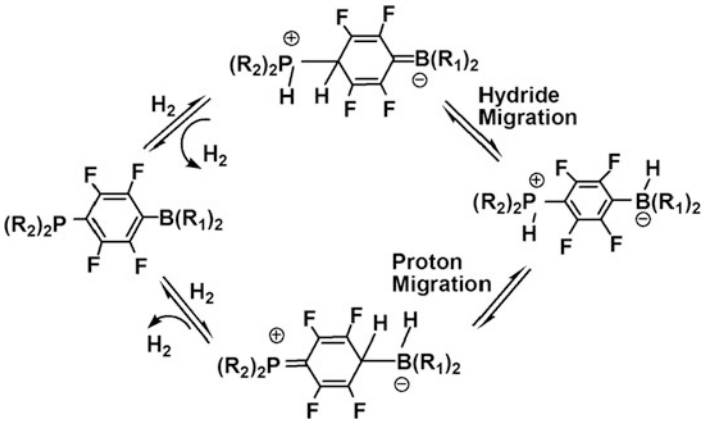

Scheme 5 Two reaction pathways suggested by Stephan et al., R_1=C_6F_5, R_2=$C_6H_2Me_3$

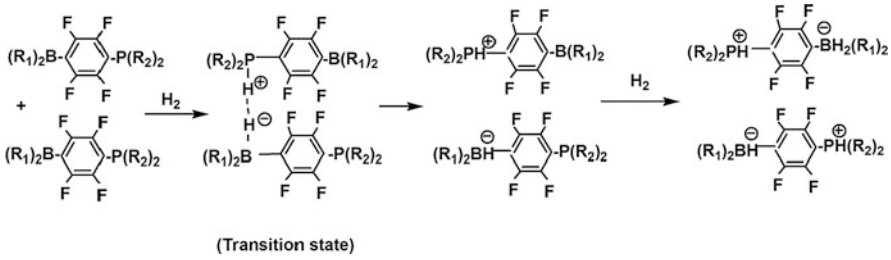

Scheme 6 The concerted Lewis acid–Lewis base mechanism for H_2 activation by the phosphonium-borate compound (R_1=C_6F_5, R_2=$C_6H_2Me_3$)

Table 1 Net natural atomic charges on some reactive atoms of the species involved in the H_2 activation step

Atoms	FLP	TS	Ion-pair intermediate
B	0.89	0.76	0.11
P	0.89	0.96	1.33
H (P–H)		0.16	0.09
H (B–H)		−0.10	−0.03

than all other possible pathways. First, two phosphine-borane monomers may form an intermolecular frustrated Lewis pair through several C–H· ·H–F hydrogen bonds. Our calculations showed that the distance between the frustrated Lewis acid B and Lewis base P centers is 5.54 Å (the distance between another pair of B and P centers is much larger). Next, an H_2 molecule enters into the region between the frustrated B and P atoms. Surprisingly, the H–H bond can be heterolytically splitted into a hydride and a proton under the concerted interaction of this frustrated Lewis acid–Lewis base pair, resulting in an ion-pair intermediate. In the located transition state, the distances of P···H, H···H, and H···B are 2.28, 0.78, and 1.75 Å, respectively. The activation free energy for this step is 33.7 kcal/mol in the solvent (toluene). To further understand the driving force of the H_2 activation, we have performed natural population analyses for the reactant, transition state, and product involved in the cleavage of the H–H bond, with the results shown in Table 1. The net natural atomic charges on the reactive atoms suggest that the heterolytic cleavage of the H–H bond is accomplished via the simultaneous electron transfer from the lone pair orbital of the Lewis base P center to the antibonding orbital of H_2 and from the bonding orbital of H_2 to the empty orbital of the Lewis acid B center. The heterolytic cleavage mechanism of H_2 found here is different from the previously known mechanisms for H_2 activation, and thus can be named the concerted Lewis acid–Lewis base mechanism. After the addition of one H_2 molecule is completed, the ion-pair intermediate may react with another H_2 to generate the final neutral products, since it possesses another frustated B and P pair. Thus, the reaction of H_2 with the phosphonium-borate compound is likely to proceed via a bimolecular channel, and the H_2 activation step involves a novel concerted Lewis acid–Lewis base mechanism.

Also in the meantime, Pápai et al. independently proposed a similar mechanism for the H_2 activation by the combination of $P(^tBu)_3$ and $B(C_6F_5)_3$ [72]. The concerted Lewis acid–Lewis base mechanism has been recognized to be general for the H_2 activation reactions by many different frustrated Lewis acid–Lewis base pairs.

1.2 H_2 Activation by Main-Group Metal Catalysts

The concept of FLPs has also been proven to be very useful for understanding the reactions of H_2 with main-group metal catalysts. In exploring the hydrogenation mechanism of a conjugated alkene, 1,1-diphenylethylene, mediated by the early main-group metal catalysts, {CaH(dipp-nacnac)(thf)}$_2$ (dippnacnac=CH{(CMe)

$(2,6\text{-}iPr_2\text{-}C_6H_3N)\}_2$), we found that a metal-containing ion-pair intermediate could heterolytically cleave the H−H bond under mild conditions [73].

Our calculations suggested that this ion-pair intermediate can be considered as an intramolecular FLP, in which the calcium center is the Lewis acid, the benzylic carbon is the Lewis base, and the distance between them is 4.010 Å. This species is formed by a hydride transfer from the actual metal-containing catalyst to the conjugated alkene, followed by a geometrical rearrangement. The X-ray structure of this species has been obtained experimentally [68]. This species could achieve the heterolytic cleavage of the H−H bond into a hydride and a proton through the concerted Lewis acid–Lewis base mechanism. In the transition state for H_2 cleavage, as shown in Scheme 7, the distance between two activated hydrogen atoms is about 1.00 Å. The Gibbs free energy barrier is calculated to be 25.1 kcal/mol in the benzene solvent at 60°C and 20 atm. The natural atomic charges on two splitted hydrogen atoms are −0.43 and 0.19 e, respectively, indicating the heterolytic nature of the H−H bond cleavage.

In addition, our calculations showed that the similar H_2 cleavage step is involved in the hydrogenation reactions of other conjugated alkenes mediated by the calcium hydride catalyst, or the hydrogenation reactions of conjugated alkenes mediated by the analogous strontium catalysts [73]. Thus, the concerted Lewis acid–Lewis base mechanism for H_2 splitting is expected to be applicable in the reactions of H_2 with many main-group metal compounds.

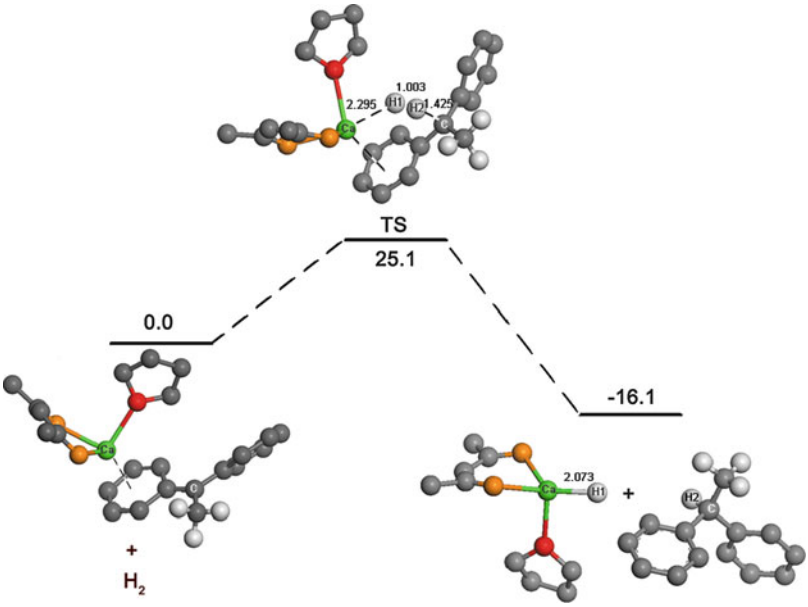

Scheme 7 H_2 activation by a calcium-containing catalyst. All the hydrogen atoms except those involved in the reaction are omitted. All the distances are in Å. The relative free energies are in kcal/mol

1.3 H_2 Activation by Transition Metal Thiolate Complexes

To understand many aspects relevant to the function of the [NiFe] or [FeFe] hydrogenases, synthetic chemists have built many transition metal thiolate model complexes. However, transition metal thiolate compounds that could react with H_2 under mild conditions are still limited. In 2008, Tatsumi and his coworkers found that transition metal thiolate complexes, [Cp*M(PMe_3)(SDmp)]($BArF_4$) (M = Ir, Rh), could split the H−H bond at low temperatures (−20°C for Ir, −40°C for Rh) and 1 atm (Scheme 1) [63]. We have explored the H_2 activation mechanism of these two metal thiolate compounds [74] using the B3LYP hybrid functional [75, 76]. Our calculations revealed that the reaction of the iridium thiolate complex with H_2 involves the oxidative addition of H_2 to the transition metal to form a dihydride intermediate as the first step, followed by the migration of one iridium-bound hydrogen to the sulfur ligand to yield the hydride thiol product (Scheme 8). During this reaction, the rate-determining step is the oxidative addition step, with a free energy barrier of 19.3 kcal/mol in the solvent (CD_2Cl_2).

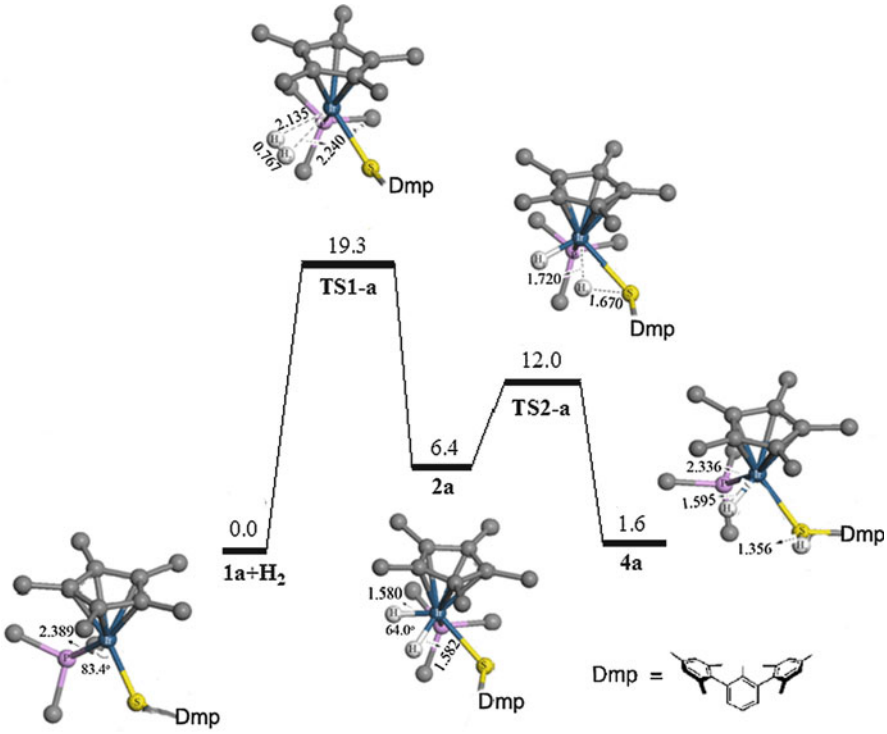

Scheme 8 The Gibbs free energy profile for the reaction of H_2 with the iridium thiolate complex. All the relative free energies are in kcal/mol

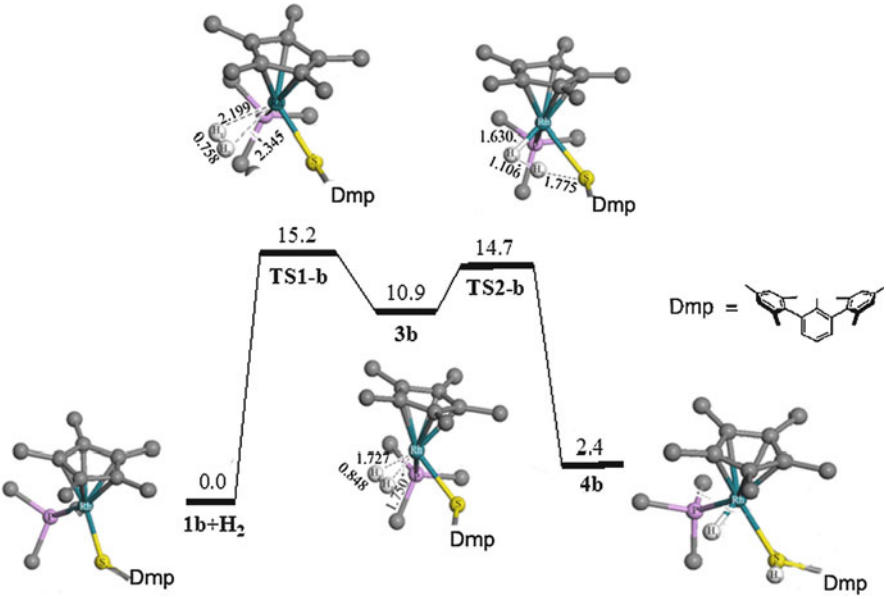

Scheme 9 The Gibbs free energy profile for the reaction of H_2 with the rhodium thiolate complex. All the relative free energies are in kcal/mol

However, the reaction of H_2 with the rhodium thiolate complex proceeds via a different pathway (Scheme 9). For this reaction, a η^2-dihydrogen complex is first formed. Then, the H−H bond is heterolytically splitted via a "four-center" transition state under the cooperation of the Rh center and thiolate ligand. The free energy barrier for the rate-determining step (the formation of the dihydrogen complex) is 15.2 kcal/mol in the solvent.

The calculation results described above account well for the experimental facts that these two metal thiolate complexes could react with H_2 reversibly under mild conditions. We proposed that the difference in the bond strength of the M–H bond (Ir–H is stronger than Rh–H at the similar environment) may be responsible for different H_2 activation mechanisms of these two metal thiolate complexes. To conclude, our theoretical study shows that the combination of the transition metals and the M–S (thiolate) bond may facilitate the H−H bond cleavage under mild conditions.

1.4 H_2 Activation by Transition-Metal-Based Pincer Ligand Catalysts

The pincer ligand complex, (PNP)Ir(C_6H_5), could react with H_2 at room temperature, producing the *trans*-dihydride complex, (PNP)Ir$(H)_2(C_6H_5)$, exclusively. We

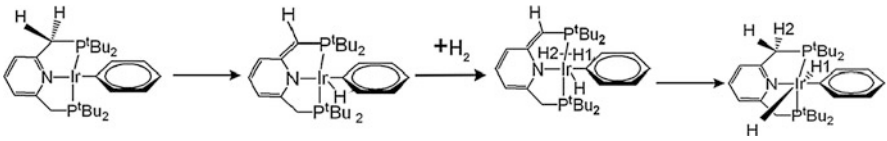

Scheme 10 The proposed mechanism for H_2 activation by the PNPIr(I)Ph complex

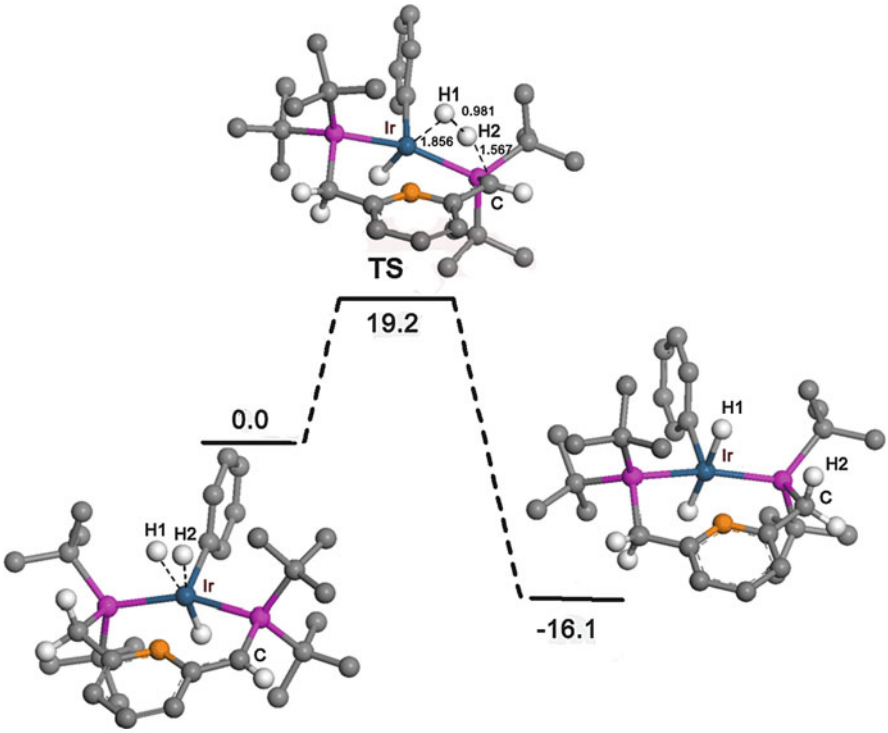

Scheme 11 Free energy profile for the H–H bond cleavage step. The relative free energies are in kcal/mol

have explored several possible reaction pathways for this novel reaction [77]. Our calculations suggested that this reaction is likely to proceed along the pathway shown in Scheme 10.

First, one of the benzylic hydrogens transfers from the methylene spacer of the PNP ligand to the metal center to form an Ir(III) hydride intermediate. Simultaneously, the PNP ligand is dearomatized. The free energy barrier for this step (the rate-determining step) is 35.9 kcal/mol. Then, H_2 adds to the metal center of this Ir(III) intermediate from the direction opposite to the hydride to form a dihydrogen intermediate. Next, the H–H bond is cleaved to produce the final *trans*-dihydride product through the cooperation of the metal center and the benzylic carbon of the PNP ligand (Scheme 11). During this process, the benzylic carbon is protonated, accompanied by the rearomatization of the PNP ligand.

The transition state for the H–H bond cleavage is calculated to be above the nonclassical dihydrogen complex by 19.2 kcal/mol. At the transition state, the natural atomic charges on two activated hydrogens (H1 and H2) are −0.17 and 0.19 e, respectively, suggesting that the H–H bond is heterolytically splitted. To summarize, the key intermediate for H_2 activation is an Ir(III) hydride intermediate, rather than the PNPIr(I)Ph reactant. For the whole reaction, the Ir center and the PNP ligand cooperate in a synergistic manner through the dearomatization/aromatization process of the pincer ligand. This molecular mechanism could provide reasonable explanations for the deuterated experimental facts.

The rate-determining step of the whole reaction has a free energy barrier of 35.9 kcal/mol, which is relatively high for a room temperature reaction. To get more accurate estimate on this energy barrier, we have performed calculations with several recently developed functionals and a larger basis set. The calculated free energy barriers are all in the range of 30–35 kcal/mol. Hence, a possible explanation for the fact that the reaction occurs at ambient temperature is that the migration of the benzylic hydrogen to the metal center may take place through a hydrogen tunneling process [78, 79].

It should be mentioned that the molecular mechanism of the same reaction has also been conducted by Milstein et al. [80]. They have proposed the similar mechanism for the whole reaction. But for the first hydrogen transfer step, their calculations indicated that this step could occur with the assistance of a two-water-molecule bridge (the free energy barrier is 20.7 kcal/mol). Further experiments may be required to verify whether this hydrogen transfer step really occurs.

2 Conclusions

In this chapter, we have presented the mechanistic details of H_2 activation by several newly developed systems. These systems include frustrated Lewis acid–Lewis base pairs, main-group metal complexes, transition metal thiolate complexes, and transition-metal-based pincer ligand catalysts. Our systematic computational investigation leads to the following conclusions: (1) In the reaction of H_2 with FLPs and main-group metal-based catalysts, the H–H bond is heterolytically cleaved by the cooperation of the Lewis acid and Lewis base centers (without a precursor). This mechanism, a concerted Lewis acid–Lewis base mechanism, differs from all the previous known mechanisms for H_2 activation; (2) In the reaction of H_2 with the iridium thiolate complex, the H–H bond is homolytically cleaved on the metal center to produce a dihydride intermediate. Whereas for the reaction with the rhodium thiolate complex, the H–H bond is heterolytically cleaved via the cooperation of the Rh center and the thoilate ligand, with a dihydrogen complex as a precursor; (3) For the reaction of H_2 with the PNPIr(I)Ph complex, the H–H bond is heterolytically cleaved through the cooperation of the metal center and the benzylic carbon of the PNP ligand. Thus, the molecular mechanism for H_2 activation strongly depends on the chemical systems. The

most important finding is that metal-free compounds or main-group metal compounds can heterolytically cleave the H–H bond under mild conditions via the concerted Lewis acid–Lewis base mechanism. We hope that new mechanistic insights into H_2 activation will help experimentalists synthesize and design more efficient and environment-friendly catalysts in the future.

Acknowledgment This work was supported by the National Natural Science Foundation of China (Grant Nos. 20625309 and 20833003)

References

1. Laser HU, Malan C, Pugin B, Spindler F, Steiner H, Studer M (2003) Adv Synth Catal 345:103
2. Saudan LA (2007) Acc Chem Res 40:1309
3. Torres GC, Ledesma SD, Jablonski EL, Miguel SRD, Scelza OA (1999) Catal Today 48:65
4. Malacea R, Poli R, Manoury E (2010) Coord Chem Rev 254:729
5. Özkar S, Finke RG (2005) J Am Chem Soc 127:4800
6. Zhao L, Li H, Lu G, Wang Z (2010) Daltan Trans 39:4038
7. Clapham SE, Hadzovic A, Morris RH (2004) Coord Chem Rev 248:2201
8. Knowles WS (1983) Acc Chem Res 16:106
9. Mikami K, Korenaga T, Terada M, Ohkuma T, Pham T, Noyori R (1999) Angew Chem Int Ed 38:495
10. Tang WJ, Zhang MX (2003) Chem Rev 103:3029
11. Shima S, Thauer RK (2006) Chem Rec 7:37
12. Frey M (2002) Chembiochem 3:153
13. Vignais PM, Billoud B, Meyer J (2001) FEMS Microbiol Rev 25:455
14. Drennan CL, Peters JW (2003) Curr Opin Struct Biol 13:220
15. Thauer RK (1998) Microbiology 144:2377
16. Huhmann-Vincent J, Scott BL, Kubas GJ (1999) Inorg Chim Acta 294:240
17. Thauer RK, Klein AR, Hartmann GC (1996) Chem Rev 96:3031
18. United Nations Development Program (2003) World Energy Assessment Report: energy and the challenge of sustainability. United Nations, New York
19. Grant PM (2003) Nature 424:129
20. Coontz R, Hanson B (2004) Science 305:957
21. Cracknell JA, Vincent KA, Armstrong FA (2008) Chem Rev 108:2439
22. Reisner E, Fonticella-Camps JC, Armstrong FA (2009) Chem Commun 550
23. Welch GC, Juan SRR, Masuda JD, Stephan DW (2006) Science 314:1124
24. Welch GC, Stephan DW (2007) J Am Chem Soc 129:1880
25. Spies P, Erker G, Kehr G, Ergander K, Fröhlich R, Grimme S, Stephan DW (2007) Chem Commun 47:5072
26. Chase PA, Stephan DW (2008) Angew Chem Int Ed 47:7433
27. Sumerin V, Schulz F, Atsumi M, Wang C, Nieger M, Leskela M, Repo T, Pyykko P, Rieger B (2008) J Am Chem Soc 130:14117
28. Chase PA, Jurca T, Stephan DW (2008) Chem Commun 1701
29. Holschumacher D, Bannenberg T, Hrib CG, Jones PG, Tamm M (2008) Angew Chem Int Ed 47:7428
30. Mömming CM, Ottem E, Kehr G, Fröhlich R, Grimme S, Stephan DW (2009) Angew Chem Int Ed 48:6643

31. Geoffrey HS, James CF, Philip PP (2005) J Am Chem Soc 127:12232
32. Koltting C, Sander W (1999) J Am Chem Soc 121:8891
33. Zuev PS, Sheridan RS (2001) J Am Chem Soc 123:12434
34. Frey GD, Lavallo V, Donnadieu B, Schoeller WW, Bertrand G (2007) Science 316:439
35. Sumerin V, Schulz F, Nieger M, Leskel M, Repo T, Rieger B (2008) Angew Chem Int Ed 47:6001
36. Holschumacher D, Bannenberg T, Hrib CG, Jones PG, Tamm M (2008) Angew Chem Int Ed 47:7428
37. Chase PA, Stephan DW (2008) Angew Chem Int Ed 47:7433
38. Herrmann WA, Denk M, Behm J, Scherer W, Klingan FR, Bock H, Solouki B, Wagner M (1992) Angew Chem Int Ed Engl 31:1485
39. Kühl O (2004) Coord Chem Rev 248:411
40. Leigh WJ, Lollmahomed F, Harrington CR, Mcdonald JM (2006) Organometallics 25:5424 and references therein
41. Kühl O (2008) Central Eur J Chem 6:365
42. Ullah F, Kühl O, Bajor G, Veszprémi T, Jones PG, Heinicke J (2009) Eur J Inorg Chem 7:221
43. Saur I, Alonso SG, Barrau J (2005) Appl Organomet Chem 19:414
44. Boughdiri S, Hussein K, Tangour B, Dahrouch M, Rivière-Baudet M, Barthelat JC (2004) J Organomet Chem 689:3279
45. Kassaee MZ, Musaki SM, Ghambarian M, Zanjani MRK (2006) J Organomet Chem 691:2933
46. Geoffrey HS, James CF, Philip PP (2005) J Am Chem Soc 127:12232
47. Peng Y, Brynda M, Ellis BD, Fettinger JC, Rivard E, Power PP (2008) Chem Commun 6042
48. Takagi N, Nagase S (2001) Organometallics 20:5498
49. Kubas GJ, Ryan RR, Swanson BI, Vergamini PJ, Wasserman HJ (1984) J Am Chem Soc 106:451
50. Kubas GJ (2004) Adv Inorg Chem 56:127
51. Kubas GJ (2001) J Organomet Chem 635:37
52. Niu S, Thomson LM, Hall MB (1999) J Am Chem Soc 121:4000
53. Amara P, Volbeda A, Fontecilla-Camps JC, Field MJ (1999) J Am Chem Soc 121:4468
54. Ogata H, Mizoguchi Y, Mizuno N, Miki K, Adachi S, Yasuoka N, Yagi T, Yamauchi O, Hirota S, Higuchi Y (2002) J Am Chem Soc 124:11628
55. Bruschi M, Zampella G, Fantucci P, DeGioia L (2005) Coord Chem Rev 249:1620
56. Teixeira VH, Baptista AM, Soares CM (2006) Biophys J 91:2035
57. Schlaf M, Lough AJ, Morris RH (1996) Organometallics 15:4423
58. Sellmann D, Rackelmann GH, Heinemann FW (1997) Chem Eur J 3:2071
59. Sweeney ZK, Polse JL, Andersen RA, Bergman RG, Kubinec MG (1997) J Am Chem Soc 119:4543
60. Sellmann D, Sutter J (1997) Acc Chem Res 30:460
61. Sellmann D, Gottschalk-Gaudig T, Heinemann FW (1998) Inorg Chem 37:3982
62. Sellmann D, Fürsattel A (1999) Angew Chem Int Ed 38:2023
63. Ohki Y, Sakamoto M, Tatsumi K (2008) J Am Chem Soc 130:11610
64. Zhang J, Leitus G, Ben-David Y, Milstein D (2005) J Am Chem Soc 127:10840
65. Ben-Ari E, Leitus G, Shimon LJW, Milstein D (2006) J Am Chem Soc 128:15390
66. Berkessel A, Schubert TJS, Müller TN (2002) J Am Chem Soc 124:8693
67. Chan B, Radom L (2005) J Am Chem Soc 127:2443
68. Spielmann J, Buch F, Harder S (2008) Angew Chem Int Ed 47:9434
69. Hohenberg P, Kohn W (1964) Phys Rev 136:B864
70. Kohn W, Sham LJ (1965) Phys Rev 140:A1133
71. Guo Y, Li S (2008) Inorg Chem 47:6212
72. Rokob TA, Hamza A, Stirling A, Soós T, Pápai I (2008) Angew Chem Int Ed 47:2435
73. Zeng G, Li S (2010) Inorg Chem 49:3361
74. Tao J, Li S (2010) Dalton Trans 39:857
75. Becke ADJ (1993) Chem Phys 9:5648

76. Lee C, Yang W, Parr RG (1988) Phys Rev B 37:785
77. Zeng G, Guo Y, Li S (2009) Inorg Chem 48:10257
78. Caldin EF (1969) Chem Rev 69:135
79. Kohen A, Cannio R, Bartolucci S, Klinman JP (1999) Nature 399:496
80. Iron MA, Ben-Ari E, Cohen R, Milstein D (2009) Dalton Trans 9433

Transition Metal-Catalyzed Hydrogenations

Aaron Forbes, Vincenzo Verdolino, Paul Helquist, and Olaf Wiest

Abstract Computational methods are an indispensible tool for the study of metal-organic reaction mechanisms. A particularly fruitful area is that of transition metal-catalyzed hydrogenations, including enantioselective versions that are extensively used at both the laboratory and the industrial scale. This review covers computational studies of rhodium-, ruthenium-, and iridium-catalyzed hydrogenation of enamides, acrylamides, carbonyls, and unactivated olefins. The evolution of the mechanistic models and the relationship of the computational studies to experimental studies are discussed.

1 Introduction

The transition metal-catalyzed hydrogenation of C=C, C=O, and C=N double bonds is an important synthetic transformation widely used in both industry and academic research. Besides being highly atom-economical and high yielding in general applications, it is also amenable to use in asymmetric synthesis. The use of chiral ligands allows, in many cases, the synthesis of a range of compounds with very high enantioselectivity. The combined features of efficiency and selectivity make transition metal-catalyzed hydrogenations the method of choice in many large-scale processes. One example is the industrial production of enantiomerically pure amino acids which uses the Rh(I)-catalyzed hydrogenation of enamides. This reaction proceeds in essentially 100% yield and 100% e.e. and can be run on a multi-ton scale. Additional

A. Forbes • P. Helquist • O. Wiest (✉)
Department of Chemistry and Biochemistry, University of Notre Dame, Notre Dame, IN 46556-5670, USA
e-mail: owiest@nd.edu

V. Verdolino
Faculty of Informatics, Università della Svizzera italiana (USI-ETH), Via Giuseppe, Buffi 13 CH-6904, Lugano

O. Wiest and Y. Wu (eds.), *Computational Organometallic Chemistry*,
DOI 10.1007/978-3-642-25258-7_4,

examples of industrial-scale enantioselective hydrogenations of alkenes, ketones, and imines include the synthesis of L-dopa (alkene), L-menthol (alkene), α-tocopherol (alkene), aliskiren (alkene), laropiprant (alkene), taranabant (alkene), sitagliptin (alkene), orlistat (ketone), adrenaline (ketone), lobeline (ketone), dextromethorphan (imine), and metolachlor (imine) [1, 2].

Together with the development of over 200 commercially available chiral ligands and a wide range of applications for these reactions, the mechanism of rhodium-, iridium-, and ruthenium-catalyzed enantioselective transition metal hydrogenations of C=C, C=O, and C=N double bonds has been elucidated in considerable detail. A range of computational methods have played essential roles in providing atomistic detail in these studies. As a result, these computational studies have exerted considerable influence in the field, for example, by providing models of the stereoselecting transition states that have allowed the continuous redesign of new and improved ligands.

This chapter provides an overview of the current state of the understanding of the mechanism of hydrogenations of double bonds catalyzed by the most commonly used transition metals, rhodium, iridium, and ruthenium. The focus of the review will be on recent computational studies, but older computational work and experimental investigations will be discussed in context. Where appropriate, open questions and mechanistic controversies will be addressed.

2 Rhodium-Catalyzed Reactions

2.1 Hydrogenation of Enamides

The reduction of olefins is a fundamental organic transformation, which with the advent of homogeneous transition metal-catalyzed hydrogenation has garnered much interest due to the range of chiral ligands that have been developed to induce stereoselectivity. In order to rationally design new ligands for rhodium-catalyzed hydrogenation, many chemists have probed the mechanism of this reaction both experimentally and computationally. Wilkinson's catalyst [$RhCl(PPh_3)_3$] is one of the most thoroughly studied catalysts and was specifically targeted in some of the first ab initio investigations.

Early theoretical work by Dedieu and coworkers focused on individual elementary transition metal (TM) reactions for the hydrogenation of ethylene using a model of Wilkinson's catalyst [$RhCl(PPH_3)_3$] [3–6]. They used LCAO-MO-SCF calculations to perform an orbital analysis of the oxidative addition step, determine intermediate stability, and analyze the olefin insertion step. Using SCF calculations and orbital correlation diagrams for the valence orbitals of the reactants and products, they analyzed the feasibility and geometry of the oxidative addition shown in (1).

$$H_2 + RhCl(PH_3)_3 \rightleftharpoons H_2RhCl(PH_3)_3 \quad (1)$$

$$H_2RhCl(PH_3)_2(C_2H_4) \rightleftharpoons HRhCl(PH_3)_2(C_2H_5) \quad (2)$$

The most stable geometry for the hexacoordinated adduct is an octahedral configuration with the hydrides *cis* to each other and one hydride *trans* to the Cl. These studies showed that the migratory insertion proceeds as an olefin insertion rather than a hydride migration, which is exothermic by 17 kcal/mol and has an energy barrier (2). An in-plane rearrangement occurring concurrently with the olefin insertion was found to be necessary to facilitate reductive elimination. The question of dissociative versus associative mechanisms for the reaction was also studied based upon the stability of intermediates within the pathway, but the accuracy of the calculations possible for a system of this size was not sufficient to determine unambiguously the preferred pathway. The associative mechanism would proceed by oxidative addition before dissociation of a phosphine ligand. The associative mechanism has since been disproved based on the experimental observation that the oxidative addition of H_2 to $[RhCl(PPh_3)_2]$ takes place 10^4 times faster than that of Wilkinson's catalyst $[RhCl(PPh_3)_3]$ and that catalysis is inhibited with excess phosphine present [7–10].

The homogeneous rhodium-catalyzed hydrogenation of olefins was the first reaction whose full catalytic cycle was investigated using ab initio calculations at the more appropriate HF and MP2/HF levels of theory to isolate the relevant intermediates and transition states along the potential energy surface (PES) [11, 12]. The proposed mechanism for the full catalytic cycle using a model of the active $14e^-$ Wilkinson catalyst ($RhCl(PH_3)_2$) and ethylene as the olefin substrate, shown in Scheme 1, was based on an earlier hypothesis by Halpern and coworkers [7]. This mechanism involves the oxidative addition, olefin coordination, insertion of ethylene, isomerization, and reductive elimination producing ethane. The isomerization step was not originally a part of the Halpern mechanism, but was found in the computational studies to be necessary to facilitate reductive elimination.

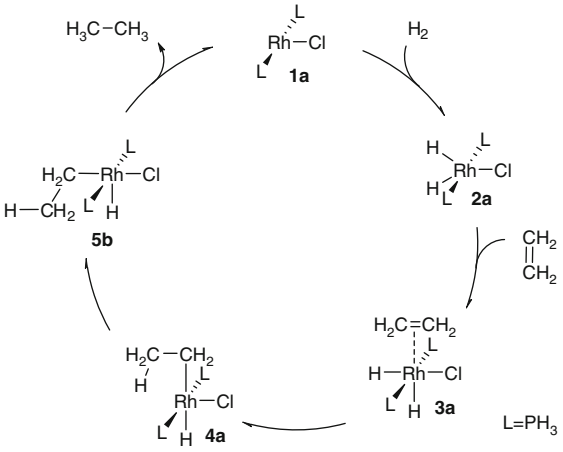

Scheme 1 Mechanism for the Rh(I)-catalyzed hydrogenation of ethylene proposed by Halpern

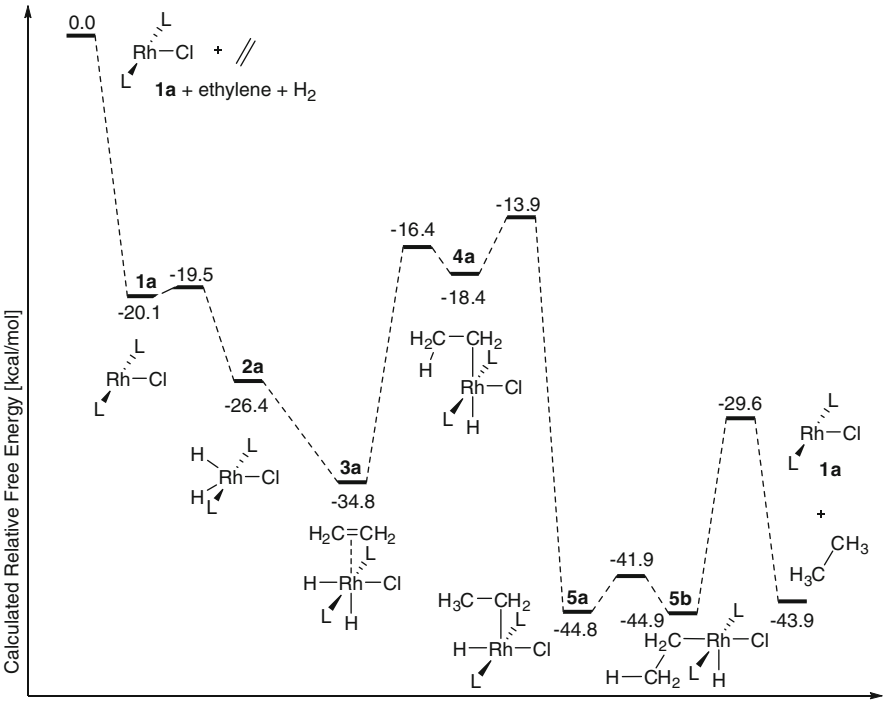

Fig. 1 PES of the Halpern mechanism for hydrogenation with Wilkinson's catalyst

The results of these studies are summarized in Fig. 1. Oxidative addition of H_2 to the $14e^-$ Rh^I complex **1a** to give the trigonal bipyramidal (TBP) Rh^{III} complex **2a** is exothermic by 26.4 kcal/mol, with a small barrier of 0.6 kcal/mol. Coordination of ethylene to complex **2a** occurs as a barrierless step in the H–H–Cl plane between H and Cl to give the octahedral complex **3a**. Migratory insertion of ethylene into the Rh^{III}–H bond is endothermic by 16.4 kcal/mol with a barrier of 18.4 kcal/mol, resulting in *trans*-ethyl hydride complex **4a**. The geometry of the *trans*-ethyl hydride complex **4a** displays a strong agostic interaction. In order for the reductive elimination to occur, the hydride needs to be *cis* to the ethyl ligand. The most facile isomerization has been calculated to be the hydride migration to **5a,** followed by subsequent chloride migration to give the *cis*-ethyl hydride complex **5b** with a barrier of 4.5 kcal/mol. Reductive elimination can then take place with a relatively high activation energy of 15.3 kcal/mol to give ethane and regenerated catalyst **1a**. The authors conclude that the rate-determining step is a combination of the olefin insertion and the isomerization of the *trans*-ethyl hydride to the *cis*-ethyl hydride with an overall activation energy of 20.9 kcal/mol.

Identifying olefin insertion as the rate-determining step, Morokuma and coworkers focused on the effect of chloride catalyst $RhCl(PH_3)_2$ versus that of hydride catalyst $HRh(PH_3)_2$ on the mechanism [13]. The olefin insertion is much more facile with the $HRh(PH_3)_2$ catalyst, but the reverse β-hydride elimination is

also more facile, making $RhCl(PH_3)_2$ a more efficient catalyst. Due to the much higher Lewis basicity and hardness, the hydride is found to have a much stronger *trans*-effect than the chloride.

Koga and Morokuma also investigated the alternative catalytic cycle proposed based on molecular modeling and NMR experiments performed by Brown [14–18], which suggested that isomerization takes place at an early stage after oxidative addition of molecular hydrogen, but before olefin coordination [19]. The cyclohexene substrate studied in this work coordinates more easily to *cis*-bisphosphine intermediates in comparison to the *trans*-bisphosphines studied previously (Scheme 2).

Using HF/3-21G calculations with double-ξ basis sets, the isomerization of H_2Rh^{III} complex **2a** to *cis*-bisphosphine complex **2b** and subsequent necessary transformations were studied to analyze the numerous isomerization pathways to various TBP and square planar (SP) complexes, which resulted in the identification of the apical preference: H > PH_3 > Cl. Phosphine migration was identified as necessary to form the proposed *cis*-bisphosphine **2b**, as shown in Fig. 2. Isomerization of *trans*-bisphosphine **2a** to *cis*-bisphosphine **2b** is endothermic by 21 kcal/mol and requires a substantial activation energy of 26.9 kcal/mol. In this pathway, ethylene coordination providing **3b** is exothermic by 23.6 kcal/mol and is essentially barrierless. Insertion is exothermic by 6.0 kcal/mol and has a barrier of only 9.6 kcal/mol, providing *cis*-ethyl hydride complex **4c**. At this point, after Cl migration, **4d** can undergo reductive elimination to provide **1b** and ethane, or PH_3 migration can occur to give **5a**, which can undergo reductive elimination to provide **1a** and ethane. It has been proposed that the large barrier of 27 kcal/mol for the isomerization to the *cis*-bisphosphine complex is prohibitive based on the more facile 18 kcal/mol barrier for the Halpern mechanism. It is possible, however, that the use of larger phosphines and olefins can make the isomerization to

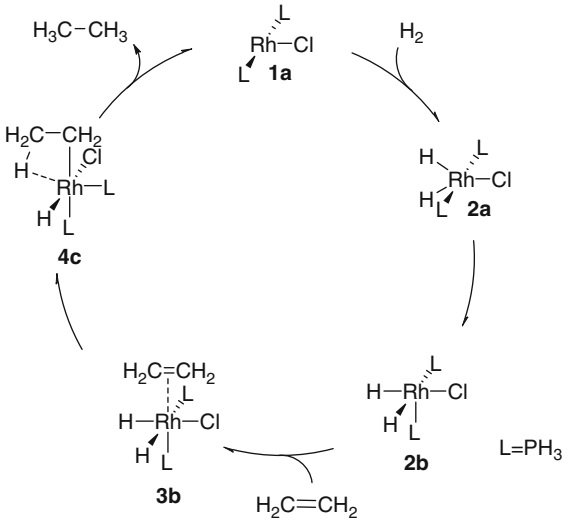

Scheme 2 Mechanism for the Rh(I)-catalyzed hydrogenation of ethylene proposed by Brown

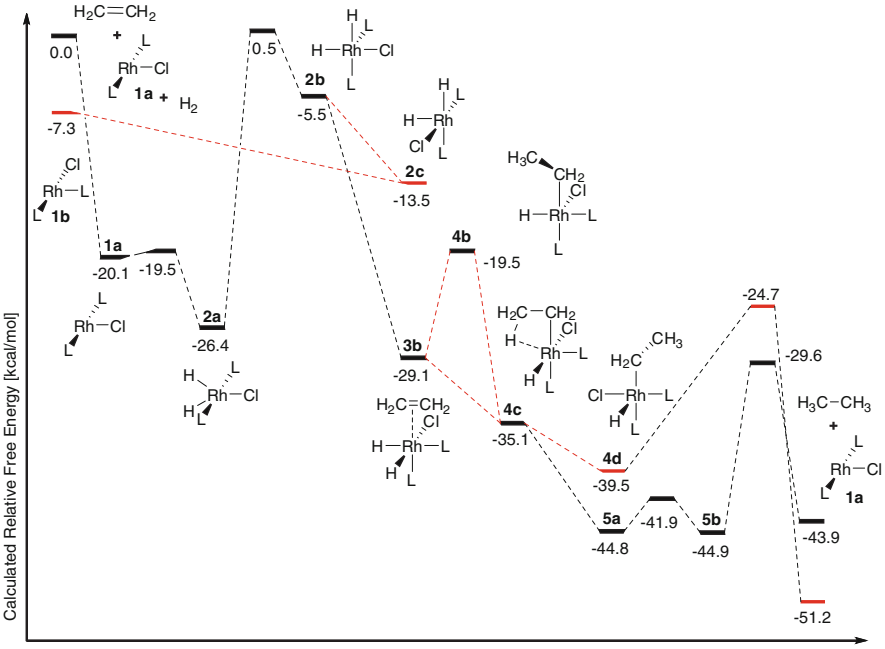

Fig. 2 PES of the Brown mechanism for hydrogenation with Wilkinson's catalyst

cis-bisphosphine hydride complexes more energetically competitive. However, such more realistic models were not be studied due to limitations in CPU power at this relatively early stage in the development of computational chemistry.

Following work on the mechanism of rhodium-catalyzed olefin hydrogenation using achiral ligands, many investigators were interested in the issue of stereoselection within the mechanism [13, 20–24], specifically the hydrogenation of enamide substrates with chiral bisphosphine rhodium catalysts [25–28]. This reaction is widely used for the large-scale production of chiral α- and β-amino acids, for example, the synthesis of L-DOPA used in the treatment of Parkinson's disease [25, 29, 30]. The importance of these reactions was also recognized by the 2001 Nobel Prize in Chemistry awarded to two developers of the reaction: William S. Knowles and Ryoji Noyori. Early stage investigations of the origin of enantiodifferentiation were performed using qualitative molecular graphics [22, 23] and molecular mechanics [24] calculations on various substrate–ligand combinations of the six-coordinate dihydride intermediates that were thought to be crucial for stereoselection. Molecular graphics methods are approximate methods that can give only qualitative information based on existing crystal structures and energy minimizations of van der Waals interactions. Explicit molecular mechanics force fields were not applied until a SHAPES/CHARMM force field in conjunction with conformer population analysis (CPA) based on NOE data was used [24]. Ultimately, the study of intermediates rather than the crucial transition states did not allow the quantitative analysis of stereoselectivity.

The asymmetric hydrogenation of enamides is a useful reaction in the production of chiral amino acids. The rhodium-catalyzed hydrogenation of enamides frequently employs bisphosphines to induce chirality. Although the hydrogenation has proven to give excellent stereoselectivity in a number of cases (Scheme 3) [28, 31–34], some substrate–ligand combinations result in poor stereoinduction [35, 36].

Extensive experimental studies by a number of groups [14–18, 37–47] were unable to unequivocally determine the turnover-limiting and stereo-determining step(s) in the enantioselective hydrogenation of prochiral enamides, and are inherently unable to provide the atomic-level detail necessary for molecular design of improved ligands. Landis and coworkers used B3LYP/LANL2DZ calculations of a simple model system $[Rh(PH_3)_2(\alpha\text{-acetamidoacrylonitrile})]^+$ to analyze four different reaction pathways based upon the possible approaches of H_2 to the $16e^-$ square planar Rh^I complex **6**, shown in Fig. 3 [48].

The results for this catalytic cycle are summarized in Fig. 4. Coordination of H_2 to the $[Rh(PH_3)_2(\alpha\text{-acetamidoacrylonitrile})]^+$ complex **6** to form a five-coordinate molecular H_2 complex **7** is followed by oxidative addition to give an octahedral dihydride complex **8.** Migratory insertion to an allyl hydride **9** before reductive elimination gives coordinated product **10**. The two pathways **B** and **D** involve H_2 approach parallel to the Rh–O bond for coordination and had energy barriers of

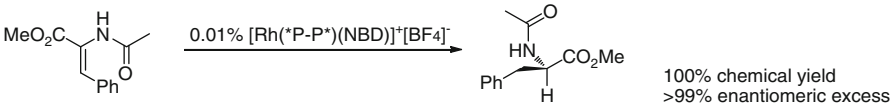

Scheme 3 Enantioselective hydrogenation of enamides to give amino acids

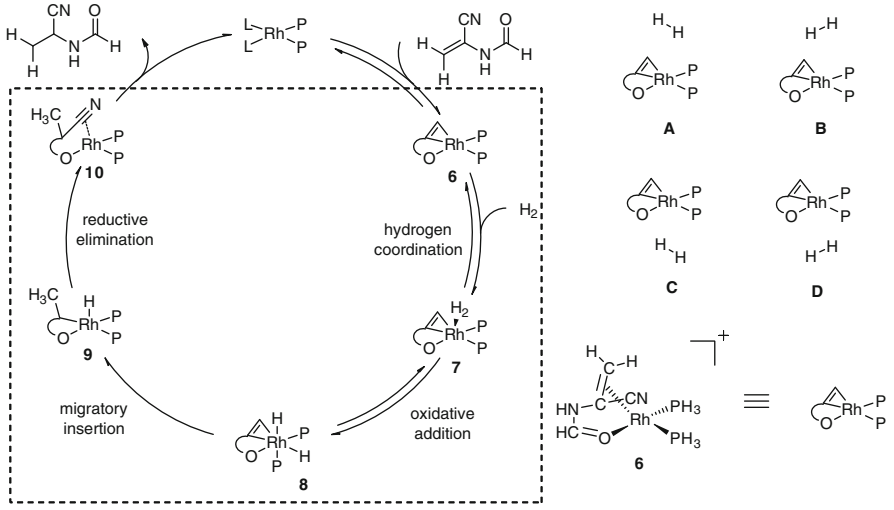

Fig. 3 Catalytic cycle based on the dominant **A** pathway as proposed by Landis and coworkers

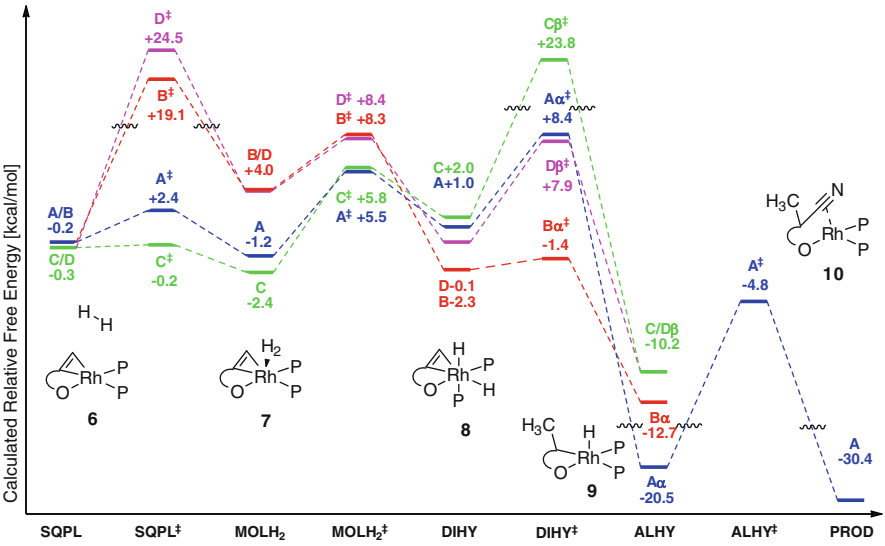

Fig. 4 PES for pathways **A**, **B**, **C**, and **D** with accompanying structures for the dominant **A** pathway

19.3 kcal/mol and 24.8 kcal/mol, respectively, making these pathways kinetically prohibited. The activation energy for olefin insertion into the Rh–H bond in pathway **A** is only 7.4 kcal/mol, much lower than that of pathway **C** at 21.8 kcal/mol. In the transformation of dihydride **8-A** to **9-A**, the axial hydride migrates to the β-carbon, leaving the α-carbon still strongly coordinated to the metal. Based on these data, pathway **A** is the only kinetically accessible mechanism, with the olefin insertion being the rate-determining step.

A stereochemically relevant side reaction is the isomerization of the five-coordinate molecular H_2 complexes by Berry pseudorotation and turnstile rotation, as well as isomerization of the dihydride species by Bailar twist or ligand dissociation pathways. The turnstile rotation structure was calculated to have a high activation energy of 22.6 kcal/mol relative to the molecular hydrogen species **7-A** to **7-C**. Double Berry pseudorotation to give molecular hydrogen complex **7-B**/**D** is also prohibited by high activation energies of >15 kcal/mol. A Bailar twist transition structure between dihydride **8** intermediates could not be located. Isomerization of dihydride **8-A** to **8-B** via alkene dissociation, translation, and recoordination had an overall barrier of 13.1 kcal/mol, 2.0 kcal/mol higher than the highest barrier in the **A** pathway. Isomerization to the **B** or **D** pathways is also kinetically unfavorable for this model system (Scheme 4).

2.2 *Stereoselectivity*

With the results of this simple model system in hand, the reaction using ZDMP as a bidentate phosphine ligand as well as with chiral ligands was investigated [49, 50].

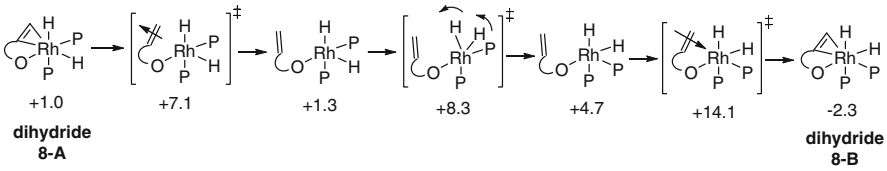

Scheme 4 Isomerization from **A** to **B** pathway involving a turnstile rotation

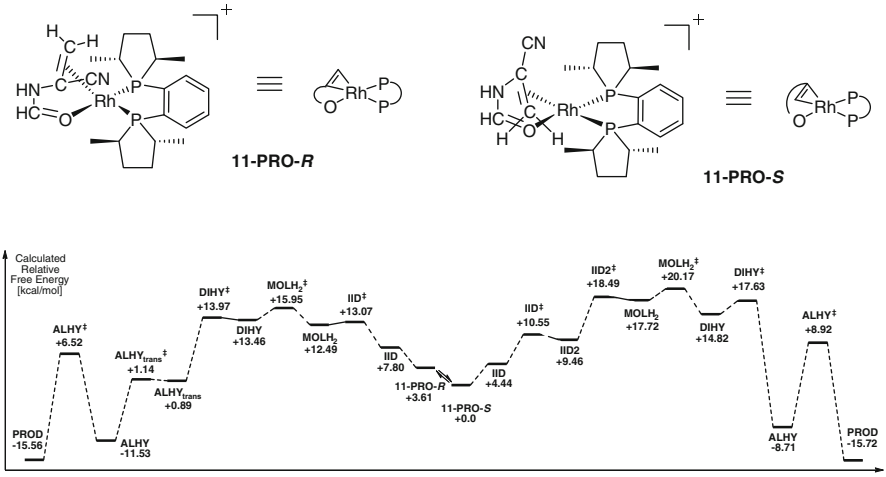

Fig. 5 PES for the minor and major manifold for the low-energy **A** pathway

It was shown that the smaller model discussed above provided a good representation of the reaction with a bidentate ligand. For the larger, chiral ligands such as for the enamide hydrogenation catalyzed by [Rh((*R*,*R*)-Me-DuPHOS)]$^+$ using α-formamido acrylonitrile as a model of the prochiral enamide, a three-layer hybrid QM/MM method (ONIOM) was used. The PES for the four different approaches of H_2 to the square planar complex is possible from the two diastereotopic sides, leading to a total of eight different PESs. Figure 5 summarizes the results for the PES for both diastereomers of the 16e$^-$ square planar complex **11-PRO-*R*** and **11-PRO-*S***.

Similar to the small model system, pathway **A** corresponds to the lowest overall energy pathway, and the activation energy for the **11-PRO-*S*** pathway is 20.4 kcal/mol, compared to 15.9 kcal/mol in the **11-PRO-*R*** pathway. This result agrees with the previously described "anti-lock-and-key" motif [51]. The turnover-limiting step identified in the previous study changes from the olefin insertion to the oxidative addition. This suggests that the catalytic cycle is dependent on the exact stereoelectronics of a given reaction and may not be universal for different ligand–substrate combinations.

Early experimental work on prochiral enamides was performed on substrates with electron-withdrawing groups and aromatic substituents in the α-position of the olefin. The results of these experiments corresponded very well with the work described

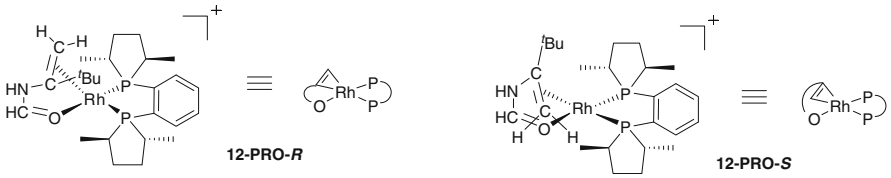

Fig. 6 Diastereomeric square planar [Rh(*N*-(1-*tert*-butylvinyl)formamide)-((*R*,*R*)-MeDuPHOS)]$^+$ complexes

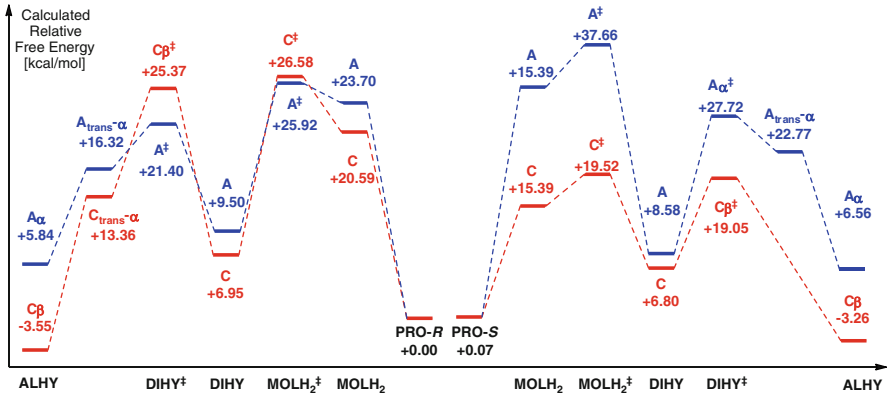

Fig. 7 PES comparing **A** and **C** pathways for both manifolds depicting a preference for the now low-energy **C** pathway and subsequent dominance of the PRO-*S* manifold

above, in that products from the (*R*,*R*)-Me-DuPHOS-Rh(I)-catalyzed reaction had the *R* configuration. However, experimental studies have shown that rhodium-catalyzed hydrogenations of prochiral enamides with alkyl substituents in the α-position give the *S* products with high enantioselectivities [34, 52]. To explore this phenomenon, an ONIOM study was conducted with large alkyl groups in the α-position, as shown in Fig. 6, instead of an electron-withdrawing group to probe a change in mechanism computationally [50]. The two diastereomeric pathways were analyzed using the [Rh(*N*-(1-*tert*-butylvinyl) formamide)-((*R*,*R*)-MeDuPHOS)]$^+$ complex, as shown in Fig. 7. Although several structures along the reaction pathway could not be fully optimized, it is clear that for these substrates, there is a preference for the **C** pathway due to destabilization of the α-alkyl hydrides relative to the β-alkyl hydrides. Similar to the previous study, the oxidative addition is turnover limiting, but the energy difference between the oxidative addition and migratory insertion transition states is much lower. The **C** pathway has a preference for the **Pro-*S*** manifold by ~6 kcal/mol, which is in agreement with the high enantioselectivity seen experimentally.

A number of other theoretical studies on the enamide system have been performed to further elucidate the enantioselectivity derived for different substrate–ligand combinations in the Rh(I)-catalyzed hydrogenation. Li and coworkers examined the PES for the [Rh(*R*,*R*)-Et-BisP*]$^+$-catalyzed asymmetric hydrogenation of α-acetamidoacrylonitrile using the B3LYP functional (Scheme 5) [53]. They chose this

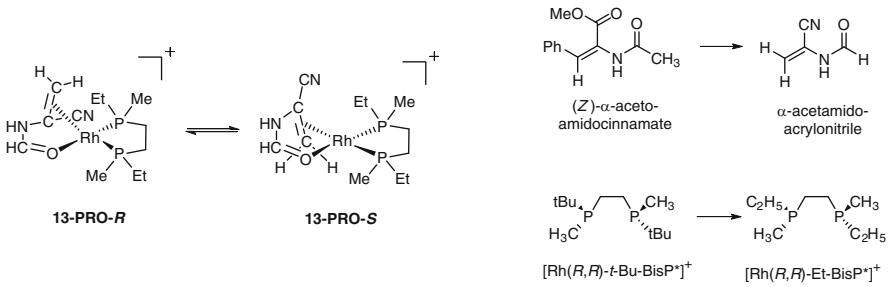

Scheme 5 Model systems for the investigation of stereoselectivity

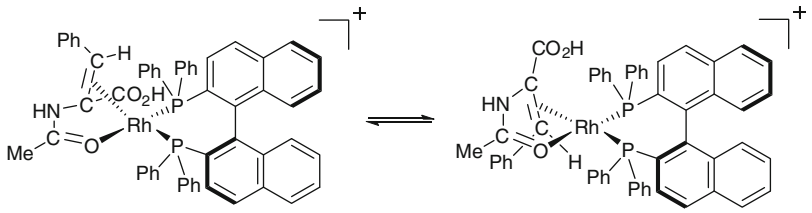

Scheme 6 Transition structures of reactions with BINAP ligands

model system to analyze the selectivity derived from the [Rh(*R*,*R*)-*t*-Bu-BisP*]$^+$-catalyzed hydrogenation of methyl (*Z*)-α-acetamidocinnamate (MAC), which has been experimentally shown to give 99% e.e. of the *R*-product [44, 54–57]. The catalytic cycle of oxidative addition of hydrogen to both diastereomers of the [Rh(α-acetamidoacrylonitrile)(*R*,*R*)-Et-BisP*]$^+$ complex **13-PRO-*R*** and **13-PRO-*S***, subsequent olefin insertion into the Rh–H bond, reductive elimination of the alkyl hydride, and final dissociation to provide product was calculated. Both diastereomeric manifolds with regard to binding to the *re* or *si* face of the olefin and the four possible *cis* additions of hydrogen, giving a total of eight potential energy profiles, were considered. The rate-limiting step was found to be the oxidative addition, and the pathway leading to the *R*-product is preferred over the one for the *S*-product by 2.2 kcal/mol. This result is consistent with previous work of [Rh((*R*,*R*)-Me-DuPHOS)]$^+$-catalyzed hydrogenation of α-formamidoacrylonitrile. It also supports the "anti-lock-and-key" motif and shows the close energy differences between the oxidative addition and olefin insertion.

The BINAP-Rh^I-catalyzed hydrogenation of enamide 2-acetylamino-3-phenylacrylic acid was studied using the hybrid IMOMM QM/MM method [58]. It was found that the relative energy differences between diastereomers (**14-PRO-*R*** and **14-PRO-*S***) in both the oxidative addition and migratory insertion steps are consistent with the experimentally observed enantioselectivity. This theoretical evidence shows a shift for this particular ligand–substrate combination as well as the hydrogenation of α-acylaminoacrylates by [Rh((S,S)-dipamp)]$^+$ to a "lock-and-key" motif (Scheme 6).

The question of how substrate electronics affects the mechanism or whether the results for the alkyl-substituted substrates are an artifact of the ONIOM calculations was studied using DFT of larger systems [59, 60]. It was shown that the reaction mechanism depends on the substrate's ability to stabilize the forming negative charge on the α- or β-carbon during the hydride transfer. The electronics of the substrate play a pivotal role and thus far overshadow the effect of ligand sterics. In the direct comparison of ONIOM versus DFT in the [Rh((*R*,*R*)-Me-DuPHOS)]$^+$-catalyzed hydrogenation of α-formamidoacrylonitrile, it was found that qualitatively the same trends are observed within the potential energy profiles of the examined pathways. The oxidative addition is rate limiting and the **A** pathway (approach of molecular hydrogen parallel to P-Rh-olefin preferring the face with the β-carbon) is found to be the lowest energy pathway. The relative energy differences calculated by DFT are consistently lower than those that were found in the ONIOM study. Comparison of the transition structure for the oxidative addition in the **A** pathway from DFT and ONIOM predicts the same enantiomeric excess for the reaction, validating the earlier studies.

This work served as the basis to create a reaction-specific transition state force field (TSFF) for the rhodium-catalyzed hydrogenation of enamides [60, 61] using the Q2MM method developed by Norrby and Liljefors [62]. The experimental and theoretical mechanistic information provides a model of the stereoselecting transition state for this reaction, which is the transition state for the hydride transfer in Landis' "**A**" pathway. Experiments show that this step is irreversible and the kinetics are consistent with it being the rate-determining step as well [40]. It was shown that the electronics of the substrate plays a vital role in the mechanism and that the **A** pathway is the only energetically feasible reaction pathway for dehydro-α-amino acids, whereas electronically dissimilar substrates such as the ones shown in Scheme 7 show a mechanistic crossover to the **C** pathway. QM calculations at the B3LYP level of theory using the LACVP** basis set were performed on this transition state with a combination of the ZDMP, DMPE, (*R*,*R*)-Me-DUPHOS, and (*R*,*R*)-Me-BPE ligands (Scheme 8) with α-formamidoacrylonitrile to create a training set for the fitting of parameters of the TSFF.

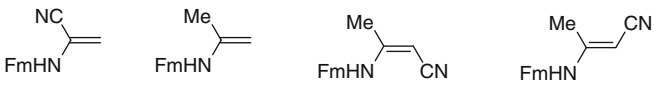

Scheme 7 Model systems studied by Donoghue et al. [59, 60]

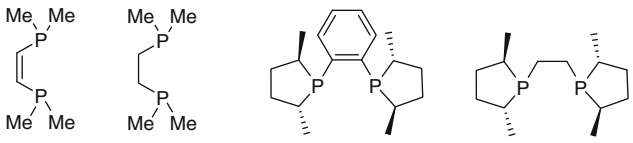

Scheme 8 Ligands studied by Donoghue et al. [59, 60]

Optimized QM transition structures were used to fit parameters of a MM3*-type force field to create a TSFF that treats the TS as a minima by inverting the PES through replacing the single negative eigenvalue of the Hessian matrix with a large positive value. The force field was validated by comparing to a test set of experimental data and gave an overall unsigned mean error of 0.6 kcal/mol for 18 data points [60]. With the validated TSFF, the method of virtually predicting enantioselectivity was screened against experimental literature data for various combinations of 13 different chiral ligands and 7 prochiral substrates for a total of 29 total data points with an overall R^2 of 0.92 [61]. This excellent correlation between experimental and computed enantioselectivity supports the hypothesis that the stereoselecting step of the reaction is the hydride transfer, at least in the case of widely studied dehydro-α-amino acid substrates.

Gridnev and Imamoto explored the mechanism and process of stereoselection in the rhodium-catalyzed hydrogenation of enamide substrates using both experimental and computational methods [43, 45, 63]. Most computational studies assumed a prior chelation of the enamide substrate to the rhodium complex before coordination and oxidative addition of hydrogen to the metal complex, labeled as the "unsaturated pathway" by Gridnev et al. Low-temperature NMR studies of the [Rh(nbd)BisP*]BF_4 catalyst suggests that oxidative addition of hydrogen across a solvated rhodium complex occurs prior to chelation of the enamide to the metal, labeled as the "dihydride mechanism" (Scheme 9) [60, 61, 64, 65]. This mechanistic proposal relies on the oxidative addition of dihydrogen across the solvated complex occurring faster than the oxidative addition of dihydrogen across the substrate-chelated complex. Computational studies of the "dihydride mechanism" using explicit solvent molecules to probe the hydrogenation of MAC with the rhodium complex of (*R*)-(*tert*-butylmethylphosphino)(di-*tert*-butylphosphino) methane were performed, and the lowest energy pathway is depicted in Scheme 10.

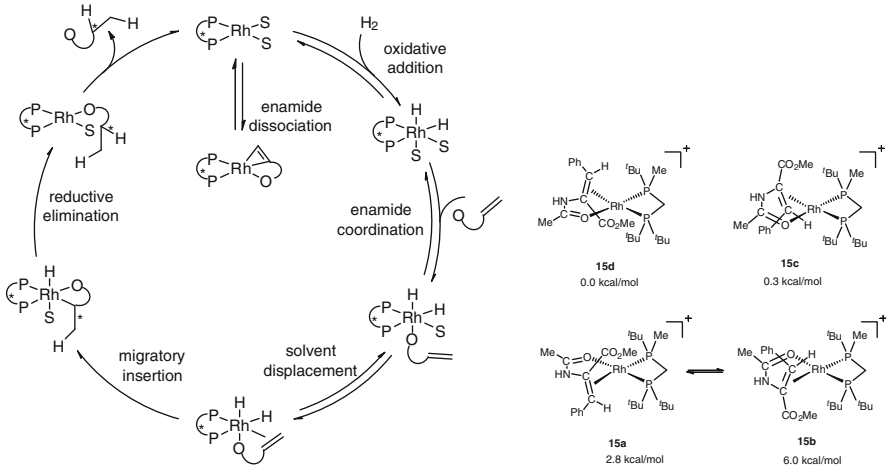

Scheme 9 Catalytic cycle for dihydride mechanism (*left*) and relative energy of key intermediates

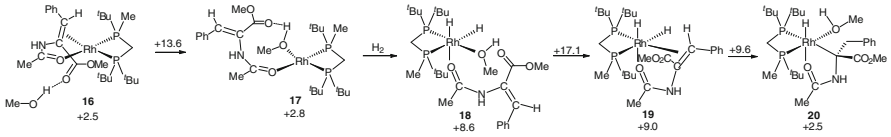

Scheme 10 Pathway of the dihydride mechanism

The computations show that the rate-determining step is the association of the olefin to the rhodium dihydride complex **18–19**, followed by migratory insertion. Both the "unsaturated" and "dihydride" mechanisms funnel into the migratory insertion as the irreversible stereoselecting step. This means that any selectivity models that rely on this TS should be accurate. The results are consistent with the PHIP investigations of Brown [42, 66] on PHANEPHOS Rh-catalyzed hydrogenation of MAC, where an agostic intermediate was proposed to be in equilibrium with a solvated Rh–ligand complex, substrate, and a solvated Rh–ligand dihydride. PHIP NMR spectroscopy showed that in the migratory insertion TS, the geometry was that of Landis' **B** pathway instead of the **A** pathway that was originally postulated to be preferred. This observation suggests either a low-energy isomerization that makes the **B** pathway accessible in the "unsaturated" mechanism since it is kinetically prohibited by a high-energy oxidative addition, or that the "dihydride" mechanism is operating. The preferred low-energy pathway found by Gridnev and Imamoto (Scheme 10) is consistent with the migratory insertion of dihydride **19** and is similar to Landis' **B** pathway.

2.3 Hydrogenation of Acrylamides

A preliminary investigation concerning the mechanism of the Rh-catalyzed hydrogenation of acrylamide substrates with model bisphosphine ligands has been reported [67]. Acrylamide was used as the model substrate and $[Rh(PH_3)_2]^+$ as the model catalyst (Fig. 8). The mechanism under investigation consists of hydrogen coordination to a $[Rh(acrylamide)(PH_3)_2]^+$ complex based on the four possible approaches of H_2, oxidative addition to form dihydrides, and olefin insertion into the Rh–H bond to form alkyl hydride complexes. Reductive elimination was not examined because it is facile in comparison to oxidative addition and olefin insertion steps.

The relevant intermediates and transition state structures were optimized at the B3LYP level of theory using a LanL2TZ(f) basis set with an ECP on Rh. The PES for each of the four possible pathways is displayed in Fig. 9.

Examination of each of the four pathways individually shows that the approach of H_2 to the metal complex is kinetically prohibited for the **B** and **D** pathways. The transition states for the oxidative addition are within 2 kcal/mol for each of the four pathways, a relatively small difference taking into account the accuracy of the calculations being performed. Olefin insertion to form alkyl hydrides is kinetically inaccessible for the **A** and **C** pathways. Such large barriers demonstrate a drastic

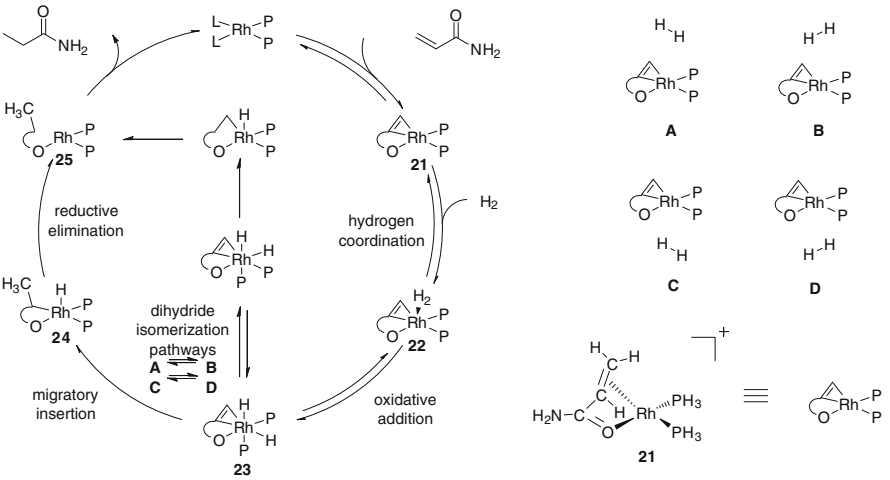

Fig. 8 Proposed catalytic cycle for rhodium-catalyzed hydrogenation of acrylamide substrate with respect to the approach of H_2

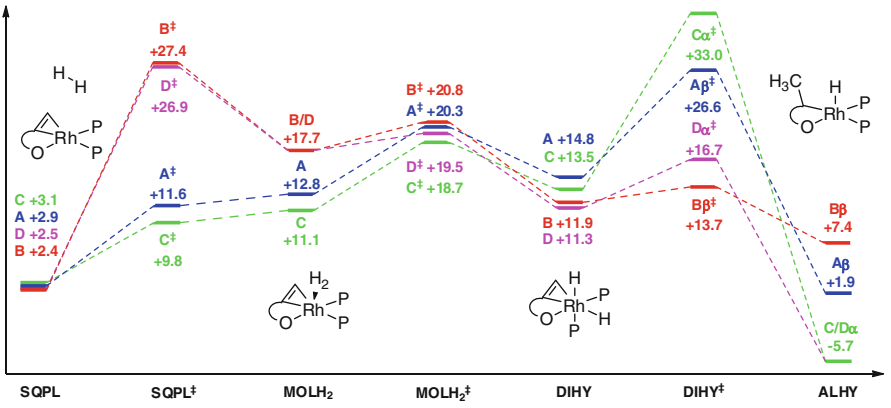

Fig. 9 PES for the four possible pathways for the hydrogenation of acrylamides

disparity between the acrylamide and enamide systems. Further studies were performed on this catalytic cycle by analyzing isomerizations between dihydride intermediates via an alkene dissociative mechanism. Isomerizations from **DIHY-23-A** to **DIHY-23-B** and **DIHY-23-C** to **DIHY-23-D** were studied. In the model enamide study, these isomerizations had energy barriers that excluded them from consideration, but as can be seen from Scheme 11, they are energetically competitive in the acrylamide system with barriers of 5.6 kcal/mol for **A**–**B** and 6.6 kcal/mol for **C**–**D**.

In this simple model system, all four pathways are potentially energetically accessible due to the possibility of isomerization, which is discouraging for the identification of the enantioselectivity determining TS. Further study of more

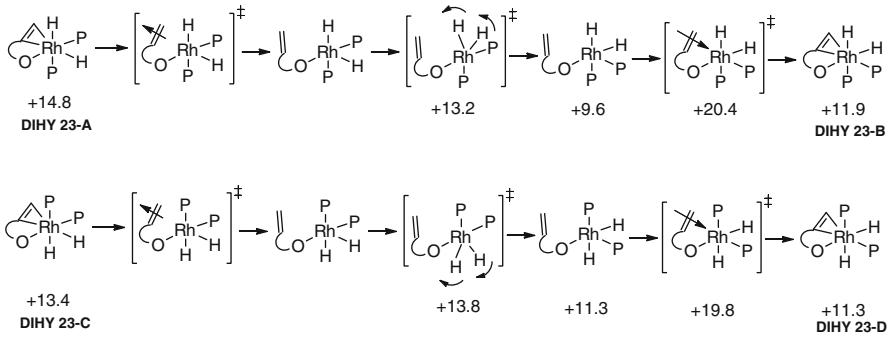

Scheme 11 Isomerization pathways for acrylamide hydrogenation

realistic substrate–ligand combinations needs to be performed to get a clearer picture of a potentially stereoselective hydrogenation of acrylamides.

3 Ruthenium-Catalyzed Reactions

3.1 Introduction

A large number of catalytic methods involving Ru-based catalysts have been successfully developed to achieve selectivity and efficiency in the hydrogenation of a large family of organic substrates. One of the most important transformations in synthetic organic chemistry is the enantioselective reduction of C=C [68–70], C=O [70–83], and C=N [84] functional groups leading to their respective chiral products [84, 85]. The design of chiral Ru(II) complexes has become a major area of research because of their ability to promote the formation of alcohols with high enantiomeric purity starting from prochiral ketones [86–98]. Many cases have been extensively investigated using both experimental and computational methods in order to cast light on the mechanistic details of the hydrogen transfer. Most of the computational investigations were aimed at identifying the preferred pathway among several possibilities [99–102]. Particular attention has been dedicated to the rationalization of the chemo- and stereoselective outcome induced by chiral catalysts [103–106]. The Ru-catalyzed hydrogenation reaction thus represents an excellent example of cooperation between experimental and theoretical investigations.

For many years, the preferred mechanism has been the center of debate, mainly because of the large number of parameters affecting the pathway. Moreover, these parameters show a synergistic influence on the mechanism and stereoselectivity, and in many cases, it was possible to distinguish the major contributions only by employing a computational approach. In particular, metal-catalyzed transfer hydrogenations are described by three different activation modes (Fig. 10): (**a**) direct transfer of a hydrogen involving both donor and acceptor covalently

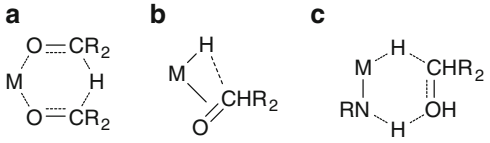

Fig. 10 General activation modes for carbonyl hydrogenations

interacting with the metal (the metal hydride complex is not involved in this mechanism), (**b**) migratory insertion of a π-coordinated substrate into a metal–hydrogen σ bond, and (**c**) an outer sphere mechanism (OSM) where both donor and acceptor never interact directly with the metal but only through hydrogen bonds (the catalyst provides both the proton and the hydride).

In this section, the most relevant investigations employing different computational approaches including MO- and DFT-based methods are reviewed. During the past 20 years, these methods have been extensively employed to address which mechanism(s) reported in Fig. 10 is (are) correct for the Ru-catalyzed hydrogen transfer by comparing calculated PESs for representative models. Such models were selected on the basis of experimental evidence, unclear catalytic behaviors, and computational time. Computational approaches have seen progressive improvements, because more complex and realistic models have been considered thanks to more efficient technology, and also because earlier studies highlighted new factors which play important roles in these reactions. A significant example is the role that the solvent plays in the hydrogen transfer.

3.2 Hydrogenation of a Carbonyl Group

The reduction of the C=O functional group has been extensively investigated with computational tools. It is important to highlight that in the case of a mild hydrogen donor such as a primary or secondary alcohol, the thermodynamic balance is very close to thermoneutral, limiting the intermediates that need to be considered along the reaction pathway. Consequently, earlier computational investigations performed by Alonso et al. [99], Noyori et al. [100], and Handgraaf et al. [102] paid particular attention to the extremely stable intermediates that could be classified as catalyst reservoirs of Ru(II). For some Ru(II) catalysts, which do not involve arene ligands as stabilizers, the suggested mechanism for the carbonyl reduction is a migratory insertion of the C=O into the Ru–H bond, as depicted in Fig. 10, mode **b** [107]. Although direct hydrogen transfer as depicted in mode **a** (Fig. 10) could not be excluded, the generally accepted mechanism for this catalyst is shown in Scheme 12.

The key to this mechanism is the ability of Ru (or other metals) to form an alkoxide complex, rearrange to form the metal hydride, and complex the ketone. One of the principle factors studied for the inner sphere mechanism (ISM) is the kinetics of the reaction with respect to the base concentration. In this mechanistic view, the base is believed to increase the concentration of the alkoxide, facilitating the overall reaction.

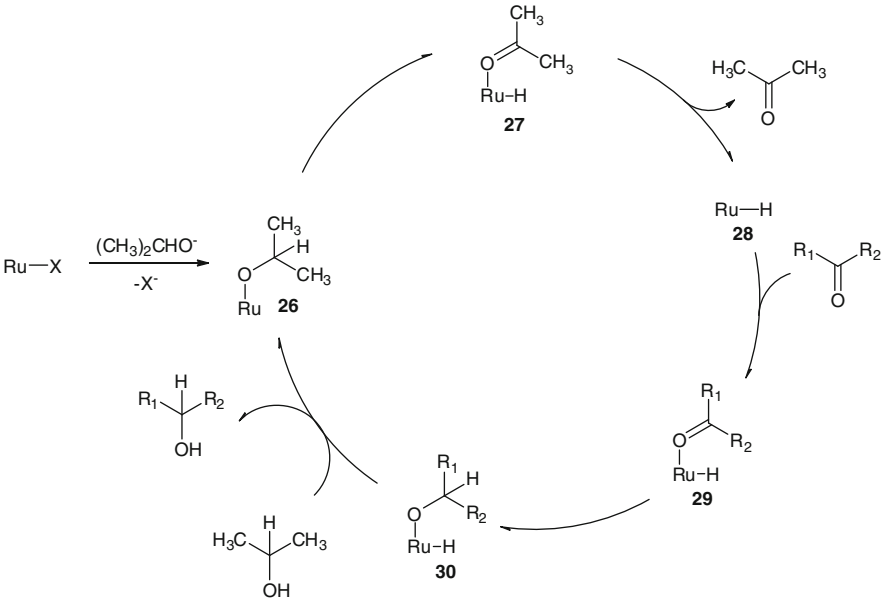

Scheme 12 Proposed catalytic cycle for ruthenium-catalyzed transfer hydrogenation

In the case where η^6 coordinated arenes stabilize the Ru catalyst with primary or secondary amine ligands, the experimental observations stimulated the investigation of a new mechanism [86–91]. Alonso and coworkers [99] performed a computational investigation using the B3PW91 functional and different basis sets in order to compare the direct insertion (Scheme 13), the migratory insertion (Scheme 14), and the concerted hydrogen transfer (Scheme 15) mechanism for the reduction of the C=O bond. The Ru catalyst has been modeled and simplified with the small 2-aminoethanol ligand and benzene as the arene. The authors were not able to describe the entire PES for all three proposed mechanisms, but they obtained a well-defined energetic picture which highlights a preferred pathway.

In the direct transfer mechanism, precursor **31** undergoes elimination of HCl, forming the $16e^-$ complex **32** (Scheme 13). The preformed alkoxide reacts with **32** generating stable alkoxide complex **33**. The ketone substrate interacts via π-coordination, leading to complex **34** after partial decoordination of the arene ligand. Complex **34** is in equilibrium with the analogous **35** through $\mathbf{TS_{34–35}}$ via hydride transfer. The concerted mechanism (Scheme 14) is described by the formation of precursor **32** which is transformed into active catalyst **37** via an outer sphere interaction with the hydrogen donor. Hydride **37** reduces the incoming ketone, which interacts with the catalyst via the outer sphere as well. Finally, the "migratory insertion" shares the same intermediates seen in the direct transfer until the generation of complex **33** (Scheme 15). Partial slippage of the arene ligand ensures the nucleophilic interaction between the forming hydride and the Ru in complex **38**. At this stage, the first hydrogen transfer takes place via an ISM

Scheme 13 Direct insertion mechanism for Ru(II)-catalyzed hydrogenation

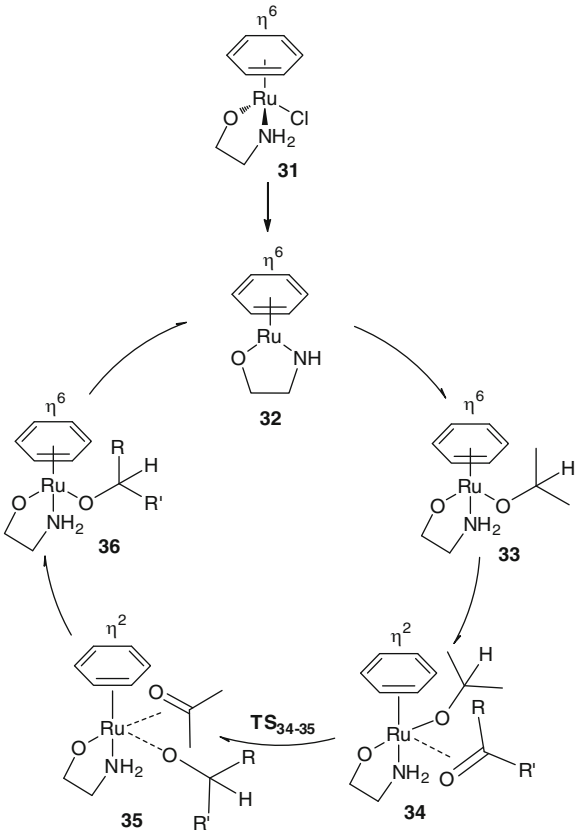

generating hydride complex **39**. $\mathbf{TS_{38–39}}$ is characterized by a four-membered ring including Ru–H–C–O. Complex **39** is in equilibrium with active catalyst **37** via decoordination of the ketone formed from the hydrogen donor and coordination of the arene back to the η^6 configuration. The incoming ketone interacts with the catalyst via π-coordination, and the second hydrogen transfer takes place through the similar $\mathbf{TS_{38a–39a}}$.

The transition states optimized at the B3PW91/LANL2DZ ECP level of theory and relative energies calculated at the B3PW91/6-311 + G** level for all atoms except for Ru where a SDD basis set augmented by *f* polarization functions have been used to show that $\mathbf{TS_{32–37}}$ is lower in energy by 7.1 kcal/mol with respect to $\mathbf{TS_{38–39}}$ and 17.9 kcal/mol with respect to $\mathbf{TS_{34–35}}$. This mechanism, initially proposed by Noyori [91], is also referred to as the OSM as neither the ketone nor the alcohol interacts directly with Ru during the process. The geometry of $\mathbf{TS_{32–37}}$ shows a rigid planar configuration for the six-membered ring involved in the hydrogen transfer (Fig. 11).

$\mathbf{TS_{32–37}}$ is characterized by a synchronous transfer of a proton from the nitrogen and a hydride from the Ru. The presence of a NH or NH_2 group in the ligand is

Scheme 14 Concerted hydrogen transfer mechanism for Ru(II)-catalyzed hydrogenation

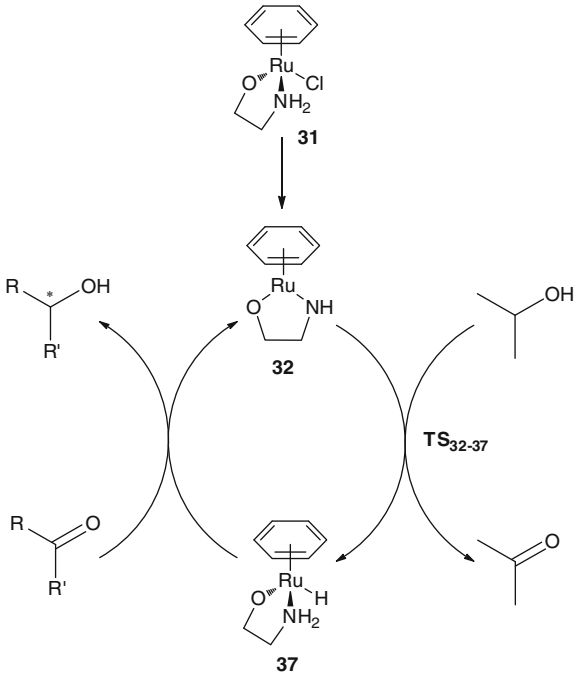

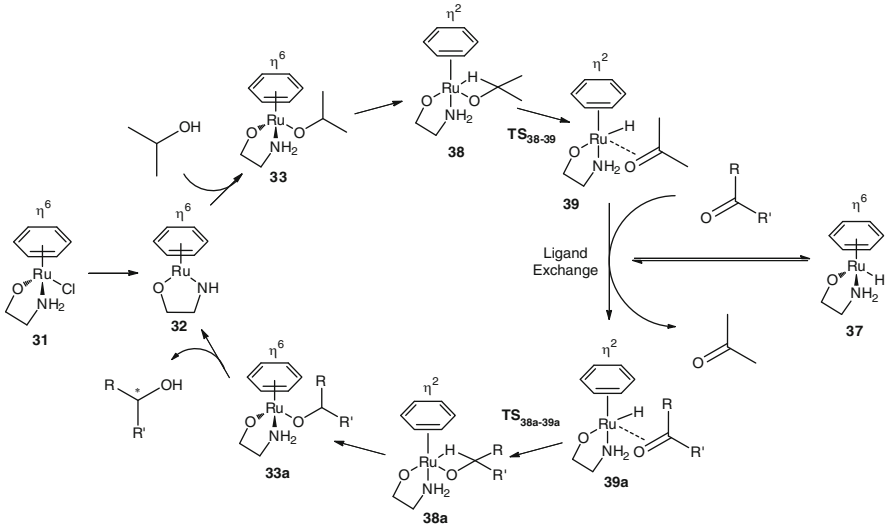

Scheme 15 Migratory insertion mechanism for Ru(II) catalyzed hydrogenation

crucial for the catalytic activity as reported by Noyori and coworkers. These computational results support this finding. Yamakawa and coworkers [100] investigated the migratory insertion and the pericyclic routes for the hydrogen transfer between methanol and formaldehyde. The authors performed a detailed

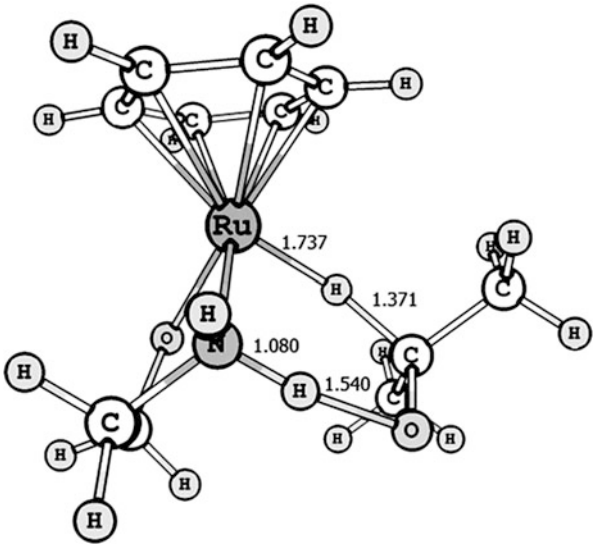

Fig. 11 Transition structure for migratory insertion

study of the PES for both mechanisms at the DFT and Moller–Plesset levels of theory. The Ru catalyst involved is formed from $RuCl_2(\eta^6$-benzene) dimer and ethanolamine or ethylenediamine in order to simulate a bifunctional ligand moiety. The mechanism proposed is summarized in Scheme 16. The authors address the base's role in catalyzing HCl elimination, which would otherwise require 36.5 kcal/mol. The formation of unsaturated $16e^-$ complex **41** is the key step in this proposed mechanism: the reaction is thermodynamically neutral (1.4–2.7 kcal/mol for the amino alcohol and the diamino catalyst, respectively), and the catalytic cycle is simplified to the exchange between **42** and **43** (respectively, in the $16e^-$ and $18e^-$ configurations) through $\mathbf{TS_{42–43}}$. The reaction is characterized by the hydride nucleophilically attacking the carbonyl carbon and a protonation of the carbonyl oxygen by the axial amine hydrogen. In the dehydrogenation process, unsaturated complex **41** shows high activity due to the highly polarized Ru–N bond. On the contrary, hydride complex **43** shows high activity in the hydrogen transfer originating from charge alternation in the H–Ru–N–H structure.

The alternative mechanism involving a migratory insertion (β-elimination in the reverse direction) appears to be less feasible with the high-energy $\mathbf{TS_{47–44a}}$ being 41.1 kcal/mol less stable than the alkoxide complex **45a** due to the interaction of the $i\text{-PrO}^-$ and the Ru. This pathway is unfavorable for two reasons: (1) the alkoxide complex is extremely stable with respect to unsaturated complex **41**, and (2) the alkoxide complex is completely saturated, forcing the partial decoordination of the arene ligand from Ru in the elimination process. As depicted in Scheme 17, the elimination process starting from complex **45a** requires 36 kcal/mol to reach $\mathbf{TS'_{46–47}}$. This step also requires the benzene stabilizer to slip from a η^6 to a η^2 coordination. The hydrogenation process through $\mathbf{TS_{47–44a}}$ requires an additional 14 kcal/mol from hydride complex **47**, making the overall migratory insertion pathway unlikely.

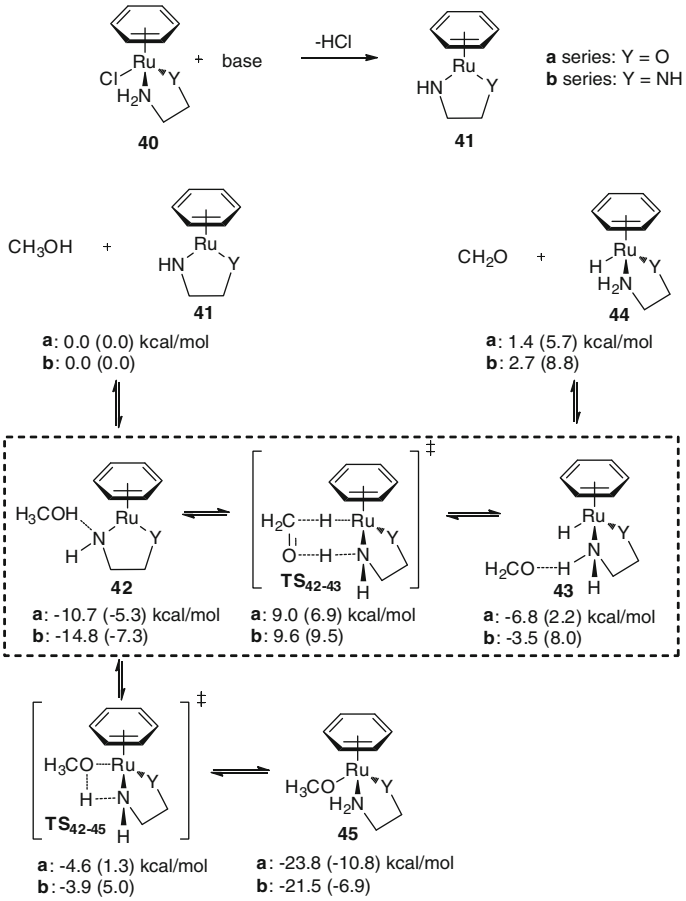

Scheme 16 Proposed mechanism for C=O hydrogenation catalyzed by Ru(II) with bifunctional ligand

Petra and coworkers [101] compared the migratory insertion and the pericyclic mechanism in the hydrogen transfer from methanol to formaldehyde catalyzed by a Ru(benzene)(NH_3)(OH)(Cl) complex. They also introduced the idea that the solvent might play an important role in the mechanism, and considered an alternative mechanism for the migratory insertion. Alonso et al. [99] already showed that the calculations, relative to the experimentally observed stereoselectivity of the hydrogenation reaction, gave significantly different results when performed using a gas phase model or using an implicit solvation model. Calculations carried out by Petra and coworkers confirmed a pericyclic mechanism for the catalytic system considered in their study. These results support the formation of a hydrogen bond between a proton of the amine with the ketone carbonyl and address its importance in the catalytic cycle. The proposed pericyclic mechanism shows a decrease in energy as the hydride complex transitions to an outer sphere interaction with the

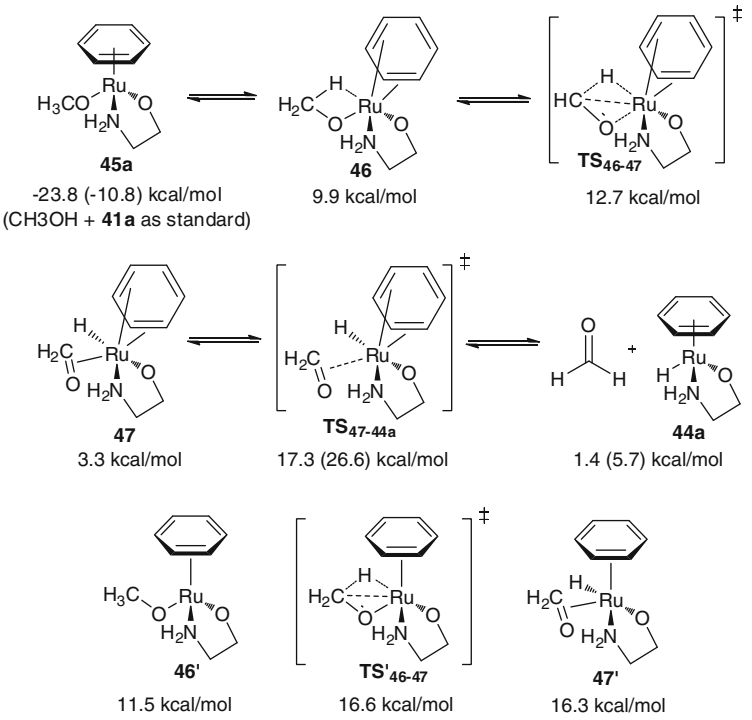

Scheme 17 Proposed migratory insertion mechanism for C=O hydrogenation catalyzed by Ru(II) with bifunctional ligand

ketone. At this point, the hydrogen transfer takes place requiring less than 1 kcal/mol, forming the unsaturated $16e^-$ complex. In the migratory insertion, the ketone has to coordinate to the Ru–hydride complex through its π electron system. As previously reported by other investigators [99, 108], this coordination implies the slippage of hapticity from η^6 to η^2 for the benzene ligand. The following two steps involve hydride transfer and ketone alkoxide protonation, which significantly destabilizes the catalytic system requiring an approximate overall energy as high as 34 kcal/mol. Interestingly, a different picture arises for the migratory insertion when an additional molecule of alcohol takes part in the hydrogen transfer. After the hydride transfer, the catalytic system is strongly stabilized by the coordination of a molecule of solvent which assists the proton transfer from the NH_3 group to the alkoxide coordinated to the Ru. With this alternative migratory insertion, the highest $TS^{\ddagger}$ is about 10 kcal/mol higher in energy than the earlier complex.

Handgraaf and coworkers [102] investigated the favored pathway for the dehydrogenation/hydrogenation of methanol/formaldehyde of the same Ru(benzene)-amino alcohol catalyst previously studied at the BLYP level of theory. Analyzing the most important optimized structures along the PES, the authors noted significant hybridization in the amine/amide N–Ru bond, transforming the catalyst from an $18e^-$ to a $16e^-$ configuration (Fig. 12), leading to a shortening of the Ru–N bond

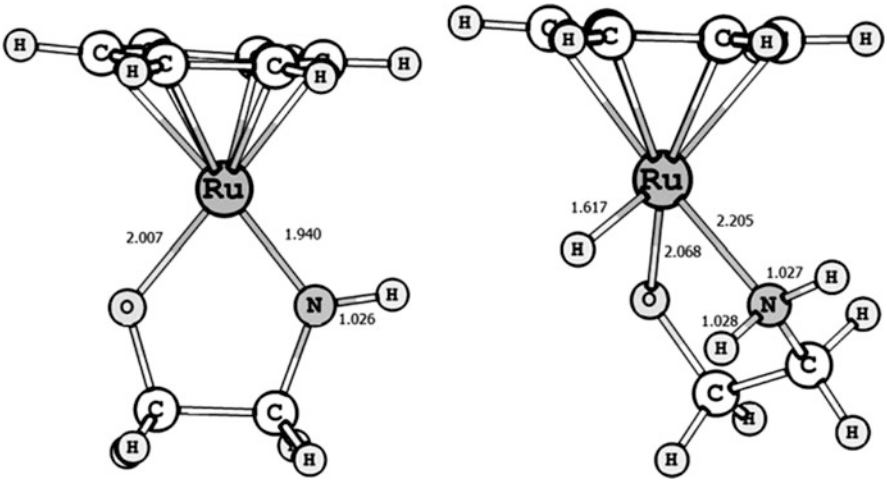

Fig. 12 Transition structures located by Handgraaf and coworkers

length after deprotonation of the amine and elimination of an auxiliary ligand (2.068 → 1.940 Å in Fig. 12 from 4 → 1). As other authors before them, Handgraaf and coworkers attributed this behavior to the delocalization of the nitrogen lone pair toward the metal which is electron poor in the $16e^-$ configuration.

The PES calculated by Handgraaf and coworkers is shown in Fig. 13. From their results obtained in the gas phase, the metal–alkoxide complex **31** is the most stable intermediate by 5 kcal/mol. As already mentioned, other investigators refer to this intermediate as a reservoir or sink [100], and it is so stable that it is kinetically inert [38]. The energy profile reported in Fig. 3 is consistent with the calculations performed by Noyori and coworkers at the B3LYP and MP4 level of theory. The hydrogenation of formaldehyde has the lowest TS in the concerted pathway, requiring only 2 kcal/mol versus 13 kcal/mol for the dehydrogenation. An important observation arising from these calculations is related to the possibility that the metal–alkoxide complex can be converted to an intermediate, which is also involved in the pericyclic mechanism. Indeed, with an energy barrier of 12 kcal/mol, alkoxide **53** can be converted into complex **49** ($16e^-$). This energy barrier is comparable to the methanol oxidation from **49** to $\mathbf{TS_{49–50}}$. In other words, the results show that the methanol dehydrogenation is the rate-determining step of this reaction and that the formaldehyde hydrogenation is facile. This finding is also supported by an experimental study which employs diamino-derived ligands [89].

The combined experimental and computational studies performed by Hedberg and coworkers [109] are in the field of hydrogen transfer using molecular hydrogen as the hydride source. Diphosphine-based Ru catalysts have proven to be very effective [110]. Experiments demonstrate that the Ru-arene/Tsdiamine catalysts can easily perform the hydrogenation transfer under mild conditions using alcohols as the hydrogen source, yet hardly react when H_2 is the hydrogen donor [89].

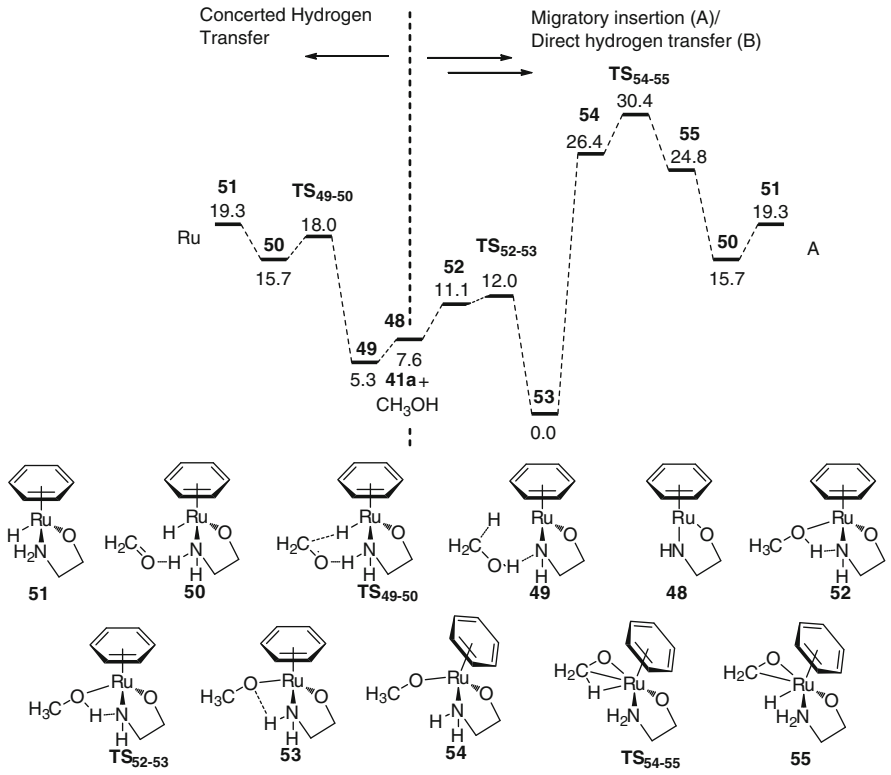

Fig. 13 Combined PES for concerted and stepwise hydrogen transfer calculated by Handgraaf and coworkers

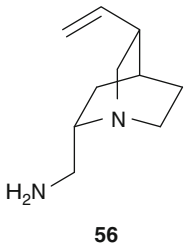

Fig. 14 Quinuclinide-based ligand **56**

In comparison, Ru-diphosphine/diamino complexes react readily with H_2. The authors investigated the activity of the catalyst formed from RuCp* and the 1,2-diamine ligand **56** (Fig. 14) used for the hydrogenation of ketones with H_2 and that it can be enhanced by quinuclinide-based ligands.

Their research, along with the experiments by Ikariya et al. [111], represents an early example of molecular hydrogen splitting catalyzed by phosphine-free Ru catalysts. In the computational investigation, they considered several diamine ligands and related the RuCp catalysts (Fig. 15). The reactions with the catalysts

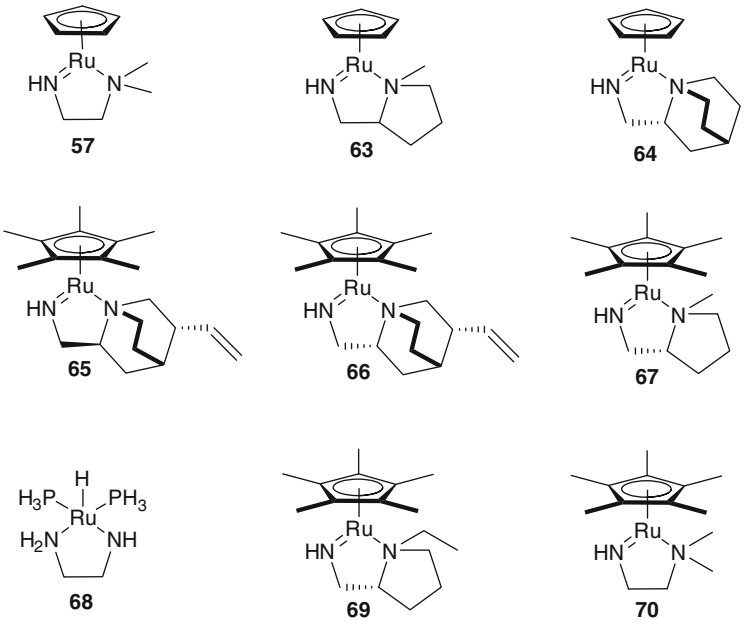

Fig. 15 Species involved in the diamine-assisted hydrogenation

alone were calculated to have high activation energies up to 25.2 kcal/mol [100, 103, 112–118], which prohibits similar heterolytic hydrogen splitting. For diamine/diphosphine complexes, similar calculations resulted in an energy barrier which was lower than 13.4 kcal/mol, and the experimental measurement of the enthalpy was between 7.6 and 8.6 kcal/mol [112]. Following the earlier observation reported by Ikariya and coworkers [111] and supported by other investigators [71, 83, 119], Hedberg and coworkers stated that the solvent played a fundamental role in the TS which splits hydrogen. Figure 16 gives the PES comparison between assisted and nonassisted hydrogen splitting catalyzed by **57**.

In the case of nonassisted hydrogen splitting, the rate-determining step of this process is the H–H bond cleavage, which requires 17.2 kcal/mol. The hydride complex is ~5 kcal/mol more stable than the initial reactants, and consequently 21 kcal/mol is required in order to reverse the process. This result is in contrast to the experimental evidence of H/D scrambling, which shows that the reactants and products equilibrate. Calculations on the solvent-assisted hydrogen splitting are in better agreement with the experimental evidence. The rate-determining step is still the H–H bond cleavage, but the alcohol stabilizes the coordinated molecular hydrogen complex by several kcal/mol, resulting in an activation energy of 7–10 kcal/mol. Similar results are obtained for catalyst **68**, finding good agreement with the earlier observation reported by Noyori and coworkers [120].

The role of the solvent environment for the reaction has been studied in detail by Rossin and coworkers [106]. They considered a catalytic model consisting of

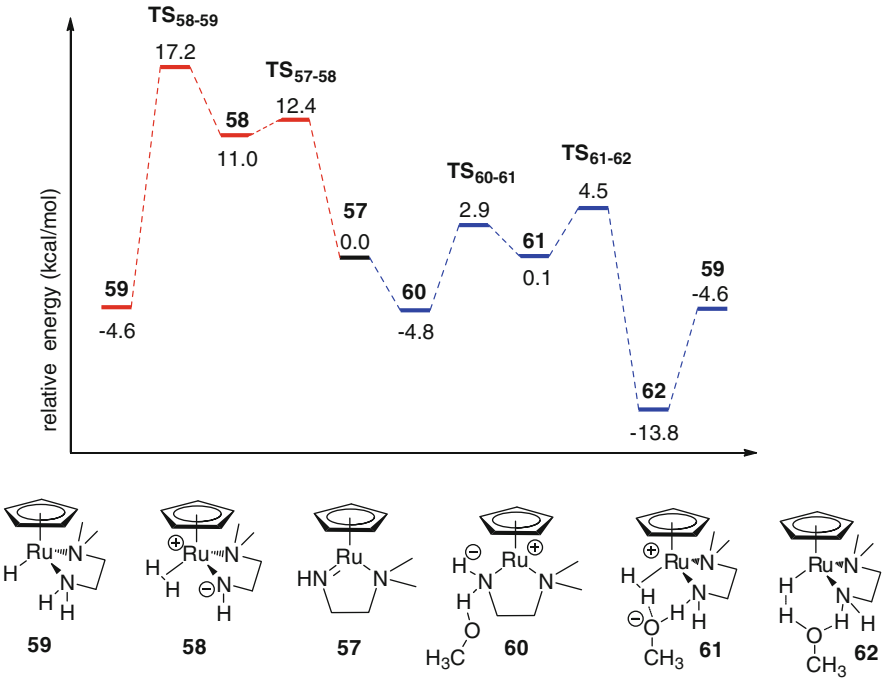

Fig. 16 PES for assisted (*blue*) and nonassisted (*red*) hydrogen splitting

$[RuH_2(PH_3)_4]$ and the α,β-unsaturated aldehyde cinnamaldehyde. The solvent effect was considered using both implicit and explicit models employing the CPCM/UAKS and a cluster of water molecules up to three units, respectively. Two different pathways were considered: (a) dissociation of a phosphine ligand from $[RuH_2(PH_3)_4]$ (**49**) followed by the coordination of the carbonyl, and (b) an associative mechanism where the active catalyst is a *cis*-$[RuH_2(PH_3)_4]$ complex. For both cases, several alternative pathways have been investigated. The authors proposed that the catalytic cycle based on hypothesis "a" is dominant (Scheme 18) based on the PES reported in Fig. 17. In this proposed mechanism, the active catalyst is the *cis*-$[RuH_2(PH_3)_3]$, and the reaction proceeds via an oxygen-bound rather than a carbon-bound intermediate. The catalyst transfers a hydride to the carbonyl and the substrate is protonated by water.

Delbecq and Joubert [121, 122] investigated the selectivity of α,β-unsaturated aldehyde hydrogenation via a water-assisted mechanism. They demonstrated, employing an Eyring kinetic model [123], that even if the C=C coordination is 12 kcal/mol [121] more favorable than the carbonyl coordination to the α,β-unsaturated aldehyde [122], the kinetics of the reaction result in a high selectivity for the C=O reduction. Kovacs and coworkers [124] investigated the mechanism and selectivity for the reduction of an α,β-unsaturated aldehyde in acidic solution catalyzed by $[(RuCl_2(m\text{tppms})_2)_2]$. In accordance with previous findings, their calculations

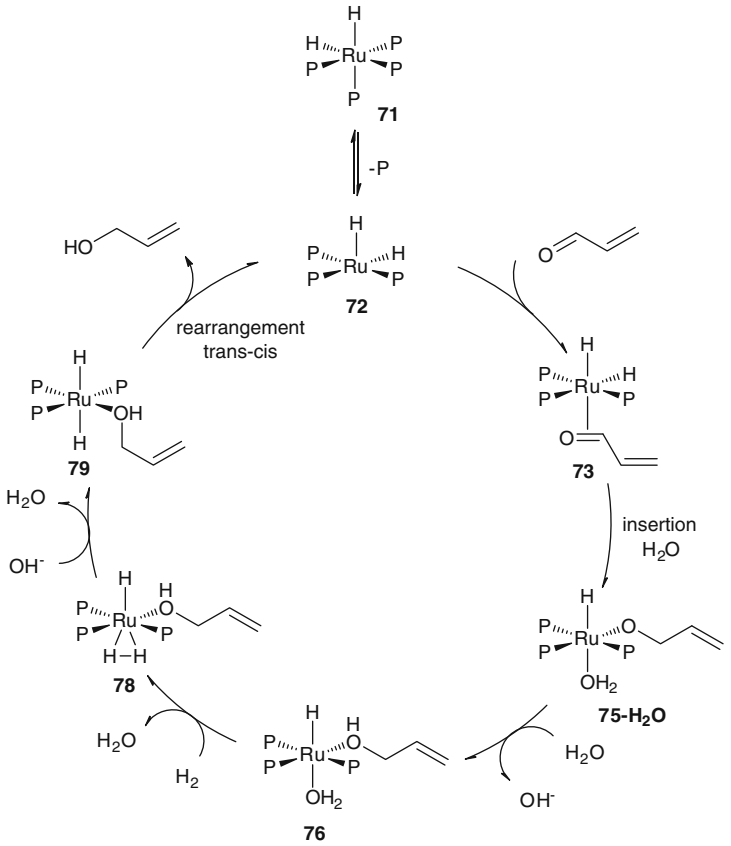

Scheme 18 $[RuH_2(PH_3)_4]$-catalyzed hydrogenation of an α,β-unsaturated aldehyde

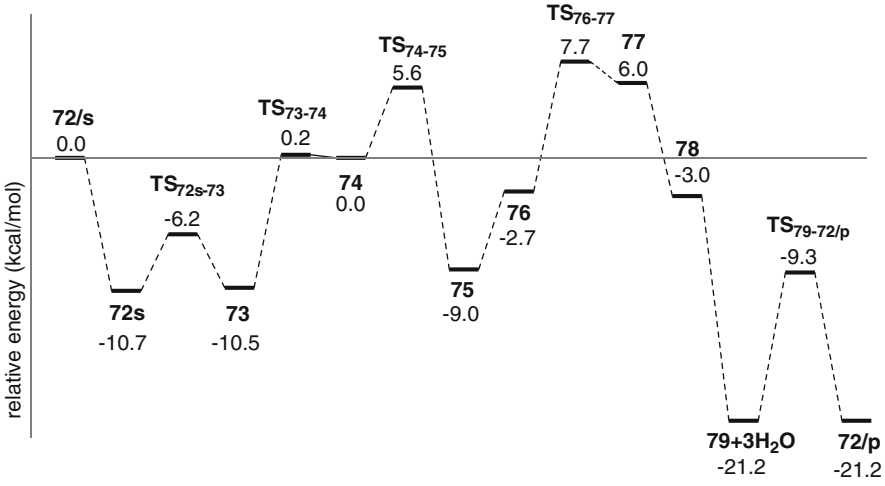

Fig. 17 PES for $[RuH_2(PH_3)_4]$-catalyzed hydrogenation of an α,β-unsaturated aldehyde

recognize the role of water molecules, which are actively involved in the mechanism by facilitating the hydrogen transfer. The authors also comment on the water's ability to saturate vacant coordination sites on the metal. Moreover, they were able to characterize both of the TSs involved in the hydrogen transfer to the C=C (5.3 kcal/mol) and the C=O (17.3 kcal/mol), confirming the experimentally high selectivity for the olefin over the carbonyl in acidic solution.

Lledos and coworkers [125] investigated several hypotheses of ISM and OSM for the hydrogenation reaction of formaldehyde catalyzed by the Shvo catalyst using a simplified model [126, 127]. They selected the two most likely hypotheses and conducted full DFT studies using the real Shvo catalyst, which confirmed the evidence obtained using the model catalyst. In all of their calculations, the solvent effect has been taken into account by means of a CPCM implicit model. The two stepwise reactions for the ISM and OSM are reported in Scheme 19.

The lowest energy pathway for the ISM studied is an associative reaction where no CO–Ru bond is broken and the Cp ring slips from η^5- to η^2-coordination in order to allow a direct covalent interaction between the formaldehyde's carbonyl group and the Ru. The reaction in THF is calculated to be exothermic by 4.5 kcal/mol, and the rate-determining step is the hydride transfer, requiring an activation energy of more than 30 kcal/mol. In the OSM, however, the substrate never interacts via a direct bond with the ruthenium (Fig. 18), and the formaldehyde approach is facilitated by the hydroxy-Cp ring. The reaction is 3.7 kcal/mol exothermic and the energy barrier for the only TS involved is lower than 8 kcal/mol. Several other computational and experimental investigations support the same conclusion with similar results [82, 120].

The role of the solvent in the active species responsible for hydrogen transfer has also been studied with a DFT-based molecular dynamics technique [128]. Handgraaf and coworkers investigated the dynamics of methanol oxidation

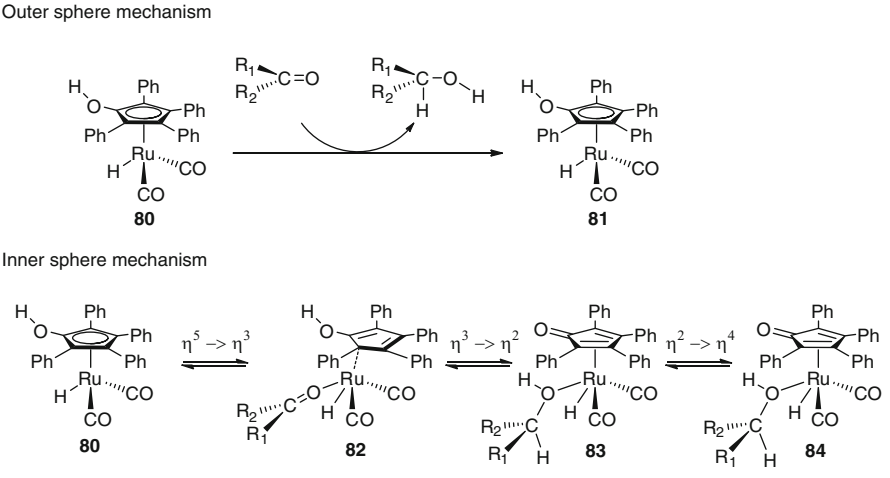

Scheme 19 Mechanisms for hydrogenation by the Shvo catalyst

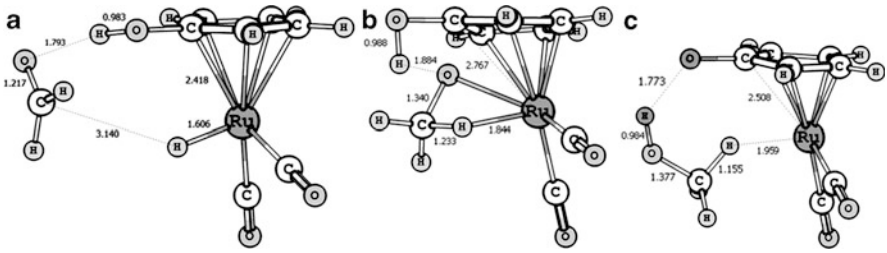

Fig. 18 Structures involved in the inner-sphere hydrogenation by the Shvo catalyst: (**a**) formaldehyde approach to the RuCp complex, (**b**) TS for the hydrogen transfer to the carbonyl, (**c**) alcohol interaction with the unsaturated Ru complex

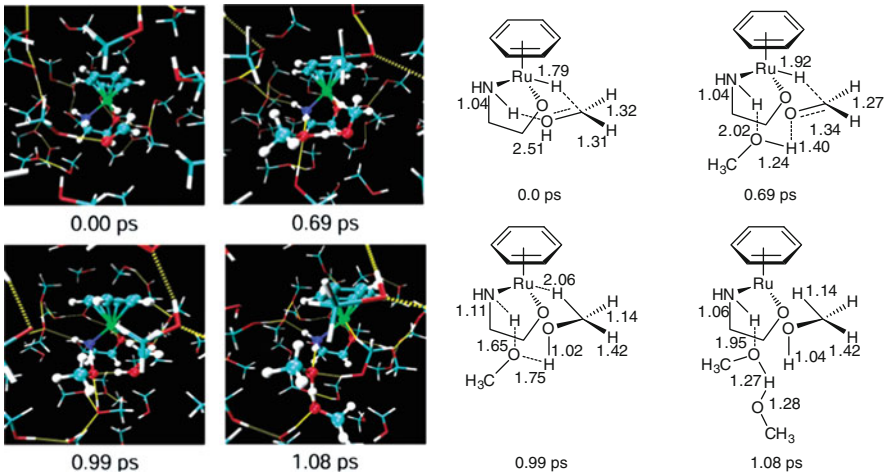

Fig. 19 Snapshots from CPMD simulation of hydrogenation

catalyzed by a Ru(benzene)ethyl-amino alcohol catalyst employing Car-Parrinello molecular dynamics (CPMD) simulations. Due to the high rate of conversion from methanol to formaldehyde, it was not possible to describe the stepwise trajectory with ab initio molecular dynamics. For this reason, the results presented are based on constrained trajectory dynamics following the asymmetric Ru–H–C bond breaking/forming. In the same context, the auxiliary protonation/deprotonation of formaldehyde/methanol has been investigated. Based on their results shown in Fig. 19, the hydride moves from the Ru to the formaldehyde carbon in the first 0.5 ps, leading to a methoxide intermediate characterized by a long H–C bond (1.2–1.4 Å) pointing toward the Ru. The simulation also highlights that the substrate oxygen is stabilized by a solvent molecule interacting via a hydrogen bond. Indeed, this hydrogen bond is involved in a bridge between the ligand nitrogen and the coordinated solvent molecule. After 0.69 ps, the C–H bond decreases to 1.1 Å. The figure depicts this proton transfer from the first solvent molecule, but then a second solvent molecule protonates the first solvent molecule. At 1.7 ps, a hydrogen

bond network forms in order to stabilize the latest hydrogen transfer. This simulation shows that the substrate appears to be converted to methoxide for a short, but finite time and that the ligand may not necessarily serve a bifunctional purpose as suggested for the first time by Noyori et al.

Recently, Pelagatti and coworkers [108] investigated an amine–phosphine-based ruthenium catalyst employed in the reductive hydrogenation of acetophenone. This *p*-cymene catalyst functionalized with an auxiliary diphenylphosphanylaniline ligand demonstrated good catalytic properties under mild conditions [108]. The authors performed a combined ESI-MS and DFT study of the mechanism. When the bidentate ligand is bis-coordinated to the metal, the complex is positively charged and strongly stabilized by polar solvents. This may cause a deviation in the traditional OSM. Experimental observations confirm the bifunctional mechanism associated with the hydrogen transfer from this catalyst. The authors tried to cast further light on the mechanism behind the formation of the active hydride catalyst, which is fundamental for an OSM. In their DFT investigation, they highlight the essential role of the solvent, demonstrating that the implicit PCM model employed is a good approximation for describing the reaction intermediates. Three alternative pathways have been considered: (a) base-catalyzed elimination in conjunction with deprotonation of the amine and hydride complex formation through an OSM (Scheme 20a), (b) nucleophilic substitution of a chlorine ion with *i*-propoxide (Scheme 20b), and (c) base-catalyzed deprotonation of the amine, and nucleophilic substitution as described in "b" (Scheme 20c).

The authors concluded that for pathways shown in Scheme 20a, b, the two TSs that limit the formation of the hydride species **67** are of an OSM and ISM type, respectively. In pathway (a), a $16e^-$ unsaturated complex (**86**) is formed after base-catalyzed elimination and reacts through an OSM TS, leading to the concerted proton and hydride transfer from isopropanol to the catalyst. This step requires an activation energy of 15.3 kcal/mol and is almost thermodynamically neutral. In pathway (b), a four-center ISM-type $\mathbf{TS_{88–89}}$ is responsible for the formation of the active hydride catalyst **89** and has an activation energy of 16.9 kcal/mol, but in this case the reaction is strongly exothermic by 15 kcal/mol. With regard to the third pathway, initial deprotonation of the amine takes place without previous loss of the chlorine, which makes the Ru more electron rich and causes the arene to slip to lower hapticity, making this alternative less favorable than the previous two hypotheses. Based on these results, the authors concluded that the combined experimental and computational investigations suggest a competitive mechanism for the active catalyst formation and confirmed an OSM for the reductive hydrogenation of the substrate considered.

3.3 Stereoselectivity

Ruthenium-catalyzed hydrogenation reactions have also been extensively studied in terms of kinetics and stereoselectivity [72, 99–101, 103, 105, 106, 109, 129].

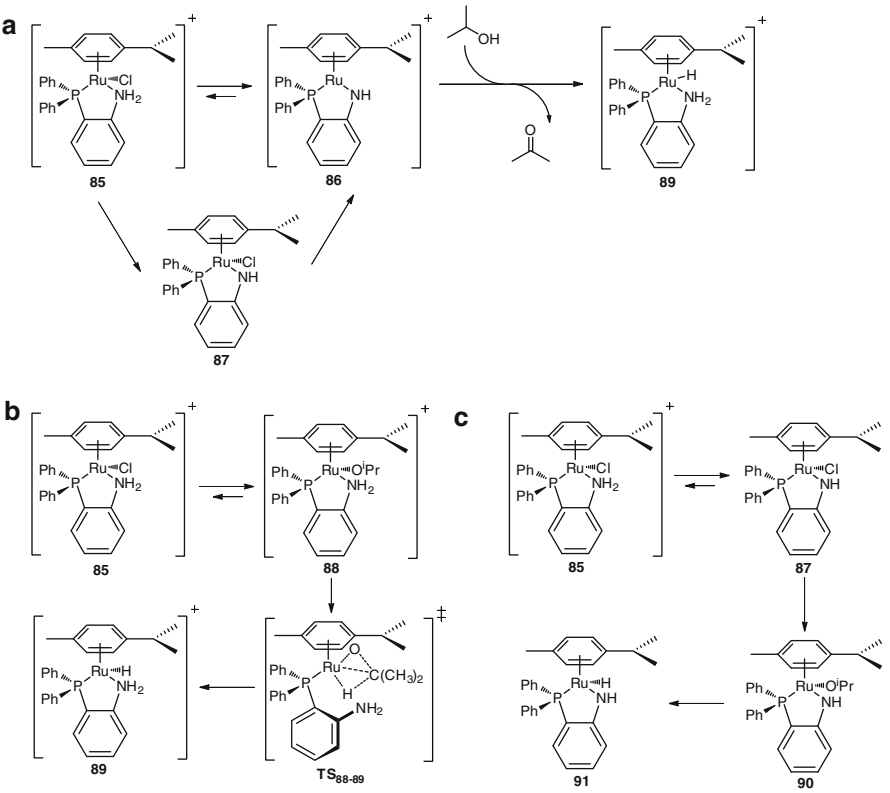

Scheme 20 Mechanistic pathways for Ru-catalyzed hydrogenation of acetophenone

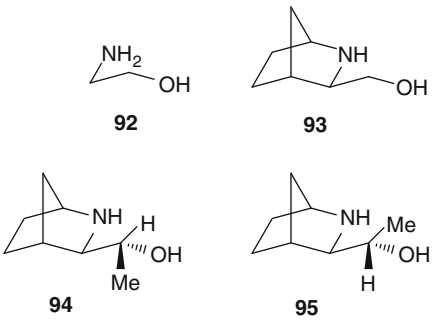

Fig. 20 Amino alcohol ligands studied by Alonso and coworkers

Alonso and coworkers [99] investigated a series of Ru-based catalysts introducing systematic variations in the ligand and arene moieties both experimentally and theoretically. Four different amino alcohols were considered in combination with benzene, DMB, hexamethylbenzene (HMB), and *p*-cymene (Fig. 20).

The authors reported that employing DMB instead of benzene increases the activation energy, effectively lowering the rate of the reaction. This is in agreement

with the experimental finding that a substitution of benzene with HMB decreases the rate by three times. However, this is not applicable to other cases like *p*-cymene, where the rate is almost the same as that for the unsubstituted arene. There are two stable conformations with either the carbonyl carbon pointing toward the hydride (α) or pointing away (β). In the case of the hydride complexes, it has been reported that the (α) conformation is the most stable due to a better binding interaction with the metal. Substitution on the carbonyl carbon effects which conformation is favored. The energy gap between the two conformers is very sensitive to the substitution on the carbonyl carbon and ranges from 1.7 to 7.5 kcal/mol. Increasing steric interactions between carbonyl substituents and the ligands are the main source of destabilization. A major contribution arises from either alkyl hydride or alkyl arene repulsion. When the authors considered a similar correlation in the OSM TS, it was not possible to establish a straightforward dependence. In addition to steric interactions, the H–Ru–N–H dihedral angle shows a linear correlation with the destabilization and a strong preference for a planar configuration.

In 1999, when Alonso et al. published their results, the theory and computational tools were not accurate enough to predict the enantiomeric excess based on DFT calculations. Their approximate results using gas-phase calculations did not take into account the origin of the well-known enantioselectivity associated with such catalysts. A polarizable continuum approach such as PCM was accurate enough to predict high stereoselectivity if the chirality was fixed on the metal. Similar investigations were conducted by Yamakawa and coworkers [100] on the ligand backbone conformations. As the hydride, chloride, and alkoxide complexes are chiral, an *R* or *S* absolute configuration of the metal is possible. Therefore and because of the two δ–λ possible orientations of the ligand backbone, it is possible to distinguish four diastereomeric configurations. All calculations reported by the authors demonstrated that the axial N–H is preferably *syn* with respect to the Ru–H, Ru–Cl, or Ru–OR bond, inducing stabilization of the δ configuration. This is also applicable to the pericyclic transition states involved in the hydride transfer, and the authors conclude that the diastereoselectivity is controlled by the equatorial instead of the axial N–H. They also pointed out that the electronic structure plays a fundamental role in stereoselection and that the suitable combination of chiral and arene ligands on the Ru can be used to increase selectivity in the asymmetric reaction. The enantioselectivity induced by the chiral catalysts employed in this reaction is determined by the chiral center on the auxiliary ligand and by its substituents. Figure 21 shows the two representative and most stable diastereomeric TSs for the reduction of prochiral ArCOR (Ar = aryl, R = alkyl) by the Ru(II)(arene)($NH_2CH(R')CH(R')YH$ catalyst (Y = NTs, $R' = C_6H_5$). The *1S*, *2S* configuration of the chiral ligand determines the δ configuration due to the steric hindrance of R′, which prefers the equatorial position. The configuration on the Ru stereocenter is set as absolute *R*. The two diastereomeric TSs originate from the pro-*R* and pro-*S* approach to the substrate, and the main forces that influence the differences in energy between the two are the steric interactions which influence the ligand backbone configuration and the specific CH-π electronic interaction between the aromatic ligand substituent and the arene. This kind of stereoinduction

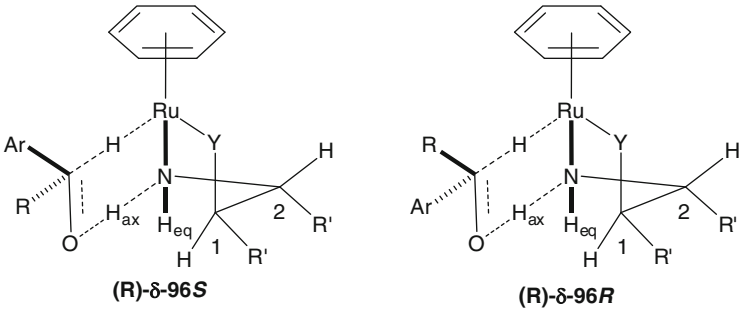

Fig. 21 Diastereomeric transition states **96**

due to ligand backbone conformation has also been reported by other investigators [101, 103]. Another important result rising from the computational study is related to the chemoselective reduction of the carbonyl. Indeed, comparison of this reductive reaction with the equivalent methylene imine and ethylene hydrogenation shows a significant energy gap between the TSs for these different substrates. It has been calculated that for carbonyl substrates, the average energy required is between 16 and 22 kcal/mol, substantially lower with respect to the average 27 kcal/mol for the other two substrates. The key factors associated with such selectivity are the double bond polarization, which is stabilized in the TS, and the entropic effect, which is unfavorable for ethylene-like substrates.

Petra and coworkers [101] performed combined experimental and computational studies for a series of catalysts summarized in Table 1. From this study, they determined the individual and cooperative effects arising from substitution patterns on the ligands.

The product configuration is mainly determined by the substitution in position 1 of the amino alcohol ligand, giving up to 0.8 kcal/mol difference (extrapolated from experimental e.e.) between the two diastereomeric TSs. The chirality of this position strongly influences the enantioselectivity of the hydrogenation. Moreover, such effects seem to originate from electronic factors because there were no differences reported with respect to the bulkiness of the substituents at this position. The relative energy difference between the two diastereomeric transition structures can be increased by up to 0.5 kcal/mol by varying the R^2 group. Finally, a substantial induction of enantioselectivity derives from the substituents on the arene ligand, showing that employing *p*-cymene instead of benzene increases the energy difference between the two diastereomeric transition states by 0.9 kcal/mol. In conclusion, the authors not only show the specific role of each key position but also highlight that an overall steric environment around the metal center is responsible for the chiral induction. In their computational investigation of catalysts **97** and **98** (Table 1), the authors reported for each optimized structure two stable conformations of the amino alcohol ring. For example, in the case of catalyst **98**, the ligand can be coordinated in a δ or λ configuration, showing an equatorial or axial orientation of the methyl substituent, respectively. This conformational

Table 1 Amino alcohol catalysts **97–109**

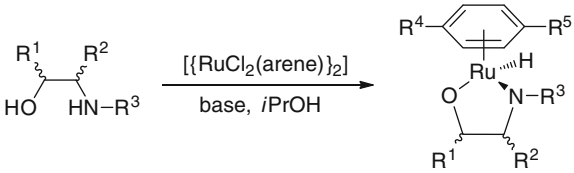

Catalyst	Amino alcohol configuration	R^1	R^2	R^3	R^4	R^5
97	2*S*	H	CH_3	H	H	H
98	1*S*	CH_3	H	H	H	H
99	2*S*	H	CH_3	H	CH_3	*i*Pr
100	1*S*	CH_3	H	H	CH_3	*i*Pr
101	2*R*	H	Ph	H	CH_3	*i*Pr
102	1*R*	*p*-OMe-Ph	H	H	CH_3	*i*Pr
103	1*R*	*p*-OMe-Ph	H	CH_3	CH_3	*i*Pr
104	1*R*	Ph	H	CH_3	CH_3	*i*Pr
105	1*R*	Ph	H	*i*Pr	CH_3	*i*Pr
106	1*R*, 2*S*	Ph	CH_3	H	CH_3	*i*Pr
107	1*R*, 2*S*	Ph	CH_3	CH_3	CH_3	*i*Pr
108	1*R*, 2*S*	Ph	CH_3	CH_2-Ph	CH_3	*i*Pr
109	1*R*, 2*S*	Ph	CH_3	CH_3	H	H
110	1*R*, 2*S*	Ph	CH_3	CH_2-Ph	H	H

flexibility, first reported by Corey and Bailar [130], around the fixed chirality on the metal center generates four diastereomeric configurations, which, according to their calculations, differ in energy by a very small amount. The authors associate this behavior to hydrogen bond stabilization between the hydride $H^{\delta-}$ and the acidic amine $H^{\delta+}$. Petra and coworkers associate small dihedral H–Ru–N–H angles with increased stabilization energy. In order to rationalize the enantioselectivity induced by catalysts **97** and **98**, the authors considered the reduction of acetophenone to 1-phenyl ethanol. For both catalysts, the *re* approach is not sterically hindered since the phenyl group points away from the ligand. On the contrary, the *si* approach does not seem to be isoenergetic since the phenyl group interacts with the methyl group in catalyst **98** than that in catalyst **97**. This finding is in agreement with experiments reported for the ligands shown in Table 1, where catalyst **98** has greater selectivity toward the *S* product. The complex induces greater enantioselectivity if the amine has a methyl or an iPr substituent, as can be seen by catalysts **102–103** (61–76%) and **104–109** (75–84%).

The optimized structures for the methylamine derivative (Fig. 22) show that the A configuration is less stable than the B configuration for two reasons: configuration A loses the stabilizing intramolecular H···H interaction since these two atoms are oriented in opposite directions, and the six-membered ring formed in the transition states is less planar. Configuration B does give a more rigid and bulkier complex in comparison to A and the unsubstituted amino alcohol. The authors

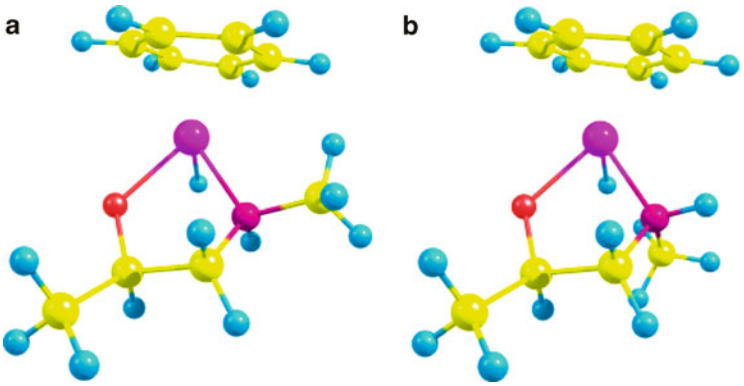

Fig. 22 Two possible isomers for (S_{Ru}-S_c)-*N*-Me-1-amino-2-propanol

speculated that the increased rigidity is due to an increase in energy between the δ and λ configurations, leading to higher enantioselectivity. However, such a conformation can be destabilized if the ligand has a bulky group in the 2-position interacting with the amino substituent. That is the case for (*1R*,*2S*)-2-amino-indanol or the *erythro* series of N-substituted (*1R*,*2S*)-2-amino-1,2-diphenylethanol. Noyori and coworkers also ascribed this selectivity to a combination of various steric and electronic effects which influence the kinetic asymmetric bias of the described octahedral Ru(II) complexes: the major role of the two substituents on the chiral amino alcohol auxiliary ligand is to set the δ (or λ) configuration of the chiral Ru complex, whereas the arene ligand plays an important role for the stereochemical outcome because of its influence on the CH/π interaction with the keto-aryl group. This last factor seems to have a major influence on the stereochemical outcome: the pre-formed Ru hydride employs a chiral amino alcohol or amino-NTos ligand, which reacts with the carbonyl substrate attaching preferentially to the *re*-face and leading to the most hindered transition state. This evidence supports the argument of a major contribution arising from a specific electronic interaction, which is stronger than the repulsive steric effects. The authors selected the reaction of $RuH(OCH_2CH_2NH_2)(\eta^6$-benzene) [103] and benzaldehyde in order to investigate the stereoselective $TS^{\ddagger}$s involved in this process at the MP2/B3LYP level of theory. The energy profile following the reaction coordinate is depicted in Fig. 23.

The chelate formed by the N,O ligand is predicted to be in a δ conformation, which fixes the absolute *R* stereochemistry on the metal. The reaction is essentially thermoneutral, with the final products being only 0.6 kcal/mol higher in energy than the starting materials. The omission of the two aminoethanol substitutents is justified because they do not influence the stereochemical outcome once the absolute configuration on the metal is determined. The stereoselectivity-determining step is associated with $\mathbf{TS_{112–113}}$, whereby *Re* $\mathbf{TS_{112–113a}}$ is 3.9 kcal/mol lower in energy than *Si* $\mathbf{TS_{112–113b}}$. Such a large energy gap is responsible for the high enantio-induction obtained within the real system. The analysis of the origin of the stereoselectivity highlights a specific CH/π interaction between the η^6-benzene and

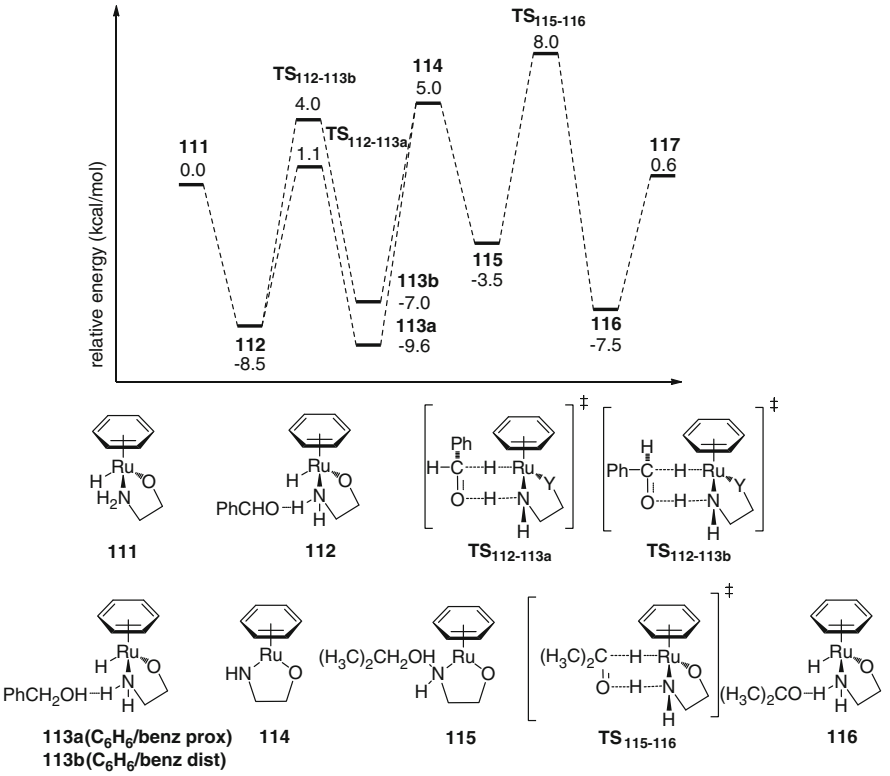

Fig. 23 PES for the reaction of $RuH(OCH_2CH_2NH_2)(\eta^6\text{-benzene})$ and benzaldehyde

the aldehyde phenyl substituent. Two pieces of evidence support this hypothesis: the distance of C(6)–H···C(15) (Fig. 24) is 2.86 Å, which is within the 2.9-Å sum of the van der Waals radii, and electrostatic and charge transfer interactions as evident by the Mulliken and NPA charge distribution; in fact in the *Re* $\mathbf{TS_{118}}$, the C(6)-H shows a significant positive charge localization, and C(15) and C(16) show significant positive charge localizations.

The origin of the charge separation is the enhanced acidity of C–H benzene hydrogens caused by metal complexation, which has also been reported for ground-state complexes. Following the reaction coordinate, the aldehyde increases in alkoxide character and, consequently, reverses the charge distribution at the *ortho*, *para*, and *meta* positions. The rate and stereoselectivity are also affected by alkylation of the η^6-arene group. Such charge reorganization has been characterized in both the $18e^-$ and $16e^-$ intermediates with consistent results. The hexamethylbenzene analog catalyzes the acetophenone reduction with a lower energy barrier than the η^6-benzene parent. Similarly, the alcohol dehydrogenation is also feasible (6.8 vs. 8.0 kcal/mol) and can be explained by the relatively high Ru–N polarization. Finally, the $C(sp^3)H/\pi$ interaction stabilizes the more congested *Re* configuration instead of the uncrowded *Si* by 1.7 kcal/mol.

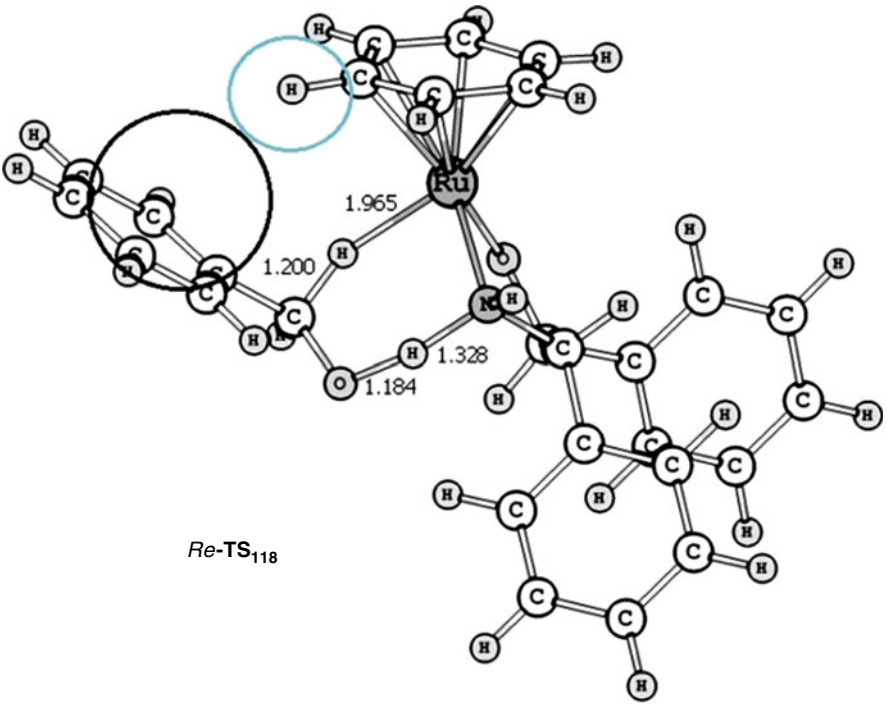

Fig. 24 Structure of *Re*-$\mathbf{TS_{118}}$

Fig. 25 Azanorbornyl ligands **119** and **120**

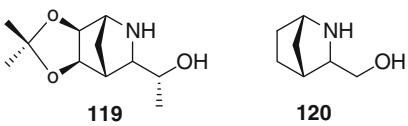

119 **120**

Andersson and coworkers [105] investigated the origin of the enantioselectivity achieved in the reduction of aromatic ketones catalyzed by ruthenium-based complexes of azanorbornyl ligands (Fig. 25). The authors experimentally analyzed the effect of aromatic ring substituents on the substrate, the effects of arene modification on the catalyst, and how the alkyl part of the substrate can influence the enantioselectivity. They further performed B3LYP calculations in parallel with their experimental investigations and correlated the enantiomeric excess with respect to the CHelpG [131]-fitted electrostatic potential charges. The first catalyst considered was a Ru(*p*-cymene) (**119**) for hydrogenation of a large series of acetophenone derivatives. The plot of the observed $\Delta\Delta G_{Exp}^{\ddagger}(R–S)$ in kcal/mol versus the sum of charges on the substrate's aromatic ring (Σq) is shown in Fig. 26.

Except for the *m*-MeO and *m*-NH_2 outliers, the correlation is linear and supports the fundamental role of the electrostatic contribution to the enantioselective outcome already proposed by Noyori and coworkers. In order to determine whether or

entry	Ar	time (min)	conv (%)	ee (%)(config)	Σ(*q*)
1	3-NH_2-C_6H_4	4	98	99 (S)	-0.26
2	3-MeO-C_6H_4	4	100	98 (S)	-0.29
3	C_6H_5	6	96	96 (S)	-0.44
4	3-Me-C_6H_4	4	99	96 (S)	-0.39
5	4-Me-C_6H_4	6	92	93 (S)	-0.38
6	4-Cl-C_6H_4	3	92	93 (S)	-0.29
7	4-Br-C_6H_4	3	98	91 (S)	-0.28
8	4-pyridyl	3	97	91 (S)	-0.26
9	3-NO_2-C_6H_4	4	99	91 (S)	-0.29
10	4-CF_3-C_6H_4	3	97	89 (S)	-0.35
11	3-pyridyl	4	98	89 (S)	-0.27
12	4-NO_2-C_6H_4	3	95	88 (S)	-0.31
13	2,6-F_2-C_6H_3	3	97	88 (S)	-0.10
14	3,4,5-F_3-C_6H_2	3	98	82 (S)	0.15
15	2,3,4,5,6-F_5-C_6	3	98	32 (S)	0.56

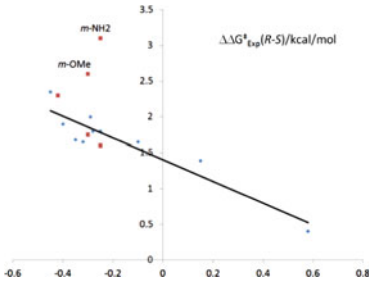

Fig. 26 Experimentally determined e.e. for transfer hydrogenation using Ru(*p*-cymene) catalyst **119** and plot of the TS energy difference with respect to CHelpG-fitted electrostatic potential charges

not the Coulomb attraction is dominant in the enantioselective outcome, the authors investigated the effect of reversing the charge distribution of the aryl group of the substrate. An effective way to accomplish this change is to replace the aromatic hydrogens with fluorine as in 2,3,4,5,6-pentafluoroacetophenone, which should lead to the opposite enantiomer of the product. This substrate is reduced with 32% e.e. while retaining the same sense of absolute asymmetric induction as for the other acetophenone derivatives. This result suggests that the enantiofacial discrimination is not simply determined by charge distribution in the aromatic ring. The *y*-intercept shown in Fig. 26 represents the energetic contribution of the non-electrostatic terms, which for this catalyst can be estimated to be ca. 1.4 kcal/mol, higher than the estimated 1.0 kcal/mol electrostatic contribution of the arene–phenyl interaction. The authors also considered a less polar arene ligand, HMB, and plotted a similar correlation in order to address the major electrostatic source. The results obtained highlight that the relative contribution from electrostatics is reduced in this case and that the intrinsic selectivity is increased. This evidence is in support of the major electrostatic contribution being the interaction between the substrate aryl ring and the ligand arene. Further modeling of the arene ligand yielded different results: with the introduction of benzene or ethylbenzoate as an arene ligand, the enantioselectivity decreases to 81% and 88%, respectively. This unexpected result can be explained by means of a decreased dispersion/solvophobic

effect rather than less positively charged aromatic hydrogens. Based on these results, any rationalization based on steric contributions is expected to be poor and gives opposite results to those found experimentally. As already mentioned earlier, some authors highlighted the role of solvent modeling in order to describe the most reasonable mechanism for ruthenium-catalyzed hydrogenation of ketones.

Andersson and coworkers investigated the role of solvation, dispersion, and steric effects on the enantioselectivity. The authors' results agree with the fact that gas-phase B3LYP calculations describe the drop in enantioselectivity of 2,3,4,5,6-pentafluoroacetophenone compared to acetophenone where steric and electrostatic effects are the only major effects, but the approximation is too crude to reproduce quantitatively the extent of enantioselection observed experimentally. In order to extract the isolated contributions of steric effects, the authors correlated the same energetic parameter with respect to an empirical steric parameter called STERIMOL B1 [132]. Their results showed that bulkier alkyl groups tend to decrease the enantioselectivity, which correlates well with the B1 parameter. Based on this observation, it seems that an intrinsic steric factor enhances or depresses the enantioselectivity in the reduction of acetophenone and other *n*-alkyl aryl ketones. However, a generalized rationalization of this effect is not trivial, and investigation of similar catalysts reveals only a small role for steric effects [105, 109].

Preliminary computational efforts to rationalize enantioselectivity and to predict e.e. were performed for the stereoselective reduction of acetophenone and 2′,2′-dimethylpropiophenone using Quincoridine (QCD)-amine ruthenium(Cp*) model catalysts **65**, **66**, and **69** (Fig. 15). For the acetophenone reduction, the experimentally extrapolated energy gap between the two diastereomeric TSs for **65**, **66**, and **69** are −0.52 (*R*, 41%), 1.15 (*S*, 75%), and −1.07 (*R*, 72%) kcal/mol, respectively. For 2′,2′-dimethylpropiophenone using catalyst **69**, the major product has an *S* configuration (90%), and the energy difference between the two transition states is 1.74 kcal/mol. The predicted energy difference for catalyst **69** is 1.9 kcal/mol, showing that the model can be used to provide quantitative and qualitative information concerning the stereoselective outcome of this reaction. The nature of the selectivity is attributed in this case to a repulsive interaction between the substrate phenyl ring and the Cp* ligand. The behavior of catalyst **69** is also predicted qualitatively correctly for the favored observed addition to the *re*-face. In regard to the catalyst **65**, the lower selectivities arise from steric interaction between the amino ligand and the phenyl group of the substrate. The increased enantioselectivity observed for the bulky substrate 2′,2′-dimethylpropiophenone was rationalized as a result of a good fit of the *t*-Bu group into the pocket formed by the H–Ru–N–H moiety and the Cp* ring, and the clash between *t*-Bu and the quinuclidine in the TS for *si*-face addition.

4 Iridium-Catalyzed Reactions

4.1 Hydrogenation of Olefins

One of the most efficient catalytic systems for reduction for unactivated olefins [133] is the phosphine oxazoline iridium complexes (**122**), which were developed by Pfaltz and coworkers (Fig. 27) [134–141] and which were followed up by other groups [142–145]. These Ir catalysts are based on the original N,P-coordinated catalysts (**121**) developed by Crabtree and coworkers [146]. The [Ir(cod) PCy_3(pyridine)][PF_6] (cod = cyclooctadiene) complex is an efficient catalyst for the hydrogenation of unfunctionalized tri- or tetrasubstituted olefins, and the irreversibility of the reaction is guaranteed by the presence of COD which undergoes reduction, releasing cyclooctane. These catalysts are complementary to the Ru- and Rh-based catalysts because they are able to mediate hydrogenation of hindered, unfunctionalized alkenes that do not possess a chelating group.

Burgess and coworkers [147, 148] demonstrated that good conversion and enantioselectivity can be reached using N-heterocyclic carbene-oxazoline (**123**) for reduction of tri- and disubstituted arylalkenes. There have been a number of investigations in the past decade aimed at addressing the mechanistic details, including the stereoselectivity-/rate-determining step of these hydrogenation reactions. Andersson and coworkers [149] performed a combined computational and experimental investigation of the iridium–phosphanooxazoline-catalyzed hydrogenation of unfunctionalized olefins. The authors first investigated the PES of this reaction catalyzed by a simplified model catalyst as reported in Fig. 28

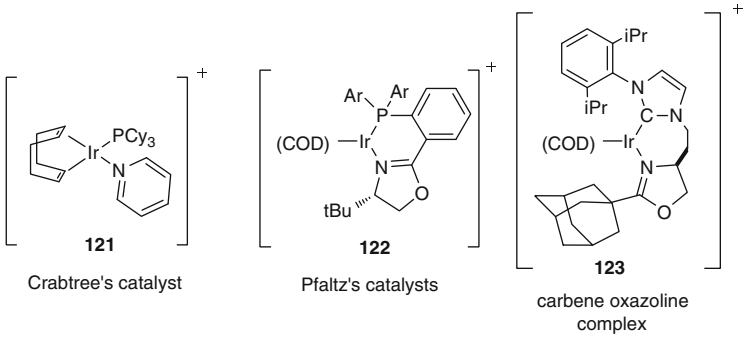

Fig. 27 Catalysts **121–123**

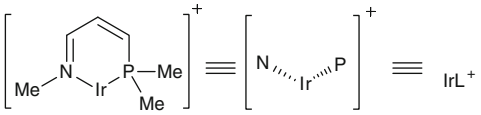

Fig. 28 General structure for P–N iridium complexes

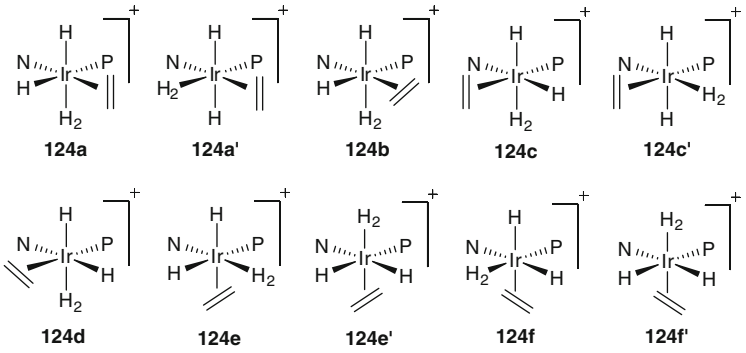

Fig. 29 Complexes for pathways **a–f**

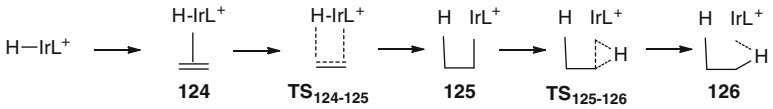

Scheme 21 Mechanism of iridium-catalyzed hydrogenation

following 10 alternative pathways (each generated from the starting configurations shown in Fig. 29).

The most important intermediates and TSs are shown in Scheme 21. B3LYP calculations confirmed the irreversible reduction of COD leading to an unsaturated Ir configuration that easily undergoes an exothermic coordination to any of the reactants. As the most abundant species present are molecular hydrogen and the solvent, the authors investigated their roles in the mechanism. As expected, the coordination of the first dichloromethane molecule releases 24 kcal/mol, followed by a less exothermic second coordination (−7 kcal/mol). The coordination of molecular hydrogen is also highly exothermic (22–34 kcal/mol) and generates a *cis*-dihydride species characterized by one axial hydride. Further coordination of a neutral solvent or molecular hydrogen leads to increased stabilization. Coordination of the substrate to the catalyst is always significantly exothermic, releasing between 5 and 10 kcal/mol depending on the axial or equatorial orientation. This step is important for understanding stereoselectivity because such strong stabilization could make it irreversible, and consequently, the olefin coordination becomes the enantioselectivity-determining step. These computational results are in agreement with several empirical observations [136, 138, 150]. The analysis of all ten dihydride pathways (Fig. 29) showed that the migratory insertion is favored if it takes place in the coordination plane and less favored when inserting into an axial Ir–H bond.

The reductive elimination step is rate determining for all ten pathways shown in Fig. 30 except for path **c**. The most feasible pathway for this model is **b**, which has a fast migratory insertion (5.6 kcal/mol) and a slower reductive elimination

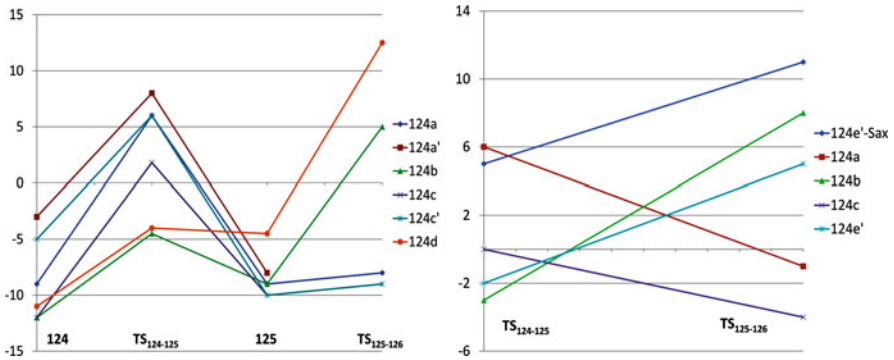

Fig. 30 PES for pathways a–d of tetrahydride mechanism for Ir-catalyzed hydrogenation of olefins

(12.9 kcal/mol). However, the overall reaction is not sufficiently exothermic to be irreversible, and for this reason, the authors investigated the effects of solvent coordination. The authors concluded that the solvent coordination to iridium is strong in some complexes, but it does not significantly affect the relative rates for different reaction pathways. Motivated by these conclusions, Andersson and coworkers suggested a tetrahydride saturation of iridium catalysts in order to fill up the sixth coordination site in the octahedral Ir(III). B3LYP calculations suggest that the coordination of an extra H_2 molecule stabilizes the complex by 10 kcal/mol with insignificant further stabilization due to solvent coordination.

Figure 30 shows the PESs for pathways **a–d** calculated assuming a tetrahydride active complex. The **b** and **d** pathways show a facile migratory insertion, but interestingly, the **c** pathway involves a concerted oxidative addition of molecular hydrogen forming an $[Ir^{V}(H_3)(ethyl)]$ complex. The reductive elimination following both the **b** and **d** pathways is inaccessible for the high activation energy, whereas the barrier is negligible for the **c** pathway. In contrast with the **c** pathway, the metal oxidation state for **a** and **d** remains Ir(III) throughout. The only potentially competitive route with the **c** pathway is the **e′** pathway, which is characterized by a reductive elimination which is only 2 kcal/mol higher in energy than the **c** migratory insertion. Using a relative rate analysis, the most relevant pathways were studied in more detailed calculations with an extended basis set.

In comparison with the small basis set discussed previously, use of the extended basis set had only a small effect on the relative energies, but did have a significant effect on the prediction of relative rates, which corroborates a preference for the **c** pathway. Based on these results, the authors proposed the mechanism depicted in Scheme 22, along with calculated relative free energies.

The mechanism begins with the dihydride Ir(III) complex **127**, and in the first two steps, the olefin coordinates in the *trans* position with respect to the phosphorus and molecular hydrogen coordinates in the axial position. Simultaneously, the olefin next undergoes a migratory insertion into the axial Ir–H bond, and H_2 undergoes oxidative addition. The resulting species **130** is extremely labile with

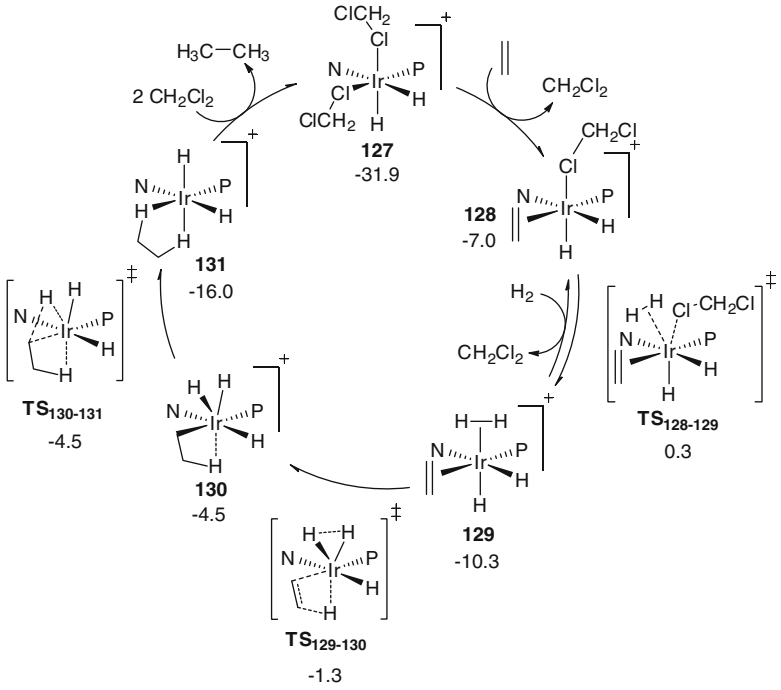

Scheme 22 Mechanism of iridium-catalyzed hydrogenation of olefins proposed by Andersson

Ir in oxidation state IV, and reductive elimination occurs with a negligible energy barrier. Based on these calculations, the Ir is never present in oxidation state I, but changes from III to V, which represents an important difference from the analogous Rh catalysts. The rate-determining step is likely either the H_2 coordination or the migratory insertion, suggesting zeroth-order kinetics with respect to the olefin, which is consistent with the extremely exothermic coordination to the metal.

Hall and coworkers [151] investigated in more detail the electronic effects on the mechanism of asymmetric hydrogenation of unfunctionalized aryl-substituted alkenes. The authors envisioned and confirmed in an initial and subsequent future papers [152] that the metal oxidation state varies between Ir(III)/Ir(V) in a cycle where a coordinated olefin reacts with a hydrogen ligand, leading to an alkyl complex characterized by a β-agostic interaction. A fast reductive elimination allows the alkane dissociation. The predicted overall energy barrier for the case of ligand **132b** is ~9–10 kcal/mol, and the reaction is exothermic (Fig. 31).

Similar calculations were performed employing catalyst **132a** (Fig. 31) on di- and trisubstituted aryl alkenes, as summarized along with predictions of the stereochemical outcome in Table 2.

From their results and structural analysis, the authors concluded that the alkyl group *cis* to the aromatic substituent encounters a steric interaction with the adamantyl group of the oxazoline ligand. This repulsive interaction decreases in the

Fig. 31 Ligand **132**

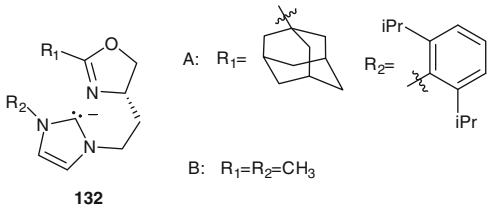

132

Table 2 Comparison of experimental and computational results for Ir-catalyzed olefin hydrogenation

Catalyst	Alkene	Calculated[a] $\Delta\Delta G^{\ddagger c}$	$\Delta\Delta G_{int}{}^{d}$	Config'n	Experimental[b] $\Delta\Delta G^{\ddagger}$	Config'n
1	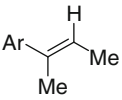	3.84	4.17	*S*	2.31	*S*
2	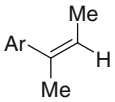	2.36	2.36	*R*	1.30	*R*
3	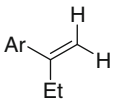	2.70	3.42	*R*	1.68	*R*

[a]Ar) Ph. [b]Ar) 4-MeOC6H4. [c]Free energy difference of the two highest-energy transition states for the same substrate's two enantiofaces. [d]Free energy difference between the intermediates labeled as **2**' in ref [151] for the same substrate's two enantiofacial sides

order of $R^1 > Ar > > R^3$, referring to the general alkene structure in Table 2. The authors were able to predict with good accuracy the stereoselective outcome as verified experimentally. Moreover, as the relative free energies of the intermediates are consistent with the respective transition states, the authors concluded that future studies on similar systems might be able to avoid the need for the location of stationary TS structures. A similar study on dienes was also conducted and gave consistent results [152].

4.2 Hydrogenation of Ketones

Several examples of chiral catalysts with Ir [92, 153–156] catalytic metal centers have been designed which give high yields and high stereoselectivities in carbonyl and imine reductions. There are three main mechanistic alternatives for the metal-catalyzed asymmetric hydrogenation transfer: the concerted hydrogen transfer to the substrate, the migratory insertion, and finally, the direct hydrogen transfer. One of the few mechanistic investigations concerning the role of Ir in stereoselective ketone hydrogenation is the study by Meijer and coworkers [102]. These authors considered two simplified models: an aminoethanol- and a 2-aminoethylmethyl-sulfide iridium catalyst, both stabilized by COD. Optimized structures for ground states and TSs were compared mainly with analogous Ru catalysts. The Ir catalysts show a reduced oxophilic character with a weaker Ir–O bond compared to a stronger intramolecular σ bond between oxygen and Ru. Another important structural difference is the O–C–C–N torsion angle of the ligand backbone, which is +53.7° and −58.1° in the Ru and Ir systems, respectively. The PESs calculated by the authors for the O- and S-chelated catalysts are shown in Fig. 32. The approach of the hydrogen donor (i.e., methanol) leads to the formation of a stable hydrogen bond with the nitrogen of the $16e^-$ catalyst and to the subsequent elongation of the Ir–O bond, which is less significant in the Ru complex. The hydrogen donor then replaces the ligand's alcohol oxygen, which dissociates without any significant energy barrier, confirming the hemilabile character of the ligand in the Ir complexes. As is the case for the Ru system, the metal–alkoxide complex represents an important structure in the ketone reduction with an extremely high energy stabilization, making this intermediate a reservoir or sink.

The data summarized in Fig. 32 show that for the amino alcohol Ir catalyst, the β-elimination and direct hydrogen transfer are competing mechanisms. For both mechanisms, the highest energy transition structures are 6 kcal/mol below that of the concerted hydrogen transfer. The direct hydrogen transfer is preferred for the elimination/migratory insertion by 4 kcal/mol. Similarly, the amino sulfide-coordinated Ir complex prefers direct transfer, revealing that the $18e^-$ complexes do not participate actively in the cycle. As the basis of such different behaviors between the Ir and Ru mechanisms, the authors address the role of the labile amino alcohol/amino sulfide ligand in Ir complexes and the arene ligand for Ru complexes. To prevent electronic oversaturation of the metal, one of the ligands needs to dissociate. For Ru, this need is achieved by partial arene decoordination, changing from the η^6 to the η^2 state, whereas for Ir, it is easily met by decoordination of a weak Ir–O bond. These two different situations are characterized by an overall energy difference of 20 kcal/mol, disfavoring decoordination of the aromatic system. An important result drawn from Meijer and coworkers' calculations is that the stereochemical outcome is determined by the choice of the hydrogen donor in the Ir-catalyzed reaction but not in the Ru-catalyzed reaction.

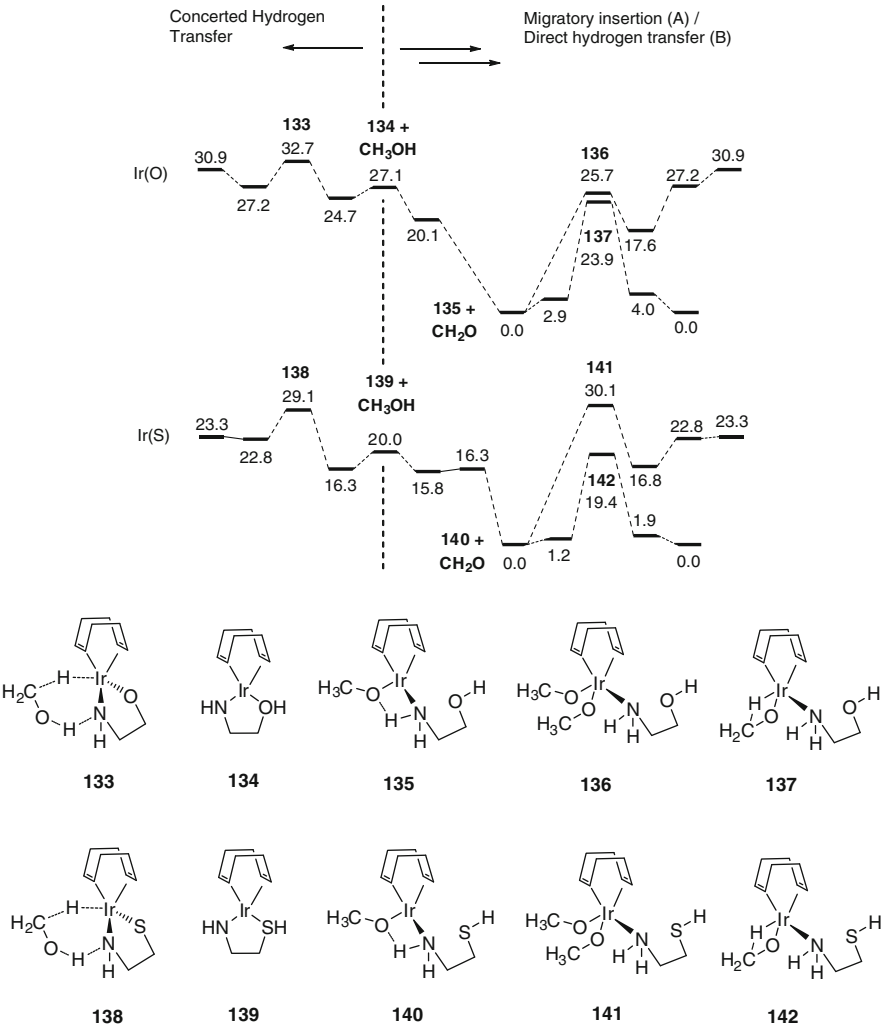

Fig. 32 Energy profiles for the concerted hydrogen transfer, migratory insertion, and direct hydrogen transfer for aminoethanol and aminosulfide iridium catalysts

5 Conclusions

In this review, the main contributions of computational chemistry to the understanding of the mechanisms of rhodium-, ruthenium-, and iridium-catalyzed hydrogenation reactions of alkenes, enamides, acrylamides, and ketones are summarized. These studies provided atomistic-level detail into the rate- and stereoselectivity-determining steps for a class of reactions that is widely used in organic synthesis at both the laboratory and the industrial scale.

Experimental and computational studies of the mechanism of the rhodium-catalyzed hydrogenation of enamide substrates by a number of different groups suggest that the irreversible migratory insertion is the enantioselecting step. An alternative proposal for the full catalytic cycle via a "dihydride" mechanism rather than the more widely accepted "unsaturated" mechanism has been studied much less and for different substrate–ligand combinations, making direct comparison impossible. It has been shown that a significant change in mechanism occurs upon substitution of an electron-withdrawing group in the α-position to a bulky alkyl group, suggesting that the mechanism is substrate and ligand dependent. Further work still needs to be done on the scope to which each of the two mechanisms is relevant for a given substrate–ligand combination. The reaction pathway for the related acrylamide substrates differs from the enamide substrates in that in addition to the pathways available to the enamides, mechanistic crossover between the pathways is possible and that the activation energies of all pathways in a simple model system are close in energy.

Three pathways for the ruthenium-catalyzed hydrogenations of ketones, aldehydes, and α,β-unsaturated aldehydes with several catalyst systems were studied: the direct insertion, the migratory insertion, and the concerted hydrogen transfer; highlighting the catalyst/substrate configurations that lead to stereoselective differentiation. The contribution of computational chemistry were essential to differentiate these mechanisms of ruthenium-catalyzed reactions and to rationalize the experimentally observed stereochemical outcome.

Iridium-catalyzed hydrogenations of olefins and ketones have also been reported. These reactions have not yet been studied computationally at the level of detail of the rhodium- and ruthenium-catalyzed reactions, and comparisons to experiments have been less clear. As a result, only a very general description of the mechanism and rationalization of the stereoselective outcome is available at this time. The results do, however, clearly demonstrates that amidst such mechanistic diversity of the iridium- and the ruthenium-catalyzed reactions, they prefer either the direct transfer after migratory insertion, or the concerted transfer.

This overview highlights the range of different models used to describe similar reactions and reinforces the importance of an accurate computational model. Indeed, comparing the general approach describing rhodium-, ruthenium-, and iridium-catalyzed reactions, it is clear how the modeling not only of the small model reaction, but also of substituent effects and the environment (i.e., gas phase or solution) significantly impacts the mechanism, re-emphasizing the need for the interplay of experimental and computational methods.

Acknowledgments We gratefully acknowledge financial support of our work by the American Chemical Society Petroleum Research Fund (Grant PRF#47810-AC1), the National Science Foundation (NSF CHE0833220 and NSF CHE 1058075), and the Notre Dame Zahm Travel fund. Generous allocations of computational resources by the TeraGrid (Grant TG-CHE090124) and the Center for Research Computing at the University of Notre Dame are also acknowledged.

References

1. Blaser HU, Schmidt E (2004) Asymmetric catalysis on industrial scale, 1st edn. Wiley-VCH, Weinheim
2. Blaser HU, Schmidt E (2010) Asymmetric catalysis on industrial scale, 2nd edn. Wiley-VCH, Weinheim
3. Dedieu A, Strich A (1979) Inorg Chem 18:2940
4. Dedieu A (1980) Inorg Chem 19:375
5. Dedieu A (1981) Inorg Chem 20:2803
6. Dedieu A, Hylakryspin I (1981) J Organomet Chem 220:115
7. Halpern J, Wong CS (1973) J Chem Soc Chem Commun 629
8. Wink DA, Ford PC (1987) J Am Chem Soc 109:436
9. Montelat S, Vanderen A, Osborn JA, Wilkinson G (1968) J Chem Soc Inorg Phys Theor 1054
10. Duckett SB, Newell CL, Eisenberg R (1994) J Am Chem Soc 116:10548
11. Koga N, Daniel C, Han J, Fu XY, Morokuma K (1987) J Am Chem Soc 109:3455
12. Daniel C, Koga N, Han J, Fu XY, Morokuma K (1988) J Am Chem Soc 110:3773
13. Musaev DG, Morokuma K (1995) J Organomet Chem 504:93
14. Brown JM, Chaloner PA (1978) J Chem Soc Chem Commun 321
15. Brown JM, Chaloner PA (1980) J Chem Soc Chem Commun 344
16. Brown JM, Chaloner PA (1980) J Am Chem Soc 102:3040
17. Brown JM, Chaloner PA, Morris GA (1983) J Chem Soc Chem Commun 664
18. Brown JM, Chaloner PA, Morris GA (1987) J Chem Soc Perkin Trans 2:1583
19. Koga NM, Morokuma K (1989) In: Salahub DRZ, MC (ed) The challenge of d and f electrons: theory and computation (ACS Symposium Series 394). American Chemical Society, Washington DC, p 77
20. Kless A, Borner A, Heller D, Selke R (1997) Organometallics 16:2096
21. Musaev DG, Morokuma K (1995) J Am Chem Soc 117:799
22. Brown JM, Evans PL (1988) Tetrahedron 44:4905
23. Bogdan PL, Irwin JJ, Bosnich B (1989) Organometallics 8:1450
24. Giovannetti JS, Kelly CM, Landis CR (1993) J Am Chem Soc 115:4040
25. Knowles WS, Vineyard BD, Sabacky MJ (1972) J Chem Soc Chem Commun 10
26. Kagan HB, Dang TP (1972) J Am Chem Soc 94:6429
27. Achiwa K (1976) J Am Chem Soc 98:8265
28. Fryzuk MD, Bosnich B (1977) J Am Chem Soc 99:6262
29. Knowles WS (2002) Angew Chem Int Ed 41:1999
30. Knowles WS (2003) Adv Synth Catal 345:3
31. Burk MJ (1991) J Am Chem Soc 113:8518
32. Burk MJ, Feaster JE, Nugent WA, Harlow RL (1993) J Am Chem Soc 115:10125
33. Noyori R, Takaya H (1990) Acc Chem Res 23:345
34. Gridnev ID, Higashi N, Imamoto T (2000) J Am Chem Soc 122:10486
35. Koenig KE, Bachman GL, Vineyard BD (1980) J Org Chem 45:2362
36. Knowles WS (1983) Acc Chem Res 16:106
37. Chan ASC, Pluth JJ, Halpern J (1980) J Am Chem Soc 102:5952
38. Halpern J (1981) Inorg Chim Acta 50:11
39. Halpern J (1982) Science 217:401
40. Landis CR, Halpern J (1987) J Am Chem Soc 109:1746
41. Chua PS, Roberts NK, Bosnich B, Okrasinski SJ, Halpern J (1981) J Chem Soc Chem Commun 1278
42. Giernoth R, Heinrich H, Adams NJ, Deeth RJ, Bargon J, Brown JM (2000) J Am Chem Soc 122:12381
43. Gridnev ID, Imamoto T (2009) Chem Commun 7447
44. Gridnev ID, Higashi N, Asakura K, Imamoto T (2000) J Am Chem Soc 122:7183
45. Gridnev ID, Imamoto T (2004) Acc Chem Res 37:633

46. Imamoto T, Itoh T, Yoshida K, Gridnev ID (2008) Chem Asian J 3:1636
47. Imamoto T, Yashio K, Crepy KVL, Katagiri K, Takahashi H, Kouchi M, Gridnev ID (2006) Organometallics 25:908
48. Landis CR, Hilfenhaus P, Feldgus S (1999) J Am Chem Soc 121:8741
49. Feldgus S, Landis CR (2000) J Am Chem Soc 122:12714
50. Feldgus S, Landis CR (2001) Organometallics 20:2374
51. Landis CR, Feldgus S (2000) Angew Chem Int Ed 39:2863
52. Burk MJ, Casy G, Johnson NB (1998) J Org Chem 63:6084
53. Li M, Tang DY, Luo XL, Shen W (2005) Int J Quantum Chem 102:53
54. Gridnev ID, Higashi N, Imamoto T (2001) Organometallics 20:4542
55. Gridnev ID, Yasutake M, Higashi N, Imamoto T (2001) J Am Chem Soc 123:5268
56. Yasutake M, Gridnev ID, Higashi N, Imamoto T (2001) Org Lett 3:1701
57. Gridnev ID, Yamanoi Y, Higashi N, Tsuruta H, Yasutake M, Imamoto T (2001) Adv Synth Catal 343:118
58. Mori S, Vreven T, Morokuma K (2006) Chem Asian J 1:391
59. Donoghue PJ, Helquist P, Wiest O (2007) J Org Chem 72:839
60. Donoghue PJ, Helquist P, Norrby PO, Wiest O (2008) J Chem Theory Comput 4:1313
61. Donoghue PJ, Helquist P, Norrby PO, Wiest O (2009) J Am Chem Soc 131:410
62. Norrby PO, Liljefors T (1998) J Comput Chem 19:1146
63. Gridnev ID, Imamoto T, Hoge G, Kouchi M, Takahashi H (2008) J Am Chem Soc 130:2560
64. Darcel C, Moulin D, Henry JC, Lagrelette M, Richard P, Harvey PD, Juge S (2007) Eur J Org Chem 2078
65. Gainsford GJ, Falshaw A, Lensink C, Seth M (2008) Polyhedron 27:2529
66. Heinrich H, Giernoth R, Bargon J, Brown JM (2001) Chem Commun 1296
67. Verdolino V, Forbes A, Helquist P, Norrby P-O, Wiest O, (2010) J. Mol. Catal. A 324:9
68. Genet J-P (2003) Acc Chem Res 36:908
69. Blaser HU, Malan C, Pugin B, Spindler F, Steiner H, Studer M (2003) Adv Synth Catal 345:103
70. Clapham SE, Hadzovic A, Morris RH (2004) Coord Chem Rev 248:2201
71. Sandoval CA, Ohkuma T, Muniz K, Noyori R (2003) J Am Chem Soc 125:13490
72. Noyori R, Ohkuma T (2001) Angew Chem Int Ed 40:40
73. Abbel R, Abdur-Rashid K, Faatz M, Hadzovic A, Lough AJ, Morris RH (2005) J Am Chem Soc 127:1870
74. Wu XF, Vinci D, Ikariya T, Xiao JL (2005) Chem Commun 4447
75. Li TS, Lough A, Churlaud R, Abdur-Rashid K, Morris RH (2003) Abstr Pap Am Chem Soc 226:U743
76. Menashe N, Salant E, Shvo Y (1996) J Organomet Chem 514:97
77. Shvo Y, Goldberg I, Czerkie D, Reshef D, Stein Z (1997) Organometallics 16:133
78. Larsson ALE, Persson BA, Backvall JE (1997) Angew Chem Int Ed 36:1211 (in English)
79. Persson BA, Larsson ALE, Le Ray M, Backvall JE (1999) J Am Chem Soc 121:1645
80. Samec JSM, Ell AH, Backvall JE (2005) Chem Eur J 11:2327
81. Casey CP, Singer SW, Powell DR, Hayashi RK, Kavana M (2001) J Am Chem Soc 123:1090
82. Casey CP, Bikzhanova GA, Cui Q, Guzei IA (2005) J Am Chem Soc 127:14062
83. Casey CP, Johnson JB, Singer SW, Cui Q (2005) J Am Chem Soc 127:3100
84. Noyori R (1994) Asymmetric catalysis in organic synthesis, Chap. 2. Wiley, New York
85. Helmchen GJ, Schaumann E (1995) Methods of organic chemistry, Stereoselective synthesis, vol E21d. Thieme Verlag, Stuttgart, New York, 3945p
86. Hashiguchi S, Fujii A, Takehara J, Ikariya T, Noyori R (1995) J Am Chem Soc 117:7562
87. Takehara J, Hashiguchi S, Fujii A, Inoue S, Ikariya T, Noyori R (1996) Chem Commun 233
88. Hashiguchi S, Fujii A, Haack KJ, Matsumura K, Ikariya T, Noyori R (1997) Angew Chem Int Ed 36:288 (in English)
89. Haack KJ, Hashiguchi S, Fujii A, Ikariya T, Noyori R (1997) Angew Chem Int Ed 36:285 (in English)

90. Gao JX, Ikariya T, Noyori R (1996) Organometallics 15:1087
91. Noyori R, Hashiguchi S (1997) Acc Chem Res 30:97
92. Mashima K, Abe T, Tani K (1998) Chem Lett 1199
93. Ohkuma T, Koizumi M, Doucet H, Pham T, Kozawa M, Murata K, Katayama E, Yokozawa T, Ikariya T, Noyori R (1998) J Am Chem Soc 120:13529
94. Chowdhury RL, Backvall JE (1991) J Chem Soc Chem Commun 1063
95. Genet JP, Ratovelomananavidal V, Pinel C (1993) Synlett 478
96. Krasik P, Alper H (1994) Tetrahedron 50:4347
97. Palmer M, Walsgrove T, Wills M (1997) J Org Chem 62:5226
98. Alonso DA, Guijarro D, Pinho P, Temme O, Andersson PG (1998) J Org Chem 63:2749
99. Alonso DA, Brandt P, Nordin SJM, Andersson PG (1999) J Am Chem Soc 121:9580
100. Yamakawa M, Ito H, Noyori R (2000) J Am Chem Soc 122:1466
101. Petra DGI, Reek JNH, Handgraaf JW, Meijer EJ, Dierkes P, Kamer PCJ, Brussee J, Schoemaker HE, van Leeuwen PWNM (2000) Chem Eur J 6:2818
102. Handgraaf JW, Reek JNH, Meijer EJ (2003) Organometallics 22:3150
103. Noyori R, Yamakawa M, Hashiguchi S (2001) J Org Chem 66:7931
104. Yamakawa M, Yamada I, Noyori R (2001) Angew Chem Int Ed 40:2818
105. Brandt P, Roth P, Andersson PG (2004) J Org Chem 69:4885
106. Rossin A, Kovacs G, Ujaque G, Lledos A, Joo F (2006) Organometallics 25:5010
107. Backvall J-E, Chowdhuri RL, Karlsson U, Wang GZ (1992) In: Williams AF, Floriani C, Merbach G (eds) Perspectives in coordination chemistry. Verlag Helvetica Chimica Acta, Basel, Switzerland, p 463
108. Bacchi A, Balordi M, Cammi R, Elviri L, Pelizzi C, Picchioni F, Verdolino V, Goubitz K, Peschar R, Pelagatti P (2008) Eur J Inorg Chem 4462
109. Hedberg C, Kallstrom K, Arvidsson PI, Brandt P, Andersson PG (2005) J Am Chem Soc 127:15083
110. Noyori R, Kitamura M, Ohkuma T (2004) Proc Natl Acad Sci USA 101:5356
111. Ito M, Hirakawa M, Murata K, Ikariya T (2001) Organometallics 20:379
112. Morris RH, Abdur-Rashid K, Clapham SE, Hadzovic A, Lough A, Harvey JN (2002) Abstr Pap Am Chem Soc 224:U733
113. Crabtree RH, Siegbahn PEM, Eisenstein O, Rheingold AL (1996) Acc Chem Res 29:348
114. Shubina ES, Belkova NV, Epstein LM (1997) J Organomet Chem 536:17
115. Crabtree RH (1998) Science 282:2000
116. Guari Y, Ayllon JA, Sabo-Etienne S, Chaudret B, Hessen B (1998) Inorg Chem 37:640
117. Grundemann S, Ulrich S, Limbach HH, Golubev NS, Denisov GS, Epstein LM, Sabo-Etienne S, Chaudret B (1999) Inorg Chem 38:2550
118. Fryzuk MD, Macneil PA, Rettig SJ (1987) J Am Chem Soc 109:2803
119. Rautenstrauch V, Hoang-Cong X, Churlaud R, Abdur-Rashid K, Morris RH (2003) Chem Eur J 9:4954
120. Ohkuma T, Ooka H, Hashiguchi S, Ikariya T, Noyori R (1995) J Am Chem Soc 117:2675
121. Joubert J, Delbecq F (2006) Organometallics 25:854
122. Joubert J, Delbecq F (2006) J Organomet Chem 691:1030
123. Eyring H (1934) J Chem Phys 3:107
124. Kovacs G, Ujaque G, Lledos A, Joo F (2006) Organometallics 25:862
125. Comas-Vives A, Ujaque G, Lledos A (2007) Organometallics 26:4135
126. Blum Y, Czarkie D, Rahamim Y, Shvo Y (1985) Organometallics 4:1459
127. Shvo Y, Czarkie D, Rahamim Y, Chodosh DF (1986) J Am Chem Soc 108:7400
128. Handgraaf JW, Meijer EJ (2007) J Am Chem Soc 129:3099
129. Leyssens T, Peeters D, Harvey JN (2008) Organometallics 27:1514
130. Corey EJ, Bailar JC (1959) J Am Chem Soc 81:2620
131. Breneman CM, Wiberg KB (1990) J Comput Chem 11:361

132. For use of STERIMOL parameters in QSAR, Hogberg T, Norinder U (1996) In: Krogsgaard-Larsen P, Liljefors T, Madsen U (eds) A textbook of drug design and development, 2nd edn. Harwood Academic, Amsterdam
133. Troutman MV, Appella DH, Buchwald SL (1999) J Am Chem Soc 121:4916
134. Pfaltz A (1999) Synlett 835
135. Helmchen G, Pfaltz A (2000) Acc Chem Res 33:336
136. Blackmond DG, Lightfoot A, Pfaltz A, Rosner T, Schnider P, Zimmerman N (2000) Chirality 12:442
137. Lightfoot A, Schnider P, Pfaltz A (1998) Angew Chem Int Ed 37:2897
138. Blankenstein J, Pfaltz A (2001) Angew Chem Int Ed 40:4445
139. Drago D, Pregosin PS, Pfaltz A (2002) Chem Commun 286
140. Menges F, Neuburger M, Pfaltz A (2002) Org Lett 4:4713
141. Menges F, Pfaltz A (2002) Adv Synth Catal 344:40
142. Bunlaksananusorn T, Polborn K, Knochel P (2003) Angew Chem Int Ed 42:3941
143. Cozzi PG, Menges F, Kaiser S (2003) Synlett 833
144. Xu GP, Gilbertson SR (2003) Tetrahedron Lett 44:953
145. Hou DR, Reibenspies JH, Burgess K (2001) J Org Chem 66:206
146. Crabtree R (1979) Acc Chem Res 12:331
147. Powell MT, Hou DR, Perry MC, Cui XH, Burgess K (2001) J Am Chem Soc 123:8878
148. Perry MC, Cui XH, Powell MT, Hou DR, Reibenspies JH, Burgess K (2003) J Am Chem Soc 125:113
149. Brandt P, Hedberg C, Andersson PG (2003) Chem Eur J 9:339
150. Crabtree RH, Felkin H, Morris GE (1977) J Organomet Chem 141:205
151. Fan YB, Cui XH, Burgess K, Hall MB (2004) J Am Chem Soc 126:16688
152. Cui XH, Fan YB, Hall MB, Burgess K (2005) Chem Eur J 11:6859
153. Mashima K, Abe T, Tani K (1998) Chem Lett 1201
154. Murata K, Ikariya T (1999) J Org Chem 64:2186
155. Zassinovich G, Bettella R, Mestroni G, Brescianipahor N, Geremia S, Randaccio L (1989) J Organomet Chem 370:187
156. Petra DGI, Kamer PCJ, Spek AL, Schoemaker HE, van Leeuwen PWNM (2000) J Org Chem 65:3010

Mechanistic Insights into Selective Oxidation of Light Alkanes by Transition Metal Compounds/Complexes

Gang Fu and Xin Xu

Abstract Selective oxidation or oxidative functionalization of light alkanes by using transition metal compounds/complexes is an area of active research, whose progress is of great importance for both academic researches and industrial applications. In this work, we have reviewed some of our recent theoretical advances on selective oxidation of alkanes upon metal-oxo species as well as Pt (II) complexes. Attention has been paid to two key topics: (1) the mechanisms of the selective oxidation of methane and propane, and (2) the structure, stability, and reaction mechanisms of the Catalytica $PtCl_2$(bpym) catalyst. Compared to the related experimental results, rich mechanistic information has been obtained. These findings would be of help to the rational design of more efficient heterogeneous and homogeneous catalysts for utilization of light alkanes.

Abbreviations

BE	Bond energy
bpym	η^2-2,2′-bipyrimidyl
DFT	Density functional theory
DHAM	Dehydrogenation–aromatization of methane
EA	Electron affinity

G. Fu
Department of Chemistry, State Key Laboratory for Physical Chemistry of Solid Surfaces, College of Chemistry & Chemical Engineering, Xiamen University, Xiamen 361005, China

X. Xu (✉)
Department of Chemistry, State Key Laboratory for Physical Chemistry of Solid Surfaces, College of Chemistry & Chemical Engineering, Xiamen University, Xiamen 361005, China

MOE laboratory for Computational Physical Science, Department of Chemistry, Fudan University, Shanghai 200433, China
e-mail: xinxu@xmu.edu.cn; xxchem@fudan.edu.cn

O. Wiest and Y. Wu (eds.), *Computational Organometallic Chemistry*,
DOI 10.1007/978-3-642-25258-7_5,

EPR	Electron paramagnetic resonance
GTL	Gas-to-liquid process
HOMO	Highest occupied molecular orbital
KIE	Kinetic isotopic effect
LUMO	Lowest unoccupied molecular orbital
MPO	Methane partial oxidation to oxygenate
NNC	η^3-6-phenyl-2,2′-bipyridine
ODHP	Oxidative dehydrogenation of propane
PA	Proton affinity
PES	Potential energy surface
Pic	η^2-*N*,*O*-picolinate
QM/MM	Quantum mechanics/molecular mechanics
QM-RP	Quantum mechanical rapid prototyping
SS-VAFR	Single-site vanadyl activation, functionalization, and reoxidation
TFA	Trifluoroacetic acid
TOF	Turnover frequency
UV–Vis	Ultraviolet visible

1 Introduction

Over 85% of our energy demands are supplied by the combustion of fossil fuels. Given the issue of CO_2 emission and global warming, there is a need to develop lower carbon-based energy economy. Light alkanes (C_2–C_4) in addition to methane, which is the main component in natural gas, are abundant in our planet and have higher hydrogen-to-carbon ratio compared to oil and coal. Currently, the well-established technology for the conversion of natural gas to liquid chemicals, the so-called GTL, proceeds via an indirect route: (1) production of syn-gas ($CO + H_2$) from steam of natural gas and (2) conversion of syn-gas into value-added products through processes such as the Fischer–Tropsch synthesis [1, 2]. However, as has been pointed out, such a technology is chemically inelegant [3], as alkanes are first over-oxidized to CO and then reduced to the desired products. In contrast, the direct route, i.e., selective oxidation or oxidative functionalization of light alkanes, in principle, might proceed more efficiently and cost effectively.

Since the 1970s, more and more attention has been paid to the direct route. Despite extensive efforts, there are limited industrial processes directly using such cheap hydrocarbon resources as feedstock [4]. The key questions for direct route are how to realize the alkane activation and the selective transformation to the desired products. In mild conditions, light alkanes are very stable, inert to be activated. The electronic factor for this inertness lies in that alkanes are made of strongly localized C–H and C–C bonds, where the HOMO is too low lying and the LUMO is too high lying, diminishing the possibility for an activation mechanism involving donation and back-donation of electrons to and from the catalysts, respectively [5]. Furthermore, the carbon atoms in alkanes undergo sp^3 hybridization. Such formed

tetrahedral structure presents a geometric hinder in contrast to water and ammonia with lone pairs which are more liable for attacking [3]. In fact, selectivity is more a severe issue than activity [6]. In harsh condition of alkane activation, the desired products (alkenes, alcohols, aldehydes, etc.) are more active than the reactants, subject to complete oxidation to CO_2. Hence, how to suppress the over-oxidation of the target products at a higher conversion of alkanes is a critical challenge. Indeed, as stated in the section of "Roadmap for research on catalysis—Technical Targets" from "Vision 2020 catalysis report," alkane activation and selective oxidation are listed in the No. 1 and 2 positions [7]. In a report entitled "Challenges for Chemists" by the former president of American Chemical Society (ACS)—C.P. Casey, the development of selective catalysts for direct oxidation of hydrocarbons by molecular oxygen is listed as top one of five advances in basic chemistry that will enable new opportunities [8]. Very recently, a special issue from "Chemical Review" highlights the development of functionalization of C–H bond. In the preface, the editor, R.H. Crabtree, advocated that "of all the fields that contribute to the C–H activation problem, computational chemistry has perhaps made the greatest strides in power and breadth of applicability" [9]. Today, with the rapid increase in computing power, parallel algorithm, and methodology advancement in quantum chemistry, both the size of systems that can be studied and the nature of the problems that can be addressed have been extended dramatically [10]. Especially, theoretical results can be used to fill the gaps when some key data are not readily obtainable experimentally. The interplay between experiment and theory is expected to be the ideal route to rational design of selective oxidation of light alkanes at the molecular level.

Numerous works concerning alkane functionalization, varied from homogeneous or heterogeneous catalysis, to biological/biomimetic systems, have been reported [3, 5, 6, 10–17]. Herein, we discuss several of these approaches with an emphasis on the computational results obtained in our own group. The following content is divided into four parts. After a brief discussion of the classification of C–H bond activation (Sect. 3), we present our effort on C–H bond oxidation by metal-oxo species (Sect. 3) and Pt(II) complexes (Sect. 4), and discuss some recent advances in these fields. A concluding remark is given in Sect. 5.

2 Classification of C–H Bond Activation

As Shilov proposed [11], C–H bond activation by metal species can be classified into three categories based on their mechanisms. The first type is called "organometallic" activation where the reaction takes place in the first coordination sphere of metal center and leads to the formation of M–C σ-bond. This mechanism includes various derivatives, such as oxidative addition, σ-bond metathesis, 1, 2 addition, and electrophilic substitution, as shown in Fig. 1. Interestingly, recent theoretical studies also revealed that there exist a few alternatives to these classic types, namely, "metal-assisted σ-bond metathesis" [18], "oxidatively added

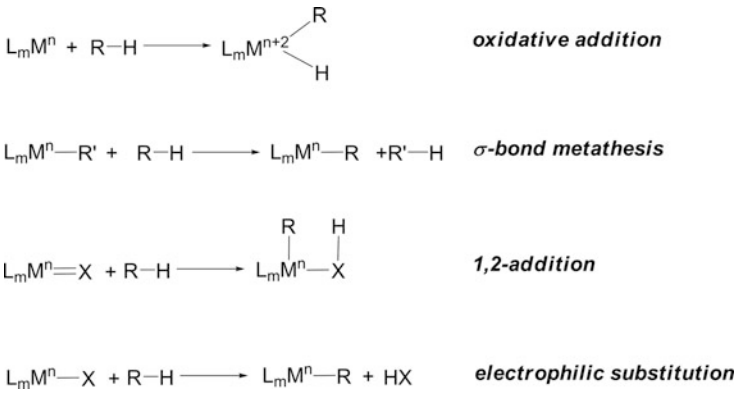

Fig. 1 Various mechanisms belonging to the so-called organometallic C–H bond activation [9]

transition state" (OATS) [19], "oxidative hydrogen migration" (OHM) [20], "σ-complex-assisted metathesis" (σ-CAM) [21], etc. This topic has been reviewed by several authors [10, 17, 22, 23].

The second type is ligand activation where the metal complex interacts with either C or H of a C–H bond only via its outer ligand (L) during the course of C–H bond activation [9]. Such kind of reaction is distinguished from the first one by avoiding the formation of the M–C bond at any stage. In this case, the metal center usually serves as an electron acceptor, while an H–L bond and/or a C–L bond is formed simultaneously or consecutively. A typical example is the hydroxylation of a C–H bond by a high-valence metal-oxo as shown in (1) and (2).

$$L_nM^{x+} = O + R - H \rightarrow L_nM^{(x-1)+} - OH + R \rightarrow L_nM^{(x-2)+} + R - O - H \quad (1)$$

$$L_nM^{x+} = O + R - H \rightarrow L_nM^{(x-2)+} + R - O - H \quad (2)$$

Such a way of activation can occur though a step-wise radical process (1) or a concerted oxygen insertion process (2). In both cases, the C–H bond breaking is initiated by the participation of the oxo ligand. The third type is an indirect mechanism in which metal complexes promote the formation of a reactive species (usually oxyradical), which then reacts with the hydrocarbon molecule without involving the metal complex [9].

Similarly, Labinger [14] introduced "hot" and "cold" approaches for the selective oxidation of alkanes. The hot approach is referred to as oxidative activation of C–H bond by metal oxide catalysts, which need to be carried out at relatively high temperature around several hundred degree Centigrade. Note that the only commercially practiced selective oxidation process, i.e., oxidation of butane to maleic anhydride over VPO, belongs to this category [4]. In addition, a more sophisticated Mo–V–Nb–(Te, Sb)–O_x system was reported to show great promise in propane oxidation to acrylic acid (46% yield) and amoxidation to acrylonitrile (62% yield) [24]. Encouraged by the success of these processes, we envision that more and more

processes involving high-temperature selective oxidation of light alkanes can be industrialized eventually after more systematic and in-depth research. On the contrary, lower temperature always leads to lower cost such that the cold approach for alkane activation has also attracted much attention. In this cold approach, transition metal complexes have been used as catalyst and the reaction works under homogeneous condition. Up to now, a variety of complexes, containing Pt (II) [25–27], Hg(II) [28], Au(I)/Au(III) [29], Pd(II) [30], etc., have been developed for the C–H bond functionalization. Among them, a key feature is that during the C–H bond activation process, alkane is coordinated to the metal center, leading to the formation of a strong M–C bond. Thereby, these cold approaches fall within the scope of the organometallic activation (cf. Fig. 1). Although at the present time such processes are not economically competitive with existing heterogeneous processes, they serve as important alternatives, deserving further development.

3 C–H Bond Activation by High-Valence Transition Metal Oxide Clusters

3.1 Importance of Metal-Oxo in Selective Oxidation of Alkanes

According to IUPAC nomenclature, oxo originally stands for a ketone functional group (C=O). Currently, the term "oxo" also denotes a single oxygen atom coordinated to a transition metal, i.e., M=O. In fact, there is a broad interest in the catalytic properties of metal-oxo species toward activation of low alkanes. Gas-phase chemistry of metal-oxo species has been studied in detail, which has been related to condensed-phase chemistry [31–33]. Heterogeneous catalysis often employs high-valence metal oxides with terminal oxygen, e.g., V_2O_5 and MoO_3, as the active component [34, 35]. While in homogenous systems, polyoxometalate is frequently used to catalyze the selective oxidation of alkanes [36]. Moreover, simple metal-oxo compounds, such as CrO_2Cl_2, OsO_4, and MnO_4^-, are applied extensively in organic synthesis for oxyfunctionalization of C–H bond [37, 38]. In biological systems, cytochromes P_{450} exhibit high activity and selectivity to hydroxylate C–H bonds by using its (porphyrin$^{+\cdot}$)Fe^{IV}=O unit [39]. All these highlight the importance and underlying relationship of various kinds of high-valence metal oxoes in selective alkane oxidation (cf. Fig. 2).

3.2 C–H Activation Related to Dehydrogenation–Aromatization of Methane

DHAM in the absence of gas-phase oxygen has been considered as a promising approach for the utilization of natural gas [40, 41]. Supported VIB group metal

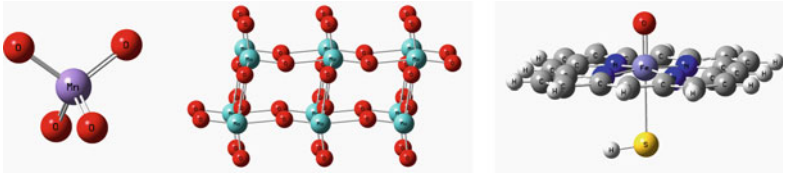

MnO_4^- α-MoO_3 P450 model

Fig. 2 Examples of transition metal-oxo compounds that can promote selective oxidation of the C–H bond

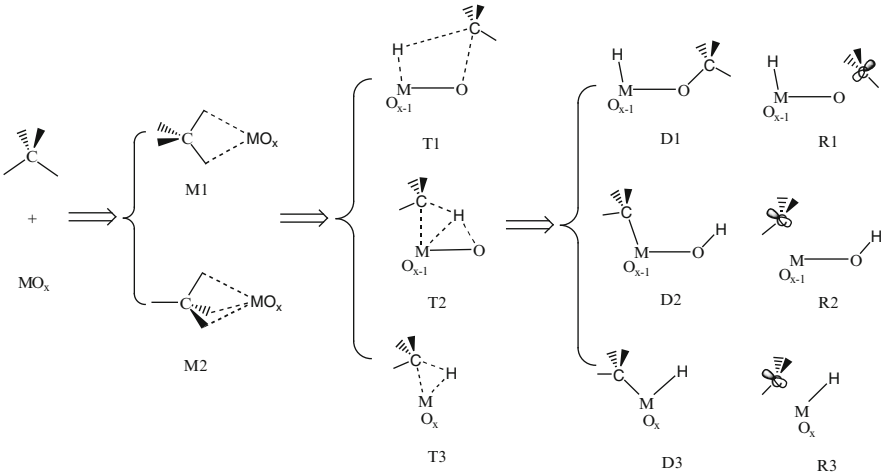

Fig. 3 Activation of the methane C–H bond by metal oxide molecules MO_x [43]

oxides, such as CrO_x, MoO_x, and WO_x, are reported to show DHAM activity. It is generally accepted that this system forms a bifunctional catalyst with the metal responsible for methane activation to C2 species and the zeolite responsible for their conversion to benzene [41, 42]. However, it is still not clear that what the active phase is and in what reaction mechanism methane is activated.

Xu et al. have performed a DFT study of methane activation by using the transition metal oxide molecules of MO_x (M = Cr, Mo, W; $x = 1, 2, 3$) as model catalysts [43]. They have considered three kinds of transition states (see Fig. 3). In the transition state T1, methane approaches the M–O bond from the O end, with H attacking the metal and the methyl group the oxygen, resulting in a hydride product (M–H). While in the transition state T2, methane approaches MO_x with its methyl group attacking the metal, leading to the formation of a carbide product. The reaction via transition state T3 is generally referred to as oxidative addition, with

the metal center M being formally oxidized. Interestingly, both T2 and T3 belong to the organometallic activation shown in Fig. 1. This indicates that in some cases, the high-temperature selective alkane oxidation might share a common mechanism with its low-temperature counterparts.

Table 1 lists the activation energies corresponding to transition states T1, T2, and T3, as shown in Fig. 3. With the exception of T3 on Cr, the activation barriers follow the trend T1 > T2 > T3. The relatively high energy of T1 with respect to T2 appears to arise mainly from its unfavorable electrostatic interactions. In T1, the interaction between the dipoles associated with the C–H and M–O bonds tends to raise the energy, which makes it no longer competitive with T2. For T2, the general trends of the reactivity of MO_x are $CrO_x > MoO_x > WO_x$ and $MO_3 > MO_2 > MO$. This is found to be roughly consistent with the strength of the M–O π bond. The abnormal behavior of the reactivity of MO_3 in T2 can be explained by considering the relative large size of d orbitals in W compared to those in Cr and Mo. T3 is a concerted process with a cyclic three-center, four-electron transition state. The activation barrier for T3 is generally low since it does not require breaking the M–O π bond. The reactivity follows the trend $WO_x > MoO_x > CrO_x$ ($x = 2, 1$), as expected from the relative size of the d orbitals, with the exception of WO.

Thus, whether the reactions involve mechanisms via T2 and/or T3 depends on the metal and the oxidation conditions. Carbide formation is favored by high oxidation states as well as by high positive charge and low s-orbital population on the metal center, whereas the oxidative addition would be preferable on the metal center with an intermediate or low oxidation state. Accordingly, the authors suggested that MO_2 (M = W, Mo) is the best oxidation state for this class of metal oxides toward methane activation and predicted that the active phase in the DHAM reaction may be W and Mo oxycarbides (MO_2C_2).

Table 1 Activation energies (in kcal/mol) for σ bond metathesis (T1 and T2) and oxidative addition (T3) of MO_x

	x		
	3	2	1
T1 mechanism			
Cr	40.5	52.0	56.0
Mo	43.7	58.6	54.5
W	32.2	63.1[a]	70.6[a]
T2 mechanism			
Cr	7.7	10.0	10.0
Mo	12.3	23.5	32.9
W	4.0	32.0[a]	58.7
T3 formation			
Cr	–	19.1[a]	25.4[a]
Mo	–	3.9[a]	7.6[a]
W	–	−0.4	18.7

All energies are relative to the corresponding ground state of $CH_4 + MO_x$ [43]

[a]Spin multiplicity changed during the reaction

3.3 C–H Activation Related to Methane Partial Oxidation to Oxygenate

Selective oxidation of methane to methanol or formaldehyde is one of the most challenging goals in catalysis [44, 45]. However, in spite of great effort, the single-pass yield of oxygenates is still quite low, usually less than 4%, which is far from fulfilling the industrial requirement [45]. Thus, how to develop an efficient catalytic system of both good activity and good selectivity calls for a detailed mechanistic understanding. By using DFT in conjunction with cluster models (cf. Fig. 4), we presented a comprehensive survey of different C–H activation pathways over various kinds of active sites [47, 48].

Fig. 5 summarizes the possible mechanisms for the activation of a C–H bond. Among these reaction pathways, (2+2) may be considered as an acid–base reaction whose valence of metal remains unchanged during the C–H bond heterolytic cleavage. (3+2) and (5+2) are correlated with the homolytic cleavage of a C–H bond, where two electrons originally located on the C–H bond are injected into the empty metal orbitals. These pathways are a two-electron process, leading to the formation of hydroxyl and alkoxy directly [46] which were observed in the IR experiments [49]. H-abstraction is a one-electron process, which provides a competitive alternative. A direct experimental support to this radical mechanism came from the EPR spectra, which showed that when n-pentane flowed through the tungstated zirconia catalyst, W^{5+} centers, and organic radicals formed [50]. Hence there is a puzzle whether C–H bond activation is a two-electron process as indicated by IR or a one-electron process as suggested by EPR.

Starting from model catalysts ($V_3O_6Cl_3$, Cr_3O_9, Mo_3O_9, and W_3O_9), we found that a terminal oxygen is more active than a bridge oxygen. As shown in Table 2, H-abstractions by the terminal M=O in an anti-mode, i.e., TS6, is the most favorable except for that on the W oxide. The calculated activation enthalpies for methane initial oxidation by V and Mo oxides are 35.5 and 45.0 kcal/mol, respectively, comparable to the corresponding experimental values (39.9 [51] and 45.2 kcal/mol [52]). It should be noted that in the literature, thermo- or photo-excited O^- was

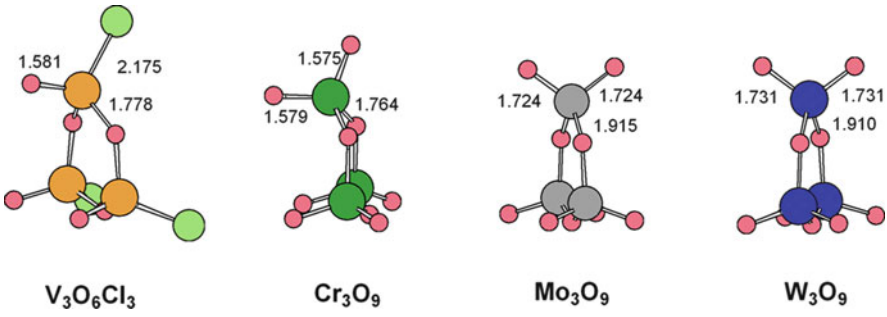

Fig. 4 $V_3O_6Cl_3$ and M_3O_9 (M = Cr, Mo, W) cluster models for metal oxoes [48]

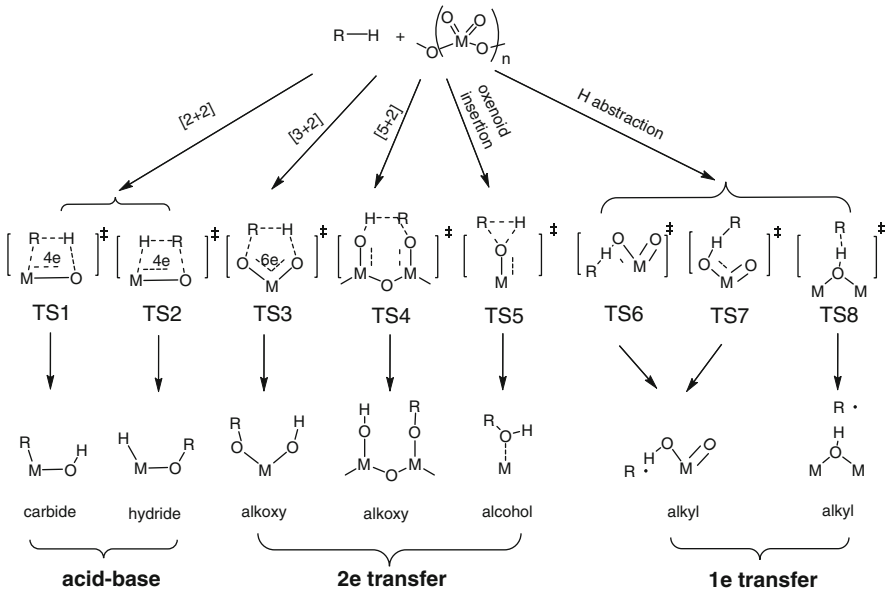

Fig. 5 Possible mechanisms for the activation of C–H bond in alkanes by metal oxoes [47]

Table 2 Calculated energetics for CH_4 activation by high-valence metal oxides (873 K, unit: kcal/mol)

Reaction pathway	Activation mode	$V_3O_6Cl_3$		Cr_3O_9		Mo_3O_9		W_3O_9	
		$\Delta H^{\neq}$	ΔH_r	$\Delta H^{\neq}$	ΔH_r	$\Delta H^{\neq}$	ΔH_r	$\Delta H^{\neq}$	ΔH_r
TS1	(2+2)	57.0	38.0	–	24.1	50.1	23.0	43.6	13.8
TS2	(2+2)	86.5	44.6	82.5	33.7	86.9	30.3	78.9	24.4
TS3	(3+2)	–	–	42.8	−14.5	68.6	30.2	83.8	37.5
TS4	(5+2)	63.6	18.4	39.7	−21.4	63.2	20.8	80.2	44.7
TS5	Oxenoid insert	69.4	16.6	39.2	−24.9	69.4	26.5	87.3	40.9
TS6	H-abstraction	35.5	35.5	20.1	18.2	45.0	44.7	56.8	56.8
TS7	H-abstraction	36.8	35.5	24.2	18.2	49.7	44.7	59.6	56.8
TS8	H-abstraction	42.7	39.1	33.1	26.1	63.6	62.3	79.3	–
Expt.	–	39.9[a]	–	–	–	45.2[b]		–	–

[a]From [51]
[b]From [52]

proposed as the active center [53, 54], and it is well documented in the gas-phase ion chemistry that reaction pathways which involve two states of different multiplicities may cross-over, which determines the minimum-energy pathway of a reaction [33]. However, in the present systems, the initial C–H bond activation goes through the singlet PES, and the triplet PES will not interfere significantly until the methyl radical is generated.

Hence, our calculations emphasized a step-wise mechanism over most oxides: H-abstraction leads to a surface hydroxyl, in conjunction with the alkyl radical formation, which rapidly rebounds to a nearby oxygen to form a surface alkoxy. This step-wise one-electron oxidation mechanism not only offers an energetically more favorable route than the one-step two-electron oxidation mechanism such as (5+2), but also provides a plausible solution to the puzzle as contrasting the EPR results [50] to the IR results [49] (cf. Fig. 6). We propose that EPR with higher time resolution (10^{-5}–10^{-10} s) detected the radical formation, whose stability was enhanced by the higher acidity of the tungstated zirconia catalyst which retarded the rebound process. On the contrary, IR with lower time resolution (10^{-1}–10^{-2} s) was unable to capture the active alkyl intermediates, showing the peaks related to the existence of both surface hydroxy and alkoxy after rebound.

It is interesting to compare our results with some recent theoretical works on related systems. Zhou et al. [55] have investigated the methane activation over the MoO_x/H-ZSM5 system with the DFT method. They only considered the reaction pathway involving a transition state as TS1 suggested here and predicted a barrier of 63.5 kcal/mol on a Mo_2O_5 dimer. Unfortunately, they did not consider the H-abstraction mechanism. Schwarz et al. [56] have studied thermal reaction of methane with tetranuclear $V_4O_{10}^+$ by using mass spectrometric techniques in conjunction with theoretical studies. Their DFT calculations demonstrated that when CH_4 approaches the cluster, CH_3 radical can be produced without a barrier and with the energy gain of −29.2 kcal/mol. This finding indicated that chemistry concerning metal cation clusters can be very different from that of neutral metal oxide clusters. Goddard et al. [57] have employed V_4O_{10} to explore the alkane C–H bond activation. They compared four possible pathways, namely, TsA, TsB, TsC, and TsD, which are corresponding to TS2, TS1, TS8, and TS6, as shown in Fig. 4,

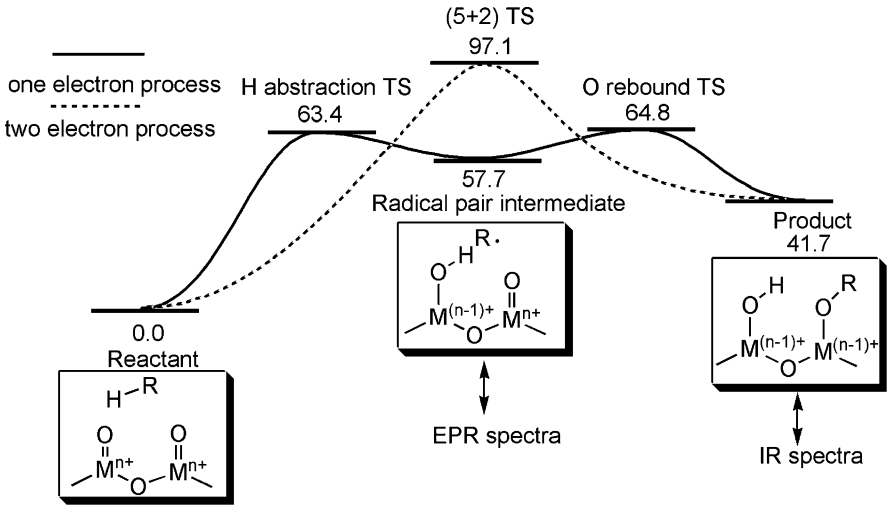

Fig. 6 H-abstraction/O-rebound mechanism versus (5+2) mechanism for oxidation of methane over Mo oxides [47]

respectively. In agreement with us, they also came to the conclusion that H-abstraction by M=O is the most feasible pathway (activation energy for TsD: 30.2 kcal/mol).

At this point, we would also like to point out that DFT calculations also suggest that when the M=O bond possesses a high polarity such as those in the tungsten oxides, the (2+2) pathway becomes a competitive pathway. The predicted activation energy for the W oxide is 43.6 kcal/mol (TS1), even lower than that via H-abstraction on the Mo oxide (45.0 kcal/mol, TS6), indicating that the W oxide is also able to activate methane though it is a weak oxidant. Again, in this case, organometallic type activation plays an important role in MPO since W–CH_3 bond has been made. This result is not inconsistent with the EPR spectra [50] which showed that when n-pentane flowed through the tungstated zirconia catalyst, W^{6+} centers were reduced to W^{5+} and organic radicals formed. Indeed when methane is replaced by pentane, the same level of calculations leads to $\Delta E_a = 43.5$ kcal/mol for H-abstraction, which is now lower than $\Delta E_a = 44.4$ kcal/mol for the (2+2) process.

3.4 C–H Activation Related to Oxidative Dehydrogenation of Propane

Oxidative dehydrogenation (ODH) of light alkanes (C_2–C_4) offers a promising route to alkenes [58–62]. Among them, ODHP has been extensively investigated. It is generally accepted that ODHP occurs via the parallel and sequential oxidation steps, as shown in Fig. 7. Thus for ODHP, the key is to realize the kinetic control so as to enhance the transformation of propane into propylene (k_1) and to suppress the over-oxidation of propylene to CO_x (k_3). Several metal oxides have been examined as catalysts for ODHP and most of them contain V or Mo oxides as the active components [58–62]. We have carried out a systematic DFT study on the activation and conversion of propane over V and Mo oxides [63, 64]. Besides the transition states of TS1–TS8 as mentioned above (see Fig. 5), novel pathways, with transition states TS9–TS11 as shown in Fig. 8, emerge to be the alternatives for the activation of propane and propylene, respectively.

For propane activation, H-abstraction via TS6 is the most favorable pathway on both V and Mo oxides. DFT calculation showed that activating the methylene C–H bond is 4.1 and 4.7 kcal/mol more favorable than activating the methyl C–H bond for VO_x and MoO_x, respectively. This regioselectivity is correlated with the

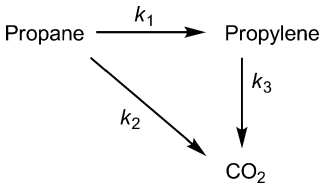

Fig. 7 Reaction network for the oxidative dehydrogenation of propane [63]

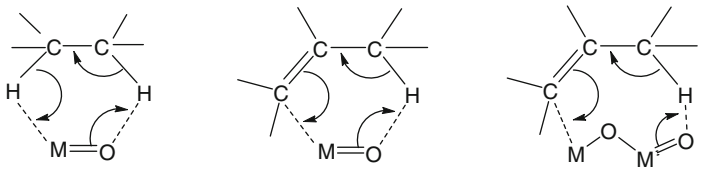

Fig. 8 Three novel pathways for the activation of propane and propylene, respectively [63]

Table 3 Calculated barriers for the most feasible pathways of propane and propylene activation by VO_x and MoO_x

Activation energy (kcal/mol)	VO_x		MoO_x	
	C_3H_8	C_3H_6	C_3H_8	C_3H_6
Calc.	25.8 (T6)	21.4 (T6)	33.2 (T6)	20.2 (T10)
Expt. [61]	23.7	12.2	28.0	14.3

The corresponding activation mode, as shown in Figs. 5 and 8, is listed in parentheses [64]

difference in strength between a methylene C–H bond and a methyl C–H bond. This theoretical result can nicely explain the KIE measured by Bell et al. [62]. Moreover, the predicted barriers of methylene C–H bond activation are consistent with the experimental data observed for ZrO_2-supported VO_x and MoO_x [61] (cf. Table 3). Table 3 also indicated that V oxides are more active than Mo oxides in propane activation. Thus for the V and Mo mixed oxides, propane C–H bond activation is preferable on the V^{5+} sites, while in the absence of V as a component of catalyst, Mo^{6+} can be the active center for propane oxidation.

Unlike propane, propylene with the electron rich π bond can interact strongly with the acidic metal cations. Indeed, we find that (2+4) (via TS10) can be an alternative pathway for the cleavage of the allylic C–H bond. TS10 is more favorable on the MoO_x than on VO_x, indicating that propylene conversion is facilitated by more acidic Mo oxides. Nevertheless, on both cases, the reaction barrier of propylene is 11.5–13.7 kcal/mol more favorable than propane such that it is difficult to stop the reaction at propylene. This finding provides a plausible reason why the yields of propylene are usually lower than 30% during ODHP [60]. Furthermore, we also indicated that addition of some acidic oxides, such as MoO_x and TeO_x, can boost the reaction to the α, β-unsaturated products, such as acrylic acid. This is consistent with the experimental observations that the Mo–V–Te–Nb–O system exhibits high reactivity as well as selectivity for the selective oxidation of propane to acrylic acid [24].

Recently, a few theoretical works also concentrated on ODHP reaction and yielded some interesting but contradicting results. Curtiss et al. [65] have performed both cluster and periodic slab model calculations to investigate the activation of propane over V_2O_5 (010). However, they only concentrated on the oxygen insertion mode (i.e., TS5 in Fig. 5) and arrived at a calculated barrier for

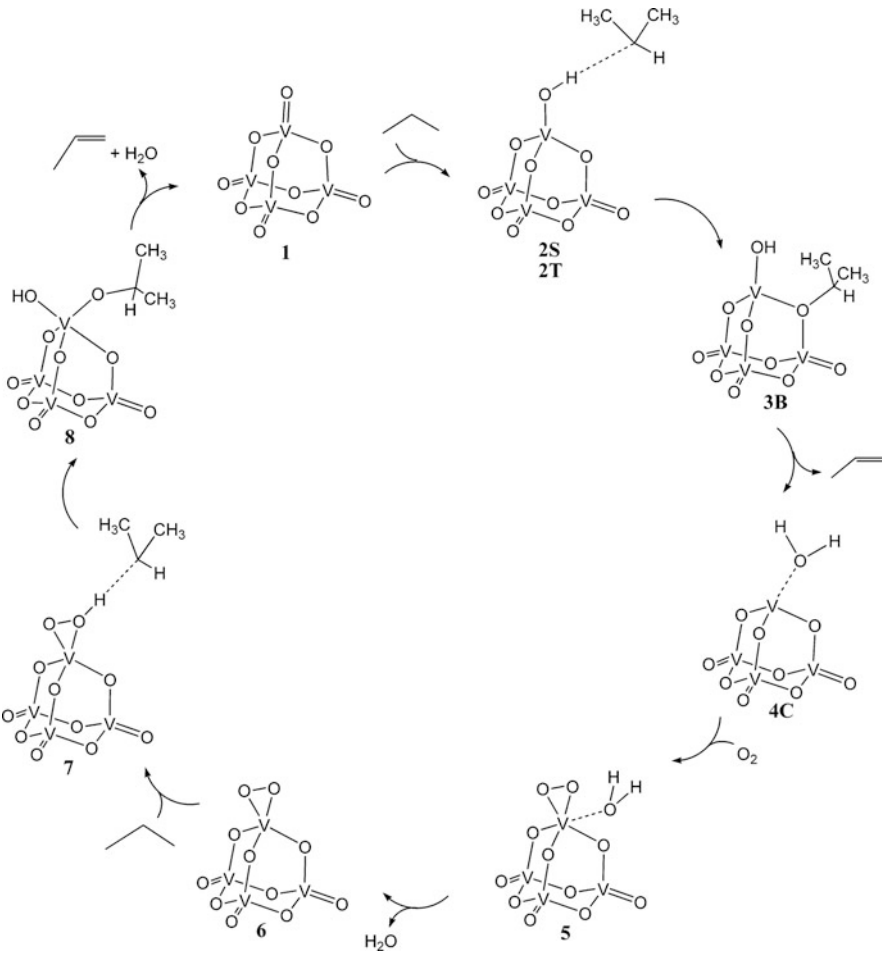

Fig. 9 The catalytic cycle for ODHP on V_4O_{10}, a prototype of the single site vanadyl activation, functionalization, and reoxidation (SS-VAFR) [57]

C–H bond cleavage as high as 79.4 kcal/mol. When the triplet PES was taken into account, the initial barrier was reduced to 55.0 kcal/mol, which is still too high to be compared with the experimental number (23.7 kcal/mol [61]). They did not study the H-abstraction mechanism. On the contrary, cluster model studies by Goddard [57] (c.f. Fig. 9) and by Sauer [66] clearly showed that H-abstraction mechanism was dominant for propane activation over V-based catalyst, consistent with our calculations. Fan et al. [67] have carried out a periodic slab calculation on mechanisms for ODHP over V_2O_5 (001) surface. Three possible mechanisms have been explored, namely, oxo-insertion mechanism, concerted mechanism, and radical mechanism, which resembles TS5, TS4, and TS6 in Fig. 5, respectively. Based on their slab model calculations, the authors claimed that for initial C–H

bond breaking, oxo-insertion by bridge oxygen could compete with H-abstraction by terminal oxygen. They suspected that the strong preference for the radical mechanism in cluster calculations might be due to the finite cluster size effects.

3.5 *Understanding the Reactivity of High-Valence Metal Oxoes Toward the C–H Bond Activation*

In most cases, the selective oxidation of hydrocarbons by oxides occurs through the so-called Mars–van Krevelen mechanism [68], in which the organic molecule reacts with the lattice oxygen, and then the oxygen vacancy is replenished by gaseous oxygen. As a result, the redox properties of oxides influence their ability to complete such a catalytic cycle. We have demonstrated that the activation of an alkane C–H bond usually undergoes H-abstraction mechanism on a transition metal oxide [69]:

$$M^{n+} = O + H - R \rightarrow M^{(n-1)+} - O - H + R \cdot \tag{3}$$

Accordingly, the reaction enthalpy is equal to the difference of the C–H/O–H bond energies (BEs):

$$\Delta H_r = BE(C - H) - BE(O - H) \tag{4}$$

In the radical chemistry, H-abstraction is believed to be an enthalpy-driven process [6, 70]. Fig. 10 shows the correlation of the calculated H-abstraction barriers versus the reaction enthalpy deduced from (4). The plot exhibits a good linearity (correlation coefficient $R^2 = 0.974$) with a slop of 0.943, reinforcing the idea that M=O behaves like an oxygen radical, even though it is not a radical [37]. However, O–H bond strength is difficult to be measured experimentally except for a few homogeneous oxo compounds. For routine use, people preferred to correlate the catalytic activity with some readily detectable properties of metal oxides, such as reducibility, M–O bond energy [71, 72], and the energy gap [73].

We showed that there are many factors that contribute to the strength of an O–H bond. Since an H atom can be viewed as a combination of an electron and a proton [74, 75], the strength of an O–H bond shall be correlated not only with the EA but also with the PA of the oxides. Table 4 summarizes the electron affinity and proton affinity of various oxides. EA is naturally associated with the reducibility of the metal center. As displayed in Table 4, EA decreases from Cr to V, to Mo, and to W, in parallel with the sequence of decreasing strength of the O–H bonds, whereas PA has no correlation with the trends of the strength of the O–H bonds. Nevertheless, for a given oxide, PA difference can be used to qualitatively differentiate the O–H binding energy difference between the terminal oxygen and the bridge oxygen site.

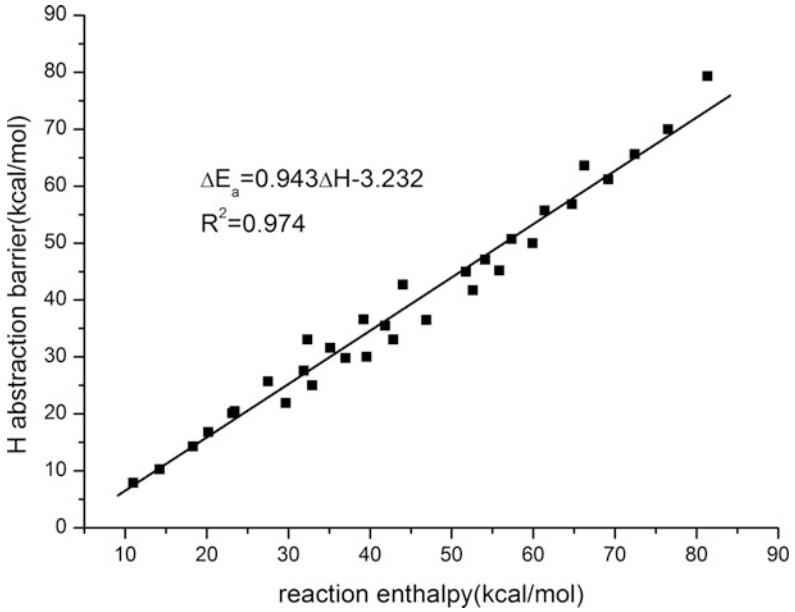

Fig. 10 Plot of the calculated H-abstraction barrier versus the corresponding reaction enthalpy [69]

Table 4 Predicted electronic properties of M_3O_9 (M = Cr, Mo, W) and $V_3O_6Cl_3$ (873 K, energy in kcal/mol) [69]

Oxidants	BE(O–H)[a]		Proton affinity[b]		Electron affinity[c]	ΔE_{ST}[d]	HOMO (eV)	LUMO (eV)
	=O	–O–	=O	–O–				
$V_3O_6Cl_3$	66.2	64.0	176.7	171.6	105.5	47.4	−9.82	−5.86
Cr_3O_9	84.9	75.7	169.6	167.0	112.8	32.5	−10.09	−6.62
Mo_3O_9	56.3	41.8	181.0	167.7	83.2	60.3	−9.94	−5.42
W_3O_9	43.3	26.7	179.2	153.9	75.4	74.5	−9.89	−4.92

[a]BE(O–H) = ΔH(M=O) + ΔH (H) – ΔH (M–O–H)
[b]PA=ΔH(M=O) + ΔH (H^+) – ΔH (M–O–H^+)
[c]EA=ΔH (M=O) – ΔH(M=O^-)
[d]ΔE_{ST} = ΔH (M – O(triplet)) – ΔH(M=O)

Singlet–triplet excitation energy, i.e., ΔE_{ST}, is usually used to estimate the strength of a M=O π bond [43]. DFT calculations showed that for the first-row transition metal oxides, such as V and Cr, the π bond strengths are relatively weak. The π bond becomes stronger as the metal goes down the column, Cr < Mo < W. Since the penalty to open the M=O π bond has to be paid upon forming the O–H bond, a stronger M=O π bond always leads to a weaker O–H bond, as shown in Table 4.

The intrinsic connections among the strengths of the M=O π bond, the ability of electron transfer, and the energy gap of oxide can be rationalized in terms of the

frontier orbital analysis. For a high-valence d^0 transition metal-oxo, the HOMO has a nonbonding character located only on the oxygen atoms, while the LUMO has a dominant $\pi^*_{M=O}$ character. On the one hand, EAs correlate well with the energy of the LUMO since the additional electron will occupy the LUMO. On the other hand, in principle, the HOMO–LUMO gap and the singlet–triplet excitation (ΔE_{ST}) both are determined by not only the LUMO but also the HOMO. However, our calculations revealed that the positions of the HOMOs for different oxides are roughly the same (−10.09 to −9.88 eV), whereas the energies of the LUMOs vary from −6.62 to −4.92 eV (see Table 4). This indicated that EA, ΔE_{ST}, and energy gap are all critically dependent on the energy level of the LUMOs.

Alkane molecules possess a low EA such that LUMO of a C–H bond is high lying. It is, thus, the HOMOs of alkanes match the LUMOs of the metal oxides to achieve the C–H bond oxidation. Accordingly, the H-abstraction barriers are closely related to the energy gaps of oxides, as shown in Fig. 11. For a given R–H, the calculated barriers increase from Cr to V, to Mo, and to W, in good agreement with the increased tendency of the energy gap. This finding corroborates Bell's proposal that rates of alkane oxidation can be roughly correlated with the UV–VIS absorption edge of the oxide catalysts [73].

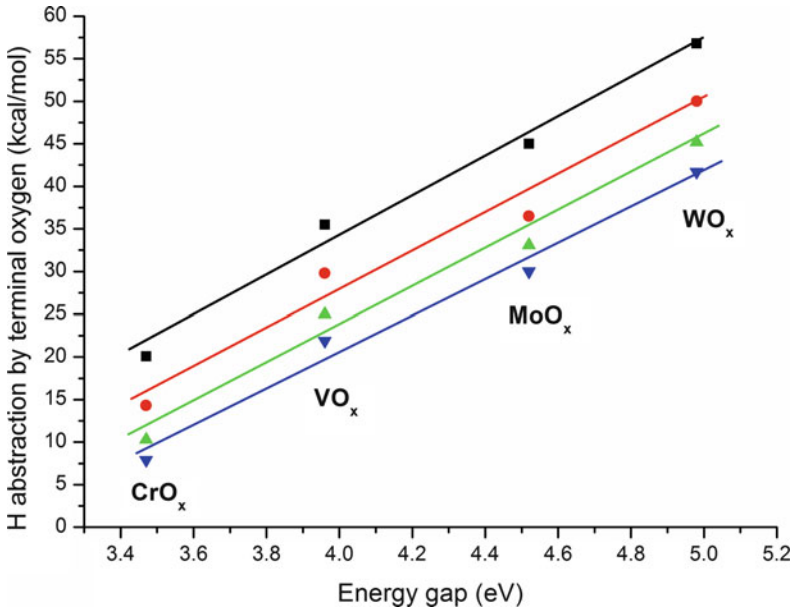

Fig. 11 Plots of the H-abstraction barrier for a given C–H bond versus the energy gap of oxides [69]

4 Catalytic Oxidation of Methane by Pt(II) Complex

4.1 Development of Pt(II) Complexes in Activation of C–H Bond

In earlier works, Garnett et al. [74] found that dissolving K_2PtCl_4 can catalyze H/D exchange in benzene and benzene derivatives. In order to obtain the functionalized products (CH_3OH or CH_3Cl), Shilov et al. [76] further introduced a catalytic system with Pt(IV) salt as oxidant, which is now named after Shilov as Shilov system. Despite the inefficiency of the process, Shilov system itself is priceless, which continuously inspires new researches in this area. In 1998, Periana et al. [27] of the then Catalytica Inc. reported a significant breakthrough in developing an effective catalyst, i.e., $PtCl_2$(bpym), for selective oxidation of CH_4 to CH_3OH. The authors suggested that the reaction involves three key steps, i.e., C–H activation, oxidation, and functionalization, as shown in Fig. 12. The Catalytica process is promising, since it has high yield at relatively low temperatures. However, it has not yet been commercialized mainly because the average reaction rate, TOF~10^{-3} s^{-1}, is below the commercially viable target of ~1 s^{-1}.

In order to provide a theoretical basis for improving these catalysts, several groups have embarked on projects to elucidate the fundamental mechanism [77–91]. Here, we provide a personal view on several key issues of this system.

4.2 Structure of a Stable Pt(II) Species in the Catalytica System

Although the Catalytica catalyst can be written conveniently as $PtCl_2$(bpym) (Fig. 12), the real catalytic form still remains unclear since the complex might undergo protonation/deprotonation or ligand substitutions in the solution. By using DFT combined with Poisson–Boltzmann continuum approximation, Kua and Xu [77] have demonstrated that the singly protonated form would be dominant under working condition, as shown in Fig. 13. Surprisingly, the structure of $PtCl_2$(bpym) hardly changes upon adding the protons, and the bpym groups in all three cases are planar when bounded to the $PtCl_2$ complex. It is suggested that the bpym group functions as a "proton sink" to facilitate the whole reaction.

Further calculations [78] revealed that in contrast to $PtCl_2(NH_3)_2$, Pt(II)–bpym bond is resistant in concentrated sulfuric acid [see (5) and (6)], even though the intrinsic Pt–N is stronger in the former than that in the latter. Indeed, if NH_3 is protonated to be NH_4^+, it loses its ability to coordinate with $PtCl_2$. On the contrary, the most stable form of free bypm in concentrated sulfuric acid is the double protonated form, which retains two uncoordinated N sites, making it apt to chelate with $PtCl_2$.

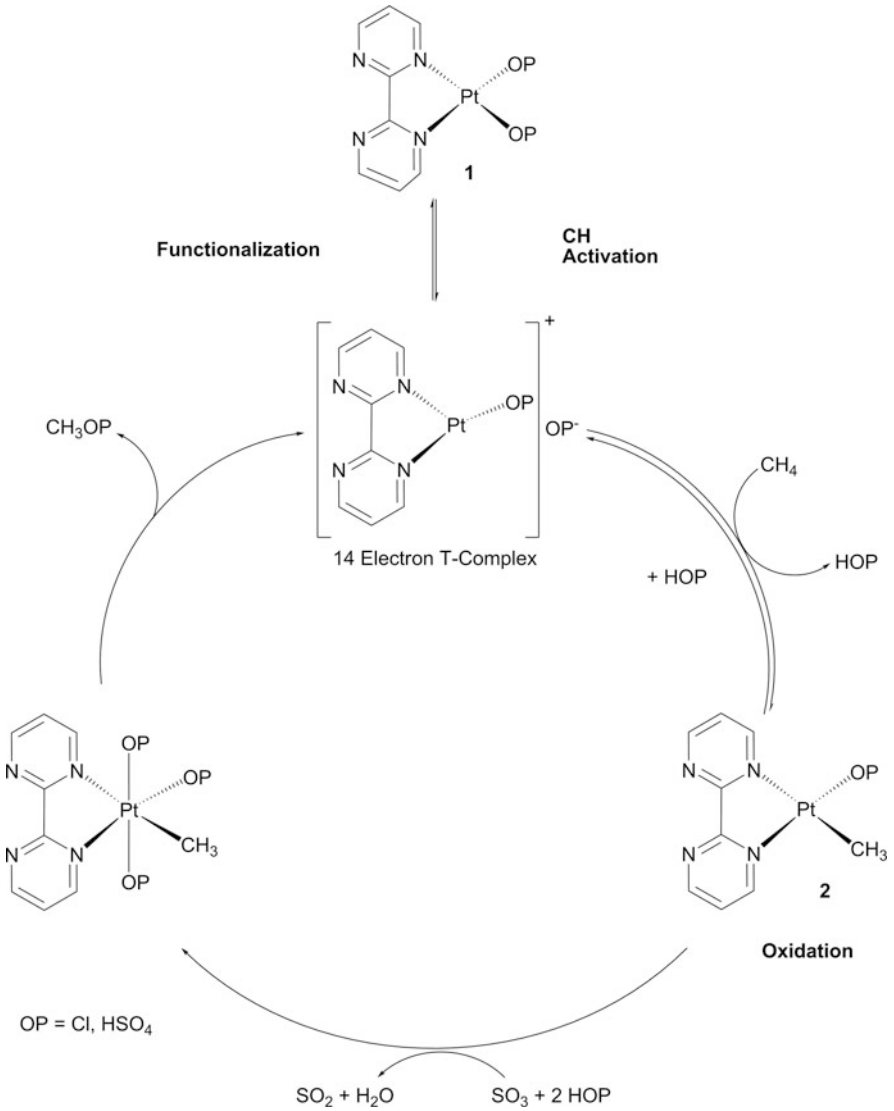

Fig. 12 Original reaction mechanism for the oxidation of methane as proposed by Periana [27]

$$PtCl_2(NH_3)_2 + 2H_2SO_4 \rightarrow \left[PtCl_2(OSO_3H)_2\right]^{2-} + 2[NH_4]^+ \qquad (5)$$

$$\Delta G_{453K} = -23.3\,\text{kcal/mol}$$

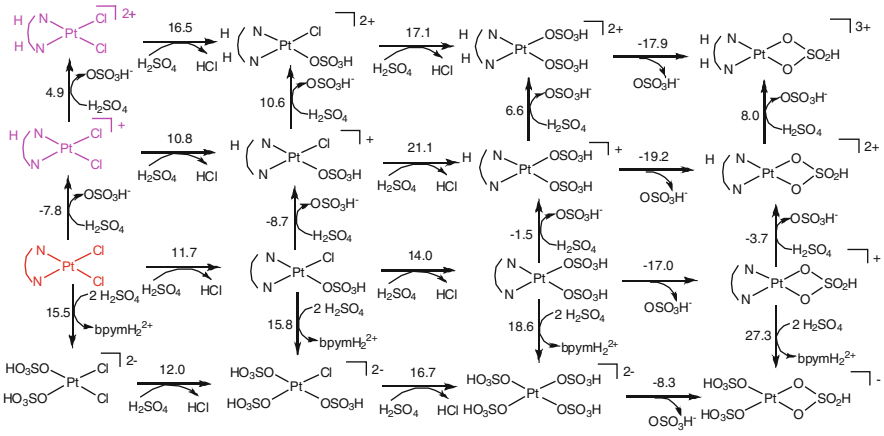

Fig. 13 Ligand exchanges in the Catalytica system. ΔG(s, 453 K) is reported [78]

$$PtCl_2(bpym) + 2H_2SO_4 \rightarrow \left[PtCl_2(OSO_3H)_2\right]^{2-} + \left[bpymH_2\right]^{2+} \qquad (6)$$

$$\Delta G_{453K} = +15.5\,\text{kcal/mol}$$

The authors also considered the possible ligand substitutions by solvent, as illustrated in Fig. 13 [78]. It was shown that replacement of the chloride ligand by bisulfate ligand is thermodynamically unfavorable. However, the concentration of sulfuric acid (the solvent) is ~10^4 times greater than that of any of the other species in solution, suggesting that there is a small but non-negligible amount of $L_2Pt(Cl)(OSO_3H)$ and $L_2Pt(\eta^2\text{-}OSO_3H)$ in solution which may act as catalyst.

As Periana originally proposed [27], the reaction begins with the coordinative unsaturated, 14-electron, T-shaped, complex (see Fig. 12). Losing one chloride or bisulfate ligand could be possible, leading to the formation of $[PtCl(bpym)]^+$ or $[Pt(OSO_3H)(bpym)]^+$, etc. DFT calculations [78] demonstrated that dissociation of the Pt–Cl bond is 22.0 kcal/mol more endothermic than that of the Pt–OSO_3H bond, indicating that OSO_3H^- is a much good leaving group than Cl^-. Hence, the roles that $L_2Pt(Cl)(OSO_3H)$ or $L_2Pt(\eta^2\text{-}OSO_3H)$ play in C–H bond oxidation cannot be overlooked. Recently, Goddard et al. [79] showed that protonation of $L_2Pt(OSO_3H)Cl^+$ would produce a sulfuric acid solvent complex $L_2Pt(OSO_3H_2)Cl^{2+}$, which is likely to coordinate methane more readily than the bisulfate complex. This is reasonable by considering that H_2SO_4 is a neutral molecule, which should be easier to depart when methane approaches.

Similarly, Ziegler et al. [80, 81] carried out DFT calculations to investigate the pure $[PtCl_4]^{2-}$ (Shilov system) and its 1:2 mixtures with $[PtX_2(H_2O)_2]$ for $X = F^-$, Cl^-, Br^-, I^-, etc. They also indicated that ligand substitution indeed takes place and the real active species is dependent not only on their equilibrium concentration but also on their reactivity toward methane. Their calculations demonstrated that in the former case, the role that $[PtCl_2(H_2O)_2]$ plays is negligible since its concentration is

extremely low, whereas in latter system, the same species is readily available and becomes an efficient catalyst when $X = F^-$, NO_2^-, and CN^-.

4.3 Stability of the bpym System

Significantly, $PtCl_2$(bpym) remains stable even after 200°C for 50 h and no insoluble $(PtCl_2)_n$ formation or decomposition to Pt metal was observed, which is in sharp contrast to that for $PtCl_2(NH_3)_2$ [27]. Xu et al. [77, 78] performed a theoretical thermodynamics analysis on such processes. Fig. 14 displays the energetics of the possible precipitation routes. Calculations showed that

$$PtCl_2(NH_3)_2 + 2H_2SO_4 \rightarrow PtCl_2 + 2[NH_4]^+ + 2[HSO_4]^- \quad (7)$$

$$\Delta G(\mathrm{s}, 453\mathrm{K}) = -24.1\ \mathrm{kcal/mol}$$

$$PtCl_2(\mathrm{bpym}) + H_2SO_4 \rightarrow PtCl_2 + [\mathrm{bpymH}]^+ + [HSO_4]^- \quad (8)$$

$$\Delta G(\mathrm{s}, 453\mathrm{K}) = 29.1\ \mathrm{kcal/mol}$$

From the viewpoint of free energies, it was clearly shown that $PtCl_2$(bpym) is not subject to the $PtCl_2$ formation, favorably retaining the bpym ligand, while $PtCl_2(NH_3)_2$ would lose its ammine ligand under severe environment, leading to the formation of $(PtCl_2)_n$ precipitation.

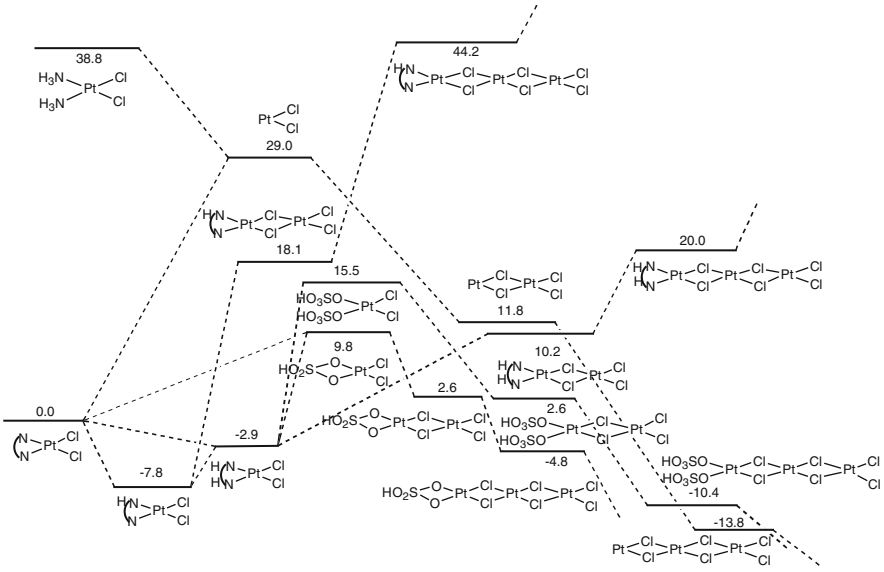

Fig. 14 Energetics, ΔG(s, 453 K) for possible precipitation routes in the Catalytica system [78]

Further calculations [78] indicated that the relative energetics for dimerization and trimerization of $[PtCl_2(bpymH_2)]^{2+}$ are unfeasible [see (9) and (10)].

$$2[PtCl_2(bpymH)]^+ \rightarrow [(bpymH)Pt_2Cl_4]^+ + [bpymH]^+ \tag{9}$$

$$\Delta G(\mathrm{s}, 453\mathrm{K}) = 25.9\,\mathrm{kcal/mol}$$

$$[(bpymH)Pt_2Cl_4]^+ + [PtCl_2(bpymH)]^+ \rightarrow [(bpymH)Pt_3Cl_6]^+ + [bpymH]^+ \tag{10}$$

$$\Delta G(\mathrm{s}, 453\,\mathrm{K}) = 26.1\,\mathrm{kcal/mol}$$

Experimentally, treatment of insoluble $(PtCl_2)_n$ with 1 equivalent of bpym (50 mM) in concentrated H_2SO_4 at 150°C leads to complete dissolution of $(PtCl_2)_n$ and formation of a homogeneous solution of $PtCl_2$(bpym) [27]. By contrast, treatment of $(PtCl_2)_n$ in hot concentrated H_2SO_4 with >100 equivalent of NH_3 does not lead to $(PtCl_2)_n$ dissolution [27]. Accordingly, DFT calculations [78] revealed that the free energy for former process is favorable, while the latter reaction is thermodynamically unfavorable [see (11) and (12)].

$$(PtCl_2)_6 + 6[bpymH_2]^{2+} \rightarrow 6[PtCl_2(bpymH_2)]^{2+} \tag{11}$$

$$\Delta G(\mathrm{s}, 453\mathrm{K}) = -1.1\,\mathrm{kcal/mol}$$

$$(PtCl_2)_6 + 12[HSO_4]^- \rightarrow 6\left[PtCl_2(OSO_3H)_2\right]^{2-} \tag{12}$$

$$\Delta G(\mathrm{s}, 453\mathrm{K}) = 109.2\,\mathrm{kcal/mol}$$

In addition, it is found experimentally that a solution of bpym (20 mM) in hot, 96% H_2SO_4 leads to the oxidative dissolution of Pt metal (in the form of Pt black) to produce a homogeneous solution of $Pt(OSO_3H)_2$(bpym) [27]. From (13), it is inferred that in the presence of bpym, metallic Pt can be dissolved in hot concentrated H_2SO_4, in full agreement with the experimental findings.

$$\begin{aligned} &Pt(0) + bpym + 4H_2SO_4 \rightarrow \\ &\quad [Pt(OSO_3H)_2(bpymH)]^+ + SO_2 + 2H_2O + [OSO_3H]^- \end{aligned} \tag{13}$$

$$\Delta G(\mathrm{s}, 453\mathrm{K}) = -108.4\,\mathrm{kcal/mol}$$

In this regard, the Catalytica catalyst behaves like a self-assembled system as it can be readily formed by mixing Pt black or indissolvable Pt salt with bypm in fumed H_2SO_4. Noteworthily, forming Pt black or Pt salt is just the formidable problem in the Wacker system [82] as well as in the Shilov system [76].

4.4 *Thermodynamics of the Diammine and bpym System in Oxidation of Methane*

It is believed that the Catalytica process involves three steps: C–H activation, oxidation, and functionalization with ligand dissociation first to form a T complex (see Fig. 12). There could be other sequence of the first two steps in a (non) dissociative way. Xu et al. [83] have examined thermodynamics of four possible reaction pathways, involving "activation-after (or -before) -oxidation" pathways, and dissociative versus associative pathways for both the diammine and the bpym systems. As depicted in Fig. 15, pathways 1 and 2 are activation-before-oxidation processes, while pathways 3 and 4 are activation-after-oxidation processes. Pathways 1 and 3 may be considered as associative pathways, where the departure of ligand Cl^- is accompanied by the coordination of CH_4, whereas pathways 2 and 4 are dissociative pathways, involving the formation of a T-complex as an intermediate [27]. The calculated reaction free energies are summarized in Table 5.

In the dry sulfuric acid solvent, it is possible that oxidation step proceeds before C–H activation. DFT calculations showed that oxidation of L_2PtCl_2 (reaction C1) is around 20 kcal/mol more endothermic than that of $L_2PtCl(CH_3)$ (reaction A2). This is reasonable as CH_3 is a better electron donor than Cl. Further calculations indicated that oxidation of $PtCl_2$(bpym) (23.4 kcal/mol) is less favorable than oxidation of $PtCl_2(NH_3)_2$ (16.8 kcal/mol), and protonation of bpym further disfavors the oxidation step. The calculations showed that C–H activation on Pt (IV) (reaction C2) is thermo-neutral (ΔG(s, 453 K) = 0.6 kcal/mol) for $L_2 = (NH_3)_2$ and mildly exothermic for the bpym ligand (−1.6 to −9.1 kcal/mol). Compared to reaction A1, this indicates that higher oxidation state of Pt is in favor of the C–H activation. Based on the thermodynamics, it was inferred that oxidation-before-activation pathway (Pathway 3: C1, C2, E1) is preferable over the

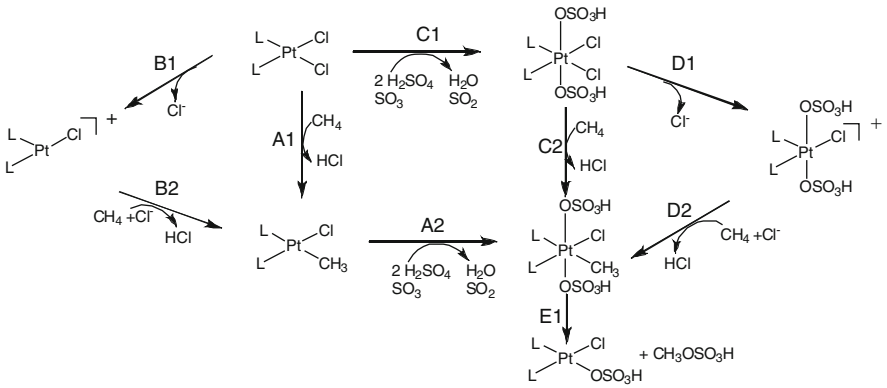

Fig. 15 Possible reaction pathways for selective oxidation of CH_4 to CH_3OH by the Catalytica catalyst [83]. Pathway 1: A1, A2, E1; Pathway 2: B1, B2, A2, E1; Pathway 3: C1, C2, E1; Pathway 4: C1, D1, D2, E1

Table 5 Reaction thermodynamics in the Catalytica system

	$(NH_3)_2$	bpym	$bpymH^+$	$bpymH_2^{2+}$
A1 (C–H activation)	25.3	24.6	21.7	18.8
A2 (Oxidation)	−8.0	−2.3	2.3	20.7
B1 (Ligand dissociation, T-complex)	9.4	21.8	25.6	35.4
B2 (C–H activation)	15.9	2.8	−3.9	−16.6
C1 (Oxidation)	16.8	23.4	33.1	44.0
C2 (C–H activation)	0.6	−1.6	−9.1	−4.5
D1 (Ligand dissociation)	29.8	35.4	40.5	53.1
D2 (C–H activation)	−29.2	−36.6	−49.7	−58.8
E1 (Functionalization)	−13.7	−18.1	−18.0	−25.4

Free energies (in kcal/mol) in sulfuric acid solution at 453 K, ΔG(s, 453 K)

oxidation-after-activation pathway (Pathway 1: A1, A2, E1) for $L_2 = (NH_3)_2$, while that pathway 1 and pathway 3 are competitive for L_2 = bpym. In addition, protonation of bpym disfavors pathway 3 but favors pathway 1.

The authors also compared the dissociative pathway with the associative pathway. For the dissociative pathways, formation of the T-complex is endothermic by 9.4 for $L_2 = (NH_3)_2$, indicating that the dissociative pathway might be preferential over the associative pathway in the diamine system. For the bpym system, calculations showed that

$$(\text{bpymH}_n{}^{n+})\text{PtCl}_2 \rightarrow [(\text{bpymH}_n{}^{n+})\text{PtCl}]^+(\text{T-complex}) + \text{Cl}^- \qquad (14)$$

$$\Delta G(\text{s}, 453\text{K}) = 21.8, 25.6, 35.4\,\text{kcal/mol for}\, n = 0, 1, 2, \text{ respectively.}$$

Thus, protonation of bpym strongly disfavors the dissociative pathways.

4.5 *Kinetics of C–H Bond Activation by bpym and the Related Systems*

Kua and Xu [77] suggested a two-step mechanism for initial CH_3–H bond activation (1) coordination of methane to form a methane complex and (2) cleavage of the C–H bond to give methyl complex. Fig. 16 displays the reaction energy profile [ΔH(0K)] in solution for $PtCl_2$(bpym). The authors did locate an intermediate **B**, in which Cl^- remains very closely associated as an ion pair. The calculations showed that the barrier for the reverse step (1) (9.9 kcal/mol) is larger than that for the forward step (2) (4.4 kcal/mol). This finding is consistent with experimental observations that reactions between D_2SO_4 and CH_4 catalyzed by $PtCl_2$(bpym) lead to multiple H–D exchange [see (15)] [27].

$$\text{CH}_4 \xrightarrow{\text{PtCl}_2(\text{bpym}),\text{D}_2\text{SO}_4} \text{CH}_3\text{D} + \text{CH}_2\text{D}_2 + \text{CHD}_3 + \text{CD}_4 \qquad (15)$$

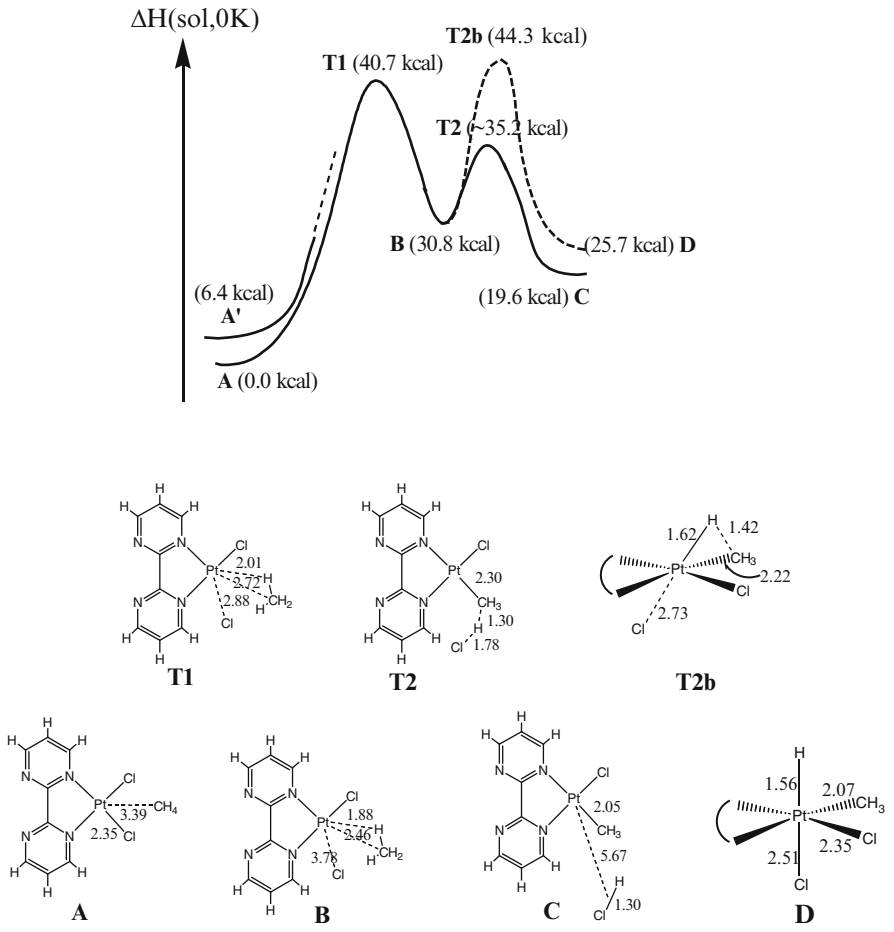

Fig. 16 C–H activation reaction energy profile of $PtCl_2$(bpym) [77]

Beginning with **B**, the C–H activation by bpym system favors electrophilic substitution (**T2**) over oxidative addition (**T2b**), distinguishing from the diamine system where oxidative addition is more favorable than electrophilic substitution. This indicated that C–H activation could involve either electrophilic substitution or oxidative addition depending upon the ligands [77]. Interestingly, activation of C–H bond by Pt(II) systems was found to be facile, whereas the most difficult step in overall reaction process is methane uptake (step (1)). Recent calculations by Zielger's group also supported this point [80, 81].

In fact, methane is the least nucleophilic (ligating) species presented in the solvent and unlikely to compete well with other more coordinating species, such as water, methanol, and bisulfate, for the metal center. Experimentally, C–H bond activation is indeed inhibited by water and/or methanol. This problem has been regarded as the "ground state stabilization" [84]. Decreasing the electrophilicity of

metal center is able to reduce the energy requirements for methane uptake; however, it usually increases barrier of the C–H bond cleavage [85, 86]. Thus, how to minimize ground state stabilization while maintaining the activity of C–H bond breaking remains a big challenge.

Very recently, Goddard's group [87] has set up a QM-RP strategy to screen the new catalyst for C–H bond activation. In this way, they postulated that replacing the neutral *N*,*N*-ligand (bpym) with a monoanionic *N*,*O*-ligand, such as Pic, would yield a complex with increased electron density at the metal center [88]. Such a complex was predicted to reduce energetics for benzene coordination compared to the *N*,*N*-ligated counterpart (5.0 vs. 14.1 kcal/mol), but retains its reactivity for C–H bond activation (16 vs. 13 kcal/mol). Thus, the whole reaction can be accelerated. Actually, H/D exchange experiment confirmed that *N*,*O*-ligated complex is 300 times more active than the *N*,*N*-ligated complex for arene C–H activation. By means of QM-RP, they also pointed out that when Ir(III) complex bears an NNC ligand, it should react with methane to form Ir(V)–CH_3 by overcoming a relative low barrier (22.1 kcal/mol) [89]. Through theoretical analysis, they also inferred that such a complex is air, protic, and thermally stable. Guided by the theoretical calculations, (NNC)Ir(III) complex was soon synthesized and showed good catalytic activity toward methane in TFA. All these representative examples demonstrate that computational chemistry can be used to solve the real problems involved in catalysis. It is expected that the close collaboration between theory and experiment can provide a much better understanding of C–H bond activation to facilitate the discovery of novel catalysts.

5 Concluding Remarks

Despite various limitations of theoretical methodologies, as well as the always-on shortage of computer power as we are dealing with more and more complex chemical problems, there is no doubt that computational chemistry has been extensively used to explore catalytic mechanisms and to understand variations in catalytic performance from one catalyst to another. We envision that this trend will certainly continue.

For the high-temperature heterogeneous oxidation, our calculations demonstrated that H-abstraction/O-rebound mechanism can account for most experimental observations from IR, EPR, KIE, UV–vis, etc. In this case, the M=O functional group behaves like an oxygen radical such that reactivity of a metal-oxo depends on the strength of the metal–oxygen π bond. Additionally, we also found that when the central metal is in low valence state or when the M=O bond processes a strong polarity, the so-called organometallic type activation (e.g., oxidative addition or 1, 2 addition) can become the alternative pathways for breaking a C–H bond. By contrast, in low-temperature homogeneous system, DFT calculations showed that the choice of ligand and solvent greatly influences the effectiveness of the catalyst. From detailed comparison between theory and experiment, it was shown that the

Catalytica catalyst, $PtCl_2$(bpym), would not lose its bpym ligand under harsh condition, which accounts for its good stability. Further calculations revealed that methane uptake is the rate-determining step, rather than the breaking of the C–H bond. These findings have stimulated intensive interest on the mechanism-directed and structure-directed catalyst design at the molecular level.

Even though we have focused here on the mechanistic aspects of the catalytic C–H bond activation, we have to admit that it is still a big challenge to develop more sophisticated electronic structure theory, favorably DFT methods in terms of cost effectiveness, to meet chemical accuracy (1 kcal/mol) for catalytic system. Most of the computational results discussed here were obtained with a well-established functional, B3LYP [91–95]. However, there are now well-documented drawbacks for this functional [96], namely, B3LYP (1) degrades as the system becomes larger, (2) underestimates reaction barrier heights, (3) yields too low bond dissociation enthalpies, (4) gives improper isomer energy differences, (5) fails to bind van der Waals systems, etc. It would be worthwhile to design a systematic correction scheme on top of B3LYP [97–107] such that all B3LYP data, already and continuously built-up in the literature, can be used with higher accuracy and thus higher reliability at no extra cost compared to B3LYP. Certainly, the quest for new density functional continues [108–118]. The new functional should maintain the advantage of B3LYP, while surmount its known difficulties, leading to a general functional with more predictive power. It can be anticipated that these new advances combined with more reasonable QM/MM scheme [119] would help to unravel the complicated problems in organometallics catalysis in general, and in selective alkane oxidation as a particular example.

References

1. Wilhelm DJ, Simbeck DR, Karp AD, Dickenson RL (2001) Fuel Proc Tech 71:139
2. Vosloo AC (2001) Fuel Proc Tech 71:149
3. Crabtree RH (2001) J Chem Soc Dalton Trans 17:2437
4. Arakawa H, Aresta M, Armor JN (2001) Chem Rev 101:953
5. Labinger JA, Bercaw JE (2002) Nature 417:507
6. Fokin AA, Schreiner PR (2002) Chem Rev 102:1551
7. Vision 2020 Catalysis Report, 1997
8. Casey CP (2004) 5th International Conference on Chemistry and Chemical Engineering, Cuba, 2004
9. Crabtree RH (2010) Chem Rev 110:575
10. Boutadla Y, Davies DL, Macgregor SA, Poblador-Bahamonde AI (2009) J Chem Soc Dalton Trans 30:5820
11. Shilov AE, Shul'pin GB (1997) Chem Rev 97:2879
12. Stahl SS, Labinger JA, Bercaw JE (1998) Angew Chem Int Ed 37:2180
13. Periana RA, Bhalla G, Tenn WJ III, Young KJH, Liu XY, Mironov O, Jones CJ, Ziatdinov VR (2004) J Mol Catal A Chem 220:7
14. Labinger JA (2004) J Mol Catal A Chem 220:27
15. Bergman RG (2007) Nature 446:391
16. Copéret C (2010) Chem Rev 110:656

17. Balcells D, Clot E, Eisenstein O (2010) Chem Rev 110:749
18. Webster CE, Fan Y, Hall MB, Kunz D, Hartwig JF (2003) J Am Chem Soc 125:858
19. Lam WH, Lin Z (2003) Organometallics 22:473
20. Oxgaard J, Muller RP, Goddard WA III, Periana RA (2004) J Am Chem Soc 126:352
21. Perutz RN, Sabo-Etienne S (2007) Angew Chem Int Ed 46:2578
22. Lin Z (2007) Coord Chem Rev 251:2280
23. Vastine BA, Hall MB (2009) Coord Chem Rev 253:1202
24. Grasselli RK, Burrington JD, Buttrey DJ (2003) Top Catal 23:5
25. Gol'dshleger NF, Tyabin MB, Shilov AE, Shteinman AA (1969) Zh Fiz Khim 43:2174
26. Gol'dshleger NF, Tyabin MB, Shilov AE, Shteinman AA (1969) Russ J Phys Chem 43:1222 (english translation)
27. Periana RA, Taube DJ, Gamble S, Taube H, Satoh T, Fujii H (1998) Science 280:560
28. Periana RA (1993) Science 259:340
29. Jones CJ, Taube D, Ziatdinov VR, Periana RA, Nielsen RJ, Oxgaard J, Goddard WA III (2004) Angew Chem Int Ed 43:4626
30. Periana RA, Mironov O, Taube D, Bhalla G, Jones CJ (2003) Science 301:814
31. Waters T, O'Hair RAJ, Wedd AG (2003) J Am Chem Soc 125:3384
32. Fialko EF, Kikhtenko AV, Goncharov VB (1998) Organomettalics 17:25
33. Schroder D, Schwarz H (1995) Angew Chem Int Ed Engl 34:1973
34. Xie S, Chen K, Bell AT, Iglesia E (2000) J Phys Chem B 104:10059
35. Yang W, Wang X, Guo Q, Zhang Q, Wang Y (2003) New J Chem 27:1301
36. Hill CL, Prosser-McCartha CM (1995) Coord Chem Rev 143:407
37. Mayer JM (1998) Acc Chem Res 31:441 and references therein
38. Limberg C (2003) Angew Chem Int Ed Engl 42:5932 and references therein
39. Ortiz de Montellano PR (2010) Chem Rev 110:932
40. Xu YD, Bao XH, Lin LW (2003) J Catal 216:386
41. Xu Y, Lin L (1999) Appl Catal A 188:53
42. Shu J, Adnot A, Grandjean PA (1999) Ind Eng Chem Res 38:3860
43. Xu X, Faglioni F, Goddard WA III (2002) J Phys Chem A 106:7171
44. Gesser HD, Hunter NR, Prakash CB (1985) Chem Rev 85:235
45. Tabata K, Teng Y, Takemoto T, Suzuki E, Banares MA, Pena MA, Fierro JLG (2002) Catal Rev 44:1
46. Haber J (1997) Stud Surf Sci Catal 110:1
47. Fu G, Xu X, Lu X, Wan HL (2005) J Am Chem Soc 127:3989
48. Fu G, Xu X, Wan HL (2006) Catal Today 117:133
49. Busca G, Finocchio E, Lorenzelli V (1999) Catal Today 49:453
50. Kuba S, Heydorn PC, Grasselli RK (2001) Phys Chem Chem Phys 3:146
51. Zhen KJ, Khan MM, Mak CJ, Lewis KB, Somorjai GA (1985) J Catal 94:501
52. Spencer ND, Pereira CJ (1987) AIChE J 33:1808
53. Spencer ND, Pereira CJ, Grasselli RK (1990) J Catal 126:546
54. Sojka Z, Che M (1995) J Phys Chem 99:5418
55. Zhou D, Zhang Y, Zhu H, Ma D, Wang Y, Liu X, Bao X (2007) J Phys Chem C 111:2081
56. Sauer J, Schwarz H (2006) Angew Chem Int Ed 45:4681
57. Cheng MJ, Chenoweth K, Oxgaard J, van Duin A, Goddard WA (2007) J Phys Chem C 111:5115
58. Kung HH (1994) Adv Catal 40:1
59. Cavani F, Trifirò F (1995) Catal Today 24:307
60. Albonetti S, Cavani F, Trifirò F (1996) Catal Rev Sci Eng 38:413
61. Chen KD, Bell AT, Iglesia E (2000) J Phys Chem B 104:1292
62. Chen KD, Iglesia E, Bell AT (2001) J Phys Chem B 105:646
63. Fu G, Xu X, Lu X, Wan HL (2005) J Phys Chem B 109:6416
64. Fu G, Yi X, Huang C, Xu X, Weng W, Xia W, Wan HL (2007) Surf Rev Lett 14:645

65. Redfern PC, Zapol P, Sternberg M, Adiga SP, Zygmunt SA, Curtiss LA (2006) J Phys Chem B 110:8363
66. Rozanska X, Fortrie R, Sauer J (2007) J Phys Chem C 111:6041
67. Fu H, Liu Z, Wang W, Fan K (2006) J Am Chem Soc 129:11114
68. Mars P, van Krevelen DW (1954) Chem Eng Sci Suppl 3:3
69. Fu G, Chen ZN, Xu X, Wan HL (2008) J Phys Chem A 112:717
70. Siegbahn PEM, Blomberg MRA, Crabtree RH (1997) Theor Chem Acc 97:289
71. Grasselli RK (2002) Top Catal 21:79
72. Grzybowska-Świerkosz B (2002) Top Catal 21:35
73. Chen K, Xie S, Bell AT, Iglesia E (2000) J Catal 195:244
74. Mayer JM (2004) Annu Rev Phys Chem 55:363
75. Cukier RI, Nocera DG (1998) Annu Rev Phys Chem 49:337
76. Shilov AE (1984) Activation of saturated hydrocarbons by transition metal complexes. Reidel, Dordrecht, The Netherlands
77. Kua J, Xu X, Periana RA, Goddard WA III (2002) Organometallics 21:511
78. Xu X, Kua J, Periana RA, Goddard WA III (2003) Organometallics 22:2057
79. Ahlquist M, Periana RA, Goddard III WA (2009) Chem Commun 2373
80. Zhu H, Ziegler T (2006) J Organomet Chem 691:4486
81. Zhu H, Ziegler T (2007) Organometallics 26:2277
82. Henry PM (1980) Palladium catalyzed oxidation of hydrocarbons. Reidel, Dordrecht, Netherlands
83. Xu X, Fu G, Goddard WA III, Periana RA (2004) Stud Surf Sci Catal 147:499
84. Conley BL, Tenn WJ III, Young KJH, Ganesh SK, Meier SK, Ziatdinov VR, Mironov O, Oxgaard J, Gonzales J, Goddard WA III, Periana RA (2006) J Mol Catal A Chem 251:8
85. Zhu H, Ziegler T (2008) Organometallics 27:1743
86. Zhu H, Ziegler T (2009) Organometallics 28:2773
87. Muller RP, Philipp DM, Goddard WA III (2003) Top Catal 23:81
88. Ziatdinov VR, Oxgaard J, Mironov OA, Young KJH, Goddard WA III, Periana RA (2006) J Am Chem Soc 128:7404
89. Young KJH, Oxgaard J, Ess DH, Meier SK, Stewart T, Goddard III WA, Periana RA (2009) Chem Commun 3270
90. Mylvaganam K, Bacskay GB, Hush NS (2000) J Am Chem Soc 122:2041
91. Mylvaganam K, Bacskay GB, Hush NS (1999) J Am Chem Soc 121:4633
92. Becke AD (1988) Phys Rev A 38:3098
93. Lee CT, Yang WT, Parr RG (1988) Phys Rev B 37:785
94. Becke AD (1993) J Chem Phys 98:5648
95. Stephens PJ, Devlin FJ, Chabalowski CF, Frisch MJ (1994) J Phys Chem 98:11623
96. Zhang IY, Wu JM, Xu X (2010) Chem Commun 3057 and references therein
97. Wu JM, Xu X (2007) J Chem Phys 127:214105
98. Wu JM, Xu X (2008) J Chem Phys 129:164103
99. Wu JM, Xu X (2009) J Comp Chem 30:1424
100. Wu JM, Zhang YI, Xu X (2010) Chem Phys Chem 11:2561
101. Delley B (2006) J Phys Chem A110:13632
102. Tirado-Rives J, Jorgensen WL (2008) J Chem Theory Comput 4:297
103. Winget P, Clark T (2004) J Comput Chem 25:725
104. Cioslowski J, Liu G, Piskorz P (1998) J Phys Chem A 102:9890
105. Friesner RA, Knoll EH, Cao Y (2006) J Chem Phys 125:124107
106. Duan XM, Song GL, Li ZH, Wang XJ, Chen GH, Fan KN (2004) J Chem Phys 121:7086
107. Hu L, Wang X, Wong L, Chen GH (2003) J Chem Phys 119:11501
108. Perdew JP, Burke K, Ernzerhof M (1996) Phys Rev Lett 77:3865
109. Adamo C, Barone V (1999) J Chem Phys 110:6158
110. Tao JM, Perdew JP, Staroverov VN, Scuseria GE (2003) Phys Rev Lett 91:146401
111. Zhao Y, Truhlar DG (2008) Theor Chem Acc 120:215

112. Mori-Sanchez P, Cohen AJ, Yang WT (2006) J Chem Phys 124:0911021
113. Grimme S (2006) J Chem Phys 124:034108
114. Xu X, Goddard WA III (2004) Proc Natl Acad Sci USA 101:2673
115. Xu X, Goddard WA III (2004) J Chem Phys 121:4068
116. Zhang Y, Xu X, Goddard WA III (2009) Proc Natl Acad Sci USA 106:4963
117. Zhang YI, Luo Y, Xu X (2010) J Chem Phys 132:194105
118. Zhang YI, Luo Y, Xu X (2010) J Chem Phys 133:104105
119. Guo WP, Wu AA, Xu X (2010) Chem Phys Lett 498:203

Computational Studies on Osmium-Catalyzed Olefin Oxidation Reactions

Dominik Munz, Alexander Poethig, and Thomas Strassner

Abstract The oxidative functionalization of olefins is an important reaction for organic synthesis as well as for the industrial production of bulk chemicals. Various processes have been explored, among them also metal-catalyzed methods using strong oxidants like osmium tetroxide. Especially, the asymmetric dihydroxylation of olefins by osmium(VIII) complexes has proven to be a valuable reaction for the synthetic chemist. A large number of experimental studies had been conducted, but the mechanisms of the various osmium-catalyzed reactions remained a controversial issue. This changed when density functional theory calculations became available and computational studies helped to unravel the open mechanistic questions. This mini review will focus on recent mechanistic studies on osmium-mediated oxidation reactions of alkenes.

Abbreviations

AH	Aminohydroxylation
B3LYP	Becke's three-parameter hybrid functional
CLB	*para*-Chlorobenzoyl-
DFT	Density functional theory
DH	Dihydroxylation
DHQ	Dihydroquinine
EHT	Extended Hueckel theory
HF	Hartree–Fock
KIE	Kinetic isotope effect
MEQ	9-*O*-(4′-methyl-2′-quinolyl)-

D. Munz • A. Poethig • T. Strassner (✉)
Technische Universität Dresden, Physikalische Organische Chemie, Bergstrasse 66, 01069 Dresden, Germany
e-mail: thomas.strassner@chemie.tu-dresden.de

O. Wiest and Y. Wu (eds.), *Computational Organometallic Chemistry*,
DOI 10.1007/978-3-642-25258-7_6,

NM	*N*-Methylmorpholine
NMO	*N*-Methylmorpholine-*N*-oxide
PES	Potential energy surface
PHAL	Phthalazine
PHN	9-*O*-(9′-phenanthryl)-
^{p}Tol	*para*-Tolyl-
Q2MM	Quantum mechanical guided molecular mechanics
QCISD(T)	Quadratic configuration interaction
QM	Quantum mechanics
QM/MM	Quantum mechanics/molecular mechanics
tert-Bu	*tert*-Butyl-
THF	Tetrahydrofuran
TON	Turnover number

1 Introduction

The oxidative functionalization of olefins mediated by transition metal oxides leads to a variety of products including epoxides, 1,2-diols, 1,2-aminoalcohols, and 1,2-diamines [1]. Also the formation of tetrahydrofurans (THF) from 1,5-dienes has been observed, and enantioselective versions of the different reactions have been developed. Although a lot of experimental data has been available, the reaction mechanisms have been a subject of controversial discussion. Especially, osmium (VIII) complexes play an important role there, as the proposal of a stepwise mechanism [2] for the dihydroxylation (DH) of olefins by osmium tetroxide (OsO_4) had started an intense discussion about the mechanism [2–11].

Generally the reaction can be found in the textbooks as shown in Scheme 1.

The dihydroxylation of olefins with osmium compounds had first been reported by Philipps [12] in 1894, and the rate acceleration effect of pyridine was described by Criegee [3] in the 1930s.

The disadvantage of using stoichiometric amounts of the expensive OsO_4 was overcome by the addition of a co-oxidant, which reoxidizes the Os(VI) *in situ*. Several reagents such as hydrogen peroxide, periodate, hexacyanoferrat(III), and also molecular oxygen [13–17] have been used to reoxidize the metal-oxo compounds and to establish catalytic versions of the reactions with high TONs.

In the case of prochiral alkenes, the dihydroxylation reaction creates new chiral centers in the products and the development of the asymmetric version of the

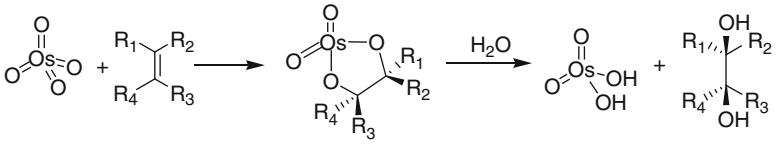

Scheme 1 Dihydroxylation reaction

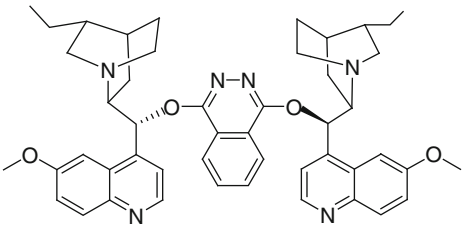

Fig. 1 Cinchona-base $(DHQ)_2PHAL$

reaction by Sharpless was one of his very important accomplishments. He received the Nobel Prize in Chemistry 2001 for the development of catalytic oxidation reactions of alkenes.

Sharpless recognized that the chirality of bases is transferred to the substrates which allowed the development of the asymmetric version of the reaction. The cinchona amines (Fig. 1) are a prominent class of ligands, which have shown to give high enantiomeric excess and are also part of the commercially available AD mix (0.4% $K_2OsO_2(OH)_4$, 1.0% $(DHQ)_2PHAL$, 300% $[K_3Fe(CN)_6]$, and 300% K_2CO_3).

He also pioneered the osmium-catalyzed vicinal aminohydroxylation reaction (AH), where imido osmium complexes react with olefins to form β-aminoalcohols [18]. Closely related to the DH and AH reactions is the amination of olefins leading to vicinal diamines, which was explored by Sharpless [19, 20] and Muniz [21, 22].

Attempts to tetrafunctionalize 1,5-dienes were the key toward the discovery of the stereoselective formation of THF derivatives, which are constituents of many natural products (Scheme 2) [25–30].

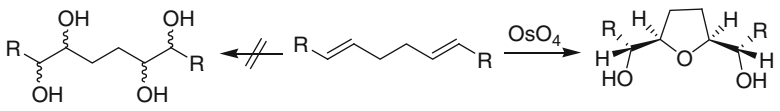

Scheme 2 Osmium-catalyzed formation of tetrahydrofuran diols [23, 24]

2 Osmium-Catalyzed Dihydroxylation

2.1 Introduction

The reaction mechanism of the osmium-catalyzed dihydroxylation was intensely discussed. Böseken [31] proposed already in 1922 that the reaction proceeds via a thermally allowed concerted (3+2) cycloaddition reaction, while Sharpless suggested the formation of a metallaoxetane intermediate via a reversible (2+2) cycloaddition, followed by irreversible reductive insertion of the Os–C bond into an Os=O bond leading to the monoglycolate ester [2] (Scheme 3).

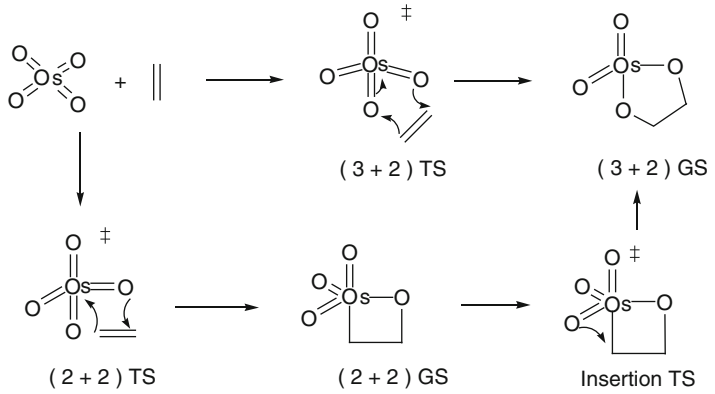

Scheme 3 (3+2) vs. stepwise (2+2) reaction

The influence of the reaction temperature on the enantioselectivity using chiral bases and prochiral alkenes was studied and revealed a nonlinearity of the modified Eyring plot [7]. The observed change in the linearity and the existence of an inversion point indicated that two different transition states should be involved, inconsistent with a concerted (3+2) mechanism. Sharpless, therefore, renewed the postulate of a reversibly formed oxetane intermediate, followed by an irreversible rearrangement to the product.

2.2 Mechanism

This mechanistic question is one of the examples of the success of density functional theory (DFT) methods for metal-organic chemistry. Earlier work on the reaction mechanism could not discriminate between the two alternatives. Analysis of the different orbitals based on Extended Hueckel theory (EHT) calculations led to the conclusion that the (3+2) pathway is more likely, but the authors could not exclude the possibility of a (2+2) pathway [4] similar to the results of HF calculations in combination with Quadratic configuration interaction (QCISD(T)) single points [32].

Attempts to use RuO_4 as a model for osmium tetroxide indicated that the formation of an oxetane is less favorable compared to the (3+2) pathway, but still possible [33, 34]. When DFT methods became available, within a short period of time, four different groups published DFT results on the reaction using different quantum chemical packages and different levels of theory [35–38].

These studies could show that the barrier for the (2+2) addition of OsO_4 to ethylene and the ring expansion are significantly higher in energy (~35 kcal/mol) than the activation energy for the (3+2) pathway. But although the available computational power had steadily increased during that time, it was still not feasible

to evaluate a potential energy surface for complexes with bases of this size. Therefore, NH_3 was used as a model in the QM studies (Table 1).

Kinetic isotope effects (KIE) for the DH of *tert*-butyl ethylene were determined using the NMR method of Singleton [39], which provided additional confirmation combining experiment and theory. The agreement between the KIE and the theoretically predicted values, based on the transition state geometries, was excellent and showed that indeed only the (3+2) pathway is feasible [36].

Although the observed energy differences between the two different pathways are large and the differences between the calculations with and without the base are small, there still have been attempts to include the mainly steric effects of the large cinchona base by QM/MM studies [40–43] and molecular dynamics calculations [44], combining the advantages of the QM treatment with the possibility of treating a large number of atoms [45].

The origin of the experimentally observed enantioselectivity in the dihydroxylation of styrene was investigated and it was found that π-interactions between the aromatic rings of ligand and reactant are responsible for the observed enantioselectivity. By parametrization of a Macromodel force field for the reaction, Norrby [42] was able to reproduce (ee_{calc}) the experimentally observed enantioselectivities (ee_{exp}). Some examples are shown in Table 2.

Table 1 Base-catalyzed dihydroxylation reaction

	(3+2) TS	(3+2) GS	(2+2) TS	(2+2) GS
Frenking [35]	+4.4	−39.8	+44.3	+5.1
Houk and Strassner [36]	+3.2	−42.0	+44.1	+5.4
Morokuma [37]	+1.4	−23.5	+50.4	+13.1
Ziegler [38]	+0.8	−28.4	+39.1	+3.6

Table 2 Calculated and experimental enantioselectivities in the AD (adapted from [42])

Alkene	DHQD Ligand	ee_{calc} (%)	ee_{exp} (%)	Ref.
1-Phenyl-cyclohexene	CLB	91	91	[46]
Styrene	CLB	70	74	[46]
β,β-Dimethyl styrene	CLB	72	74	[46]
β-Vinyl naphthalene	CLB	94	88	[46]
trans-Stilbene	CLB	98	99	[46]
tert-Butyl ethene	CLB	70	44	[46]
α-Methyl styrene	CLB	65	62	[42]
cis-β-Methyl styrene	CLB	78	35	[42]
Styrene	MEQ	94	87	[46]
Styrene	PHN	98	78	[46]
tert-Butyl ethene	PHN	89	79	[46]
β-Vinyl naphthalene	PHAL	100	98	[47]
Styrene	PHAL	97	97	[48]
α-Methyl styrene	PHAL	99	94	[48]
trans-Stilbene	PHAL	100	100	[48]

A thorough discussion of computational methods (including QM, MM, Q2MM, QM/MM, molecular dynamics, and genetic algorithms) applied to study the enantioselectivity of the DH has been published elsewhere by Maseras [49].

3 The Oxidative Cyclization of 1,5-Dienes

3.1 Introduction

In 1965, Klein and Rojahn [50] tried to dihydroxylate 1,5-dienes using permanganate in order to synthesize tetroles. Instead, they observed the diastereoselective formation of THF diols due to an intramolecular cyclization of the intermediate manganese(V) ester. Depending on the configuration of the diene, the THF diols are formed with *cis*-selectivity (Scheme 4).

It was later found that this transformation can be also carried out using other transition metal-oxo compounds like ruthenium-oxo species [51] and osmium tetroxide [23, 24], which has been reviewed by Piccialli in 2007 [52].

The resulting motif of *cis*-configurated THF diols can be found in a remarkable number of natural products of different classes, e.g., annonaceous acetogenins such as *cis*-sylvaticin or membrarollin, polyether antibiotics such as monensin A, and squalene-derived metabolites such as glabrescol (Fig. 2) [25–30].

After the initial observation by Klein and Rojahn, the permanganate-promoted reaction was studied intensively by several groups, which led to miscellaneous suggestions for the mechanism [53–55]. There is a general agreement on the first reaction step being a (3+2) cycloaddition [56, 57]. Experiments with ^{18}O-labeled water [53] as well as previous results of our group, investigating the mechanism of this transformation by DFT studies [58], support the suggestion of the addition of water prior to the cyclization. We carefully evaluated the potential energy surfaces (PES) for all possible spin multiplicities (singlet, triplet, and quintet), which showed a multistate reactivity for manganese, leading to a high-spin product.

Donohoe [23] and Piccialli [24] were able to perform analogous transformations using osmium tetroxide. Even an enantioselective version was established by Donohoe who first introduced a defined stereochemistry by an asymmetric dihydroxylation followed by workup and isolation of the diol, which was then treated with another equivalent of OsO_4 [59].

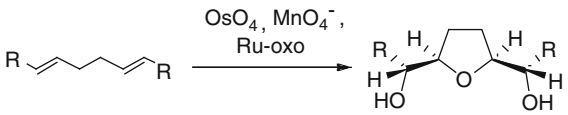

Scheme 4 Transformation of 1,5-dienes to tetrahydrofuran diols by different transition metal-oxo compounds

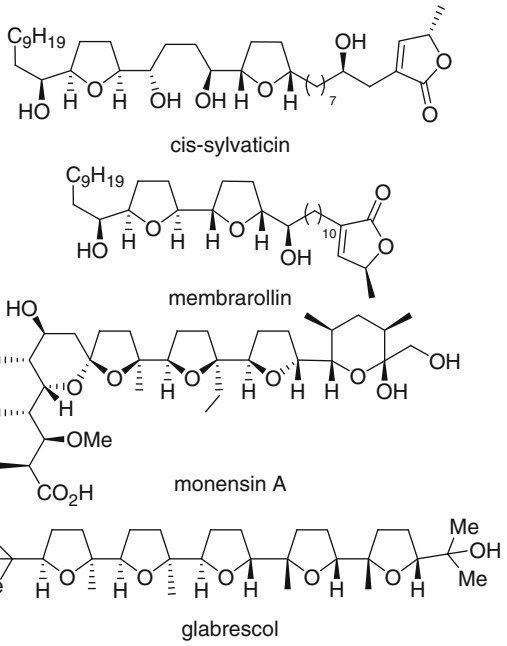

Fig. 2 Examples for natural products with tetrahydrofuran motif

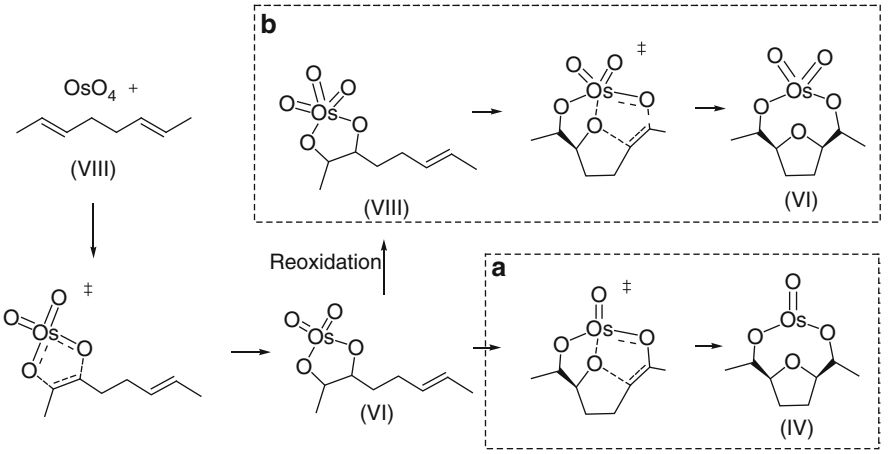

Scheme 5 Osmium-catalyzed cyclization: Possible reaction pathways with (b) or without reoxidation (a) of the intermediate Os(VI)

3.2 Pathways

For the oxidative cyclization with OsO_4, an analogous reaction pathway could be suggested (Scheme 5). Based on previous results on the mechanism of the dihydroxylation (DH), the first reaction step again could be expected to be a (3+2)

cycloaddition leading to an osmium(VI) ester. The (2+2) reaction pathway was ruled out based on thorough mechanistic investigations by DFT calculations for osmium tetroxide [37, 38, 60–62].

Since the osmium reaction is conducted catalytically, there are more possibilities for the nature of the oxidizing metal-oxo species which have to be considered. One possible reaction is the formation of an osmium(IV) ester, followed by reoxidation to Os(VIII) (Scheme 5a).

Another pathway is the reoxidation of the intermediate osmium(VI) to an Os (VIII) species prior to the cyclization step (Scheme 5b). Hence, the oxidation state of osmium would just change between (VIII) and (VI), which has been observed before for double bond oxidations using osmium [63]. We also needed to consider the addition of a water molecule, as it is known from the so-called ligand accelerating effect that osmium tetroxide can add ligands to its coordination sphere [64].

As we previously did for permanganate, we investigated the reaction mechanism for the different possible PES, wondering whether osmium tetroxide shows a similar behavior. We also calculated a possible addition of water as well as the intermediate reoxidation [65].

3.3 Computational Results

The calculations were performed with GAUSSIAN-03 [66], using the density functional/Hartree–Fock (HF) hybrid model Becke3LYP [67–70] and the split valence triple-ζ (TZ) basis set 6-311+G(d) [71–78]. For Os, a Hay–Wadt VDZ (n+1) ECP was used [79]. The results shown are for the different PES, which are the singlet (s), the triplet (t), and the quintet PES (q). The calculated structures are denominated by numbers, and additions **s**, **t**, and **q** refer to the corresponding PES. The structures resulting from the addition of a water molecule are described by the superscript "water," and those of oxidation by NMO by the superscript "ox." Approximate free energies (ΔG) and enthalpies (ΔH) were obtained through thermochemical analysis of frequency calculations, using the thermal correction to Gibbs free energy, as reported by GAUSSIAN-03.

The simplest mechanism possible for the oxidation of octa-2,6-diene **1** with OsO_4 (**2**) was first examined on the singlet PES, as shown in Fig. 3. The exergonic step of the reaction ($\Delta G = -22.8$ kcal/mol) on the singlet surface, leading to the osmium(VI) ester **4s** via the transition state **3**, has an activation barrier of 15.9 kcal/mol (Table 1). The following reaction step (**4s** → **6s**), also a (3+2) cycloaddition, has an activation barrier of 25.7 kcal/mol and proceeds through transition state **5s** ($\Delta G = 2.9$ kcal/mol). This almost thermoneutral cyclization step finally leads to the resulting product **6s**, which is only 1 kcal/mol lower in energy than **4s**.

Starting from intermediate **4**, different PES with singlet (**4s**) and triplet (**4t**) multiplicity become accessible. The osmium(VI) ester **4t** was calculated to be significantly higher in energy (21.2 kcal/mol) than the corresponding intermediate **4s**. This rules out a possible change in the PES as found in the case of permanganate [58].

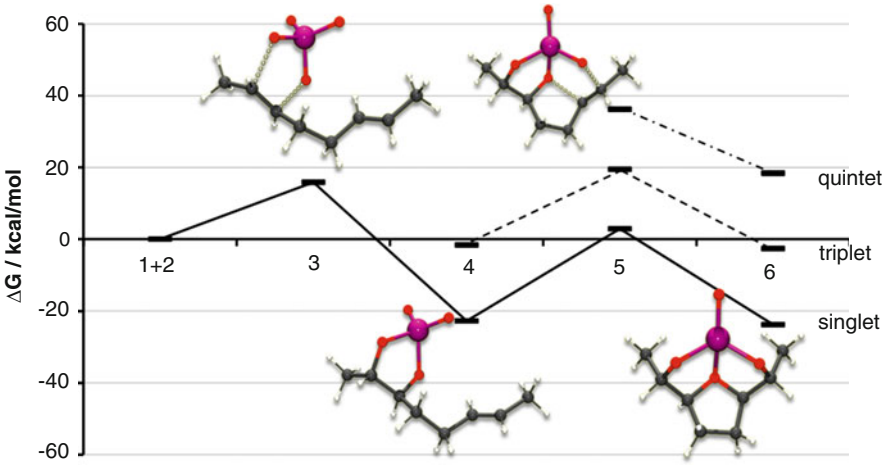

Fig. 3 Reaction pathway Os(VIII) → Os(VI) → Os(IV) for the given PES, relative to octadiene and OsO_4

For osmium, we also found the transition states as well as the products with higher multiplicities to be significantly higher in energy compared to those on the singlet PES. With $\Delta G = 19.5$ kcal/mol (**5t**) and $\Delta G = 36.2$ kcal/mol (**5q**), the transition state on the triplet PES is 16.6 kcal/mol and on the quintet PES is 33.3 kcal/mol higher in energy compared to **5s**. The results for products **6** differ about 21 kcal/mol for the different hypersurfaces (**6s**: $\Delta G = -23.8$ kcal/mol; **6t**: $\Delta G = -2.6$ kcal/mol; **6q**: $\Delta G = 18.4$ kcal/mol).

3.3.1 Addition of Water

The addition of a water molecule to the osmium intermediates **4** did not lead to a comparable stabilization in energy like in the case of permanganate (Fig. 4). The overall reaction becomes endergonic, although the intermediate $\mathbf{4s}^{\mathbf{water}}$, formed by the addition of the water molecule to **4s**, is 4.2 kcal/mol lower in energy. The slightly exergonic reaction step (**4s** → **6s**) would be changed into an endergonic step ($\mathbf{4s}^{\mathbf{water}} \rightarrow \mathbf{6s}^{\mathbf{water}}$) with an activation barrier of 30.5 kcal/mol (Fig. 4: $\mathbf{4s}^{\mathbf{water}}$, $\mathbf{5s}^{\mathbf{water}}$, $\mathbf{6s}^{\mathbf{water}}$). This is a significant difference to the permanganate promoted reaction, where the addition of a water molecule after the cycloaddition to the first double bond lowered the activation barriers as well as the absolute Gibbs free energies for the product complexes on the PES for every multiplicity, but to a greater extent for the higher multiplicities [58]. This is not true for the osmium-catalyzed reaction, for which the free energies of the higher multiplicities are always higher compared to the singlet surface and consequently do not play a role in the reaction mechanism (Fig. 4). Therefore, we can rule out a similar addition of water to the osmium(VI) species.

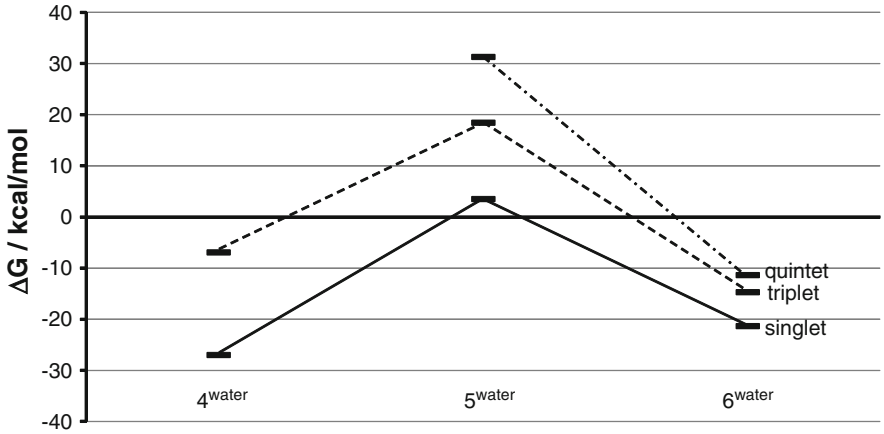

Fig. 4 Cyclization step after addition of a water molecule for the given PES. Energies are referenced to the individual starting materials

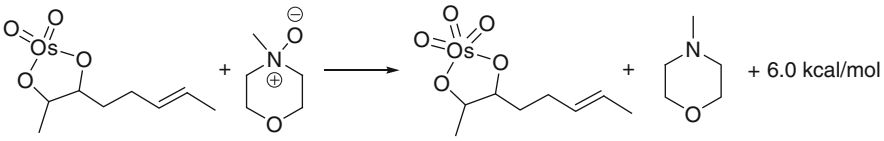

4s **4s^{ox}**

Scheme 6 Reoxidation of the intermediate Os(VI) ester **4s** to the Os(VIII) ester **4s^{ox}**

3.3.2 Reoxidation

Due to the catalytic nature of this reaction, new reaction pathways become accessible. Therefore, the reoxidation of the intermediate osmium(VI) ester **4s** to the osmium(VIII) ester **4s^{ox}** using, e.g., *N*-methylmorpholine-*N*-oxide (NMO) as a co-oxidant was calculated using the lowest energy conformations of NMO and *N*-methylmorpholine (NM) (Scheme 6).

Besides this slightly exergonic oxidation, also the following cyclization step, starting from the reoxidized Os(VIII) intermediate **4s^{ox}** (Scheme 5, pathway B), was found to be energetically favored compared to starting from the osmium(VI) species **4s** (Fig. 5).

The activation barrier of the cyclization step (**4s^{ox}** → **6s^{ox}**) is reduced to 13.1 kcal/mol compared to the 25.7 kcal/mol without reoxidation (**4s** → **6s**). Furthermore, the product-forming transition state **5s^{ox}** with $\Delta G = -15.6$ kcal/mol is 18.5 kcal/mol lower in energy than the corresponding transition state **5s** (Scheme 5, pathway A) without reoxidation. The product **6s^{ox}** even shows a larger stabilization of 30.8 kcal/mol compared to its corresponding Os(IV) compound **6s**. Due to the additional oxygen atom at **6s^{ox}**, the oxygen atoms form only a slightly

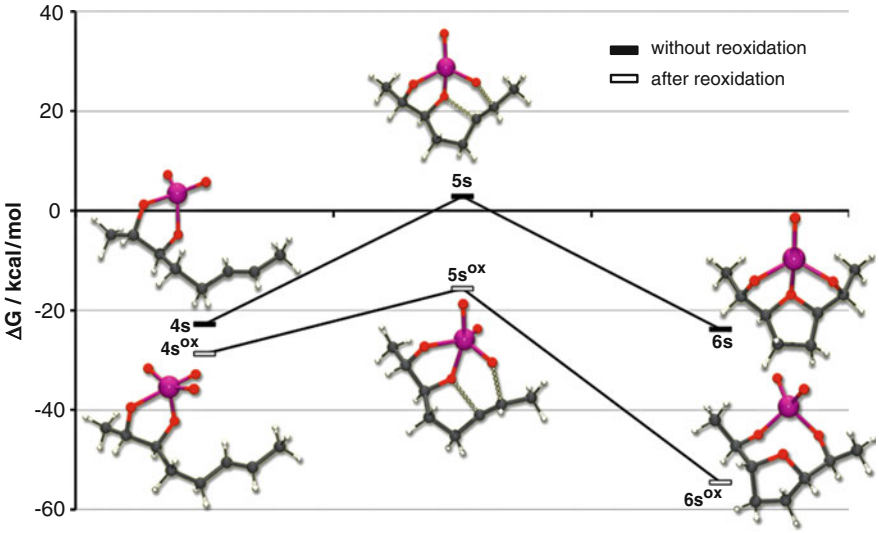

Fig. 5 Cyclization step without and after reoxidation

distorted tetrahedron around the osmium. In the case of **6s,** the open coordination site is filled by a THF molecule, which leads to a more distorted tetrahedral geometry. This could be the reason that the Os–O(THF) bond in **6s** is shorter compared to **6s^{ox}** (2.50 Å) and that **6s^{ox}** is more stable. With −25.9 kcal/mol, the cyclization step after reoxidation is also thermodynamically favored in comparison to the cyclization without reoxidation. As a result, the overall reaction starting from diene **1** and OsO_4 leading to **6s^{ox}** including the reoxidation with NMO is exergonic by −4.6 kcal/mol.

We also evaluated a possible stabilizing effect of the addition of a water molecule to the oxidized species. But the transition state **5s^{ox,water}** (Fig. 6, left) is found to be significantly higher in energy than **5s^{ox}**, which leads to a higher activation barrier for the cyclization step and, therefore, makes this reaction pathway unlikely.

Although **6s^{ox,water}** shows a stabilization of 12.6 kcal/mol due to the addition of the water molecule, we can rule out that this addition of water has a crucial effect on the formation of the THF ring, since the stabilization takes place after the ring closure (Table 3).

3.4 Conclusion

According to B3LYP/6-311+G(d) calculations, the osmium tetroxide-catalyzed oxidative cyclization of 1,5-dienes proceeds on the singlet hypersurface via the

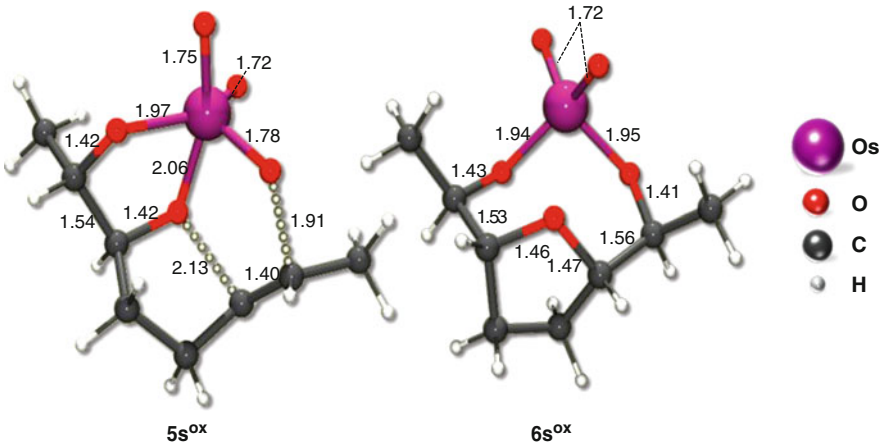

Fig. 6 Product-forming transition state **5s^{ox}** and product **6s^{ox}** with selected bond lengths (in Å)

Table 3 Thermodynamic data of all calculated structures and stabilization effects due to the addition of a water molecule

Structure	Without water			With water			Stabilization Δ(Δ*G*)/ kcal/mol
	Δ*H*/ kcal/mol	Δ*G*/ kcal/mol	Δ*S*/cal/ (K mol)	Δ*H*/ kcal/mol	Δ*G*/ kcal/mol	Δ*S*/cal/ (K mol)	
1+2	0.0	0.0	0.0	–	–	–	–
3	3.4	**15.9**	−41.8	–	–	–	–
4s	−36.6	**−22.8**	−46.5	−52.7	−27.0	−86.2	−4.2
4t	−14.9	−1.6	−44.4	−31.4	−7.0	−82.0	−5.4
5s	−15.3	2.9	−61.0	−25.6	3.5	−97.7	0.6
5t	2.4	19.5	−57.6	−10.2	18.4	−96.0	−1.1
5q	19.6	36.2	−55.9	4.1	31.3	−91.2	−4.9
6s	−42.1	−23.8	−61.7	−50.0	−21.4	−96.2	2.4
6t	−19.3	−2.6	−56.1	−42.4	−14.7	−92.9	−12.1
6q	2.2	18.4	−54.2	−38.4	−11.4	−90.7	−29.8
4s^{ox}	−42.4	**−28.7**	−46.0	−30.0	−5.1	−83.6	−23.6
5s^{ox}	−33.0	**−15.6**	−58.2	−23.9	4.9	−96.4	−20.5
6s^{ox}	−72.0	**−54.6**	−58.6	−96.6	−67.2	−98.7	12.6

The bold values show the free energies of the proposed reaction pathway
s singlet, *t* triplet, *q* quintet structures

oxidation states Os(VIII) → Os(VI) → Os(VIII) → Os(VI). It includes a reoxidation of the osmium(VI) species to osmium(VIII) after the first (3+2) cycloaddition, which leads to a lower activation energy of the following cyclization step (Fig. 7).

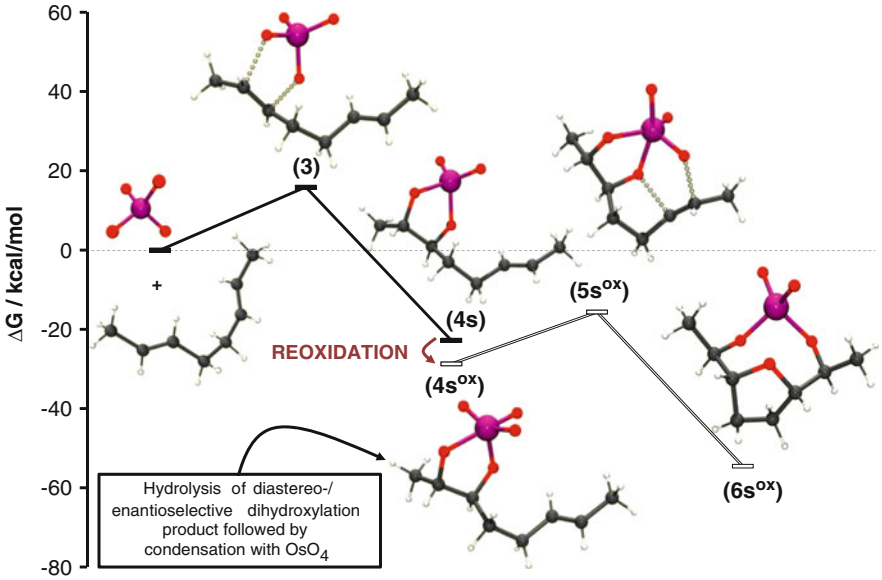

Fig. 7 Most favorable calculated pathway

4 Osmium-Mediated Amination Reactions

4.1 The Aminohydroxylation

4.1.1 Introduction

Contrary to the osmium-catalyzed dihydroxylation (DH) [80], the aminohydroxylation (AH) [18, 81] adds two different heteroatoms (N, O) to double bonds. It provides straightforward access to the amino alcohol fragment present in a broad variety of natural products (Fig. 8). Numerous reviews [20, 22, 82–87] have been published, among others, by its inventor K. B. Sharpless [17, 20, 88], who also rendered it asymmetric and catalytic at the same time in 1996 [89, 90].

The asymmetric version relies on the coordination of chiral cinchona alkaloid ligands, which are also known from the asymmetric DH (Fig. 1). Overall, at least [85] two catalytic cycles may be operating in the AH (Scheme 7). In the primary cycle, the chiral ligand controls the enantioselectivity and to a certain extent also the chemo- and regioselectivity. The second cycle, on the contrary, lacks the beneficial effects of the ligand. It can usually be avoided by controlling the experimental conditions, although it proceeds with remarkably low catalyst loadings and high reaction rates [91–95].

In the AH, not only *peri-* ((3+2) versus (2+2) mechanism) and *stereoselectivity* like in the DH have to be addressed, but furthermore the questions of *chemo-*

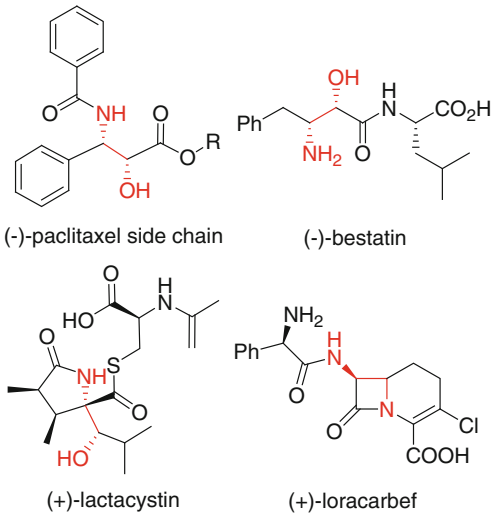

Fig. 8 Vicinal amino alcohols in natural products

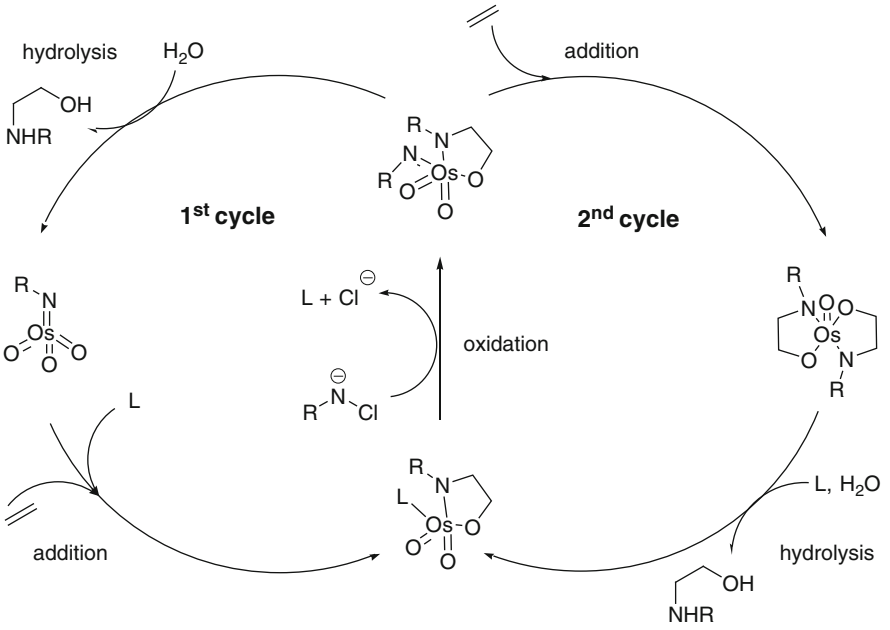

Scheme 7 Catalytic cycles of the AH

(DH vs. AH) and *regioselectivity* (leading to either α- or β-amino alcohols) also arise for unsymmetrical alkenes like propene (Scheme 9).

Different factors determining the regioselectivity have been discussed: These include steric and electronic contributions of the chiral cinchona ligands, substrates, and solvent effects, which all depend on each other.

Sharpless observed that the choice of the particular cinchona-derived chiral ligand can invert the regioselectivity in the reaction with styrenes [96–98]. Janda [96, 97] proposed that this effect might be due to steric reasons and aryl–aryl interactions [99, 100] of the olefin with the aromatic linker of the ligand. Moreover, it was shown that substituents on the aromatic ring of the styrene can influence the stereoselectivity [101], which prompted Ojima [102] to propose a relation between the regioselectivity and the dipole moment of the aromatic group of the olefin.

The nitrogen atom of the osmium complex often is preferentially added to the β-carbon atom of olefins bearing electron-withdrawing groups [96]. This is commonly attributed to the nucleophilic character of the imido group [20, 96]. Experimentally observed solvent effects [98] on the regioselectivity might be connected to the substitution pattern of the olefin: Depending on the hydrophilicity of the solvent, olefins bearing hydrophobic substituents might rather be oriented toward the interior of the binding pocket of the chiral ligand [103].

Common solvents used in experiment are water/alcohol mixtures. Three major groups of substituents R on the imido nitrogen atom are known [20]: These are sulfonyl groups (e.g., mesyl or tosyl substituents), esters (e.g., *tert*-Bu-carbamate substituent), and carbonyl groups (e.g., acetamido substituents) (Scheme 8). Early publications referred to alkyl imido osmium compounds [18, 90, 104]. The reaction is, depending on the nature of R, usually accelerated by nitrogen ligands [20].

As diol by-products are frequently observed, it is highly probable that also osma-2,5-dioxolanes like **11·L** or **12·L** (Scheme 9) are formed. They could be formed either by reaction with OsO_4·L (**2·L**), which could be formed hydrolytically, or by reaction of the olefin with O=Os=O rather than N=Os=O of the trioxo imido osmium complexes **8·L** (Scheme 9) [103, 105].

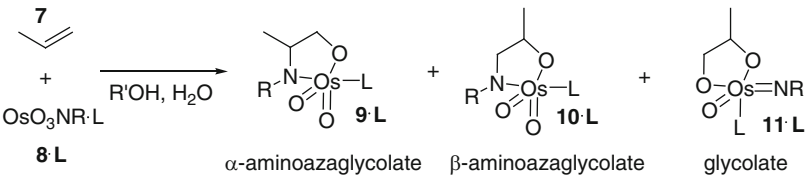

Scheme 8 Regio- and chemoselectivity of the aminohydroxylation

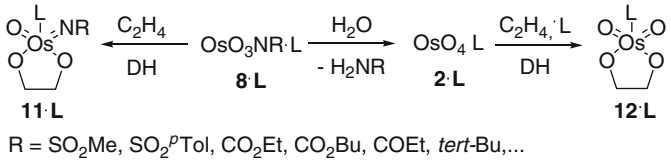

Scheme 9 Pathways leading to dihydroxylated byproducts

4.1.2 Mechanism

Theoretical investigations have been focusing rather on the DH than the AH reaction. The first study concerning the peri-, chemo-, and regioselectivities of the first cycle of the AH reaction was published on the B3LYP/SCRF(CPCM)/6-31G(d)//B3LYP/6-31G(d) level of theory in 2010 [106]. Different olefins **7** (ethylene, propene, acrolein, acrylonitrile, butadiene, and butene) and imido osmium complexes **8** (R = CN, H, Me, SO_2Me, $SO_2{}^pTol$) were studied (Scheme 10); the nitrogen ligand L was modeled by ammonia. The coordination of the ammonia ligand L is denominated in the following with the addition ·L, the substituents R by the superscript CN, H, Me, SO_2Me, or $SO_2{}^pTol$ at the number describing a structure.

The question of *periselectivity* addresses the issue whether the AH proceeds via a concerted (3+2) cycloaddition pathway or via a (2+2) mechanism (Scheme 11), which was studied for ethylene interacting with the cyano-substituted imido osmium complex.

The (2+2) addition may proceed either across the imido functionality (**13**, **13·L**) or across the O=Os bond (**14**, **14·L**). The rearrangement to the five-membered metallacycles **11·L** or **9·L** could be triggered by the coordination of the nitrogen ligand L to **13** or **14**, or could take place after the formation of the compound **13·L** or **14·L**.

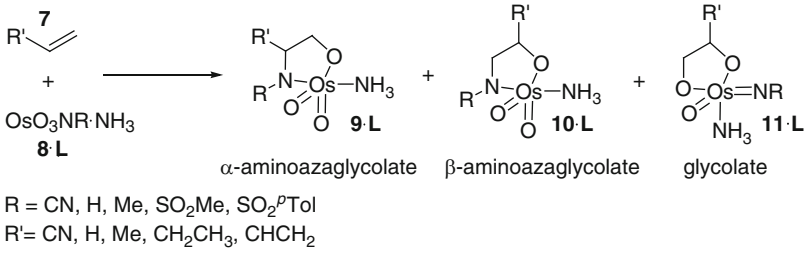

Scheme 10 Investigated trioxo imido osmium complexes and olefins

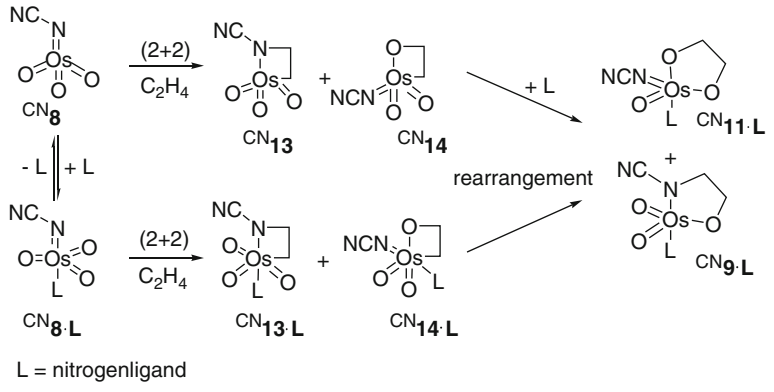

Scheme 11 (2+2) Mechanism and nitrogen ligand addition

In case of the (3+2) mechanism, two reaction steps had to be investigated: one was the pre-equilibrium reaction between the nitrogen ligand L and the osmium complex, and the other the (3+2) cycloaddition step (Scheme 12).

According to previous work on various metal-oxo species, a (2+2) mechanism appeared to be very unlikely [35–38, 60, 107–112]. Indeed the (2+2) mechanisms were calculated to be kinetically not competitive with a reaction barrier of at least 41.9 kcal/mol (entries 1–4; Table 4) compared to the (3+2) mechanism (entry 5, Table 4).

The influence of the chiral nitrogen ligand on the reaction was studied as well. Table 5 shows the results ($\Delta G^{\neq}$) for the (3+2) additions of ethylene to

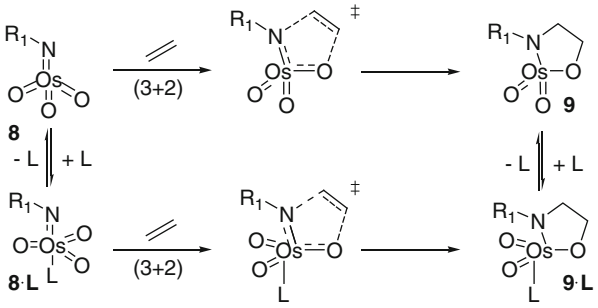

Scheme 12 Different possibilities of ligand coordination in the (3+2) mechanism

Table 4 Activation ($\Delta H^{\neq}$) and reaction enthalpies (ΔH) as well as Gibbs free energies ($\Delta G^{\neq}$ and ΔG) of the (2+2) reaction pathways in comparison to the (3+2) addition (in kcal/mol at 298.15 K)

Entry	Reaction	$\Delta H_{CPCM}{}^{\neq}$ ($\Delta H^{\neq}$)	$\Delta G_{CPCM}{}^{\neq}$ ($\Delta G^{\neq}$)	ΔH_{CPCM} (ΔH)	ΔG_{CPCM} (ΔG)
1	^{CN}**8** → ^{CN}**13**	37.7	52.2	28.8	42.9
	(2+2)	(42.4)	(56.8)	(35.5)	(49.6)
2	^{CN}**8** → ^{CN}**14**	32.3	45,9	−5.0	9,2
	(2+2)	(32.9)	(46.6)	(−3.8)	(10.4)
3	^{CN}**8·L** → ^{CN}**13·L**	29.2	44.7	28.3	43.8
	(2+2)	(37.5)	(53.0)	(33.5)	(51.1)
4	^{CN}**8·L** → ^{CN}**14·L**	27.8	41.9	1.2	15.6
	(2+2)	(40.2)	(54.3)	(4.6)	(18.9)
5	^{CN}**8·L** → ^{CN}**9·L**	−0.2	12.5	−62.1	−46.6
	(3+2)	(−0.1)	(12.7)	(−55.6)	(−40.2)

Gas phase results are given in parentheses

Table 5 $\Delta G^{\neq}$ for the (3+2) additions of OsO_3N–R·L (**8·L**) to ethylene and ΔG for the nitrogen ligand addition according to Scheme 11

Entry	Reactant	$\Delta G^{\neq}$ **8·L** → **9·L**	ΔG **8** → **8·L**	$\Delta G^{\neq}$ **8** → **9**
1	^{CN}**8·L**	12.5 (12.7)	−3.5 (−2.8)	15.2 (14.0)
2	^{H}**8·L**	13.6 (12.8)	3.3 (1.5)	14.0 (13.2)
3	^{Me}**8·L**	15.8 (15.3)	4.1 (2.3)	21.0 (19.7)
4	^{SO_2Me}**8** · **L**	11.7 (10.9)	1.2 (1.4)	15.1 (13.7)
5	$^{SO_2{}^{p}Tol}$**8** · **L**	13.0 (12.3)	−1.2 (0.5)	14.0 (13.4)

Values are given in kcal/mol at 298.15 K. Gas phase results are given in parentheses

$OsO_3NR{\cdot}NH_3$ and OsO_3NR, and the pre-equilibrium reaction of OsO_3NR with the model ligand ammonia (ΔG).

The coordination of the nitrogen ligand proceeds either exergonically (e.g., entry 1, column 4) or endergonically (e.g., entry 2, column 4) depending on the substituent R. On the contrary, the (3+2) cycloaddition step is always accelerated (cf. columns 3 and 5) by coordination of the nitrogen ligand.

Furthermore, the competing dihydroxylation mechanisms were examined (*chemoselectivity*). Figure 9 shows the most favorable[1] calculated dihydroxylation pathways (left side) for R = Me, $SO_2{}^{p}$Tol ($^{Me}\mathbf{8} \cdot \mathbf{L}$, $^{SO_2{}^{p}Tol}\mathbf{8} \cdot \mathbf{L}$) in comparison to the aminohydroxylation reaction (right side). The dihydroxylation reaction by OsO_3NR was calculated to proceed without coordination of ammonia, whereas in the course of the aminohydroxylation, it interacts with the osmium center.

Dihydroxylated by-products might indeed result from dihydroxylation mediated by the imido osmium compound $^{SO_2{}^{p}Tol}\mathbf{8} \cdot \mathbf{L}$, as a very low kinetic selectivity of only 0.9 kcal/mol (14.3–13.4 kcal/mol) has been obtained. In case of the methyl-substituted imido osmium, another pathway becomes more probable, which is the dihydroxylation by *in situ* formed $OsO_4{\cdot}NH_3$. It was predicted to have a reaction barrier of only 17.0 kcal/mol and might be responsible for the experimental observation of a significant amount of dihydroxylated by-product in case of R = *tert*-Bu [18, 90].

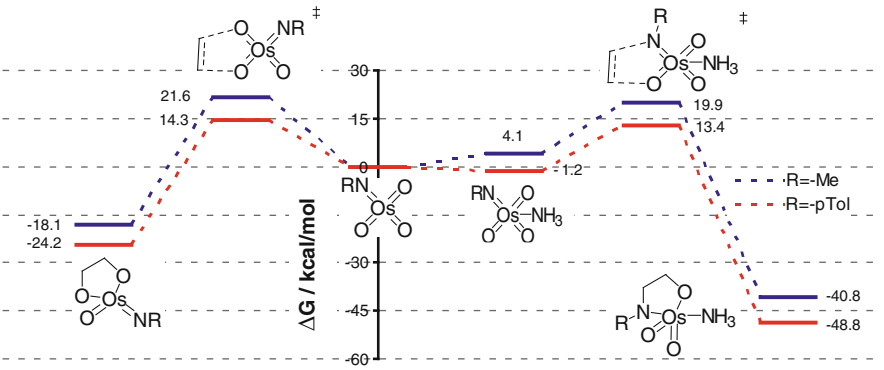

Fig. 9 Most favorable dihydroxylation and aminohydroxylation pathways for OsO_3NR with R = Me and $SO_2{}^{p}$Tol. Values are given in kcal/mol at 298.15 K on the B3LYP/SCRF(CPCM)/6-31G (d)//B3LYP/6-31G(d) level of theory

[1] Dihydroxylation transition states with coordinated nitrogen ligand are more favorable with *syn*-position of NH_3 regarding the imido group, whereas the aminohydroxylation transition states proceed with *anti*-position. Therefore the Gibbs free reaction energies given in Table 5, column 4, do *not* apply for a dihydroxylation pathway with NH_3-coordination.

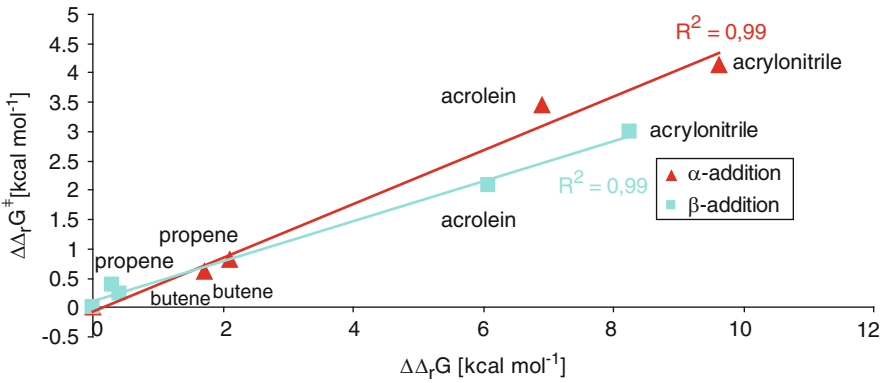

Fig. 10 Hammett plot of the (3+2) addition in the gas phase to $OsO_3NCN{\cdot}NH_3$, $\Delta\Delta G/\Delta\Delta G^{\neq}$ is given relative to the addition of ethylene

To study electronic effects on the regioselectivity (α- vs. β-addition), a systematic variation of R and R′ (selected by their assigned *para*-Hammett parameters [113]) was conducted. It revealed a kinetic and thermodynamic preference for the β-product. This is in good agreement with the experimental observation that the nitrogen atom usually ends up at the less substituted carbon of the olefin and away from the most electron-withdrawing group [20, 83, 96].

A relationship between the electronic situation of the reacting olefin and the calculated regioselectivity could be predicted. Figure 10 shows the linear free-energy relationship (Hammett plot) between the α- and β-(3+2) additions of five electronically different olefins (R′ = –H, $–CH_3$, $–CH_2CH_3$, –CHO, –CN) to $OsO_3NCN{\cdot}NH_3$.

It was predicted that the degree of regioselectivity α- vs. β-addition is lower for electron-rich olefins, as the reaction barriers could be correlated to the substituent's R *para*-Hammett values.

Therefore, a better regioselectivity should be obtained if electron-poor imido osmium complexes react with electron-poor olefins. This corresponds to the substrate-based methodology developed by Janda [96].

The absolute height of the reaction barriers for the different olefins is predicted to show an inverse relationship, which is indicated by the positive slope of the regression line in Fig. 10. Electron-deficient olefins lead to higher reaction barriers for the (3+2) cycloaddition.

The imido complexes $^{SO_2Me}\mathbf{8}\cdot\mathbf{L}$ and $^{SO_2{}^pTol}\mathbf{8}\cdot\mathbf{L}$ were predicted to exhibit a very similar behavior, whereas no linear relationship could be determined for the rather electron-rich imido osmium complexes $^{Me}\mathbf{8}\cdot\mathbf{L}$ and $^{H}\mathbf{8}\cdot\mathbf{L}$. Those in general seem to differentiate little between electronically different substrates and for $^{CN}\mathbf{8}\cdot\mathbf{L}$, even an inverse α-selectivity was predicted, in agreement with experimental observations of α-selectivity in reactions with conjugated substrates like cyclohexadiene [81].

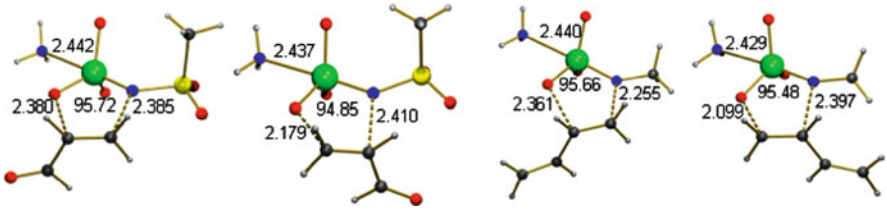

Fig. 11 Structural parameters (bond lengths/angles given in Å/deg) of exemplary (3+2) transition states (R = SO_2Me, Me; R′ = CHO, $CHCH_2$)

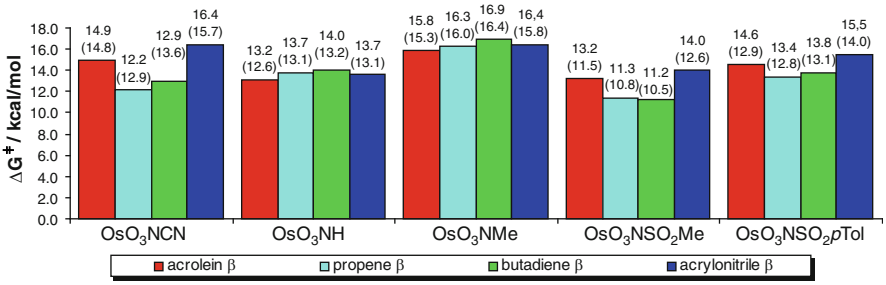

Fig. 12 Gibbs free energies of activation for the (3+2) β-transition states of different olefins. Gas phase results are given in *parentheses*

The activation energies calculated for the β-transition states are lower in energy and the bonds in the transition state are formed more synchronous than in the corresponding α-transition states (Fig. 11). For example, in case of R = SO_2Me and R′ = CHO, the lengths of the developing O–C and N–C bonds do not differ significantly in case of β-addition (2.385–2.380 Å), whereas for the α-addition a difference of 0.22 Å (2.410–2.179 Å) is calculated.

Figure 12 is a summary of calculated Gibbs free energies of activation for the (3+2) cycloaddition step leading to the β-products **10**·**L**. Four olefins **7** (C_2H_3R' with R′ = CHO, CN, Me, $CHCH_2$) reacting with different imido osmium compounds $OsO_3NR{\cdot}NH_3$ **8**·**L** ($^{CN}\mathbf{8}\cdot\mathbf{L}$, $^{H}\mathbf{8}\cdot\mathbf{L}$, $^{Me}\mathbf{8}\cdot\mathbf{L}$, $^{SO_2Me}\mathbf{8}\cdot\mathbf{L}$, and $^{SO_2{}^{p}Tol}\mathbf{8}\cdot\mathbf{L}$) are compared.

Both substituents R and R′ play an important role and exhibit an influence on the calculated activation energy of the reaction. Lower activation energies were predicted for imido osmium compounds bearing electron-withdrawing substituents R in reaction with electron-rich olefins (e.g., $^{SO_2Me}\mathbf{8}\cdot\mathbf{L}$ + butadiene, 11.2 kcal/mol). The combination of an electron-rich olefin and an electron-rich imido osmium complex, however, was calculated to be unfavorable (e.g., $^{Me}\mathbf{8}\cdot\mathbf{L}$ + butadiene, 16.9 kcal/mol). For the mesyl-substituted complex $^{SO_2Me}\mathbf{8}\cdot\mathbf{L}$, better results are predicted compared to that for the tosyl-substituted $^{SO_2{}^{p}Tol}\mathbf{8}\cdot\mathbf{L}$.

Very recently [114] investigations on the cycloaddition of ethylene to $O_2Os(CH_2)_2$ [115] and $O_3Os(CH_2)$ [116, 117] were extended to imido substituents in order to explore the initial step of the aminohydroxylation reaction and

second-cycle reactivities. It examined an aminohydroxylation protocol developed by Muñiz [95], which is based on in situ created oxo-tris(imido) osmium compounds and reports energies on the B3LYP/6-311+G(d,p)//B3LYP/6-31G(d)+ZPE level of theory. Numerous potentially competing pathways [(1+2), (2+2), (3+2), rearrangement of the reactant] were investigated (Scheme 13). None of the explored pathways turned out to be kinetically competitive to the (3+2) diamination addition to **15**, although the rearrangement of **15** to **16** was calculated to be exothermic by −6.4 kcal/mol.

Nevertheless, the authors mention that their model system might not be completely transferable to the osmium compounds used in experimental work because of the influence of the different substituent R (R = H).

The second-cycle (3+2) addition of ethylene to compound **17** (Scheme 14) was calculated to be highly exothermic with a small barrier (ΔE) of only 2.9 kcal/mol (aminohydroxylation, leading to **18**) and 5.1 kcal/mol (dihydroxylation, leading to **19**). Reaction barriers for the corresponding first-cycle cycloadditions were reported [114] to be 5.5 kcal/mol (aminohydroxylation) and 11.2 kcal/mol (dihydroxylation).

4.2 The Diamination

4.2.1 Introduction

The $OsO_2(NR)_2$-mediated diamination reaction, which is closely related to the DH and AH, adds two nitrogen atoms to a double bond and provides access to vicinal diamines [19]. Unfortunately, it could not be rendered catalytic until now [21, 22, 118–125]. A DFT study of this transformation has been published in 2004 [111] at the B3LYP/6-311+G(d,p)//B3LYP/6-31G(d) level.

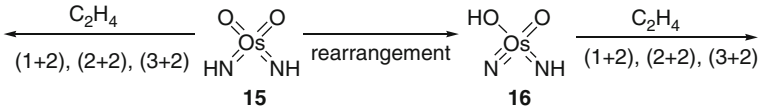

Scheme 13 Competing pathways of the diamination reaction

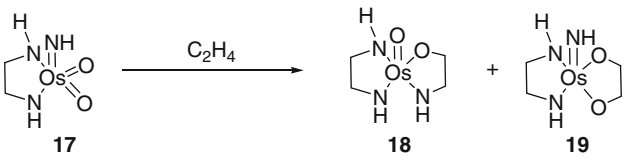

Scheme 14 Second-cycle chemoselectivity

4.2.2 Mechanism

Different (2+2) and (3+2) mechanisms, leading to the dihydroxylated, oxyaminated, and diaminated products, have been explored by Deubel (Scheme 15) [111].

The results indicated that the (3+2) addition to $OsO_2(NH)_2$ should finally lead to the diamine ($\Delta G^{\neq} = 12.1$ kcal/mol) and is favored over the two different (2+2) mechanisms ($\Delta G_{Os-O}{}^{\neq} = 59.8$ kcal/mol; $\Delta G_{Os-N}{}^{\neq} = 56.3$ kcal/mol), oxyamination ($\Delta G^{\neq} = 19.9$ kcal mol^{-1}), dihydroxylation ($\Delta G^{\neq} = 22.8$ kcal/mol), or the cycloadditions to OsO_3NH or OsO_4.

Moreover, the authors reasoned that electron-withdrawing substituents R (e.g., R = $-CF_3$) on $OsO_2(NR)_2$ facilitate the cycloaddition step, whereas the reoxidation of Os(VI) to Os(VIII) is hindered. For electron-donating substituents R (R = −Me, *tert*-Bu), the opposite behavior was predicted. The coordination of a chiral amino ligand (which might transfer stereochemical information) turned out to be hardly feasible due to the reduced Lewis acidity of the bisimido osmium complexes. All bisimido dioxo osmium compounds were calculated to be thermodynamically instable toward hydrolysis, with the degree of stability depending on the substituents R (Table 6).

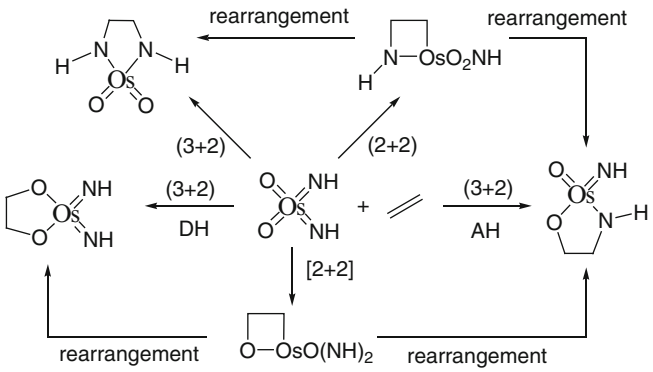

Scheme 15 Reaction pathways for the reaction of $OsO_2(NH)_2$ with ethylene

Table 6 Calculated free energies for the hydrolysis of $OsO_2(NR_2)$ (R = Me, *tert*-Bu, CF_3) in kcal/mol [126]

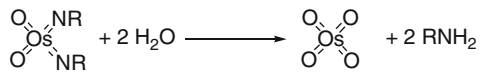

R =	ΔG_r [kcal/mol]
Me	−2.4
tert-Bu	−0.6
CF_3	−35.7

4.3 Conclusion

The osmium-catalyzed aminohydroxylation and diamination most likely proceed by [3+2] and not by [2+2] mechanisms.

Evidence was found that the aminohydroxylation reaction is accelerated by ligand coordination. Various experimentally used nitrogen sources with different Hammett parameters were modeled by electron-withdrawing and donating substituents. These model substituents were chosen according to their *para*-Hammett values in order to describe the experimentally employed groups. Additionally, the cycloaddition with alkenes bearing different electron-withdrawing and donating substituents has been investigated. It was predicted that the β-addition is favored and that electron-deficient OsO_3N–R complexes should show higher reaction rates, while for olefins with electron-withdrawing groups, higher activation barriers are predicted. The olefin reactivity can be correlated to the *para*-Hammett values of the olefin's substituents.

The second cycle of the aminohydroxylation probably shows a higher affinity for the cycloaddition with olefins than the first cycle, and the aminohydroxylation pathway is favored over the dihydroxylation pathway. Likewise, the diamination of $OsO_2(NR)_2$ is predicted to proceed faster than the corresponding aminohydroxylation reaction.

References

1. Torrent M, Sola M, Frenking G (2000) Chem Rev 100:439
2. Sharpless KB, Teranishi AY, Backvall JE (1977) J Am Chem Soc 99:3120
3. Criegee R (1936) Justus Liebigs Ann Chem 522:75
4. Joergensen KA, Hoffmann R (1986) J Am Chem Soc 108:1867
5. Corey EJ, Noe MC (1993) J Am Chem Soc 115:12579
6. Becker H, Ho PT, Kolb HC, Loren S, Norrby P-O, Sharpless KB (1994) Tetrahedron Lett 35:7315
7. Gobel T, Sharpless KB (1993) Angew Chem Int Ed 32:1329
8. Corey EJ, Noe MC, Grogan MJ (1996) Tetrahedron Lett 37:4899
9. Nelson DW, Gypser A, Ho PT, Kolb HC, Kondo T, Kwong H-L, McGrath DV, Rubin AE, Norrby P-O, Gable KP, Sharpless KB (1997) J Am Chem Soc 119:1840
10. Corey EJ, Sarshar S, Azimioara MD, Newbold RC, Noe MC (1996) J Am Chem Soc 118:7851
11. Vanhessche KPM, Sharpless KB (1996) J Org Chem 61:7978
12. Philipps FC (1894) Z Anorg Allg Chem 6:229
13. Dobler C, Mehltretter GM, Sundermeier U, Beller M (2001) J Organomet Chem 621:70
14. Mehltretter GM, Dobler C, Sundermeier U, Beller M (2000) Tetrahedron Lett 41:8083
15. Doebler C, Mehltretter GM, Sundermeier U, Beller M (2000) J Am Chem Soc 122:10289
16. Dobler C, Mehltretter G, Beller M (1999) Angew Chem Int Ed 38:3026
17. Kolb HC, Sharpless KB (1998) Transition Met Org Synth 2:243
18. Sharpless KB, Patrick DW, Truesdale LK, Biller SA (1975) J Am Chem Soc 97:2305
19. Chong AO, Oshima K, Sharpless KB (1977) J Am Chem Soc 99:3420
20. Kolb HC, Sharpless KB (2004) Transition Met Org Synth (2^{nd} Ed.) 2:309

21. Muniz K, Nieger M, Mansikkamaeki H (2003) Angew Chem Int Ed 42:5958
22. Muniz K (2004) Chem Soc Rev 33:166
23. Donohoe TJ, Winter JJG, Helliwell M, Stemp G (2001) Tetrahedron Lett 42:971
24. De Champdore M, Lasalvia M, Piccialli V (1998) Tetrahedron Lett 39:9781
25. Morris CL, Hu Y, Head GD, Brown LJ, Whittingham WG, Brown RCD (2009) J Org Chem 74:981
26. Bhunnoo RA, Hobbs H, Laine DI, Light ME, Brown RCD (2009) Org Biomol Chem 7:1017
27. Brown LJ, Spurr IB, Kemp SC, Camp NP, Gibson KR, Brown RCD (2008) Org Lett 10:2489
28. Elliott MC (2002) J Chem Soc Perkin Trans I 2301
29. Koert U (1995) Synthesis 02:115
30. Boivin TLB (1987) Tetrahedron 43:3309
31. Boeseken J, de Graaff C (1922) Recl Trav Chim Pays-Bas Belg 41:199
32. Veldkamp A, Frenking G (1994) J Am Chem Soc 116:4937
33. Norrby PO, Kolb HC, Sharpless KB (1994) Organometallics 13:344
34. Norrby P-O, Becker H, Sharpless KB (1996) J Am Chem Soc 118:35
35. Pidun U, Boehme C, Frenking G (1997) Angew Chem Int Ed 35:2817
36. DelMonte AJ, Haller J, Houk KN, Sharpless KB, Singleton DA, Strassner T, Thomas AA (1997) J Am Chem Soc 119:9907
37. Dapprich S, Ujaque G, Maseras F, Lledos A, Musaev DG, Morokuma K (1996) J Am Chem Soc 118:11660
38. Torrent M, Deng L, Duran M, Sola M, Ziegler T (1997) Organometallics 16:13
39. Singleton DA, Thomas AA (1995) J Am Chem Soc 117:9357
40. Ujaque G, Maseras F, Lledos A (1999) J Am Chem Soc 121:1317
41. Ujaque G, Maseras F, Lledos A (1997) J Org Chem 62:7892
42. Norrby P-O, Rasmussen T, Haller J, Strassner T, Houk KN (1999) J Am Chem Soc 121:10186
43. Drudis-Sole G, Ujaque G, Maseras F, Lledos A (2005) Chem Eur J 11:1017
44. Moitessier N, Maigret B, Chretien F, Chapleur Y (2000) Eur J Org Chem 995
45. Maseras F (1999) Top Organomet Chem 4:165
46. Sharpless KB, Amberg W, Beller M, Chen H, Hartung J, Kawanami Y, Lubben D, Manoury E, Ogino Y et al (1991) J Org Chem 56:4585
47. Kolb HC, Andersson PG, Sharpless KB (1994) J Am Chem Soc 116:1278
48. Sharpless KB, Amberg W, Bennani YL, Crispino GA, Hartung J, Jeong KS, Kwong HL, Morikawa K, Wang ZM et al (1992) J Org Chem 57:2768
49. Drudis-Sole G, Ujaque G, Maseras F, Lledos A (2005) Top Organomet Chem 12:79
50. Klein E, Rojahn W (1965) Tetrahedron 21:2353
51. Carlsen PHJ, Katsuki T, Martin VS, Sharpless KB (1981) J Org Chem 46:3936
52. Piccialli V (2007) Synthesis 2585
53. Wolfe S, Ingold CF (1981) J Am Chem Soc 103:940
54. Walba DM, Wand MD, Wilkes MC (1979) J Am Chem Soc 101:4396
55. Sable HZ, Powell KA, Katchian H, Niewoehner CB, Kadlec SB (1970) Tetrahedron 26:1509
56. Houk KN, Strassner T (1999) J Org Chem 64:800
57. Strassner T, Busold M (2001) J Org Chem 66:672
58. Poethig A, Strassner T (2007) Collect Czech Chem Commun 72:715
59. Donohoe TJ, Butterworth S (2005) Angew Chem Int Ed 44:4766
60. Deubel DV, Frenking G (2003) Acc Chem Res 36:645
61. DelMonte AJ, Haller J, Houk KN, Sharpless KB, Singleton DA, Strassner T, Thomas AA (1997) J Am Chem Soc 119:9907
62. Pidun U, Boehme C, Frenking G (1997) Angew Chem Int Ed 35:2817
63. Kolb HC, VanNieuwenhze MS, Sharpless KB (1994) Chem Rev 94:2483
64. Jacobsen EN, Marko I, Mungall WS, Schroeder G, Sharpless KB (1988) J Am Chem Soc 110:1968
65. Poethig A, Strassner T (2010) J Org Chem 75:1967

66. Gaussian 03, Rev E01, Frisch MJ, Trucks GW, Schlegel HB, Scuseria GE, Robb MA, Cheeseman JR, Montgomery Jr JA, Vreven T, Kudin KN, Burant JC, Millam JM, Iyengar SS, Tomasi J, Barone V, Mennucci B, Cossi M, Scalmani G, Rega N, Petersson GA, Nakatsuji H, Hada M, Ehara M, Toyota K, Fukuda R, Hasegawa J, Ishida M, Nakajima T, Honda Y, Kitao O, Nakai H, Klene M, Li X, Knox JE, Hratchian HP, Cross JB, Bakken V, Adamo C, Jaramillo J, Gomperts R, Stratmann RE, Yazyev O, Austin AJ, Cammi R, Pomelli C, Ochterski JW, Ayala PY, Morokuma K, Voth GA, Salvador P, Dannenberg JJ, Zakrzewski VG, Dapprich S, Daniels AD, Strain MC, Farkas O, Malick DK, Rabuck AD, Raghavachari K, Foresman JB, Ortiz JV, Cui Q, Baboul AG, Clifford S, Cioslowski J, Stefanov BB, Liu G, Liashenko A, Piskorz P, Komaromi I, Martin RL, Fox DJ, Keith T, Al-Laham MA, Peng CY, Nanayakkara A, Challacombe M, Gill PMW, Johnson B, Chen W, Wong MW, Gonzalez C, Pople JA (2004) Wallingford, CT
67. Becke AD (1993) J Chem Phys 98:5648
68. Lee C, Yang W, Parr RG (1988) Phys Rev B Condens Matter 37:785
69. Stephens PJD, Chabalowski CF, Frisch MJ (1994) J Phys Chem 98:11623
70. Vosko SH, Wilk L, Nusair M (1980) Can J Phys 58:1200
71. Binning RC Jr, Curtiss LA (1990) J Comput Chem 11:1206
72. Clark T, Chandrasekhar J, Spitznagel GW, PvR S (1983) J Comput Chem 4:294
73. Frisch MJ, Pople JA, Binkley JS (1984) J Chem Phys 80:3265
74. Hay PJ (1977) J Chem Phys 66:4377
75. Krishnan R, Binkley JS, Seeger R, Pople JA (1980) J Chem Phys 72:650
76. McGrath MP, Radom L (1991) J Chem Phys 94:511
77. Raghavachari K, Trucks GW (1989) J Chem Phys 91:2457
78. Wachters AJH (1970) J Chem Phys 52:1033
79. Hay PJW, Wadt WR (1985) J Chem Phys 82:299
80. Kolb HC, Sharpless KB (2004) Transition Met Org Synth (2nd edn) 2:275
81. Sharpless KB, Chong AO, Oshima K (1976) J Org Chem 41:177
82. O'Brien P (1999) Angew Chem Int Ed 38:326
83. Bodkin JA, McLeod MD (2002) J Chem Soc Perkin Trans 1:2733
84. Nilov D, Reiser O (2002) Adv Synth Catal 344:1169
85. Lohray BB, Thombare PS, Bhushan V (2002) PINSA-A Proc Indian Natl Sci Acad A 68:391
86. Bolm C, Hildebrand JP, Muniz K (2000) Catal Asymmetric Synth (2nd edn) 399
87. Bayer A (2004) Compr Asymmetric Catal Suppl 2:43
88. Schlingloff G, Sharpless KB (2001) Asymmetric Oxid React 104
89. Li G, Chang H-T, Sharpless KB (1996) Angew Chem Int Ed 35:451
90. Rubinstein H, Svendsen JS (1994) Acta Chem Scand 48:439
91. Fokin VV, Sharpless KB (2001) Angew Chem Int Ed 40:3455
92. Rubin AE, Sharpless KB (1997) Angew Chem Int Ed 36:2637
93. Andersson MA, Epple R, Fokin VV, Sharpless KB (2002) Angew Chem Int Ed 41:472
94. Wu P, Hilgraf R, Fokin VV (2006) Adv Synth Catal 348:1079
95. Muniz K, Almodovar I, Streuff J, Nieger M (2006) Adv Synth Catal 348:1831
96. Han H, Cho C-W, Janda KD (1999) Chem Eur J 5:1565
97. Tao B, Schlingloff G, Sharpless KB (1998) Tetrahedron Lett 39:2507
98. Bruncko M, Schlingloff G, Sharpless KB (1997) Angew Chem Int Ed 36:1483
99. Bodkin JA, Bacskay GB, McLeod MD (2008) Org Biomol Chem 6:2544
100. Harding M, Bodkin JA, Issa F, Hutton CA, Willis AC, McLeod MD (2009) Tetrahedron 65:831
101. Morgan AJ, Masse CE, Panek JS (1999) Org Lett 1:1949
102. Chuang C-Y, Vassar Victor C, Ma Z, Geney R, Ojima I (2002) Chirality 14:151
103. Reddy KL, Sharpless KB (1998) J Am Chem Soc 120:1207
104. Patrick DW, Truesdale LK, Biller SA, Sharpless KB (1978) J Org Chem 43:2628
105. Lohray BB, Bhushan V, Reddy GJ, Reddy AS (2002) Indian J Chem Sect B Org Chem Incl Med Chem 41B:161

106. Munz D, Strassner T (2010) J Org Chem 75:1491
107. Gisdakis P, Roesch N (2001) J Am Chem Soc 123:697
108. Pietsch MA, Russo TV, Murphy RB, Martin RL, Rappe AK (1998) Organometallics 17:2716
109. Deubel DV, Frenking G (1999) J Am Chem Soc 121:2021
110. Deubel DV, Schlecht S, Frenking G (2001) J Am Chem Soc 123:10085
111. Deubel DV, Muniz K (2004) Chem Eur J 10:2475
112. Deubel DV, Loschen C, Frenking G (2005) Top Organomet Chem 12:109
113. Hansch C, Leo A, Taft RW (1991) Chem Rev 91:165
114. Celik MA, Haunschild R, Frenking G (2010) Organometallics 29:1560
115. Hoelscher M, Leitner W, Holthausen MC, Frenking G (2005) Chem Eur J 11:4700
116. Cappel D, Tuellmann S, Loschen C, Holthausen MC, Frenking G (2006) J Organomet Chem 691:4467
117. Haunschild R, Loschen C, Tuellmann S, Cappel D, Hoelscher M, Holthausen MC, Frenking G (2007) J Phys Org Chem 20:11
118. Almodovar I, Hoevelmann CH, Streuff J, Nieger M, Muniz K (2006) Eur J Org Chem 704
119. Muniz K (2005) New J Chem 29:1371
120. Muniz K, Nieger M (2005) Chem Commun (Cambridge, UK) 2729
121. Muniz K (2004) Eur J Org Chem 2243
122. Muniz K, Nieger M (2003) Synlett 211
123. Cardona F, Goti A (2009) Nat Chem 1:269
124. Anhaus JT, Kee TP, Schofield MH, Schrock RR (1990) J Am Chem Soc 112:1642
125. Schofield MH, Kee TP, Anhaus JT, Schrock RR, Johnson KH, Davis WM (1991) Inorg Chem 30:3595
126. Fukui K (1981) Acc Chem Res 14:363

Reactivity of Metal Carbene Clusters $Pt_nCH_2^+$ and $PtMCH_2^+$ (M = Cu, Ag, Au, Pt, Rh) Toward O_2 and NH_3: A Computational Study

Zexing Cao

Abstract DFT calculations at various levels have been used to elucidate the mechanistic details of dehydrogenation of methane by Pt cationic clusters and the reactivity of metal carbene clusters $Pt_4CH_2^+$ and $PtMCH_2^+$ (M = Cu, Ag, Au, Pt, Rh) toward O_2 and NH_3. On the basis of theoretical analyses, the size dependence of reactivity and the cooperative effect of the bimetallic cluster in the dehydrogenation reactions of CH_4 and NH_3 have been discussed. Plausible mechanisms for the reactions of $Pt_4CH_2^+$ with O_2 and $PtMCH_2^+$ with NH_3, leading to C–O and C–N bond couplings, respectively, have been proposed. The calculated results show good agreement with the experimental observations and provide a reasonable basis for understanding of the gas-phase chemistry of bare Pt-containing cationic clusters and their organometallic systems.

1 Introduction

Activation and functionalization of methane by bare transition metals in the gas phase are of fundamental importance in organometallic, biological, and industrial chemistry [1–6]. Gas-phase reaction models exclude effects of solvent and aggregation on organometallic systems and make experimental and theoretical characterization of the intrinsic chemical behavior of transition metals and isolated molecules become possible. Furthermore, the transition metal clusters as simplified models for study of heterogeneous catalysis might provide significant implication for the mechanistic details of the surface reaction. In the past two decades, methane activation by gaseous metal ions and their transition metal complexes has been intensely studied [7–58], both experimentally and theoretically. One of the most promising metals in catalytic applications is platinum, and it has been widely used

Z. Cao (✉)
Department of Chemistry and State Key Laboratory of Physical Chemistry of Solid Surfaces, College of Chemistry and Chemical Engineering, Xiamen University, Xiamen 361005, China
e-mail: zxcao@xmu.edu.cn

O. Wiest and Y. Wu (eds.), *Computational Organometallic Chemistry*,
DOI 10.1007/978-3-642-25258-7_7,

for the inert C–H bond activation of methane [6, 59]. Over the past 10 years, lots of experimental and theoretical investigations on the gas-phase reactions of methane with the neutral and cationic Pt-containing metal clusters have been carried out [3, 7, 8, 14–19, 22, 23, 29, 50, 59–73].

Early experimental studies by Cox and coworkers [74, 75] showed that methane can be efficiently activated by neutral Pt_n clusters ($n \leq 24$), and their reactivities vary with the cluster size. For example, polyatomic clusters Pt_n ($n = 2$–5) are more reactive than single platinum atom in dehydrogenation. Carroll et al. [76] calculated the potential energy curve of dehydrogenation reaction of single Pt atom with methane, and they found that the most stable intermediate is a hydride H–Pt–CH_3, since the d^9s^1 configuration of Pt atom can accommodate two covalent bonds. The entire reaction is slightly endothermic by 7.2 kcal mol^{-1}, yielding the neutral carbene $PtCH_2$ and H_2. Cui et al. [77, 78] explored the C–H bond activation mechanism of methane by neutral platinum dimers and trimers theoretically. Their calculations indicate that neutral clusters Pt_2 and Pt_3 can activate the first C–H bond of methane with small barriers. Xiao et al. [71] investigated methane activation on Pt and Pt_4 by B3LYP and PW91 functionals, and dehydrogenation of CH_4 on Pt_4 is faster kinetically than on the Pt atom, whereas the catalytic dehydrogenation of CH_4 by Pt is more favorable thermodynamically. The interaction mechanism of carbene with the first-row transition metals was investigated by theoretical calculations [52, 79–82]. The metal carbene MCH_2 complexes from Sc to Mn were predicted to have a ground state with high multiplicities, while the low multiplicity is favored from Mn to Cu [79].

Transition metal cluster cations generally exhibit relatively higher reactivity in catalysis than their neutral counterparts in the gas phase. Irikura et al. [83, 84] found that methane can be spontaneously activated by the third-row metal ion Os^+, Ir^+, Pt^+, etc., yielding the metal carbene cation and H_2. The third-row transition metal elements generally are more reactive with methane than the first- and second-row metals. This notable difference in reactivity can be attributed basically to much stronger π bonding interactions as the shell number of elements in the periodic table increases. Extensive calculations at different levels of theory have been conducted on the bonding and thermodynamic properties of cationic metal methylenes MCH_2^+ [52, 72, 79, 80, 85].

The remarkable reactivity of cationic transition metal clusters, especially small cationic platinum clusters toward methane, has been elucidated by a series of experiments [7, 8, 50, 86] in detail, in combination with theoretical calculations [50, 73, 87]. The overall reaction of Pt^+ and methane is calculated to be exothermic by 0.8 kcal mol^{-1} by the B3LYP approach [73]. Furthermore, Wesendrup et al. [88] noted that the bare Pt^+ cation catalyzes the reaction of methane with molecular oxygen to yield methanol, formaldehyde, and other oxygen-containing products. Aschi et al. [14] proposed a gas-phase model for the single Pt^+-catalyzed coupling of methane and ammonia to account for the industrial synthesis of hydrogen cyanide. In addition, small cationic platinum clusters can induce dehydrogenation of simple hydrocarbons [27, 89, 90].

Recently, Achatz et al. [7] and Koszinowski et al. [69] have observed that methane could be dehydrogenated effectively by Pt_n^+ clusters ($n \leq 9$), giving rise to the species $Pt_nCH_2^+$ through the dehydrogenation reaction $Pt_n^+ + CH_4 \rightarrow Pt_nCH_2^+ + H_2$, but there is an exception for the metal tetramer Pt_4^+. The reactivity of Pt_4^+ toward CH_4 is sharply dropped to the minimum among all cationic clusters, whereas the anionic Pt_4^- tetramer is quite reactive. Interestingly, Koszinowski et al. [17, 18] reported that the heteronuclear metal dimers PtM^+ (M = Cu, Ag, Au, Pt) are capable of efficiently dehydrogenating methane, leading to metal carbenes $PtMCH_2^+$.

The metal methylenes $PtMCH_2^+$ (M = Cu, Ag, Au, Pt) can be served as the important precursors to C−N and C−O bond coupling for the synthesis of HCN and HCOOH in the gas phase [15, 64, 67, 70]. For example, the metallic carbenes $PtAuCH_2^+$ and $Pt_nCH_2^+$ react with NH_3 to produce H_2, AuH, and important C–N bond coupling intermediates according to reactions (1–4b). The reactions of $Pt_nCH_2^+$ with O_2 can produce the C–O bond coupling products [C, H_2, O_2] according to reaction (5). Further experimental studies reveal that the reactivity of species $Pt_nCH_2^+$ (n = 2–4) with O_2 depends on the cluster size. For example, the measured reaction efficiency of $PtCH_2^+$ is 0.028, while that of $Pt_4CH_2^+$ is 0.17, much more efficient than the former [74]. In the C–N bond coupling, the carbene species $PtCH_2^+$ reacting with NH_3 may result in three different products, whereas the clusters $Pt_nCH_2^+$ ($n \geq 2$) exclusively dehydrogenate the CH_2 moiety [75]. Theoretically, the reactions of metal carbenes $PtMCH_2^+$ with small molecules NH_3 and O_2 have been investigated, and recent calculations in this area have been reviewed herein.

$$PtAuCH_2^+ + NH_3 \rightarrow [Pt, Au, C, H_3, N]^+ + H_2 \quad (1)$$

$$[Pt, Au, C, H_3, N]^+ + NH_3 \rightarrow [Pt, Au, C, H_4, N_2]^+ + H_2 \quad (2)$$

$$\rightarrow [Pt, C, H_5, N_2]^+ + AuH \quad (3)$$

$$Pt_nCH_2^+ + NH_3 \rightarrow [Pt_n, C, N, H_3]^+ + H_2 \quad (4a)$$

$$[Pt_n, C, N, H_3]^+ + NH_3 \rightarrow [Pt_n, C, N_2, H_6]^+ \quad (4b)$$

$$Pt_nCH_2^+ + O_2 \rightarrow Pt_n^+ + [C, H_2, O_2] \quad (5)$$

2 Computational Methods

The hybrid B3LYP [91, 92] and BPW91 [93, 94] functionals were used to search for the structure of stationary points on the potential energy surface (PES). The nature of minima and transition states on PES was assessed by frequency calculations. All

B3LYP and BPW91 calculations have been performed by Gaussian 98 [95] and ADF [96–99] packages, respectively. In geometry optimization and frequency calculations by B3LYP, the double zeta basis set augmented by polarization functions was used, where the standard 6-31G* basis set was employed for C, N, and H atoms, and the Lanl2dz basis set in combination with Hay and Wadt's relativistic effective core potential (ECP) [100–102] was used for Pt and Au atoms. Relative energies along the reaction channel were predicted by single-point energy calculations with the 6-311 + G(3df,2df,2p) basis set for the nonmetal atoms and the Lanl2dz ECP basis set augmented with an f-polarization function [103] for the transition metal atoms. A metal dimer $PtAu^+$ has been used to validate the reliability of the B3LYP functional. DFT calculations predict that the energy difference between the ground state $^1\Sigma^+$ and the excited triplet state $^3\Delta$ is 7 kcal mol^{-1}, which is intermediate between 9 kcal mol^{-1} by CCSD and 4.3 kcal mol^{-1} by CCSD(T). At the MRSDCI level [104], the low-lying state $^3\Delta$ is higher in energy than the ground state by 4.7 kcal mol^{-1}. In previous theoretical investigations on the interaction of Pt_2/Pd_2 with H_2/CH_4, B3LYP calculations show good agreement with the sophisticated treatment [105].

In BPW91 calculations by the ADF package, the zero-order regular approximation formalism (ZORA) without the spin–orbit effect was used [106, 107]. The 1s–2p orbitals for Cu, 1s–3d orbitals for Ag, 1s–4f orbitals for Pt and Au, and 1s–2s orbitals for C and N are kept frozen, respectively, in the frozen core approximation, and the valence orbitals based on the Slater-type orbital are expanded within the triple zeta basis set augmented with two polarization functions. Frequency analyses have been used to assess the stability of the optimized structures. Calculated zero-point energy (ZPE) corrections have been incorporated into total energies in estimation of relative energies.

To calibrate the performance of the chosen BPW91 functional, selected bimetallic dimers have been calculated. A comparison of present results with those from Dirac four-component relativistic calculations [108] is shown in Table 1. As Table 1 displays, the BPW91-optimized bond lengths within the ZORA approximation are in good agreement with those by the Dirac four-component-MP2 (4c-MP2) calculations and by experiment. For example, the optimized Pt–Cu bond length of PtCu is 2.313 Å, which is comparable with the Dirac 4c-MP2 value of 2.328 Å and the experimental value of 2.335 Å [109]. Generally, the nonrelativistic BPW91 calculations strikingly overestimate the internuclear distances of dimers,

Table 1 Comparison of calculated internuclear distances (in Å) by the ZORA BPW91 and nonrelativistic BPW91 approaches with Dirac four-component relativistic MP2 calculations

Dimers	4c-MP2 [108]	ZORA	Nonrelativistic	Expt. [109]
$PtCu^+$	2.419	2.317	2.569	
PtCu	2.328	2.312	2.458	2.335
$PtAg^+$	2.699	2.675	2.874	
PtAg	2.530	2.543	2.700	
$PtAu^+$	2.501	2.481	2.950	
PtAu	2.455	2.509	2.755	

Table 2 Comparison of predicted and experimental internuclear distances (R_e in Å) and adiabatic ionization potential (AIP in eV) for neutral metal dimers

Species	Property	BP86	BLYP	BPW91	Expt. [109, 111–114]
$Pt_2(^3\Sigma_g^-)$	R_e	2.3503	2.3786	2.3504	2.3329
	AIP	8.80	8.61	8.67	8.68
$PtCu(^2\Delta)$	R_e	2.3006	2.3395	2.3123	2.3353
	AIP	8.81	8.62	8.62	8.26
$CuAg(^1\Sigma^+)$	R_e	2.3978	2.4002	2.3983	2.3735
	AIP	8.29	8.19	8.04	7.78
$CuAu(^1\Sigma^+)$	R_e	2.3365	2.3684	2.3426	2.3302
	AIP	8.60	8.94	8.50	8.74

particularly for the positively charged species such as $PtAu^+$. This implies that the relativistic effect plays an important role to enhance metal–metal bonding due to the well-known 6s contraction in $PtAu^+$ and PtAu. As Table 2 shows, at the ZORA level, the predicted internuclear distances and adiabatic ionization potentials (AIP) of neutral metal dimers by the gradient-corrected functionals BP86 [93, 110], BLYP [92, 93], and BPW91 [93, 94] are reasonably in agreement with available experimental values [109, 111–114]. The BPW91-predicted dissociation energy of Pt_2 is 3.67 eV, higher than the experimental value by 0.5 eV [115], but it is comparable with the sophisticated CASPT2 treatment [77]. Accordingly, the BPW91 calculations within the ZORA approximation may present reliable description of thermodynamic and structural properties of these bimetallic systems involved in the gas-phase reactions.

3 Formation of the Platinum–Carbene Cations

3.1 Reactions of Pt_n^+ (n = 1–4) with CH_4

3.1.1 $Pt^+ + CH_4$

Extensive experimental and theoretical studies on the reaction of Pt^+ with methane show that the ground-state Pt^+ ions can efficiently dehydrogenate CH_4 to generate $PtCH_2^+$, and this exothermic process is only observed at low energies [50]. The activation of methane generally follows an oxidative addition mechanism, in which the oxidative addition of a C−H bond to Pt^+ forms an intermediate of $H-M^+-CH_3$ at first, and followed by the reductive elimination of H_2, the metallic carbene $PtCH_2^+$ is formed. The dihydrogen coupling in $H-M^+-CH_3$, leading to $(H_2)M^+CH_2$, was predicted to be the rate-determining step with a barrier of 1.05 eV by B3LYP/TZ + HW [50]. The remarkable reactivity of Pt^+ toward methane dehydrogenation may be attributed to the relativistic stabilization of the metal carbene cluster $PtCH_2^+$ [72].

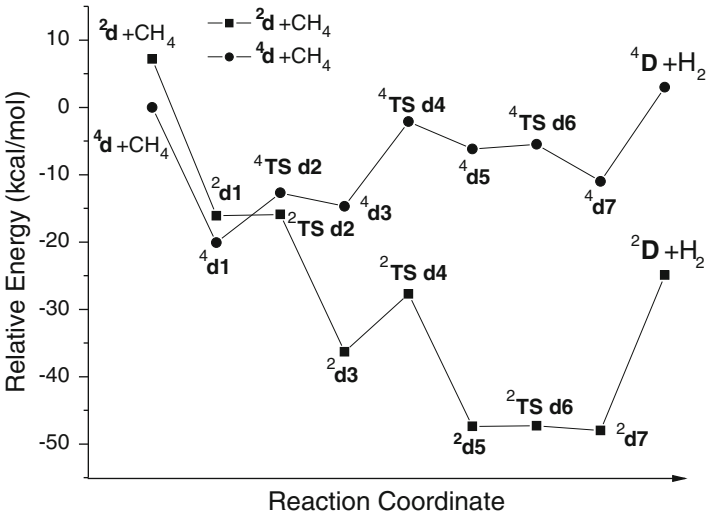

Fig. 1 Potential energy profiles of reactions of CH_4 and Pt_2^+ in quartet and doublet states

3.1.2 $Pt_2^+ + CH_4$

The neutral Pt_2 cluster was predicted to have a triplet ground state of $^3\Sigma_g^-$ [77, 115–118]. The $X^3\Sigma_g^-$ state has a bond length of 3.350 Å and an AIP of 8.67 eV by BPW91, which are in good agreement with experimental values [112]. The cationic Pt_2^+ cluster was predicted to have a quartet ground state of $^4\Sigma_u^-$, and the next stable doublet state $^2\Sigma_u^-$ is only 7.2 kcal mol^{-1} above the ground state [119]. Since both states have comparable stabilities, they can be served as initial states of Pt_2^+ in the dehydrogenation reaction. Figure 1 displays the relative energy profiles for the reaction of Pt_2^+ and CH_4 on the doublet and quartet PESs. Optimized structures and thermodynamic values of species in reaction are shown in Fig. 2 and Table 3, respectively.

Figure 1 displays two plausible mechanisms for dehydrogenation of methane mediated by Pt_2^+. In the quartet route, formation of the molecule–ion complex $Pt_2(CH_4)^+$ (**^{4}d1**) releases an energy of 20.1 kcal mol^{-1}. The complex **^{4}d1** proceeds to a hydride intermediate $PtPt(CH_3)H^+$ (**^{4}d3**) via the C–H bond activation with a barrier of 7.4 kcal mol^{-1}. Followed by the second C–H bond activation and association of two hydrogen atoms, the molecular complex $(H_2)Pt(\mu\text{-}CH_2)Pt^+$ (**^{4}d7**) is formed. The loss of H_2 in the complex **^{4}d7** requires an energy of 14.0 kcal mol^{-1}, giving rise to products $Pt(\mu\text{-}CH_2)Pt^+$ (**^{4}D**) and H_2. The overall reaction on the quartet-state PES has free energies of reaction ΔG of 4.0 kcal mol^{-1}.

The reaction in the doublet pathway follows the same mechanism with the quartet state. The doublet reaction is significantly exothermic by 32.1 kcal mol^{-1}. The free energies of reaction ΔG is −30.9 kcal mol^{-1}. As Fig. 1 shows, the reactive species is likely to change its spin multiplicity from the quartet state to the doublet state in reaction [120]. The lowest cost reaction pathway will start from the quartet

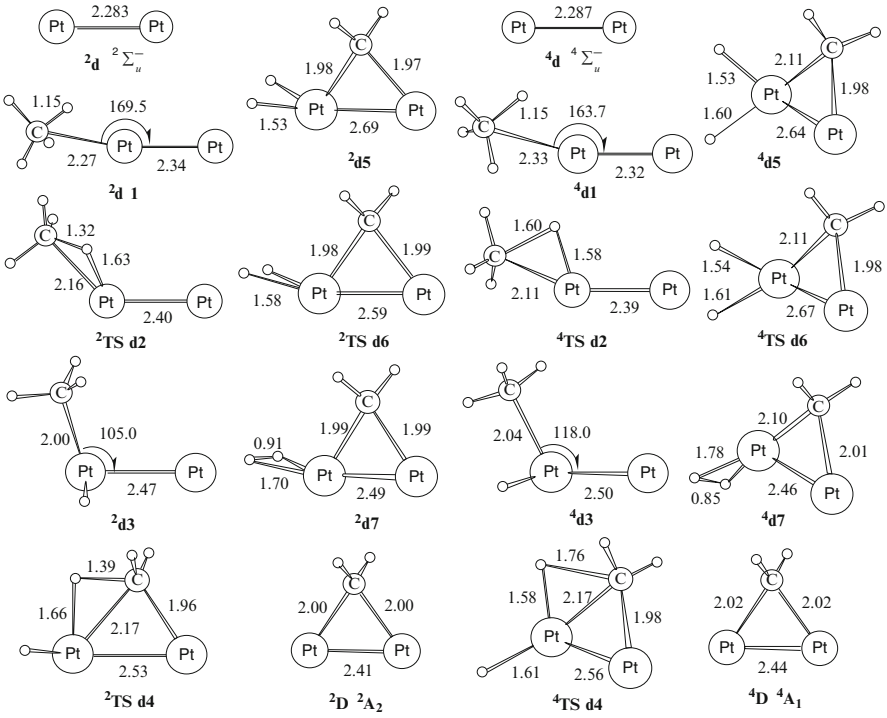

Fig. 2 Optimized structures of transition states and intermediates corresponding to Fig. 1 (Bond lengths in angstroms and bond angles in degrees)

Table 3 The calculated thermodynamic values (kcal mol^{-1}) at 298.15 K of the reaction of Pt_2^+ with CH_4 in doublet and quartet states

Species	ΔE°	ΔH°	ΔG°	Species	ΔE°	ΔH°	ΔG°
^{2}d + CH_4	7.2	9.2	9.2	**^{4}d** + CH_4	0.0	0.0	0.0
^{2}d1	−16.1	−16.7	−9.2	**^{4}d1**	−20.1	−20.1	−14.3
^{2}TS d2	−15.9	−16.6	−9.3	**^{4}TS d2**	−12.7	−13.1	−6.1
^{2}d3	−36.3	−36.8	−29.9	**^{4}d3**	−14.7	−15.0	−8.5
^{2}TS d4	−27.7	−28.5	−20.5	**^{4}TS d4**	−2.1	−2.9	5.0
^{2}d5	−47.4	−48.1	−40.7	**^{4}d5**	−6.2	−6.8	0.7
^{2}TS d6	−47.3	−48.2	−39.9	**^{4}TS d6**	−5.5	−5.8	0.3
^{2}d7	−48.0	−48.8	−40.7	**^{4}d7**	−11.0	−11.7	−3.9
^{2}D + H_2	−24.9	−24.4	−23.7	**^{4}D** + H_2	3.0	3.5	4.0

state. Followed by the first C–H bond activation, the quartet molecular complex $Pt_2(CH_4)^+$ (**^{4}d1**) may evolve into the doublet intermediate $PtPt(H)(CH_3)^+$ (**^{2}d3**) with spin flip. Subsequently by consecutive isomerizations and elimination of H_2, the reaction gives the doublet product $Pt(\mu\text{-}CH_2)Au^+$ (**^{2}D**). The loss of H_2 from the molecular complex $(H_2)Pt(\mu\text{-}CH_2)Pt^+$ (**^{2}d7**) as a rate-determining step requires 23.1 kcal mol^{-1}. The spin transition here will enhance the reactivity of Pt_2^+. This

is consistent with the experimental finding that Pt_2^+ is more efficient than single Pt^+ in dehydrogenating methane [7, 69]. The effects of spin flip on the gas-phase ion–molecule reactions have been reviewed by Schwarz [120].

3.1.3 $Pt_3^+ + CH_4$

The relative energy profiles of reaction of Pt_3^+ with CH_4 are shown in Fig. 3, and corresponding structures of species in reaction are displayed in Fig. 4. The most stable structure **e** of the trimer is equilateral triangle in D_{3h} symmetry, as shown by previous calculations [119]. The Pt–Pt separation in the ground state ($^2A_1''$) is 2.45 Å.

The formation of complex $Pt_3(CH_4)^+$ (**e1**) of **e** with CH_4 has an exothermicity of 18.5 kcal mol^{-1}, in agreement with the previous predicted binding energy of 16.6 kcal mol^{-1} [121]. The effort to locate other isomers of the complex $Pt_3(CH_4)^+$ has been made and only an isoenergetic analog of **e1** was found. Cleavage of the first C–H bond gives rise to an intermediate **e3** with a small barrier of 4.0 kcal mol^{-1}. Through consecutive hydrogen transfers, **e3** evolves to the more stable isomer **e7**. The intermediate **e7** undergoes the second C–H bond activation with a barrier of 12.0 kcal mol^{-1} and intramolecular isomerizations, yielding a dihydrogen complex **e13**. The molecular complex **e13** requires 28.5 kcal mol^{-1} to release H_2, yielding the product **E**. As Fig. 3 displays, the loss of dihydrogen is the rate-determining step for the reaction of Pt_3^+ with CH_4. The entire reaction has an exothermicity of 10.8 kcal mol^{-1} and free energies of reaction ΔG of −8.9 kcal mol^{-1}.

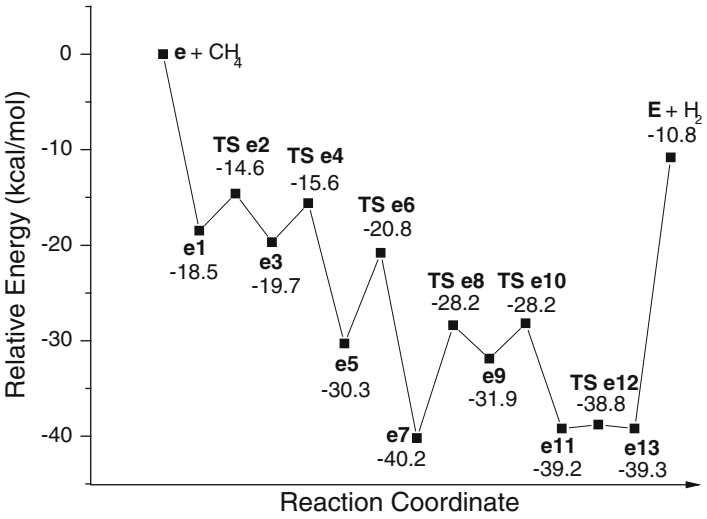

Fig. 3 Potential energy profiles of reactions of PtM^+ (M = Cu, Ag, Au, Pt) and CH_4

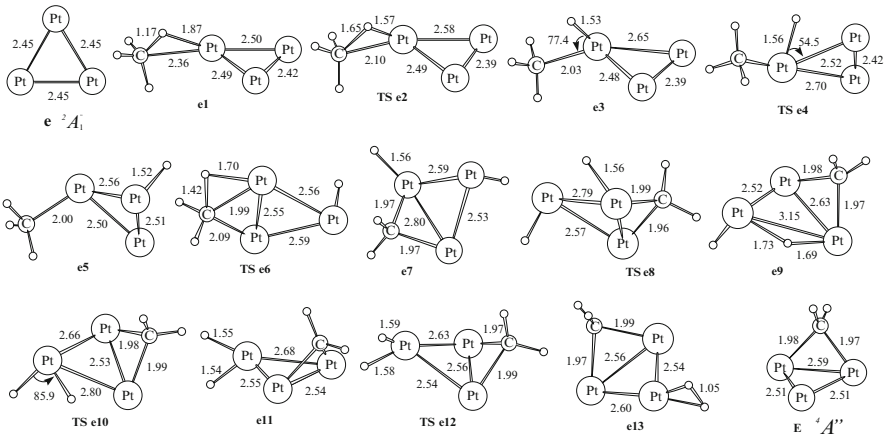

Fig. 4 Optimized structures of transition states and intermediates corresponding to Fig. 3 (Bond lengths in angstroms and bond angles in degrees)

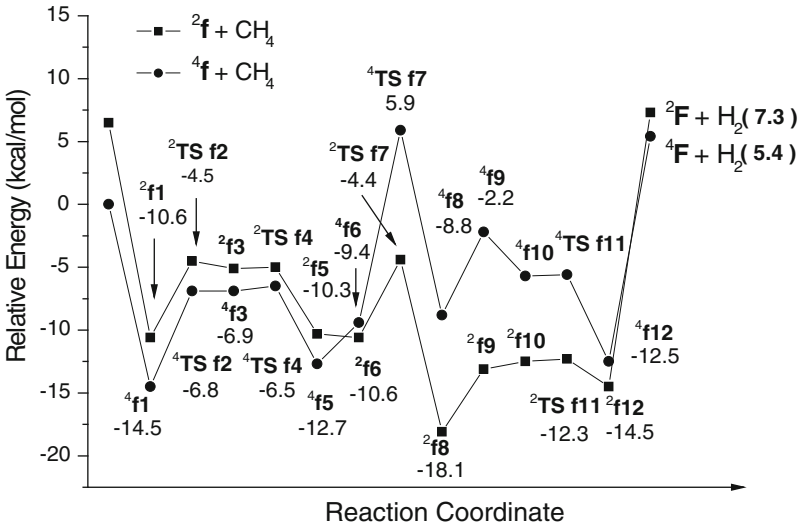

Fig. 5 Potential energy profile of reaction of Pt_3^+ and CH_4

3.1.4 $Pt_4^+ + CH_4$

The doublet and quartet potential energy profiles of the reaction of Pt_4^+ with CH_4 are shown in Fig. 5. The corresponding structures of species in reaction are displayed in Fig. 6. The Pt_4^+ tetramer has been predicted to be a stable tetrahedral structure (**^{4}f**) in T_d symmetry [119]. The lowest energy state $^4A_1$ arises from an electronic configuration of $a_1{}^4e^8t_2{}^{18}t_1{}^6t_1{}^3$. The next stable doublet state $^2A_1$ has a

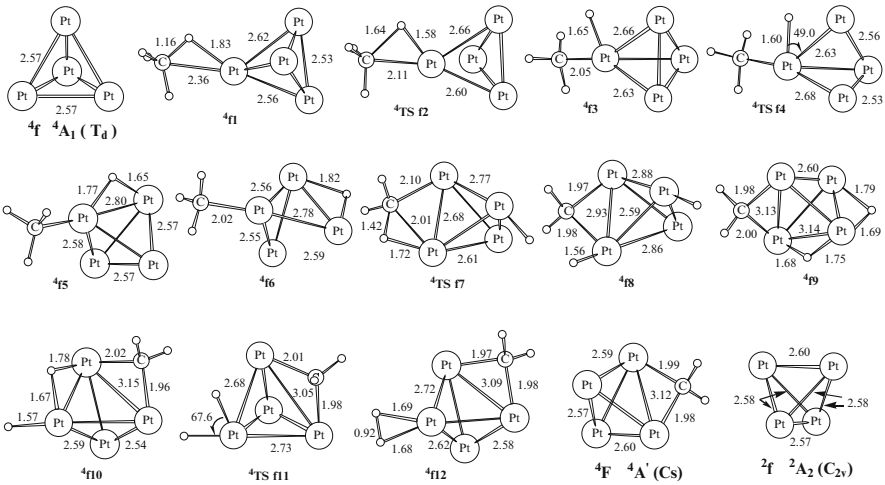

Fig. 6 Optimized structures of transition states and intermediates corresponding to Fig. 5 (Bond lengths in angstrom and bond angles in degree)

stable C_{2v} structure (**^{2}f**), which is less stable than the quartet state **^{4}f** by 6.5 kcal mol^{-1}.

On the quartet PES, the formation of complex **^{4}f1** of Pt_4^+ with CH_4 releases an energy of 14.5 kcal mol^{-1}. In full geometry optimization, distinct initial structures of the complex $Pt_4(CH_4)^+$ evolve to **^{4}f1** or its analog with the same Pt···(CH_4) coordination. The isoenergetic isomers arise from internal rotation of the distal Pt_3 subunit around Pt···(CH_4). Followed by cleavage of the first C–H bond and hydrogen migration, a less stable intermediate **^{4}f5** is generated. The intermediate **^{4}f5** requires 3.3 kcal mol^{-1} to yield **^{4}f6**. **^{4}f6** proceeds to **^{4}f8** through the transition state **^{4}TS f7** with a barrier of 15.3 kcal mol^{-1}. The intermediate **^{4}f8** evolves to the dihydrogen complex **^{4}f12** via hydrogen shifts. The release of H_2 from **^{4}f12** requires 17.9 kcal mol^{-1}. The overall reaction on the quartet PES is slightly endothermic by 5.4 kcal mol^{-1}, and the calculated free energies of the entire reaction ΔG is 6.7 kcal mol^{-1}.

As Fig. 5 shows, the reaction on the doublet PES follows similar mechanisms with the quartet state. The overall reaction is endothermic by 7.3 kcal mol^{-1}. Note that the spin transition from the quartet to doublet state is probably involved in the hydrogen transfer process from **^{4}f5** to **^{4}f6**. The spin transition from **^{4}f6** to the more stable **^{2}f6** will significantly lower the barrier height for the second C–H bond activation.

Unlike Pt_2^+ and Pt_3^+, the dehydrogenation of CH_4 by Pt_4^+ has free energies of reaction ΔG of 6.7 kcal mol^{-1}. Thus the overall reaction of Pt_4^+ with CH_4 is not favorable thermodynamically. The calculated results support the experimental finding that Pt_4^+ has an anomalously reactivity toward dehydrogenation of CH_4 with respect to other Pt_n^+ (n = 1, 2, 3, 5) [7, 69]. However, the predicted barriers are generally low and the reaction may be favorable dynamically. Once the

insufficient thermodynamic drive is compensated, the reactivity will be improved strikingly as observed experimentally [27].

Contrary to the dehydrogenation process, the reverse reaction $Pt_4CH_2^+ + H_2 \rightarrow Pt_4^+ + CH_4$ should be facile thermodynamically, and the barrier of the rate-determining step from **e7** to **e5** is 19.4 kcal mol^{-1} in the formation of methyl group. Experimentally, the reverse reaction was observed for $Pt_4CH_2^+$ [69], whereas the other species $Pt_nCH_2^+$ ($n = 2, 3$) did not react with H_2.

3.2 *Reactions of PtM^+ (M = Cu, Ag, Au) with CH_4*

Theoretical studies of the heteronuclear bimetallic PtM (M = Cu, Ag, Au) clusters are relatively scarce [104, 122, 123]. Previous calculations by Dai et al. [104] reveal that the ground state of the cationic $PtAu^+$ cluster is $^1\Sigma^+$ with a valence electron configuration of $1\sigma^2 2\sigma^2 1\pi^4 1\pi^4 1\delta^4 2\delta^4$. Similarly, present relativistic DFT calculations show that these cationic bimetallic clusters PtM^+ (M = Cu, Ag, Au) have the same ground states of $^1\Sigma^+$.

Among mononuclear cations M^+ (M = Pt, Cu, Ag, Au), the oxidation addition catalyzed by Pt^+ constitutes the first step in the dehydrogenation reaction of methane [5, 58, 120], whereas other metal cations are inactive toward CH_4 due to relatively weak metal–carbon bonds and closed-shell structures in their ground states. Generally, the methane activation to form MCH_2^+ requires a metal carbene bond strength of 111.0 kcal mol^{-1} thermodynamically [4, 124]. For Au^+, the reactive excited state of $d^9s^1(^3D_3)$ as a precursor to Au–H and Au–C couplings is higher in energy than the ground state of d^{10} ($^1S_0$) by 43.0 kcal mol^{-1} [83, 84]. Therefore, the reactive states of Au^+, Ag^+, and Cu^+ are less accessible energetically, and the terminal Pt with an open "d" subshell configuration in these bimetallic cationic clusters should have relatively high activity. Further calculations show that the hydride $Pt–M(CH_3)H^+$ from C–H activation at the M site (M = Cu, Ag, Au) is less stable than $M–Pt(CH_3)H^+$. For example, $Pt–Au(CH_3)H^+$ is 20 kcal mol^{-1} above $Au–Pt(CH_3)H^+$. The terminal Pt is thus considered as the initial active site for the first C–H bond activation of methane.

Figure 7 presents relative energy profiles of reactions of PtM^+ (M = Cu, Ag, Au) with methane. Corresponding geometries and thermodynamic values of selected species in reaction are shown in Fig. 8 and Table 4, respectively. As shown in Table 4 and Fig. 7, formation of additive products $AuPt(CH_3)H^+$ (**i1**), $AgPt(CH_3)H^+$ (**h1**), and $CuPt(CH_3)H^+$ (**g1**) releases an energy of 68.5, 64.6, and 63.2 kcal mol^{-1}, respectively. Detailed PES scan reveals that the first C–H activation of methane mediated by these cationic clusters is barrier free to yield the hydride complexes. Followed by the second C–H activation, the stable intermediates $(H)_2Pt(\mu\text{-}CH_2)Au^+$(**i3**), $(H)_2Pt(\mu\text{-}CH_2)Ag^+$(**h3**), and $(H)_2Pt(\mu\text{-}CH_2)Cu^+$(**g3**) are formed through transition states **TS i2**, **TS h2**, and **TS g2**, respectively. Corresponding barriers are 25.2, 36.0, and 28.1 kcal mol^{-1}, respectively. Such

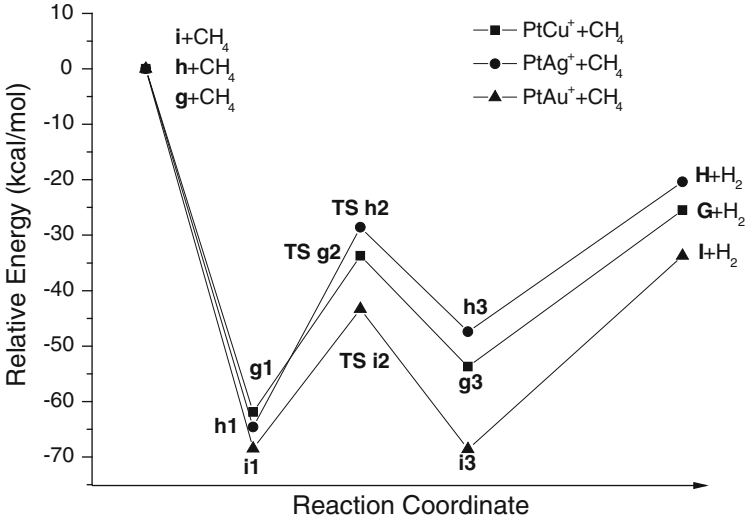

Fig. 7 Potential energy profiles of reactions of methane and Pt_4^+ in quartet and doublet states

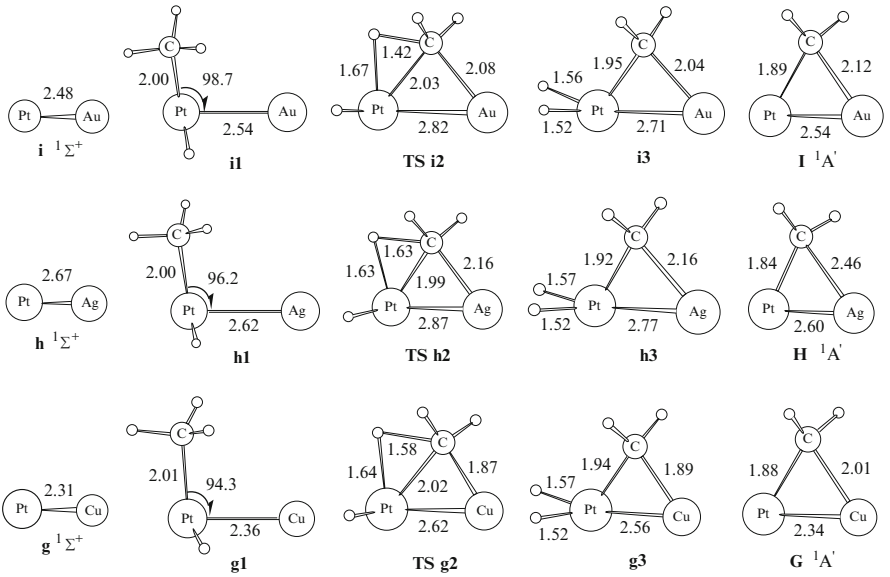

Fig. 8 Optimized structures of transition states and intermediates corresponding to Fig. 7 (Bond lengths in angstrom and bond angles in degree)

transition states have been confirmed by further frequency analyses and IRC [125, 126] calculations.

The elimination of dihydrogen in the intermediates **i3**, **h3**, and **g3** requires energies of 21.6, 19.7, and 28.3 kcal mol^{-1}, respectively, yielding bimetallic

Table 4 The calculated thermodynamic values (kcal mol^{-1}) at 298.15 K of species in the reactions of PtM^+ (M = Cu, Ag, Au) with CH_4

Species	ΔE°	ΔH°	ΔG°	Species	ΔE°	ΔH°	ΔG°
i + CH_4	*0.0*	*0.0*	*0.0*	**G** + CH_4	*0.0*	*0.0*	*0.0*
i1	−68.5	−68.9	−61.6	**g1**	−63.2	−63.1	−56.0
TS i2	−43.3	−44.2	−35.9	**TS g2**	−35.1	−35.3	−27.1
i3	−68.6	−69.4	−61.0	**g3**	−55.0	−55.2	−47.0
I + H_2	−33.7	−33.1	−32.7	**G** + H_2	−26.8	−25.5	−25.4
h + CH_4	*0.0*	*0.0*	*0.0*				
h1	−64.6	−65.2	−57.5				
TS h2	−28.6	−29.5	−20.9				
h3	−47.4	−48.3	−39.5				
H + H_2	−20.4	−19.5	−19.8				

carbenes Pt(μ-CH_2)Au^+(**I**), Pt(μ-CH_2)Ag^+(**H**), and Pt(μ-CH_2)Cu^+(**G**). These products as precursors can react with ammonia [15, 17, 18, 64, 67, 70], giving rise to C–N coupling and consecutive hydrogenation. Unlike the case of methane activation by Pt^+ [73, 87], no stable dihydrogen complex was found in calculation. The overall hydrogenation reactions catalyzed by the cationic PtM^+ clusters (M = Au, Ag, Cu) have free energies of reaction ΔG of −32.7, −19.8, and −25.4 kcal mol^{-1}.

3.3 *Electronic Structure and Reactivity of PtM^+ (M = Cu, Ag, Au)*

As illuminated by experimental studies, the calculated results indicate that the bimetallic clusters PtM^+ (M = Cu, Ag, Au, Pt) exhibit dissimilar reactivity with the single Pt^+. Generally, the bimetallic clusters exhibit higher activity toward CH_4 activation with respect to Pt^+. The remarkable reactivity of heteronuclear clusters PtM^+ (M = Cu, Ag, Au) toward the first C–H activation can be understood through the frontier orbital interaction and the simple donor–acceptor model [127, 128]. As Scheme 1 displays, when CH_4 approaches $PtAu^+$, the lowest unoccupied molecular orbital (LUMO) of $PtAu^+$ and the C–H bonding orbital of CH_4 have the same phase patterns and these phase-adaptation frontier orbitals can efficiently interact to activate the C–H bond. Note that the highest occupied molecular orbital (HOMO) of $PtAu^+$ is mainly from Au and thus, the presence of Au will enhance interaction between the HOMO and the σ* orbital (LUMO) of CH_4 with respect to single Pt^+. The cooperative bonding interactions in the complex of $PtAu^+$ with CH_4, where the metal cationic cluster behaves as an acceptor to reduce bonding electrons in the C–H σ bond and also as a donor to increase antibonding electrons in the C–H σ* bond of methane, result in the cleavage of C–H bond. For other PtM^+/CH_4 systems, there are similar orbital interaction mechanisms for the C–H bond activation.

Similarly, such cooperative bonding interactions among the frontier orbitals of bimetallic clusters and the H–H σ and σ* orbitals will make the dihydrogen

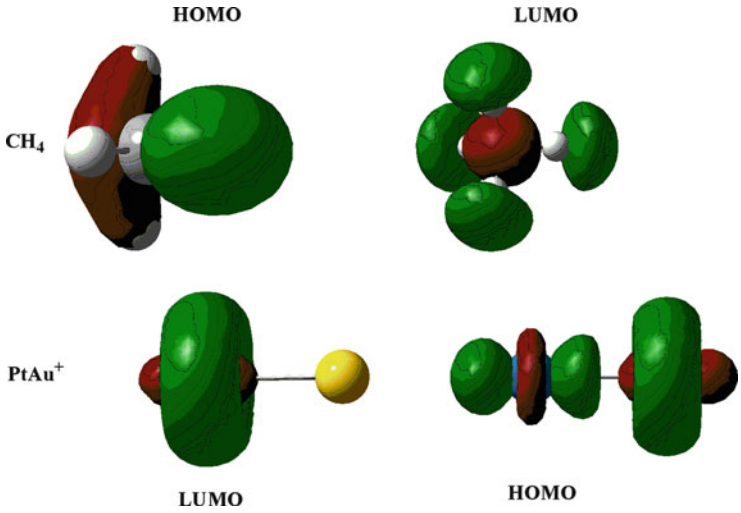

Scheme 1 HOMOs and LUMOs of CH_4 and $PtAu^+$

Table 5 Mulliken populations of PtM^+ (M = Cu, Ag, Au) and Pt_n^+ (n = 2–4)

Species	Atoms	Mulliken populations	Species	Atoms	Mulliken populations
$PtAu^+$	Pt	$6s^{0.48}\ 5d^{8.82}\ 6p^{0.06}$	$^2Pt_2^+$	Pt	$6s^{0.99}\ 5d^{8.38}\ 6p^{0.08}$
	Au	$6s^{0.81}\ 6d^{9.68}\ 6p^{0.08}$	$^4Pt_2^+$	Pt	$6s^{0.99}\ 5d^{8.39}\ 6p^{0.08}$
$PtAg^+$	Pt	$6s^{0.25}\ 5d^{9.25}\ 6p^{0.04}$	$^2Pt_3^+$	Pt	$6s^{0.77}\ 5d^{8.71}\ 6p^{0.13}$
	Ag	$5s^{0.39}\ 4d^{9.95}\ 5p^{0.08}$	$^2Pt_4^+$	Pt1, Pt2	$6s^{0.71}\ 5d^{8.77}\ 6p^{0.19}$
$PtCu^+$	Pt	$6s^{0.54}\ 5d^{8.88}\ 6p^{0.02}$		Pt3, Pt4	$6s^{0.67}\ 5d^{8.89}\ 6p^{0.17}$
	Cu	$6s^{0.64}\ 5d^{9.70}\ 6p^{0.12}$	$^4Pt_4^+$	Pt	$6s^{0.68}\ 5d^{8.84}\ 6p^{0.17}$
Pt^+	Pt	$6s^0\ 5d^9$			

complexes of PtM^+ (M = Cu, Ag, Au) unstable and thus, no stable molecular complexes of H_2 have been found in the dehydrogenation of CH_4, as DFT calculations show.

Mulliken atom populations in Table 5 reveal that the platinum in PtM^+ (M = Cu, Ag, Au) has an approximate $5d^9$ configuration similar to Pt^+, and Cu, Ag, and Au have an approximate $(n-1)d^{10}$ structure and partial ns populations. Such almost closed "d" subshell configurations suggest that the Cu, Ag, and Au terminals are inert toward methane in their ground states. Thus, the terminal platinum with the open "d" subshell in PtM^+ is still the active site for the C–H bond activation.

Mulliken populations of Pt_2^+ display that the platinum in the doublet and quartet states has an approximate s^1d^8 configuration with three unpaired electrons, similar to the excited Pt^+ cation. Such active electronic structure of Pt in Pt_2^+ is able to form three covalent bonds and may facilitate the second C–H bond activation with a low barrier of 8.6 kcal mol^{-1}, as shown in Fig. 1. This consecutive C–H activation energy in $PtPt(CH_3)H^+$ (^{2}**d3**) is much smaller than corresponding barriers of 28.1 for $CuPt(CH_3)H^+$ (**g1**), 36.0 for $AgPt(CH_3)H^+$ (**h1**), and 25.2 kcal mol^{-1} for $AuPt(CH_3)H^+$ (**i1**), respectively.

4 Reactions of $Pt_nCH_2^+$ with O_2

4.1 Structure and Stability of Complex of $Pt_4CH_2^+$ with O_2

The carbene cation $Pt_4CH_2^+$ has a ground state of $^4A_1$ in C_{2v} symmetry, and a low-energy doublet state of $^2B_2$ is slightly less stable than the ground state by 1.9 kcal mol^{-1} [61]. Our BPW91 calculations show that the intramolecular hydrogen transfer from the CH_2 moiety of $Pt_4CH_2^+$ to the vicinal platinum has a high barrier of 27.6 kcal mol^{-1}, yielding a less stable isomer. Therefore, the isolated quartet $Pt_4CH_2^+$ has relatively high stability in the gas phase, and the bridging CH_2 moiety can be involved in further reactions with O_2, NH_3, and H_2O [67].

Figure 9 displays the optimized structures and relative energies of the complex $Pt_4CH_2(O_2)^+$ in different spin states and configurations, where the predicted energies of the doublet and quartet complexes in parentheses are relative to the energy sum of the ground states of $Pt_4CH_2^+$ and O_2. The superscripts **2** and **4** such as in structures **^{2}complex1** and **^{4}complex1** denote the doublet and quartet states, respectively. Calculations indicate that the structures of **^{2}complex1** and **^{4}complex1**

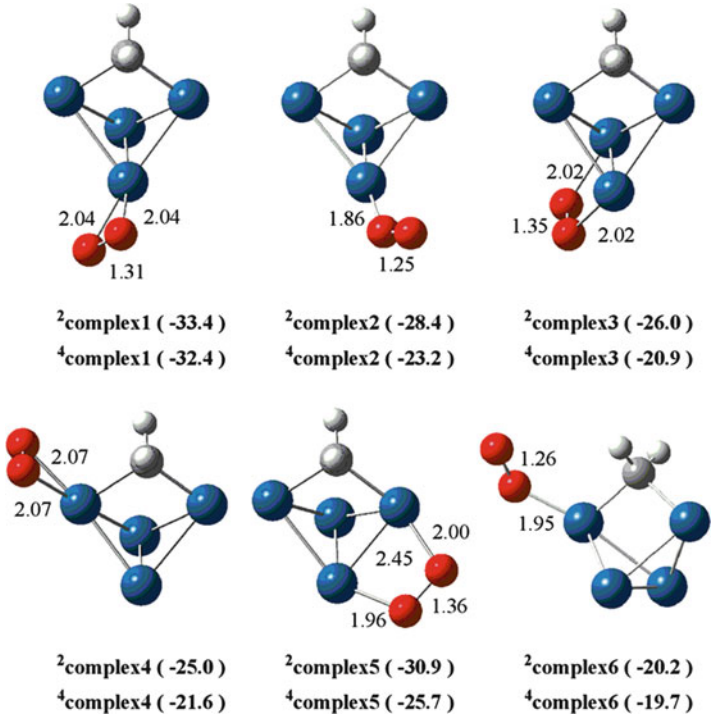

Fig. 9 Optimized structures (in angstrom) of $Pt_4CH_2(O_2)^+$ and calculated relative energies (in kcal mol^{-1}) with respect to the reactants of $Pt_4CH_2^+$ and O_2 in their ground states

with the side-on dioxygen are the most favorable coordination patterns energetically, where the doublet state is slightly lower in energy than the quartet counterpart by 1.0 kcal mol^{-1}. The small doublet–quartet energy difference of 1.0 kcal mol^{-1} may give rise to the spin flip between the different spin states [129]. The formation of the low-energy doublet structure can be rationalized through the visual frontier orbital theory and donor–acceptor interactions [125–128]. The schematic illustration for the frontier orbital interactions of $Pt_4CH_2^+$ with O_2 is depicted in Fig. 10. As shown in Fig. 10a, the symmetries of the singly occupied molecular orbitals (SOMOs) of $Pt_4CH_2^+$ are b_1, b_2, and a_2, respectively. The degenerate antibonding π* orbitals of O_2 have b_1 and a_2 symmetries under the C_{2v} point group. These electrons in b_1 and a_2 SOMOs of $Pt_4CH_2^+$ may couple with the two unpaired electrons in the symmetry-adaptation antibonding π* orbitals of O_2 to form two bonding electron pairs in the doublet **^{2}complex1**. As Fig. 10b displays, there are many possible local orbital-phase adaptation patterns for the association of $Pt_4CH_2^+$ with O_2. Hence, the formed complexes exhibit distinct structural varieties, as shown in Fig. 9. Among these complexes, **^{2}complex1** in the doublet state is the lowest energy species and it should be taken as the precursor of consecutive reactions of $Pt_4CH_2^+(O_2)$.

4.2 *Mechanisms of Reactions of $Pt_4CH_2^+$ with O_2*

Herein we proposed plausible mechanisms for the reaction of $Pt_4CH_2^+$ with O_2, which are different from those for the reaction of $PtCH_2^+$ with O_2 suggested by Pavlov et al. [73]. Owing to the presence of sp^2-hybrid carbon atom in the carbene species $PtCH_2^+$, the direct C–O bond coupling between $PtCH_2^+$ and O_2 is available.

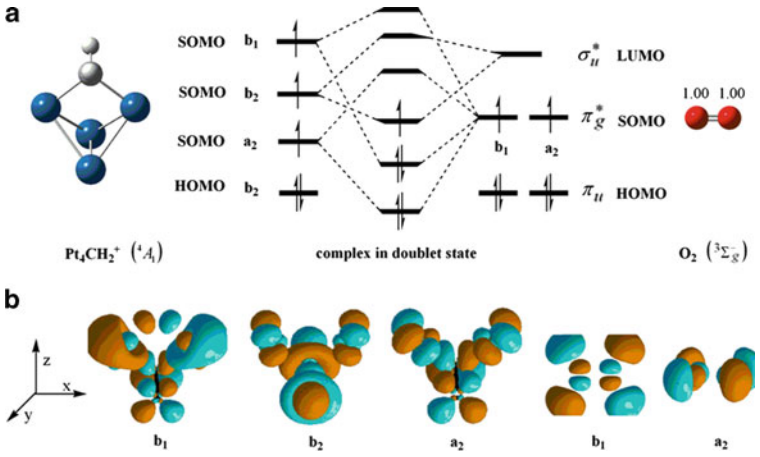

Fig. 10 (**a**) Schematic illustration of the frontier orbital interactions between $Pt_4CH_2^+$ and O_2. (**b**) Contours of related SOMOs of $Pt_4CH_2^+$ and O_2

However, the direct attack of metal-bound dioxygen toward the carbon atom is not favorable energetically in an end-on complex $Pt_4CH_2^+(O_2)$, in which the sp^3-hybrid carbon atoms in the CH_2 moiety are coordinately saturated. The formation of the lowest energy precursor **^{2}complex1** has an exothermicity of 33.4 kcal mol^{-1}, and the energy release may drive the hydrogen transfer from CH_2 to metal atoms in **^{2}complex1**, which was verified to be the most favorable elementary step energetically in preliminary calculations.

Since the presence of multi-metal centers makes the reaction channels become much complicated, it is important to contrive subsequent reaction processes. In the reaction of $PtCH_2^+$ with O_2 [73], it was noted that the branch channels to products of H_2O/CO and HCOOH request the occurrence of the O–O bond activation of dioxygen and the O–H bond coupling, while the generation of H_2/CO_2 does not. On the basis of the analysis of product varieties, two types of reaction mechanisms for the loss of H_2 and the oxidation of CH_2 to H_2O/CO or HCOOH have been considered here for the reaction of $Pt_4CH_2^+$ with O_2.

4.2.1 Reaction Pathway to Elimination of H_2

Figure 11 presents the relative energy profiles of dehydrogenation of $Pt_4CH_2^+$ with O_2. The ground-state reactants of $Pt_4CH_2^+$ and O_2 serve as the reference state in determining the relative energetics. As Fig. 11 shows, the formation of **^{2}complex1** releases an energy of 33.4 kcal mol^{-1}, which is enough to overcome the barrier of 24.8 kcal mol^{-1} for the first C–H bond activation of the CH_2 moiety in **^{2}complex1**. Through the transition state **TS c1/c2**, the precursor **^{2}complex1** evolves to a more stable hydride **c2**. Followed by the second C–H bond activation via the transition state **TS c2/c3**, a dihydride **c3** is formed with a barrier of 35.8 kcal mol^{-1}, and the

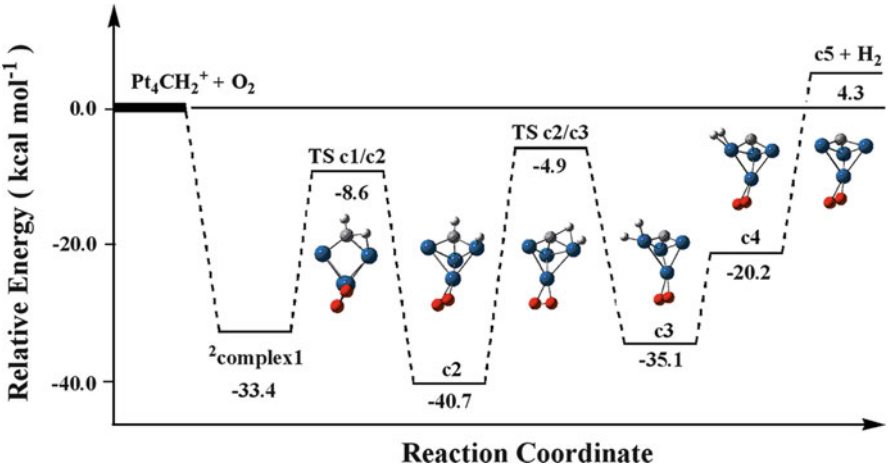

Fig. 11 Relative energy profiles of dehydrogenation reaction of $Pt_4CH_2^+$ with O_2

transition state **TS c2/c3** is slightly lower in energy than the reactant entrance by 4.9 kcal mol^{-1}. The dihydride **c3** evolves into a dihydrogen complex **c4** with an endothermicity of 20.2 kcal mol^{-1}. There is no transition state to be located between **c3** and **c4** due to strong interactions of dihydrogen with the metal cluster [61]. Finally, the liberation of H_2 from **c4** requires 24.5 kcal mol^{-1} to yield the products **c5**. The overall reaction of dehydrogenation is predicted to be endothermic by 4.3 kcal mol^{-1}, and the Gibbs free energy of reaction ΔG is 5.4 kcal mol^{-1} (at 298.15 K). The calculated results indicate that the dehydrogenation of $Pt_4CH_2^+$ with O_2 is likely to occur in the gas phase. However, this channel to loss of H_2 is less efficient thermodynamically in comparison with other branch channels (vide infra), and thus the further reaction to yield CO_2 has not been explored here.

4.2.2 Reaction Pathway to H_2O/CO

In the dehydrogenation route as shown in Fig. 11, the most stable intermediate **c2** is a local minimum on the PES, and as a precursor, it can be involved in other reaction channels. Here, we explored the reaction channel to H_2O and CO from the lowest energy intermediate **c2**, where the elementary reaction steps of O–O bond activation as well as C–O and O–H bond couplings are involved. Figure 12 displays the relative energy profiles and corresponding structures of intermediates and transition states along this reaction channel.

As Fig. 12 displays, the hydrogen transfer from metal to dioxygen in **c2** forms an intermediate **c6** via a four-membered ring transition state **TS c2/c6** with a barrier of 35.9 kcal mol^{-1}. The Pt–H and O–O bond lengths of **TS c2/c6** are 1.68 Å and 1.34 Å, respectively, and the O–OH bond length in **c6** is 1.45 Å. Followed by the O–O bond fission, the intermediate **c6** proceeds to a more stable intermediate **c7** with a Pt-bound hydroxyl. The formation of the intermediate **c7** has a remarkable exothermicity of 71.1 kcal mol^{-1} relative to the reaction entrance in Fig. 11, which may facilitate further hydrogen transfer. The second C–H bond activation leads to a less stable intermediate **c8** with a barrier of 25.8 kcal mol^{-1}. The C–O bond coupling in **c8** via the transition state **TS c8/c9** has a substantial barrier of 42.2 kcal mol^{-1}, generating the primary product **c9** with the bridged μ_2-CO structure. The overall process is exothermic by 76.6 kcal mol^{-1} relative to **c2**.

The metal-bound hydrogen, hydroxyl, and carbonyl in **c9** can undergo consecutive rearrangements to yield the products of H_2O/CO or HCOOH. Possible mechanisms for subsequent branch channels and optimized structures of transition states and intermediates in reaction are displayed in Fig. 13. In **c9**, the hydrogen migration results in an intermediate **c10**. Followed by the coupling of hydrogen with hydroxyl, the more stable complex **c11** with the Pt-bound water is formed with a barrier of 15 kcal mol^{-1}. The formation of **c11** has the enormous exothermicity of 125.6 kcal mol^{-1} relative to $Pt_4CH_2^+ + O_2$. Such striking energy release may cause the eliminations of H_2O or CO from complex **c11**, yielding primary products **c13** or **c12** and ultimate products Pt_4^+/H_2O/CO. Calculations indicate that the release of water from **c11** requires 28.1 kcal mol^{-1}, while the liberation of CO needs

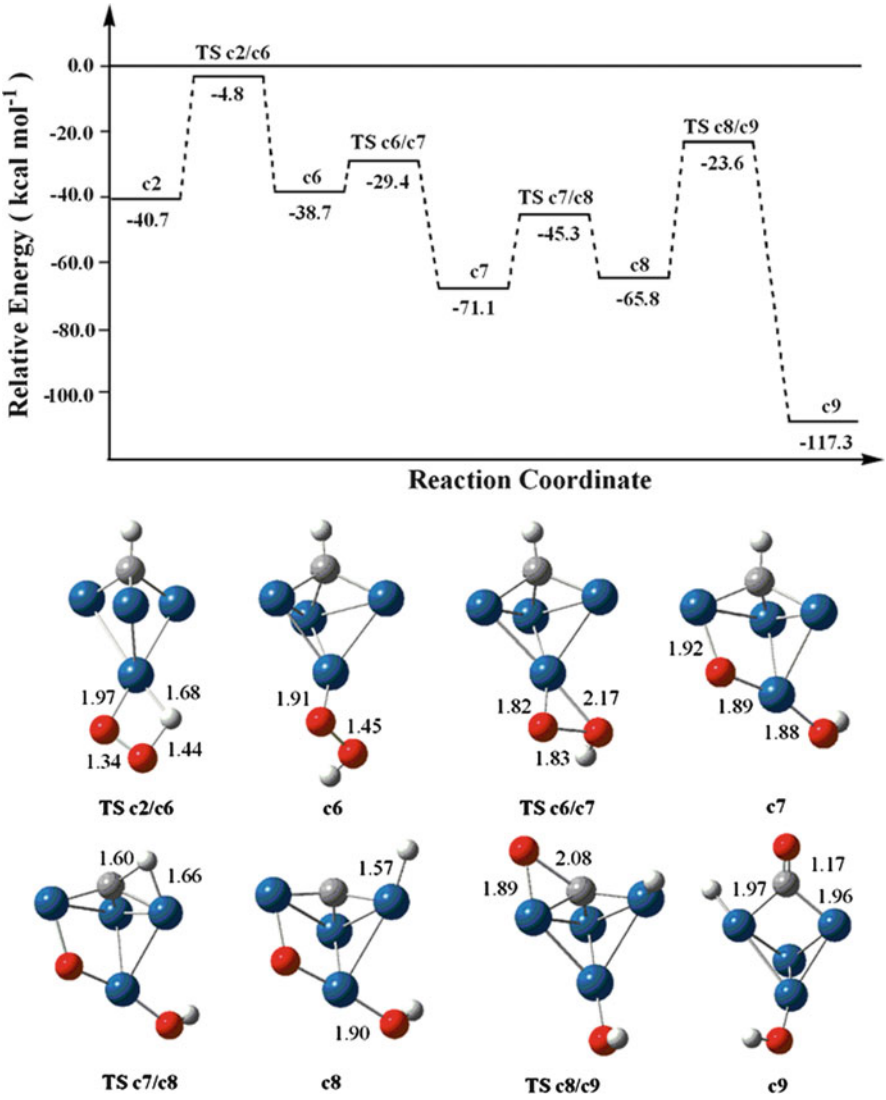

Fig. 12 Relative energy profiles for the O–O bond activation and C–O bond coupling, as well as the corresponding structures of intermediates and transition states. Bond lengths are in angstroms

46.1 kcal mol^{-1}. The overall channel to the products H_2O/CO has an exothermicity of 57.1 kcal mol^{-1} and free energy of reaction ΔG of 66.2 kcal mol^{-1} relative to the reaction entrance $Pt_4CH_2^+ + O_2$.

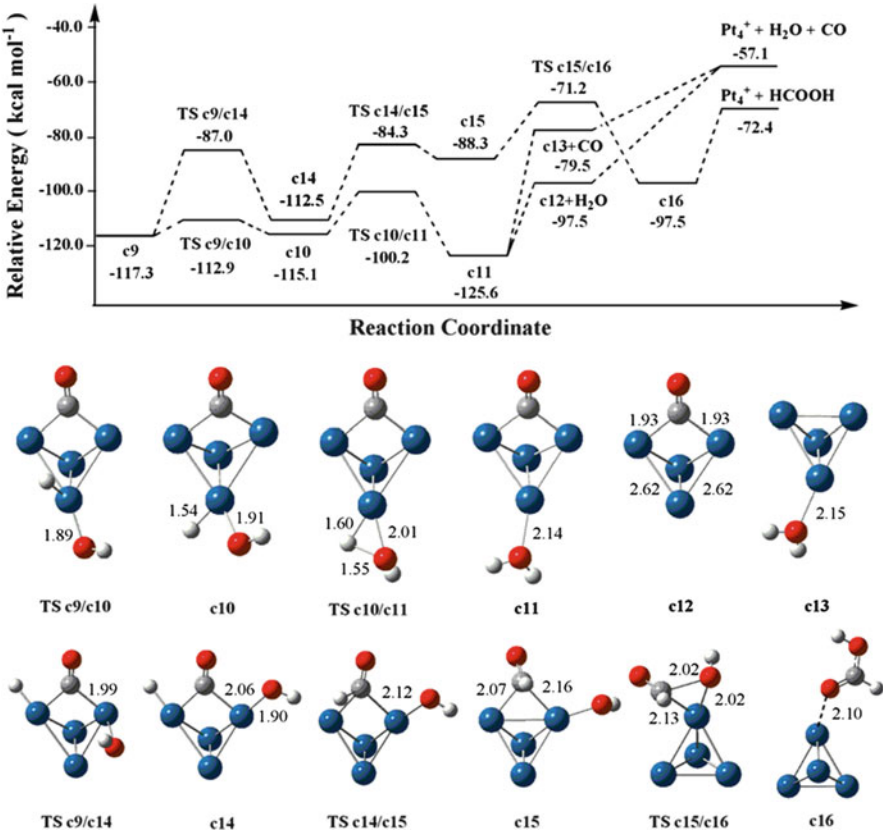

Fig. 13 Relative energy profiles along the channels to H_2O/CO and HCOOH and the corresponding structures of intermediates and transition states. Bond lengths are in angstroms

4.2.3 Reaction Pathway to HCOOH

Another branch channel to the products of Pt_4^+ and HCOOH starting from **c9** is also shown in Fig. 13. Obviously, the formation of the formic acid molecule requires the consecutive couplings of the metal-bound hydrogen and hydroxyl with the carbonyl group in the intermediate **c9**. First, the hydroxyl transfer in **c9** yields **c14** with the activation barrier of 30.3 kcal mol^{-1}. The intermediate **c14** evolves to **c16** through transition states **TS c14/c15** and **TS c15/c16** with barriers of 28.2 and 17.1 kcal mol^{-1}, respectively. The C–H and C–OH bond couplings are involved in the formation of **c16**. The structure of **c16** can be viewed as the molecular complex of the cationic cluster Pt_4^+ with the neutral formic acid molecule through the charge–dipole interactions. The final elimination of formic acid from **c16** requires the energy of 25.1 kcal mol^{-1}.

As Fig. 13 displays, the predicted relative energy profiles for the branch channels to H_2O/CO and HCOOH indicate that the initial elementary steps for the products H_2O/CO are more favorable energetically, whereas the ultimate product HCOOH is more stable than H_2O/CO by 15.3 kcal mol^{-1}. The calculated Gibbs free energy of reaction ΔG for the formation of HCOOH is 73.5 kcal mol^{-1}, 7.3 kcal mol^{-1} lower than that of H_2O/CO. Therefore, both branch channels should be competitive in reaction, and the mixtures of H_2O/CO and HCOOH might be the primary components of neutral products [C, H_2, O_2] observed in experiments.

4.3 *Reactivity of $Pt_nCH_2^+$ (n = 2, 3) Toward O_2*

In contrast to $Pt_4CH_2^+$, the smaller cluster $Pt_2CH_2^+$ is unreactive and $Pt_3CH_2^+$ is much less efficient in the reaction with O_2 [67]. Such remarkable differences in reactivity may arise from their intrinsic reaction energetics as well as the possible spin flip. In the reactions mediated by transition metals, the spin change plays an important role in controlling the reactivities [120, 129–131].

Previous calculations [61] showed that $Pt_2CH_2^+$ has the doublet ground state ($^2A_2$), while the low-lying quartet state ($^4A_1$) is 27.9 kcal mol^{-1} higher than the ground state. The association of the closed-shell NH_3 to $Pt_2CH_2^+$ is thus unlikely to modify the spin state of their complexes, and subsequent reactions proceed on the doublet PES. On the contrary, the dioxygen molecule has the triplet ground state, and the total spin multiplicity of complex of $Pt_2CH_2^+$ with O_2 is either doublet or quartet. The different spin states might be involved in the following reaction process:

$$Pt_nCH_2^+ + O_2 \rightarrow Pt_nCH_2(O_2)^+ \rightarrow \cdots \rightarrow Pt_n^+ + [C, H_2, O_2] \quad (n = 2, 3)$$

Like the reaction of $Pt_4CH_2^+$ with O_2, the formation of the complex as the reaction precursor was assumed to be involved in the first elementary step of the reactions of the smaller clusters $Pt_nCH_2^+$ (n = 2, 3) with O_2. Figure 14 displays three sorts of optimized structures of the complex $Pt_2CH_2(O_2)^+$ in the doublet and quartet states and their relative energies (in kcal mol^{-1}) with respect to the isolated $Pt_nCH_2^+$ and O_2. The calculated energies in parentheses are relative to the ground states of $Pt_2CH_2^+$ ($^2A_2$) and O_2 ($^3\Sigma_g^-$). The most stable structure of their complexes is the doublet ^{2}**a1** with the complexation energy of 32.8 kcal mol^{-1}. The corresponding quartet state ^{4}**a1** is higher in energy than ^{2}**a1** by 16.1 kcal mol^{-1}.

The most stable complex ^{2}**a1** might be viewed as the complex of $Pt_2CH_2^+$ with the singlet O_2 ($^1\Delta_g$). Alternatively, the spin flip between the quartet and doublet states may yield ^{2}**a1**. As Fig. 15 shows, the symmetry (or phase) mismatch of related frontier orbitals makes the side-on coordination ^{2}**a1** inaccessible for the direct association of $Pt_2CH_2^+$ with O_2, and the large energy splitting of 16.1 kcal mol^{-1} between ^{2}**a1** and ^{4}**a1** might block the spin transition. Therefore,

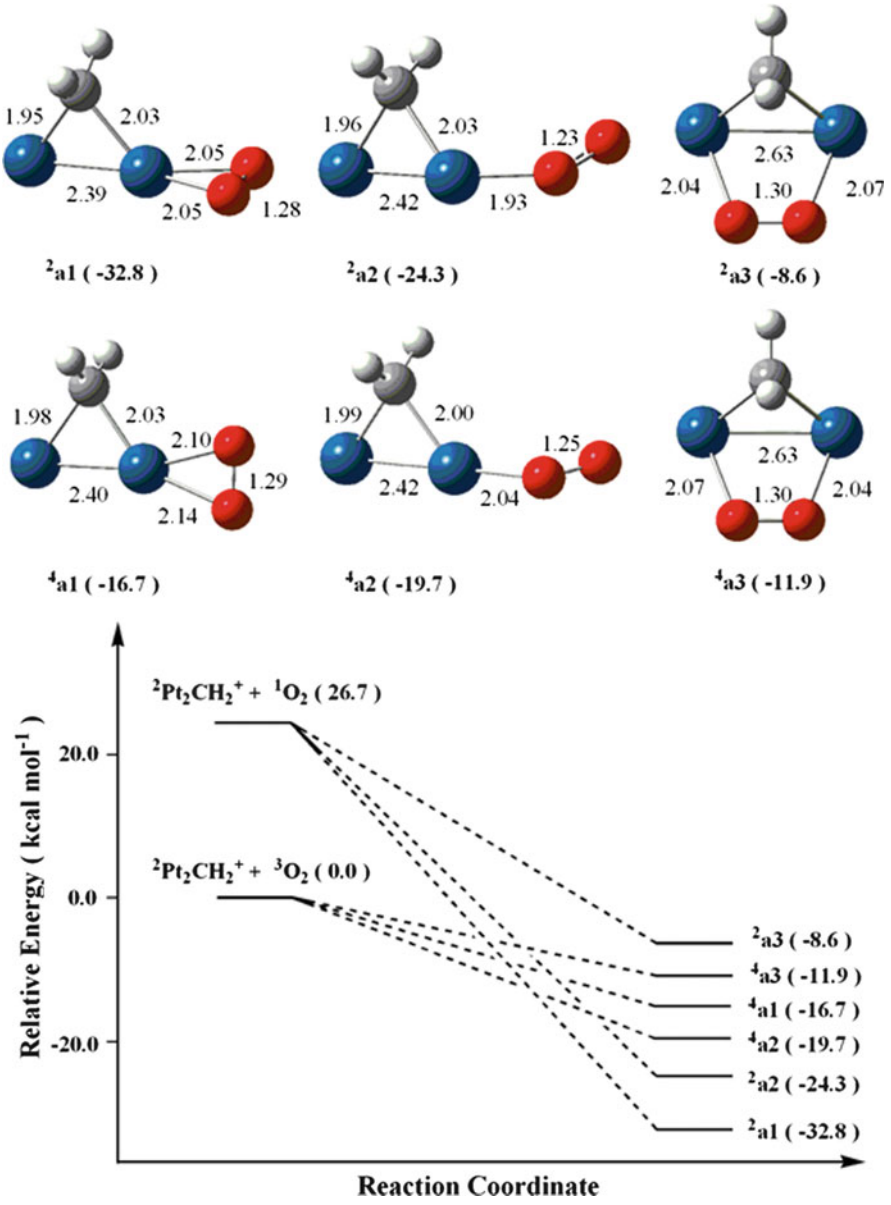

Fig. 14 Optimized structures (in angstrom) of the complex $Pt_2CH_2(O_2)^+$ and relative energies (in kcal mol^{-1}) with respect to $Pt_2CH_2^+$ and O_2 (in *parentheses*)

the lowest energy side-on **^{2}a1** is unlikely to form through direct association of $Pt_2CH_2^+$ with O_2. Similarly, the side-on species **^{2}b1** and **^{4}b1** of $[Pt_3CH_2(O_2)]^+$ in Fig. 16 have remarkable energy differences and thus the spin flip is less possible.

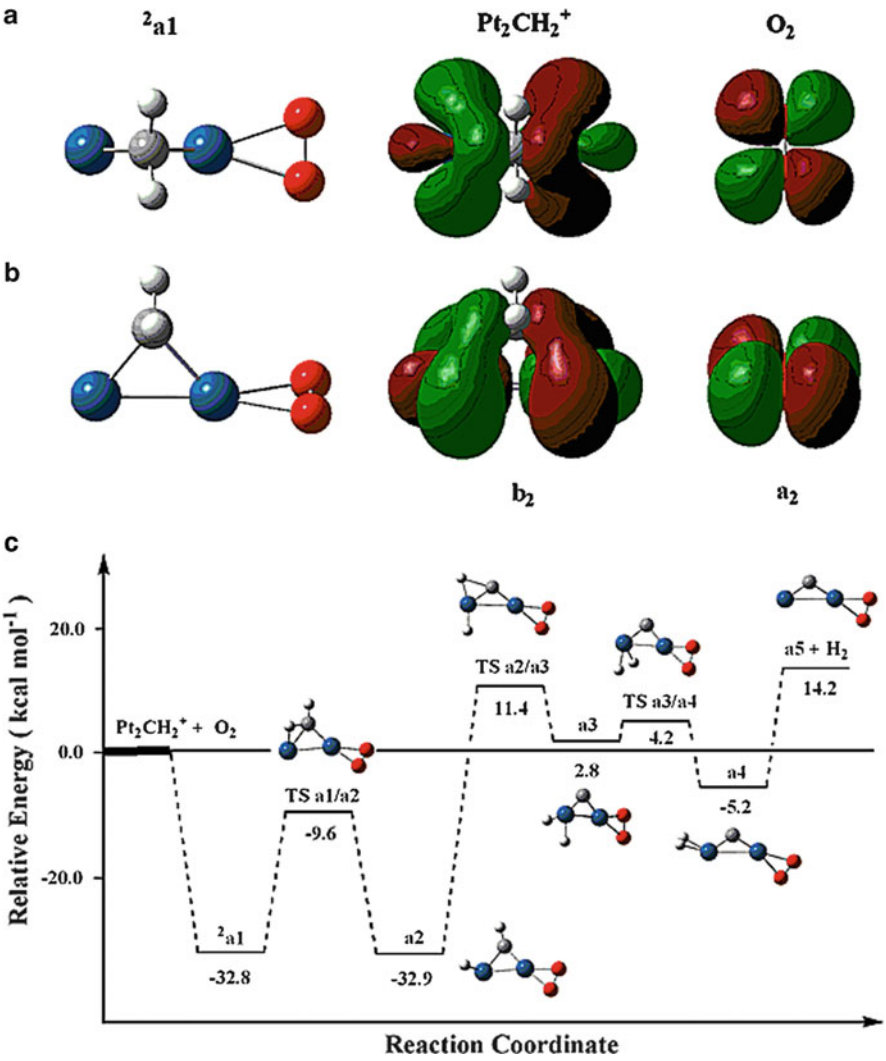

Fig. 15 Contours of related frontier orbitals of $Pt_2CH_2^+$ and O_2 [the top view (**a**) and the side view (**b**)] and the relative energy profiles of dehydrogenation reaction (**c**)

Such inaccessibility of the most stable reactive precursors might be crucial for the relative reactivity of the small clusters $Pt_nCH_2^+$ ($n = 2, 3$) toward O_2.

The predicted relative energies between the initial reactants and the final products for selected reaction channels of $Pt_nCH_2^+$ ($n = 2$–4) with O_2 are collected in Table 6. As shown in Table 6, the channel to H_2/CO_2 or H_2O/CO or HCOOH for the reaction of $Pt_nCH_2^+$ ($n = 2, 3$) with O_2 is less favorable energetically in comparison with corresponding process of $Pt_4CH_2^+$ with O_2. Similarly, the

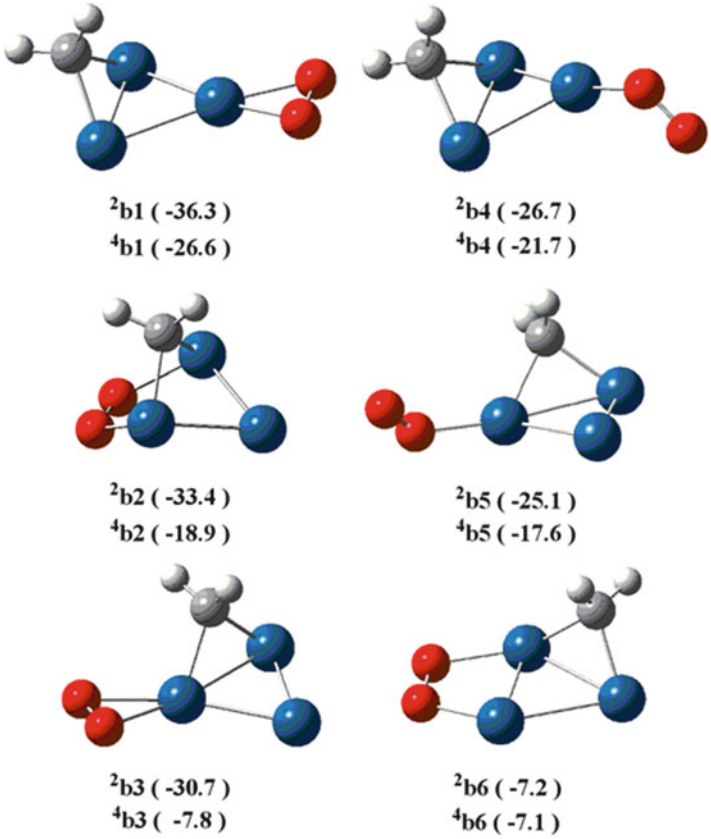

Fig. 16 Optimized structures (in angstrom) of $Pt_3CH_2(O_2)^+$ and calculated relative energies (in kcal mol^{-1}) with respect to $Pt_3CH_2^+$ and O_2

Table 6 Relative energies between the initial reactant and the final products for the reaction of $Pt_nCH_2^+$ (n = 2–4) with O_2

Reactants	Products	Relative energies
$Pt_2CH_2^+ + O_2$	$Pt_2^+ + H_2 + CO_2$	−48.0
	$Pt_2^+ + H_2O + CO$	−27.4
	$Pt_2^+ + HCOOH$	−42.7
$Pt_3CH_2^+ + O_2$	$Pt_3^+ + H_2 + CO_2$	−61.5
	$Pt_3^+ + H_2O + CO$	−41.0
	$Pt_3^+ + HCOOH$	−56.2
$Pt_4CH_2^+ + O_2$	$Pt_4^+ + H_2 + CO_2$	−77.6
	$Pt_4^+ + H_2O + CO$	−57.1
	$Pt_4^+ + HCOOH$	−72.4

dehydrogenation process in $Pt_2CH_2^+(O_2)$ also requires more energy than that in $Pt_4CH_2^+(O_2)$, as shown in Figs. 11 and 15c, lending further support to the experimental fact that $Pt_4CH_2^+$ has a relatively high reactivity. However, these reactions

considered in Table 6 are predicted to be exothermic, and their remarkable differences in reactivity may arise from the formation of the lowest energy precursor in the low spin state modulated by the spin flip. For $Pt_4CH_2^+$, the phase adaptation of related frontier orbitals and the relatively small doublet–quartet energy difference make the reactive precursor accessible easily. On the contrary, the lowest energy precursor for the reaction $Pt_nCH_2^+$ ($n = 2, 3$) with O_2 is less accessible due to the mismatch of the related frontier orbital phases and the large energy splitting between the doublet and quartet states.

5 Reactivity of $PtMCH_2^+$ (M = Cu, Ag, Au, Pt, Rh) Toward NH_3

5.1 Structure and Stability of $PtMCH_2^+$

BPW91-optimized structures of the bimetallic species $PtMCH_2^+$ (M = Cu, Ag, Au, Pt, Rh) with different spin multiplicities are shown in Fig. 17. Relative energies and isomerization barriers from the closed- to unclosed-triangular structure along with corresponding electronic states are presented in Fig. 17 and Table 7 for selected metal carbene cations. The low-energy structures of the bimetallic cation species $PtMCH_2^+$ (M = Cu, Ag, Au, Pt, Rh) with a tetrahedral carbon atom are denoted as **G**, **H**, **I,** **J**, **K**, and **L**, respectively, and they might be considered as the final products from the reactions of the bimetallic ions PtM^+ with CH_4 via dehydrogenation.

Relativistic DFT calculations indicate that the ground-state structures **G**, **H**, **I,** and **K** of heteronuclear carbene clusters are almost isoenergetic with their isomers **G1**, **H1**, **I1**, and **K1** (Fig. 17), and corresponding interconversion barriers generally are small as shown in Table 7. Therefore, both closed and unclosed forms of $PtMCH_2^+$ (M = Cu, Ag, Au, Rh) in Fig. 17 can be served as reactive precursors to the reactions of the heteronuclear bimetallic clusters with ammonia. Owing to similarity of the reactive precursors for $PtMCH_2^+$ (M = Cu, Ag, Au), it can be expected that they exhibit similar reactivity toward NH_3 as observed experimentally [18].

For $Pt_2CH_2^+$, the optimized closed structure **J** has the ground state of $^2A_2$ in C_{2V} symmetry, which is 24.8 kcal mol^{-1} lower in energy than its unclosed isomer **J1** with a planar structure. Furthermore, the corresponding interconversion barrier from **J** to **J1** is 28.3 kcal mol^{-1}. Accordingly, the lowest energy structure **J** of $Pt_2CH_2^+$ should be the only form as the precursor to the reaction of $Pt_2CH_2^+$ with NH_3, which is responsible for the formation of the carbide product without C–N coupling. Similarly, the homonuclear bimetallic carbene $Rh_2CH_2^+$ has similar structural features and stabilities with $Pt_2CH_2^+$. These differences in structural diversities of low-energy isomers between the homonuclear and heteronuclear

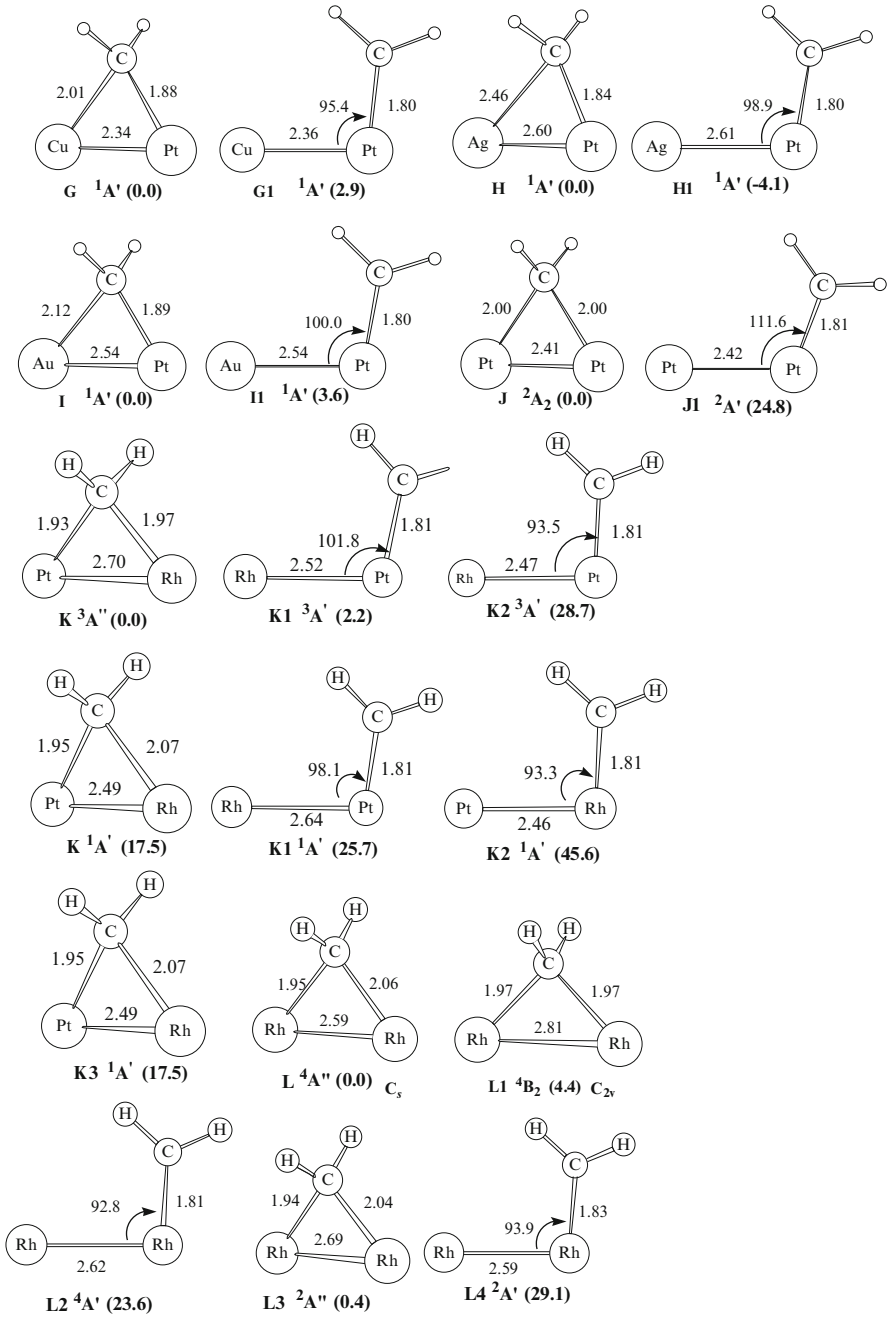

Fig. 17 Optimized geometries (bond lengths in angstrom and bond angles in degree) and relative energies in parentheses (kcal mol^{-1}) of the low-energy isomers of $PtMCH_2^+$ (M = Cu, Ag, Au, Pt, Rh)

Table 7 Relative energies ($\Delta E = E$(right) − E(left), in kcal mol^{-1}) of isomers of $PtMCH_2^+$ (M = Pt, Cu, Ag, Au) and corresponding interconversion barriers (E_b in kcal mol^{-1}) by BPW91

Species	Isomerization	ΔE	E_b
$PtCuCH_2^+$	**G** (^{1}A′, Cs) → **G1** (^{1}A′, Cs)	2.9	4.7
$PtAgCH_2^+$	**H** (^{1}A′, Cs) → **H1** (^{1}A′, Cs)	−4.1	1.2
$PtAuCH_2^+$	**I** (^{1}A′, Cs) → **I1** (^{1}A′, Cs)	3.6	7.8
$Pt_2CH_2^+$	**J** ($^2A_2$, C_{2v}) → **J1** (^{2}A′, Cs)	24.8	28.3

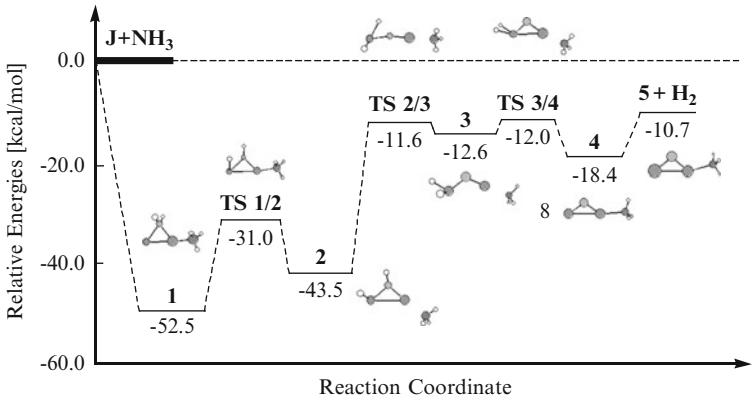

Fig. 18 Doublet potential energy profiles along the pathway to loss of H_2 from the moiety of CH_2 in the reaction of $Pt_2CH_2^+$ with NH_3

carbene clusters may be responsible for their distinct reactivities as observed experimentally [16, 67, 70].

5.2 *Reactions of $Pt_2CH_2^+$ with NH_3*

B3LYP-predicted low-energy reaction channels of $Pt_2CH_2^+$ with NH_3, giving rise to loss of H_2, and corresponding relative energies along the reaction path are shown in Fig. 18, where the ZPE is included. Optimized structures of intermediates, transition states, and dehydrogenated products in the reaction are given in Fig. 19. Table 8 collects selected thermodynamic values.

The dehydrogenation reaction starts from coordination of NH_3 to the terminal Pt in **J**, and the formation of a complex **1** releases an energy of 52.5 kcal mol^{-1} (see Fig. 18). In the complex **1**, the Pt−N bond length is 2.12 Å. NBO analyses indicate that strong donor–acceptor interactions (~56 kcal mol^{-1}) arising from a lone pair of NH_3 and an antibonding orbital of the Pt_2 subunit are responsible for the Pt–N bond. The complex **1** proceeds to an intermediate **2** through the transition state **TS1/2** with a barrier of 21.5 kcal mol^{-1}. The consecutive hydrogen atom migration from carbon to Pt results in a dihydride **3** with a barrier of 31.9 kcal mol^{-1}. Both processes

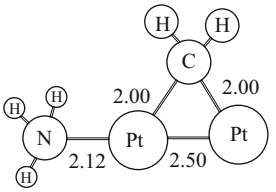

1

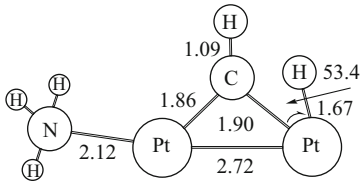

TS 1/2

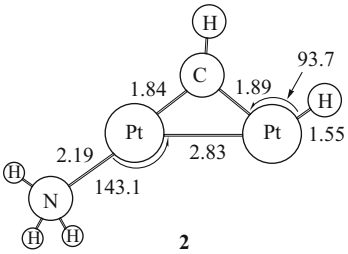

2

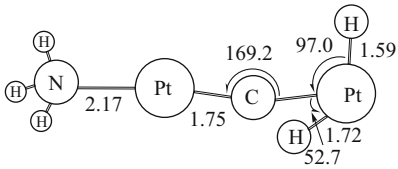

TS 2/3

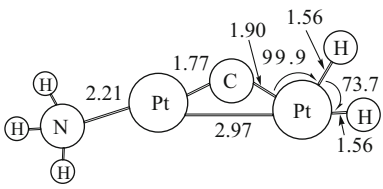

3

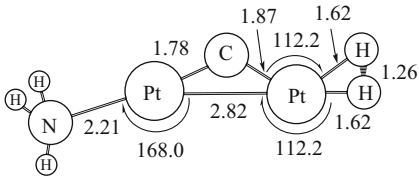

TS 3/4

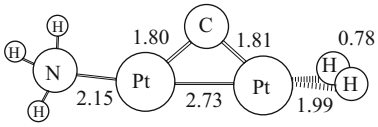

4

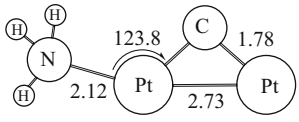

5

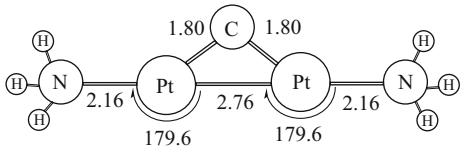

6

Fig. 19 B3LYP-optimized structures of intermediates and transition states corresponding to Fig. 18 (bond lengths in angstroms and bond angles in degrees)

Table 8 Relative energies and thermodynamic values (kcal mol^{-1}) of selected species in reactions of $PtMCH_2^+$ with NH_3 by the B3LYP approach

Species	ΔE^a + ΔZPE	ΔE + ΔZPE	ΔH^0	ΔG^0
$Pt_2CD_2^+$ + NH_3	0.0	0.0	0.0	0.0
2	−43.5	−48.5	−48.8	−40.5
TS 2/3	−11.6	−12.4	−13.0	−3.8
5 + D_2	−10.7	−14.1	−13.1	−12.5
$AuPtCD_2^+$ + NH_3	0.0	0.0	0.0	0.0
Loss of D_2				
7	−47.1	−53.15	−53.6	−44.8
TS 7/8	−15.3	−18.32	−19.3	−9.4
8	−45.6	−48.2	−49.0	−39.2
TS 8/9	−11.2	−7.6	−8.3	1.5
11 + D_2	8.6	5.58	6.7	7.1
Loss of HD				
12	−43.7	−49.7	−50.3	−41.2
TS 12/14	−16.5	−22.5	−23.4	−13.7
14	−39.3	−42.9	−48.9	−37.9
TS 14/15	−16.1	−21.1	−22.6	−11.2
18 + HD	−30.2	−35.7	−35.3	−33.1
Loss of H_2				
15	−50.4	−54.5	−55.9	−44.6
TS 15/20	−9.4	−13.8	−14.6	−4.64
20	−43.6	−47.5	−48.3	−38.3
TS 20/21	−34.6	−38.5	−39.4	−29.6
22 + H_2	−14.2	−20.5	−20.1	−18.0
$AuPtCHNH_2^+$ +NH_3	0.0	0.0	0.0	0.0
26	−25.7	−22.2	−23.0	−12.8
TS 26/27	−6.7	−5.3	−9.3	0.0
27	−20.2	−24.2	−25.0	−14.8
28 + H_2	−9.7	−14.6	−14.1	−11.6
19 +29	5.2	0.5	6.4	0.8

[a]Relative energies from B3LYP calculations with the 6-311+G(3df,2df,2p) basis set for nonmetals and the Lanl2dz ECP basis set augmented with an f-polarization function at the optimized geometries with the basis sets of 6-31G* for nonmetal atoms and Lanl2dz ECP for transition metal atoms

include cleavage of the strong C–H bond ($D_0(CH_3–H)$ = 103.4 kcal mol^{-1}) [132] and formation of a relatively weak Pt–H bond ($D_0(Pt–H)$ = 74.0 kcal mol^{-1}) [133], and they are the rate-determining steps. Followed by dihydrogen formation, **3** evolves into a more stable intermediate **4** with a negligible barrier. Finally, loss of H_2 in **5** requires ~8 kcal mol^{-1}.

The overall dehydrogenation reaction of $Pt_2CH_2^+$ with NH_3 has an exothermicity of 10.7 kcal mol^{-1} and free energies of reaction ΔG of −12.5 kcal mol^{-1}(298.15 K). The dehydrogenation only occurs at CH_2 as shown in the isotopic labeling experiment for the homonuclear platinum cluster [67]. The significant exothermicity for the formation of intermediate **1** may facilitate the loss of H_2 in the reaction. The

dehydrogenated product **5** has a bridging-carbon structure. The presence of the carbide moiety of Pt_2C^+ in product **5** was confirmed by the collision-induced dissociation (CID) experiment [67]. The coordination of a second NH_3 to **5** yields **6** with an exothermicity of 44.5 kcal mol^{-1}. Such high stability of **6** as well as the relatively coordinated saturated metal center makes the platinum site in these species less active, and the consecutive reactions concerning NH_3 activation cannot occur as observed in experiments [16–18, 67, 70]. Predicted structures **5** and **6** can serve as candidates for the observed ion products $[Pt_2,C,N,H_3]^+$ and $[Pt_2,C,N_2,H_6]^+$ in experimental studies [17].

5.3 *Reactions of $PtAuCH_2^+$ with NH_3*

Isotopic labeling experiments demonstrate that the dehydrogenation reaction of $PtAuCD_2^+$ with NH_3 yields a mixture of D_2, HD, and H_2 in a comparable ratio. This shows that both C–H and N–H activations can occur in the dehydrogenation reaction. Figures 20, 22, and 24 present possible mechanisms and relative energies for loss of D_2, HD, and H_2, respectively. Optimized geometries of intermediates and transition states are depicted in Figs. 21, 23, and 25. Selected thermodynamic values are incorporated in Table 8.

5.3.1 Loss of D_2

Calculations reveal that the reaction of the isomer **I1** with NH_3 undergoes a lower barrier than that of **I** with NH_3 in the dehydrogenation process. As a branch of the

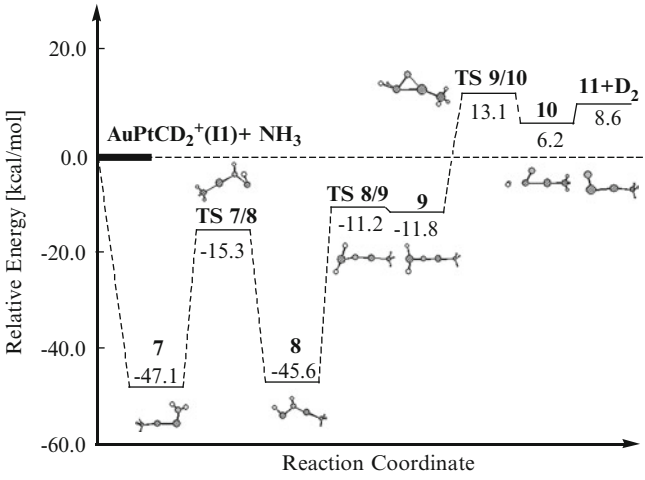

Fig. 20 Singlet potential energy profiles along the pathway to loss of H_2 from the moiety of CH_2 in the complex $(NH_3)PtAuCH_2^+$

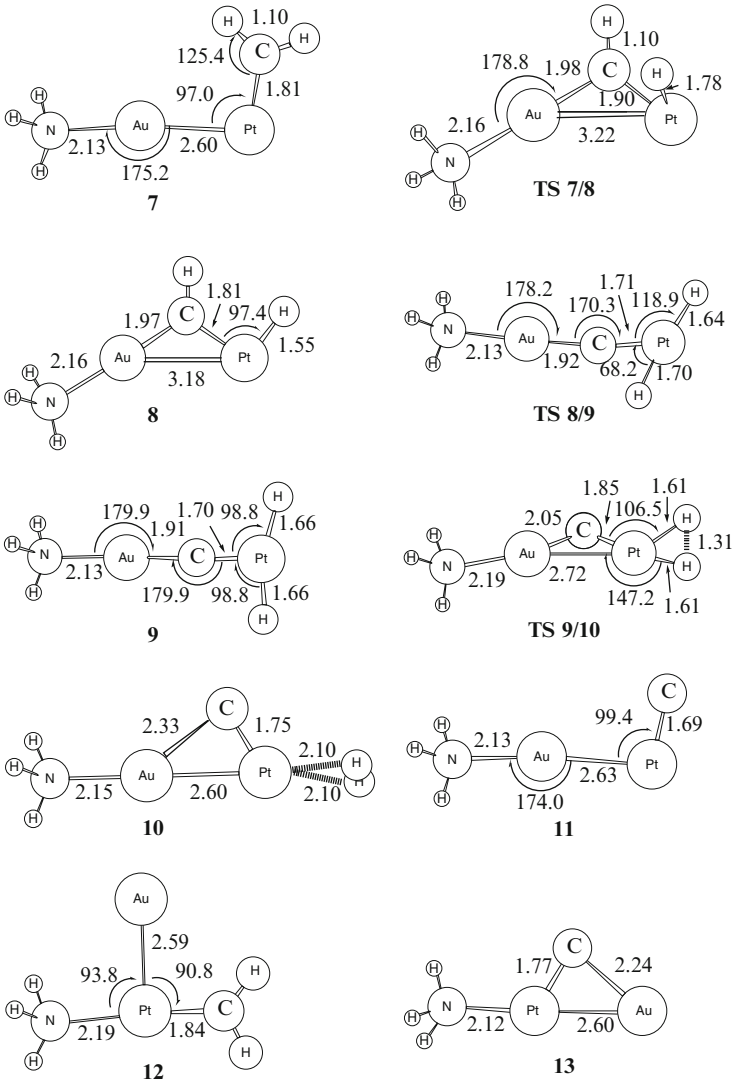

Fig. 21 B3LYP-optimized structures of selected intermediates and transition states corresponding to Fig. 20 (bond lengths in angstroms and bond angles in degrees)

reaction (1), the low-energy mechanistic scheme for loss of D_2 from the heteronuclear carbene $PtAuCD_2^+$ is shown in Fig. 20. The terminal Au in $PtAuCD_2^+$ binds NH_3 with an exothermicity of 47.1 kcal mol^{-1}, yielding a stable complex **7**. Like complex **1**, strong donor–acceptor interactions are responsible for the Au–N bond in **7**, where NH_3 behaves as a donor and the PtAu subunit behaves as an acceptor. The complex **7** is converted into **8** through a hydrogen shift from C to Pt with a barrier of 31.8 kcal mol^{-1}, which is higher than the hydrogen-transfer barrier in **1** by ~10 kcal mol^{-1}, as shown in

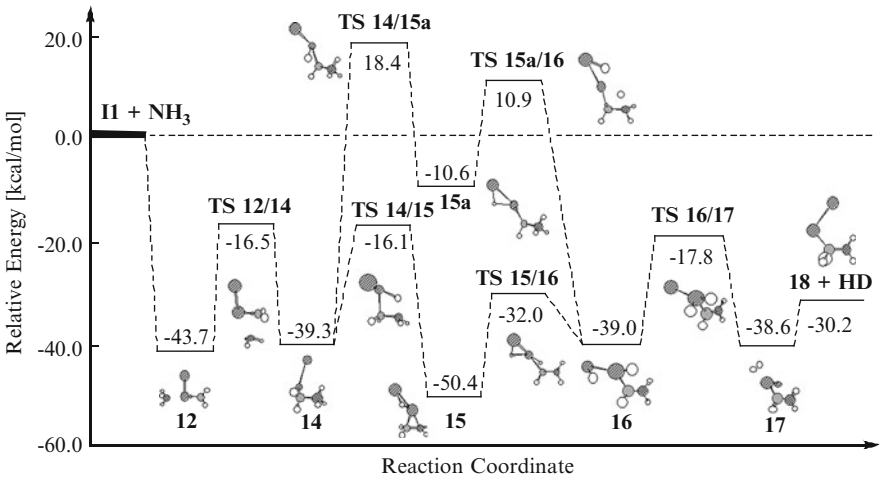

Fig. 22 Singlet potential energy profiles along the pathway to loss of H_2 from the stepwise N–H and C–H activation in the complex $(NH_3)PtAuCH_2^+$

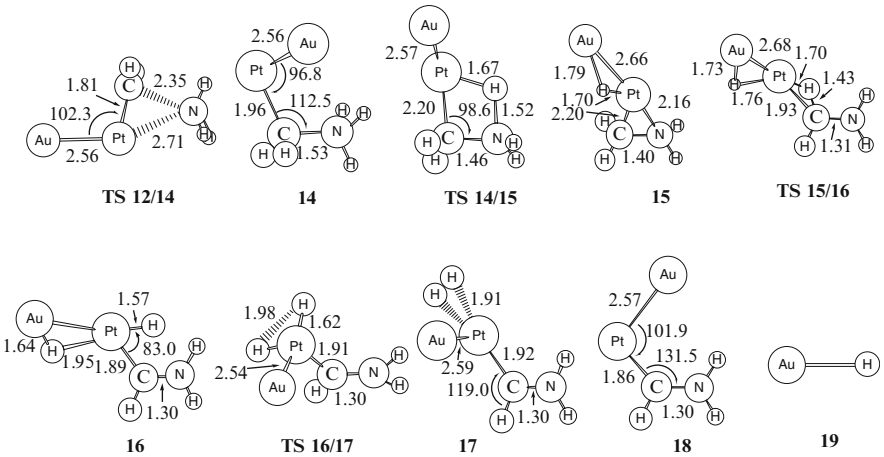

Fig. 23 B3LYP-optimized structures of selected intermediates and transition states corresponding to Fig. 22 (bond lengths in angstroms and bond angles in degrees)

Fig. 18. Such relatively high barrier can be ascribed to a closed-shell bimetallic core $PtAu^+$. The subsequent hydrogen transfer results in **9** with a barrier of 33.8 kcal mol^{-1}. Association of two hydrogen atoms in **9** gives a dihydrogen complex **10**. This process is endothermic by 18 kcal mol^{-1}. The elimination of D_2 from **10** leads to the ion product **11**, requiring an energy of 2.4 kcal mol^{-1}. As Fig. 20 and Table 8 show, the overall reaction has an endothermicity of 8.6 kcal mol^{-1} and free energies of reaction ΔG of 7.1 kcal mol^{-1}(298.15 K).

Similarly, NH_3 attacks the central Pt in $PtAuCD_2^+$ to form a complex **12** (Fig. 21) with an exothermicity of 43.7 kcal mol^{-1}. Nevertheless, calculations indicate that **12** evolves into an ultimate product **13** through dehydrogenation and consecutive reactions with substantially high energies of ~60 kcal mol^{-1}, and it seems not to take place in the gas-phase reaction. The complex **12** as a precursor to loss of HD can be involved in subsequent reactions (vide infra).

5.3.2 Loss of HD

The detailed mechanism and relative energetics for the loss of the HD in the reaction of $PtAuCD_2^+$ with NH_3 are shown in Fig. 22. Selected optimized structures of relevant species in the reaction are collected in Fig. 23. NBO analyses indicate that the N–Pt bond in **12** arises from strong donor–acceptor interactions of the lone pair of NH_3 with an antibonding orbital of the PtC subunit. The N–C bond coupling through migration of NH_3 to C produces an intermediate **14** with a barrier of 27.2 kcal mol^{-1}. The intermediate **14** isomerizes into **15** with a barrier of 23.2 kcal mol^{-1}, where the N–H bond activation is involved. DFT calculations reveal that the H shift from methylene to Pt in **14** has a quite high barrier of 57.7 kcal mol^{-1}. Therefore, this step via **TS 14/15a** could not occur prior to the H transfer from NH_3 to the bimetallic core. The intermediate **15** is the global minimum in the reaction process, where Au–H and Pt–H bond lengths are 1.79 and 1.70 Å, respectively. It is a typical η^2-H bridged compound. The intermediate **15** undergoes subsequent H shift from methylene to Pt and H–D association to produce a dihydrogen complex **17.** The complex **17** requires energies of 8.4 kcal mol^{-1} to dissociate into **18** and HD. The metal cationic aminocarbene **18** has a planar structure in which the Pt and C atoms adopt approximately respective sd^2 and sp^2 hybrid orbitals to bond together. The aminocarbene **18** with high stability can be assigned to a main form of the ion product $[Pt,Au,C,H_2,D,N]^+$ in experiment [18].

The overall reaction for the HD loss is exothermic by 30.2 kcal mol^{-1} and the corresponding free energies of reaction ΔG (298.15 K) are −33.1 kcal mol^{-1}. In comparison with the D_2 elimination, the HD channel is much favored both thermodynamically and dynamically. This is comparable with the experimental gain for D_2 and HD in a ratio of 70(±15):100 [17, 18].

5.3.3 Loss of H_2

Experimentally, the channel to loss of H_2 in the reaction of $PtAuCD_2^+$ with NH_3 was observed [18]. This fact shows that NH_3 can afford the dehydrogenation in the case of the $PtAuCD_2^+$ cluster. On the basis of calculations, the plausible mechanism for this channel is proposed in Fig. 24. Corresponding structures in the reaction path are given in Fig. 25.

As Fig. 22 shows, the first dehydrogenation step prefers NH_3 activation to C–H bond activation in the loss of HD. The stable intermediate **15** can serve as a

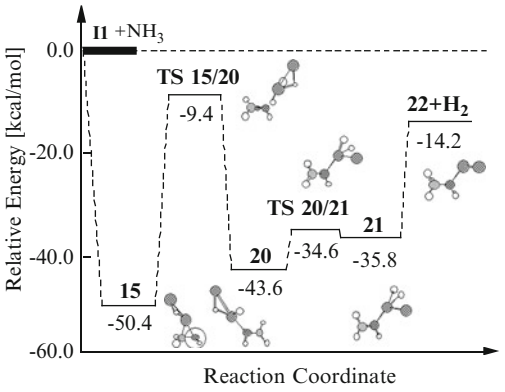

Fig. 24 Singlet potential energy profiles along the pathway to loss of H_2 from NH_3 activation mediated by $PtAuCH_2^+$

precursor to the second dehydrogenation of ammonia. DFT energetics shown in Fig. 24 reveals that the intermediate **15** surmounts a barrier of 41.0 kcal mol^{-1} to give the isomer **20**. The IRC calculations indicate that the cleavage of a strong C−Pt bond ($D_0(Pt^+–CH_2)$ = 113 kcal mol^{-1}) [73] is involved in the second N–H bond activation. The intermediate **20** proceeds to a dihydrogen complex **21** with a barrier of 9 kcal mol^{-1}. The complex **21** requires an energy of 21.6 kcal mol^{-1} to lose H_2, giving **22** as a possible form of the ion product $[Pt,Au,C,H,D_2,N]^+$. The overall reaction to products **22** + H_2 has an exothermicity of 14.2 kcal mol^{-1} and free energies of reaction ΔG of −18 kcal mol^{-1} (298.15 K).

Combining relative energies and barriers displayed in Figs. 20, 22, and 24, as well as thermodynamic values listed in Table 8, the channel to loss of HD by dehydrogenating both methylene and ammonia is the most favored route for dihydrogen elimination in the reaction (1). The next one is the loss of H_2 from NH_3 activation. This accords approximately with the experimental characterization of dihydrogen products D_2, HD, and H_2 in a ratio of 70(±15):100:80(±15) [17, 18].

5.4 *Reactions of $[Pt,Au,C,H_3,N]^+$ and NH_3*

Experimentally, the consecutive reactions (2) and (3) of the ionic product $[Pt,Au,C,H_3,N]^+$ with a second NH_3 under loss of H_2 or degradation of the metal core were observed [17]. To gain an insight into these consecutive reactions, we investigated the reaction of the ionic product with a second NH_3 by DFT calculations. As mentioned above, structure **18** is the most stable candidate among the possible ionic products $[Pt,Au,C,H_3,N]^+$. The stable aminocarbene species **18** has an unsaturated Pt site, which can bind NH_3. Figure 26 displays the relative energy diagram along the possible reaction path to loss of H_2 and AuH. Optimized geometries of intermediates and transition states involved in the reaction are shown in Fig. 27.

As shown in Fig. 26, coordination of NH_3 to **18** releases an energy of 31.8 kcal mol^{-1}, forming a complex **23**. In **23**, the C−N coupling via **TS 23/24** leads to an intermediate **24** with a barrier of 36.5 kcal mol^{-1}. The less stable

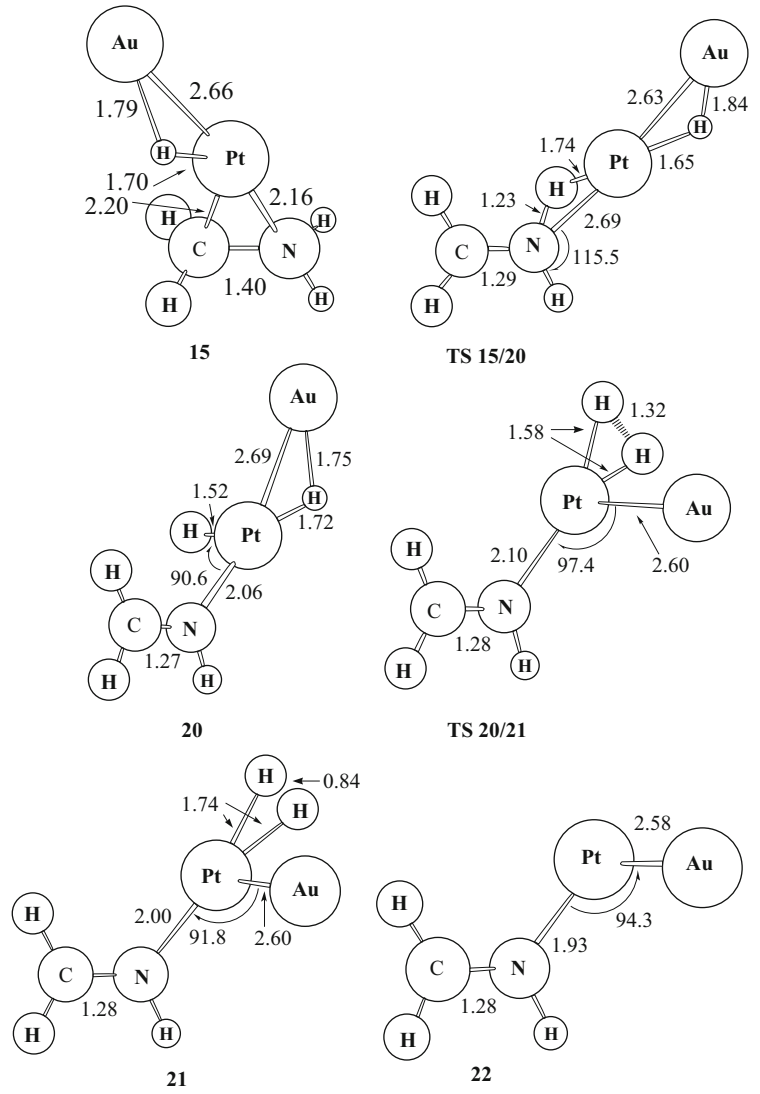

Fig. 25 B3LYP-optimized structures of selected intermediates and transition states corresponding to Fig. 24 (bond lengths in angstroms and bond angles in degrees)

intermediate **24** proceeds to **25** via NH_3 activation with a barrier of 19.8 kcal mol^{-1}. Followed by C−H bond activation, **25** converts into an intermediate **26**. In **26**, the Au−H, Pt−H, and Au−Pt bond lengths are 1.65, 1.90, and 2.80 Å, respectively. Such geometrical features indicate that elimination of the hydride AuH in **26** can take place in the gas-phase reaction. On the contrary, **26** can be formed through C−H activation in **24** first, followed by N−H activation in **25**. As Fig. 26 shows,

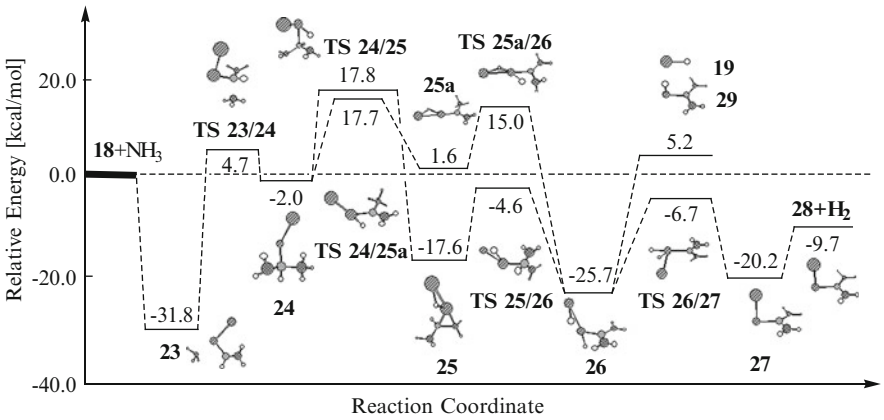

Fig. 26 Singlet potential energy profiles along the pathway to loss of H_2 and AuH in the reaction of the aminocarbene $AuPtCHNH_2^+$ with NH_3

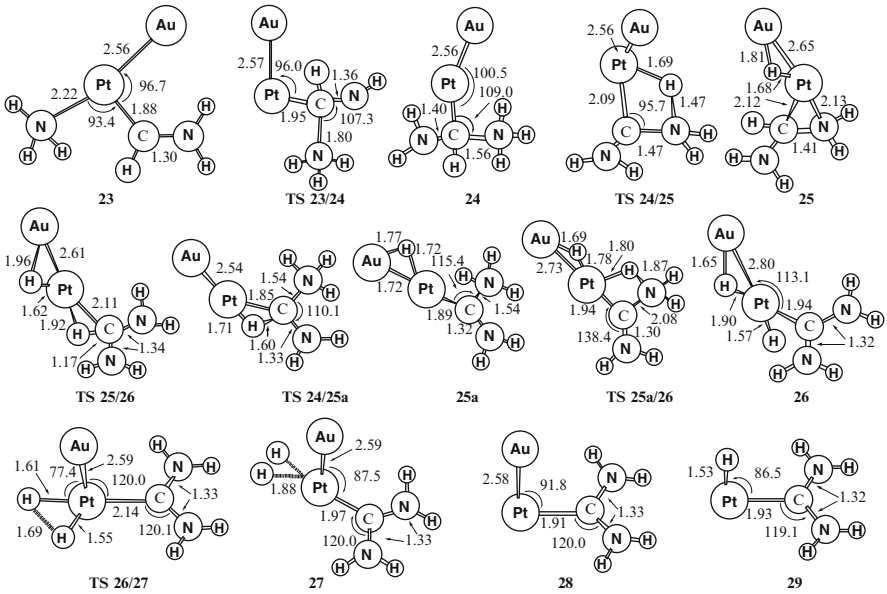

Fig. 27 B3LYP-optimized structures of selected intermediates and transition states corresponding to Fig. 26 (bond lengths in angstrom and bond angles in degree)

this process is less favored dynamically. The H−H coupling in **26** gives the dihydrogen complex **27** with a barrier of 19 kcal mol^{-1}. The dihydrogen complex **27** requires an energy of 10.5 kcal mol^{-1} to lose H_2, giving the biaminocarbene product **28**. The biaminocarbene **28** can be assigned as a candidate for the ionic product $[Pt,Au,C,H_4,N_2]^+$ in experiment [17].

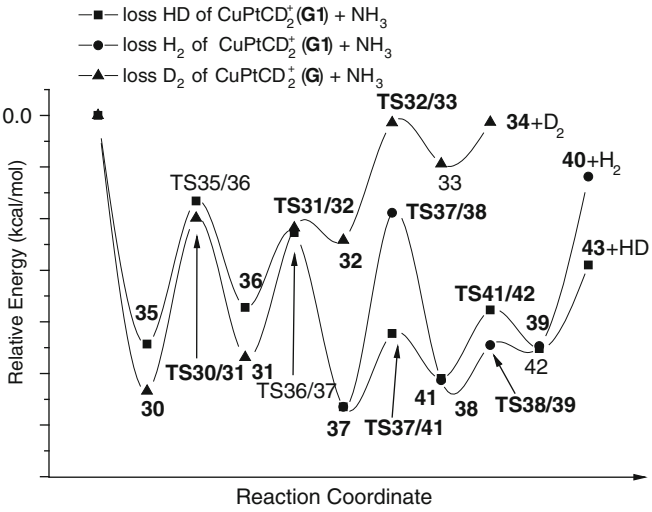

Fig. 28 Schematic energy profiles for the dehydrogenation channels to D_2, H_2, and HD in the reactions of $PtCuCH_2^+$ with NH_3

5.5 *Relative Dehydrogenation Reactivity of $PtMCH_2^+$ ($M = Cu, Ag, Au, Pt$) Toward NH_3*

The structural and electronic resemblances of the bimetallic species $PtMCH_2^+$ ($M = Cu, Ag, Au$) imply that they have similar reactivity toward NH_3 as observed experimentally [18]. Like $PtAuCH_2^+$, in the dehydrogenation channel of the reaction of $PtMCH_2^+$ ($M = Cu, Ag$) with NH_3, loss of dihydrogen may follow three possible routes: the elimination of H_2 arises from the moieties of CH_2 and NH_3, or C–H and N–H activation in the adduct of $(NH_3)PtMCH_2^+$. Presumably, the bimetallic species $PtMCH_2^+$ ($M = Cu, Ag, Au$) follow similar dehydrogenation mechanisms in the reaction with NH_3. Figure 28 presents relative energy profiles of three dehydrogenation channels in the reaction of $PtCuCH_2^+$ with NH_3, and corresponding intermediates and transition states are displayed in Fig. 29. Detailed relative energies for the dehydrogenation reactions of $PtMCH_2^+$ ($M = Cu, Ag, Au$) with NH_3 are collected in Table 9.

As Fig. 28 and Table 9 show, the reaction of $PtCuCH_2^+$ (**G**) and NH_3 to lose D_2 is less favored energetically compared with elimination of H_2 or HD. Both H_2 and HD channels share the intermediate **37**. The intermediate **37** evolves to a dihydrogen compound **39** with a barrier of 37.6 kcal mol^{-1} for the key step from **37** to **38**. The molecular complex **39** requires an energy of 32.8 kcal mol^{-1} to loss H_2. On the contrary, the barrier of the key step from **37** to **41** for the formation of a dihydrogen compound **42** through C–H and N–H bond activations is 14.2 kcal mol^{-1}, and the molecular complex **42** losses HD with an endothermicity of 16.2 kcal mol^{-1}. The channel to HD is thus more favorable than those to D_2 and H_2, both energetically

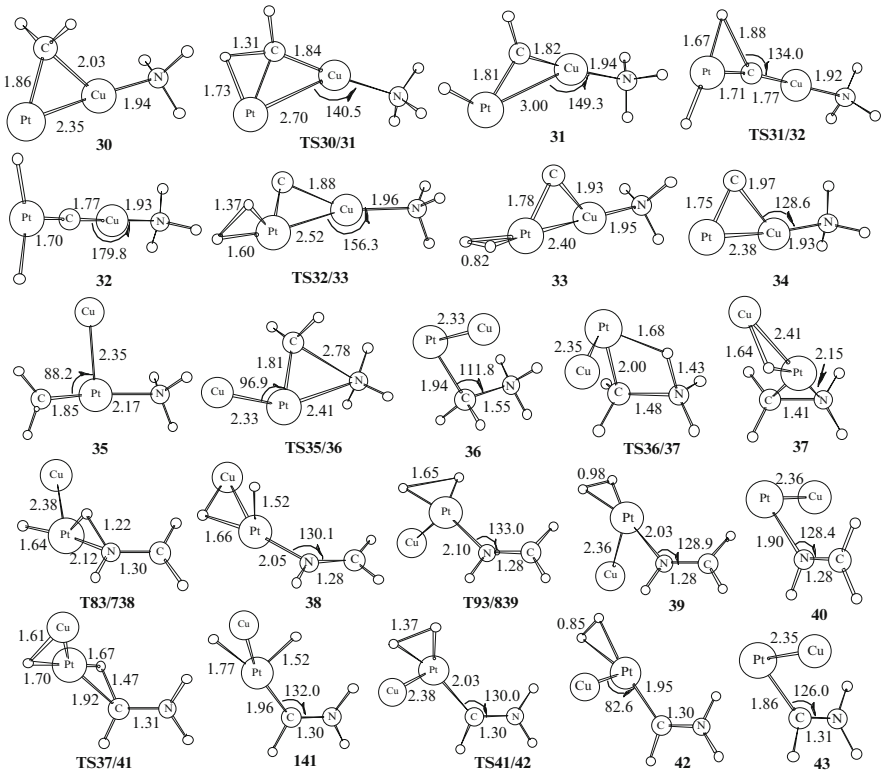

Fig. 29 Optimized structures of intermediates and transition states in the dehydrogenation reaction of $PtCuCH_2^+$ with NH_3 (bond lengths in angstrom and bond angles in degree)

and dynamically. As Table 9 displays, $PtAgCH_2^+$ and $PtAuCH_2^+$ have similar dehydrogenation reactivity toward NH_3. Corresponding intermediates and transition states have comparable geometries with those of $PtCuCH_2^+$ shown in Fig. 29.

Figure 30 displays the low-energy optimized structures of the dehydrogenation products. The calculated free energies of the whole reactions ΔG° (298.15 K), enthalpies of the reactions ΔH° (298.15 K), and the sum of key reaction barriers are presented in Table 10. From Table 10, it can be seen that the calculated free energies of the reaction ΔG° for the elimination of D_2 in the reaction of $Pt_2CD_2^+$ with NH_3 is -16.5 kcal mol^{-1}, which accords with -12.5 kcal mol^{-1} by the previous relativistic ECP DFT calculation [64]. Dehydrogenation of the adduct $(NH_3)Pt_2CD_2^+$ leads to the product **53** without occurrence of C–N bond coupling. For the reactions of bimetallic species $PtMCH_2^+$ (M = Cu, Ag, Au) with NH_3, the competitive dehydrogenation channels might take place due to the presence of the closed and open reactive precursors, as shown in Fig. 17. For example, both **I** and **II** of $PtAuCD_2^+$ can react with NH_3 to eliminate D_2, HD, or H_2 [16].

The calculated free energies of the reactions ΔG° (298.15 K) and the sum of the key barriers can approximately measure the yield of products. As Table 10 shows, the loss of HD from C–H and N–H activation is the most favored both

Table 9 Calculated relative energies (ΔE in kcal mol^{-1}) of selected species in the reactions of $PtMCH_2^+$ (M = Cu, Ag, Au) with NH_3 to lose D_2, H_2, and HD[a]

Species	ΔE	Species	ΔE	Species	ΔE
$CuPtCD_2^+ + NH_3$		$AgPtCD_2^+ + NH_3$		$AuPtCD_2^+ + NH_3$	
Loss of D_2					
NH_3 + G	0.0	**NH_3 + H**	0.0	**NH_3 + I**	0.0
30	−53.4	**30g**	−39.1	**30u**	−49.5
TS30/31	−19.9	**TS30g/31g**	−5.3	**TS30u/31u**	−17.0
31	−46.9	**31g**	−31.9	**31u**	−49.7
TS31/32	−21.8	**TS31g/32g**	−7.5	**TS31u/32u**	−22.6
32	−24.2	**32g**	−9.84	**32u**	−23.6
TS32/33	−1.4	**TS32g/33g**	13.3	**TS32u/33u**	−5.9
33	−9.4	**33g**	5.7	**33u**	−9.8
34 + D_2	−1.3	**34g** + D_2	12.6	**34u** + D_2	5.3
Loss of H_2					
NH_3 + G1	0.0	**NH_3 + H1**	0.0	**NH_3 + I1**	0.0
35	−44.3	**35g**	−43.3	**35u**	−45.0
TS35/36	−16.6	**TS35g/36g**	−14.8	**TS35u/36u**	−19.4
36	−37.2	**36g**	−32.4	**36u**	−39.4
TS36/37	−22.7	**TS36g/37g**	−21.5	**TS36u/37u**	−25.4
37	−56.5	**37g**	−53.2	**37u**	−58.6
TS37/38	−18.9	**TS37g/38g**	−28.0	**TS37u/38u**	−20.0
38	−51.3	**38g**	−47.8	**38u**	−52.6
TS38/39	−44.5	**TS38g/39g**	−43.9	**TS38u/39u**	−41.4
39	−44.7	**39g**	−45.0	**39u**	−44.1
40 + H_2	−11.9	**40g** + H_2	−10.9	**40u** + H_2	−12.9
Loss of HD					
NH_3 + G1	0.0	**NH_3 + H1**	0.0	**NH_3 + I1**	0.0
TS37/41	−42.3	**TS37g/41g**	−38.8	**TS37u/41u**	−43.4
41	−51.0	**41g**	−46.5	**41u**	−55.7
TS41/42	−37.7	**TS41g/42g**	−37.2	**TS41u/42u**	−34.3
42	−45.2	**42g**	−44.6	**42u**	−45.3
43+ HD	−29.0	**43g** + HD	−28.0	**43u** + HD	−31.9

[a]The lower letters **u** and **g** indicate the species with bimetallic cores PtAg and PtAu, respectively

thermodynamically and dynamically, which is in reasonable agreement with the experimental yield. We note that the D_2 ratio in the reaction of $PtAuCD_2^+$ with NH_3 is 70 ± 15, remarkably higher in comparison with other corresponding reactions of $PtMCD_2^+$ with NH_3 (M = Cu, Ag), although the free energies of the overall reaction ΔG° (298.15 K) is 3.2 kcal mol^{-1}. This may be ascribed to relatively high stability of the precursor **I** responsible for loss of D_2. Present calculations indicate that the initial reactant **I** is more stable than **II** by 3.6 kcal mol^{-1}, and the interconversion barrier from **I** to **II** is 7.8 kcal mol^{-1}. The open planar structure **II** is a precursor to loss of H_2 and HD, as shown in previous calculations [16]. Such thermodynamic and dynamic stability of **I** effectively enhances the proportion of

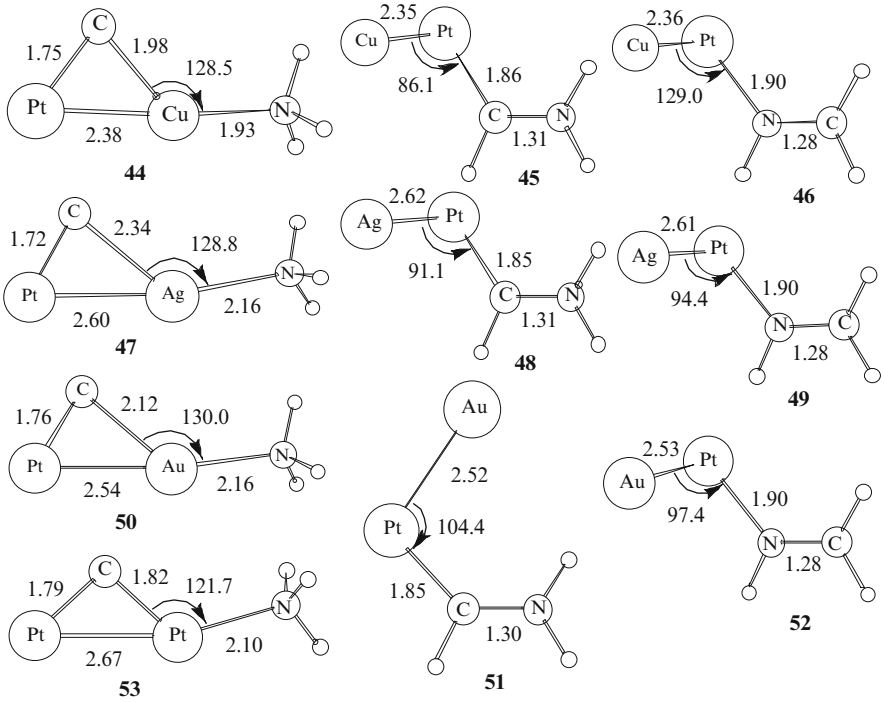

Fig. 30 Optimized geometries of the dehydrogenating products of the adduct of $(NH_3)PtMCH_2^+$ (M = Cu, Ag, Au, Pt) (bond lengths in angstroms and bond angles in degrees)

D_2 among plausible dehydrogenation channels, leading to product **50** (Fig. 30). Overall, the distribution ratio of products is essentially proportional to predicted free energies of the reactions ΔG° (298.15 K).

5.6 Dehydrogenation Reactivity of $RhMCH_2^+$ (M = Rh, Pt) Toward NH_3

5.6.1 Reactions of $PtRhCH_2^+$ with NH_3

Although the bimetallic species $PtRhCH_2^+$ has a triplet ground state ($^3A''$), the reactive channels on the triplet and the singlet PES profiles have been investigated here. In consideration of different terminals Rh and Pt in the precursors **K** and **K3**, the dehydrogenation process mediated by Rh or Pt may take place. Corresponding reactive channels have been explored, and they are denoted as pathway **I** and pathway **II**, respectively.

Table 10 Calculated Gibbs free energies of the reactions ΔG° (298.15 K), enthalpies of the reactions ΔH° (298.15 K), the sum of key barriers (E_b in kcal mol^{-1}) along the reactive channels, and experimental branch ratios of the dehydrogenation products [18]

Species	Ratio	ΔH^0	ΔG^0	E_b	Species	Ratio	ΔH^0	ΔG^0	E_b
$PtCuCD_2^+$ +NH_3					**$PtAgCD_2^+$ +NH_3**				
NH_3 + G		0.0	0.0	**31** → products	**NH_3 + H**		0.0	0.0	**31 g** → products
D_2	15 ± 10	−2.0	−2.8	45.6	D_2	≤ 5	11.5	10.0	44.5
NH_3 + G1			0.0	**37** → products	**NH_3 + H1**			0.0	**37 g** → products
HD	100	−29.4	−30.1	27.5	HD	100	−27.4	−28.1	25.2
H_2	25	−11.5	−12.2	44.6	H_2	30 ± 5	−10.4	−11.1	42.3
$PtAuCD_2^+$ + NH_3					**$Pt_2CD_2^+$ +NH_3**				
NH_3 + I		0.0	0.0	**31u** → products	**NH_3 + J**		0.0	0.0	
D_2	70 ± 15	4.2	3.2	55.0	D_2	100	−15.4	−16.5	
NH_3+ I1			0.0	**37u** → products					
HD	100	−31.0	−32.0	26.7					
H_2	80 ± 15	−12.0	−13.0	45.7					

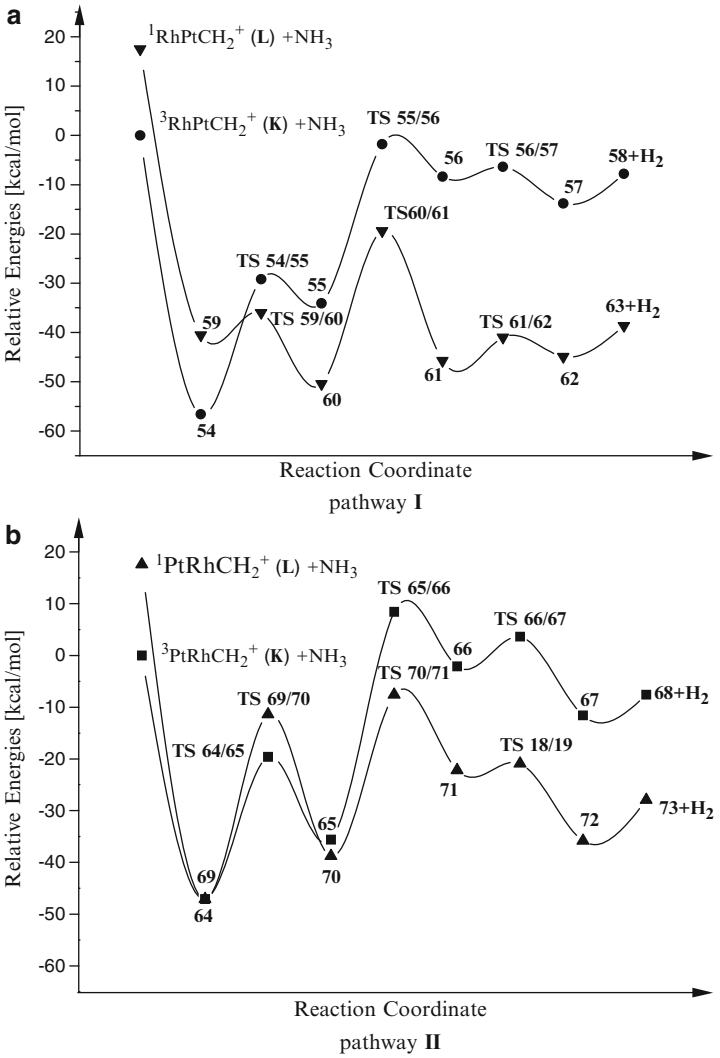

Fig. 31 Potential energy profiles for the hydrogenation channels in the reaction of $PtRhCH_2^+$ with NH_3, where (**a**) and (**b**) indicate pathways **I** and **II**, respectively

Dehydrogenation at the Rh Terminal (Pathway I)

The calculated energy profiles of the reactions of $RhPtCH_2^+$ with NH_3 on the triplet and singlet PESs are shown in Fig. 31a. Corresponding structures of intermediates, transition states, and products are presented in Fig. 32. Calculated thermodynamic values along the triplet and the singlet channels are collected in Table 11.

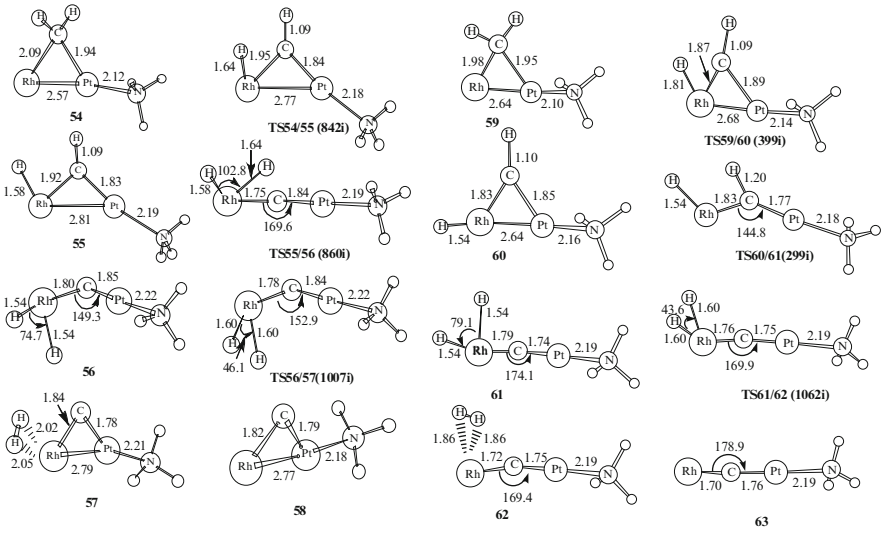

Fig. 32 Optimized structures corresponding to Fig. 31a. Imaginary frequencies of transition states (TS) are showed in parentheses (bond lengths in angstrom and angles in degree)

Table 11 Selected relative energies and key thermodynamic values (in kcal mol^{-1}) for the reactions of $RhPtCH_2^+$ with NH_3 by B3LYP

Pathway **I**	ΔE°	ΔH°	ΔG°	Pathway **II**	ΔE°	ΔH°	ΔG°
^{3}**RhPtCH$_2^+$ + NH$_3$**	0.0	0.0	0.0	^{3}**PtRhCH$_2^+$ + NH$_3$**	0.0	0.0	0.0
^{3}**54**	−56.6	−57.2	−47.6	^{3}**64**	−47.1	−47.7	−38.3
^{3}**TS 54/55**	−29.2	−29.8	−20.6	^{3}**TS 64/65**	−19.6	−20.2	−11.0
^{3}**55**	−34.1	−34.2	−26.8	^{3}**65**	−35.6	−35.8	−27.6
^{3}**TS 55/56**	−1.8	−1.9	6.4	^{3}**TS 65/66**	8.4	8.4	15.5
^{3}**56**	−8.4	−8.5	−0.8	^{3}**66**	−2.1	−2.0	5.6
^{3}**TS56/57**	−6.4	−6.6	1.9	^{3}**TS66/67**	3.6	3.5	11.6
^{3}**57**	−13.8	−13.2	−6.7	^{3}**67**	−11.6	−10.9	4.9
^{3}**58 + H$_2$**	−7.8	−6.5	−6.8	^{3}**68 + H$_2$**	−7.6	−6.3	−6.9
^{1}**RhPtCH$_2^+$ + NH$_3$**	17.6	17.9	18.2	^{1}**PtRhCH$_2^+$ + NH$_3$**	17.6	17.9	18.2
^{1}**59**	−40.5	−41.1	−30.9	^{1}**69**	−47.1	−48.1	−37.0
^{1}**TS 59/60**	−36.0	−36.8	−26.3	^{1}**TS 69/70**	−11.4	−12.2	−1.7
^{1}**60**	−50.4	−50.8	−41.6	^{1}**70**	−38.8	−39.2	−29.7
^{1}**TS 60/61**	−19.4	−19.8	−10.7	^{1}**TS 70/71**	−7.6	−8.0	1.7
^{1}**61**	−45.7	−45.9	−37.6	^{1}**71**	−22.2	−22.1	−14.4
^{1}**TS 61/62**	−41.0	−41.3	−32.3	^{1}**TS71/72**	−20.9	−20.8	−12.4
^{1}**62**	−44.9	−45.0	−37.2	^{1}**72**	−35.8	−35.3	−27.6
^{1}**63 + H$_2$**	−38.6	−37.3	−37.0	^{1}**73 + H$_2$**	−27.9	−26.7	−25.4

For the triplet channel, coordination of NH_3 to Pt of $RhPtCH_2^+$ **K** releases an energy of ~57 kcal mol^{-1}, forming the complex ^{3}**54**. Followed by this step, the consecutive hydrogen transfers take place. The first C–H bond cleavage needs to overcome a barrier of 27.4 kcal mol^{-1} to form an intermediate ^{3}**55**, and then

migration of the second hydrogen atom from C to Rh yields the dihydride ^{3}**56** through ^{3}**TS55/56** with a barrier of 32.3 kcal mol^{-1}. The intermediate ^{3}**56** evolves into a more stable dihydrogen complex ^{3}**57** with a small barrier of 2.0 kcal mol^{-1}. The loss of H_2 in ^{3}**57** gives rise to a complex of carbide $RhPtC^+$ with NH_3. The overall reaction has an exothermicity of 7.8 kcal mol^{-1} and free energies of reaction ΔG of −6.8 kcal mol^{-1} (298.15 K) relative to **K** + NH_3.

The dehydrogenation reaction of **K3** with NH_3 on the singlet PES follows a similar mechanism with the triplet channel. As shown in Fig. 31a, the overall dehydrogenation process on the singlet PES is significantly exothermic by 56.2 kcal mol^{-1}. The rate-determining step has a barrier of 31.0 kcal mol^{-1}. The whole dehydrogenation process has free energies of reaction ΔG of −37.0 kcal mol^{-1} (298.15 K) relative to **K3** + NH_3.

As Fig. 31a displays, the singlet reactant is higher in energy than the triplet reactant by 17.6 kcal mol^{-1}, while the singlet dehydrogenating product is much more stable than the triplet product by 30.8 kcal mol^{-1}. Presumably, the spin transition probably takes place along the dehydrogenation pathway. The dehydrogenating reaction proceeds on the triplet PES first, and it will be terminated at a more stable singlet product with the loss of H_2.

To better understand the spin effect on reactivity, the spin crossover from the singlet to triplet state has been investigated on the reaction pathway. A simple strategy by Yoshizawa et al. has been used to approximately locate the crossing point of two PESs with different spin multiplicities [134, 135]. Such approach has been successfully used to locate the crossing points of different spin PESs [47]. Present calculations indicate that a crossing point **SI** along the triplet IRC is located at IRC = 1.65, the relative energy being 26.3 kcal mol^{-1} with respect to ^{3}**54**. Another crossing point **SII** along the singlet IRC is located at IRC = 1.85 with an energy of 4.7 kcal mol^{-1} relative to that of ^{1}**59**. The optimized structures of the crossing points **SI** and **SII** are incorporated in Fig. 32. According to Yoshizawa et al., **SII** is an energy-minimum crossing point and **SI** is an energy-maximum crossing point between the triplet and singlet surfaces along the reaction pathway. Therefore, there is a crossing seam between **SI** and **SII**. The spin conversion from the triplet to the singlet states is most likely to occur in the region, and the singlet PES is responsible for a low-energy reaction pathway toward the product.

Overall, the Rh-mediated dehydrogenation reaction has the two-state reactivity (TSR). The low-cost reaction pathway can be described as $^3RhPtCH_2^+$ (**K**) + NH_3 → $^3RhPtCH_2^+(NH_3)$ (**54**) → $^1HRhPtCH^+(NH_3)$ (**60**) → $^1RhPtC^+(NH_3)$ (**63**) + H_2.

Dehydrogenation at the Pt Terminal (Pathway II)

The dehydrogenation process mediated by Pt is quite analogous to that of the Rh terminal. The schematic energy profiles are shown in Fig. 31b, and the corresponding structures in the dehydrogenating process are presented in Fig. 33.

As Fig. 31b displays, coordination of NH_3 to Rh in species **K** and **K3** gives almost isoenergetic complexes ^{3}**64** and ^{1}**69**. Subsequently, the first hydrogen

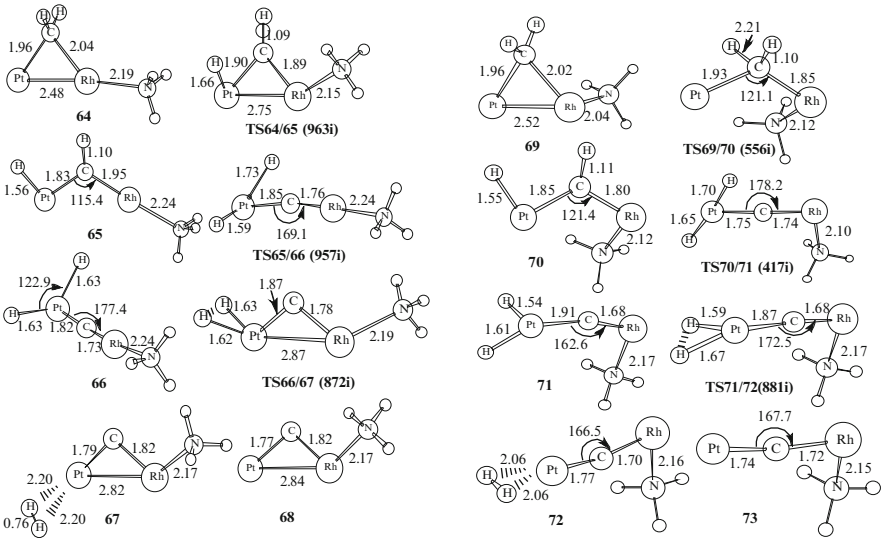

Fig. 33 Optimized structures corresponding to Fig. 31b. Imaginary frequencies of transition states (TS) are showed in parentheses (bond lengths in angstrom and angles in degree)

migration from C to Pt has barriers of 27.5 kcal mol^{-1} for the triplet state and 35.7 kcal mol^{-1} for the singlet state. The barriers of second hydrogen migration on the triplet and the singlet PESs are 44.0 and 31.2 kcal mol^{-1}, respectively. Followed by consecutive isomerizations, the dihydrogen complexes ^{3}**67** and ^{1}**72** are formed with relatively small barriers. The elimination of H_2 from ^{3}**67** and ^{1}**72** gives rise to the dehydrogenating products ^{3}**68** and ^{1}**73**. The entire reaction is exothermic by 7.6 kcal mol^{-1} at the triplet PES and by 45.5 kcal mol^{-1} at the singlet PES, respectively.

Like pathway **I**, the spin transition is probably involved in pathway **II**. As shown in Fig. 31b, the complex is most likely to change its spin multiplicity from the triplet to the singlet states in the reaction pathway. The low-energy reaction can be described as $^{3}PtRhCH_2^{+}$ (**K**) + NH_3 → $^{3}PtRhCH_2^{+}(NH_3)$ (**64**) → $^{1}HPtRhCH^{+}(NH_3)$ (**70**) → $^{1}PtRhC^{+}(NH_3)$ (**73**) + H_2.

As Fig. 31 and Table 10 show, the low-energy route in pathway **I** is more favorable than that in pathway **II** thermodynamically. The spin inversion will significantly modify the dehydrogenation reactivity of $RhPtCH_2^{+}$ toward NH_3. In the dehydrogenation reaction of $PtRhCH_2^{+}$ with NH_3, the predicted products **58** and **68** have a carbide core of $RhPtC^{+}$ structurally. Such structural feature has been confirmed by the CID experiments for observed species $[Pt,Rh,C,N,H_3]^{+}$ [16].

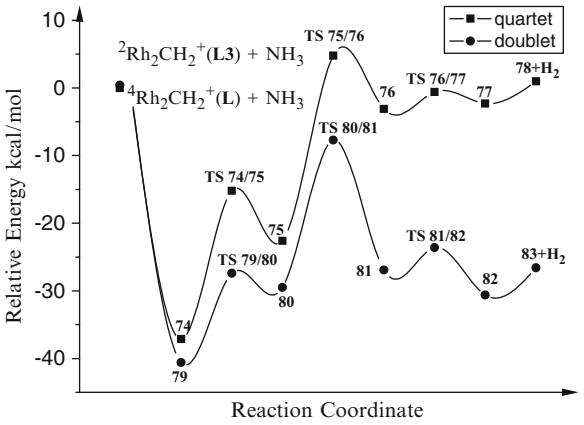

Fig. 34 Potential energy profiles for the reaction of $Rh_2CH_2^+$ with NH_3

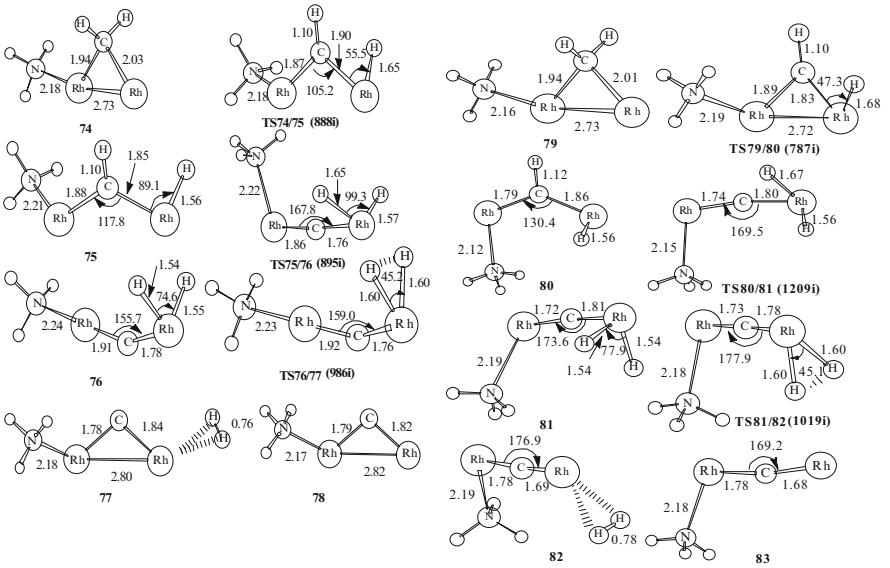

Fig. 35 Optimized structures corresponding to Fig. 34. Imaginary frequencies of transition states (TS) are showed in parentheses (bond lengths in angstrom and angles in degree)

5.6.2 Reactions of $Rh_2CH_2^+$ with NH_3

The calculated potential energy profiles of the dehydrogenation reaction on the quartet and the doublet PESs are shown in Fig. 34. The corresponding structures of intermediates, transition states, and products are presented in Fig. 35. The predicted thermodynamic values in the reaction are collected in Table 12.

Table 12 Selected relative energies and key thermodynamic values (in kcal mol^{-1}) for the reactions of $Rh_2CH_2^+$ with NH_3 by B3LYP

Species	ΔE°	ΔH°	ΔG°	Species	ΔE°	ΔH°	ΔG°
^{4}**$Rh_2CH_2^+ + NH_3$**	0.0	0.0	0.0	^{2}**$Rh_2CH_2^+ + NH_3$**	0.4	0.5	0.9
^{4}**74**	−37.1	−37.7	−28.5	^{2}**79**	−40.6	−41.2	−31.3
^{4}**TS 74/75**	−15.2	−16.2	−6.3	^{2}**TS 79/80**	−27.4	−28.0	−18.6
^{4}**75**	−22.6	−22.8	−14.9	^{2}**80**	−29.5	−29.9	−20.9
^{4}**TS 75/76**	4.8	4.6	12.7	^{2}**TS 80/81**	−7.7	−8.0	0.6
^{4}**76**	−3.1	−3.1	4.3	^{2}**81**	−26.9	−27.0	−18.9
^{4}**TS76/77**	−0.6	−0.8	7.7	^{2}**TS81/82**	−23.6	−23.7	−15.6
^{4}**77**	−2.3	−1.5	4.4	^{2}**82**	−30.6	−30.0	−23.8
^{4}**78 + H_2**	1.0	2.2	2.4	^{2}**83 + H_2**	−26.6	−25.3	−25.2

As mentioned above, the homonuclear metal species $Rh_2CH_2^+$ has isoenergetic isomers **L** and **L3**. Both species as precursors are involved in the quartet and the doublet reactions. Figure 34 reveals that the doublet channel is generally favorable thermodynamically. In the low-cost doublet channel, the rate-determining step is the migration of second hydrogen from C to Rh, and corresponding barrier is 21.8 kcal mol^{-1}. The overall reaction can be described as $^2Rh_2CH_2^+$ (**L3**) + NH_3 → $^2Rh_2CH_2^+(NH_3)$ (**79**) → $^2H_2Rh_2C^+(NH_3)$ (**81**) → $^2Rh_2C^+(NH_3)$ (**83**) + H_2. The Gibbs free energies of reaction ΔG is −26.1 kcal mol^{-1} (298.15 K). The final doublet product **83** should be assigned to the experimental ionic product $[Rh_2,C,N,H_3]^+$ [16].

Acknowledgments Zexing Cao thanks his students and collaborators as cited in the references for their key contributions to this research. This work was supported by the National Science Foundation of China (20673087, 20733002, 20873105) and the Ministry of Science and Technology (2011CB808504).

References

1. Lunsford JH (1995) Angew Chem Int Ed 43:970
2. Crabtree RH (1995) Chem Rev 95:987–1007
3. Schwarz H, Schroder D (2000) Pure Appl Chem 72(12):2319–2332
4. Martinho Simoes JA, Beauchamp JL (1990) Chem Rev 90:629
5. Weisshaar JC (1993) Acc Chem Res 26:213
6. Lersch M, Tilset M (2005) Chem Rev 105:2471
7. Achatz U, Berg C, Joos S, Fox BS, Beyer MK, Niedner-Schatteburg G, Bondybey VE (2000) Chem Phys Lett 320(1–2):53–58
8. Achatz U, Beyer M, Joos S, Fox BS, Niedner-Schatteburg G, Bondybey VE (1999) J Phys Chem A 103(41):8200–8206
9. Adhart C, Uggerud E (2006) Int J Mass Spectrom 249:191–198
10. Armentrout PB (2006) J Phys Chem A 110(27):8327–8338
11. Armentrout PB (2007) Organometallics 26(23):5486–5500
12. Armentrout PB, Shin S, Liyanage R (2006) J Phys Chem A 110(4):1242–1260
13. Armentrout PB, Sievers MR (2003) J Phys Chem A 107(22):4396–4406

14. Aschi M, Bronstrup M, Diefenbach M, Harvey JN, Schroder D, Schwarz H (1998) Angew Chem Int Ed 37(6):829–832
15. Bronstrup M, Schroder D, Schwarz H (1999) Organometallics 18(10):1939–1948
16. Koszinowski K, Schlangen M, Schroder D, Schwarz H (2004) Int J Mass Spectrom 237 (1):19–23
17. Koszinowski K, Schroder D, Schwarz H (2003) J Am Chem Soc 125(13):3676–3677
18. Koszinowski K, Schroder D, Schwarz H (2004) Angew Chem Int Ed 43(1):121–124
19. Oncak M, Cao Y, Beyer MK, Zahradnik R, Schwarz H (2008) Chem Phys Lett 450 (4–6):268–273
20. Schlangen M, Schroder D, Schwarz H (2007) Angew Chem Int Ed 46(10):1641–1644
21. Schlangen M, Schwarz H (2009) Dalton Trans 46:10155–10165
22. Schroder D, Schwarz H (2005) Can J Chem Revue Canadienne De Chimie 83(11):1936–1940
23. Schwarz H (2003) Angew Chem Int Ed 42(37):4442–4454
24. Almeida HJ, Duarte HA (2009) Organometallics 28:3203–3211
25. Di Santo E, Michelini MC, Russo N (2009) J Phys Chem A 113(52):14699–14705
26. Di Santo E, Michelini MD, Russo N (2009) Organometallics 28(13):3716–3726
27. Hanmura T, Ichihashi M, Kondow T (2002) J Phys Chem A 106(47):11465–11469
28. Hinrichs RZ, Willis PA, Stauffer HU, Schroden JJ, Davis HF (2000) J Chem Phys 112 (10):4634–4643
29. Kummerlowe G, Balteanu I, Sun Z, Balaj OP, Bondybey VE, Beyer MK (2006) Int J Mass Spectrom 254(3):183–188
30. Lang SM, Bernhardt TM, Barnett RN, Landman U (2010) Angew Chem Int Ed 49 (5):980–983
31. Li JH, Xia WS, Wan HL (2006) Chem J Chin Univ 27(12):2357–2361, in Chinese
32. Liu F, Zhang XG, Armentrout PB (2005) Phys Chem Chem Phys 7(5):1054–1064
33. Li FX, Armentrout PB (2006) J Chem Phys 125(13):133114
34. Michelini MC, Rivalta I, Sicilia E (2008) Theor Chem Acc 120(4–6):395–403
35. Michelini MD, Sicilia E, Russo N, Alikhani ME, Silvi B (2003) J Phys Chem A 107 (24):4862–4868
36. Parke LG, Hinton CS, Armentrout PB (2006) Int J Mass Spectrom 254(3):168–182
37. Parke LG, Hinton CS, Armentrout PB (2007) J Phys Chem C 111(48):17773–17787
38. Parke LG, Hinton CS, Armentrout PB (2008) J Phys Chem A 112(42):10469–10480
39. Russo N, Sicilia E (2001) J Am Chem Soc 123(11):2588–2596
40. Sandig N, Koch W (1997) Organometallics 16(24):5244–5251
41. Schroder D (2010) Angew Chem Int Ed 49(5):850–851
42. Shayesteh A, Lavrov VV, Koyanagi GK, Bohme DK (2009) J Phys Chem A 113 (19):5602–5611
43. Sicilia E, Russo N (2002) J Am Chem Soc 124(7):1471–1480
44. Sievers MR, Chen YM, Haynes CL, Armentrout PB (2000) Int J Mass Spectrom 195:149–170
45. Simon A, MacAleese L, Boissel P, Maitre P (2002) Int J Mass Spectrom 219(3):457–473
46. van Koppen PAM, Perry JK, Kemper PR, Bushnell JE, Bowers MT (1999) Int J Mass Spectrom 187:989–1001
47. Zhang GB, Li SH, Jiang YS (2003) Organometallics 22(19):3820–3830
48. Zhang Q, Kemper PR, Bowers MT (2001) Int J Mass Spectrom 210(1–3):265–281
49. Zhang Q, Kemper PR, Shin SK, Bowers MT (2001) Int J Mass Spectrom 204(1–3):281–294
50. Zhang XG, Liyanage R, Armentrout PB (2001) J Am Chem Soc 123(23):5563–5575
51. Zhang XH, Schwarz H (2009) Chemistry 15(43):11559–11565
52. Bauschlicher CW, Partridge H, Scuseria GE (1992) J Chem Phys 97:7471
53. Armentrout MM, Li FX, Armentrout PB (2004) J Phys Chem A 108:9660–9672
54. Westerberg J, Blomberg MRA (1998) J Phys Chem A 102:7303–7307
55. Husband J, Aguirre F, Thompson CJ, Laperle CM, Metz RB (2000) J Phys Chem A 104:2020–2024

56. Perry JK, Ohanessian G, Goddard WA (1994) Organometallics 13:1870–1877
57. Santo ED, Michelini MC, Russo N (2009) Organometallics 28:3716–3726
58. Schwarz H (1991) Angew Chem Int Ed 30:820
59. Eller K, Schwarz H (1991) Chem Rev 91:1121
60. Chen J, Xia F, Cao ZX, Lin MH (2007) J Mol Struct (Theochem) 808(1–3):9–16
61. Xia F, Cao ZX (2006) J Phys Chem A 110(33):10078–10083
62. Xia F, Cao ZX (2007) Organometallics 26(25):6076–6081
63. Xia F, Chen J, Cao ZX (2006) Chem Phys Lett 418(4–6):386–391
64. Xia F, Chen J, Zeng K, Cao ZX (2005) Organometallics 24(8):1845–1851
65. de Macedo LGM, Pyykko P (2008) Chem Phys Lett 462(1–3):138–143
66. Diefenbach M, Bronstrup M, Aschi M, Schroder D, Schwarz H (1999) J Am Chem Soc 121 (45):10614–10625
67. Koszinowski K, Schroder D, Schwarz H (2003) Organometallics 22(19):3809–3819
68. Koszinowski K, Schroder D, Schwarz H (2003) Chemphyschem 4(11):1233–1237
69. Koszinowski K, Schroder D, Schwarz H (2003) J Phys Chem A 107(25):4999–5006
70. Koszinowski K, Schroder D, Schwarz H (2004) Organometallics 23(5):1132–1139
71. Xiao L, Wang LC (2007) J Phys Chem B 111(7):1657–1663
72. Heinemann C, Hertwig RH, Wesendrup R, Koch W, Schwarz H (1995) J Am Chem Soc 117:495–500
73. Pavlov M, Blomberg MRA, Siegbahm PEM, Wesendrup R, Heinemann C, Schwarz H (1997) J Phys Chem A 101:1567–1579
74. Trevor DJ, Cox DM, Kaldor A (1990) J Am Chem Soc 112:3742
75. Kaldor DA, Cox DM (1990) Pure Appl Chem 62:79
76. Carroll JJ, Weisshaar JC (1995) J Chem Phys 99:14388
77. Cui Q, Musaev DG, Morokuma K (1998) J Chem Phys 180:8418
78. Cui Q, Musaev DG, Morokuma K (1998) J Phys Chem A 102:6373
79. Dalmazio I, Duarte HA (2001) J Chem Phys 115:1747
80. Villaume S, Strich A, Ndoye CA, Daniel C, Perera SA, Bartlett RJ (2007) J Chem Phys 126:154318
81. Chiodo S, Rivalta I, Michelini MC, Russo N, Sicilia E, Ugalde JM (2006) J Phys Chem A 110:12501–12511
82. Ogliaro F, Loades SD, Cooper DL, Karadakov PB (2000) J Phys Chem A 104:7091–7098
83. Irikura KK, Beauchamp JL (1991) J Am Chem Soc 113:2769
84. Irikura KK, Beauchamp JL (1991) J Phys Chem 95:8344
85. Irikura KK, Goddard WA (1994) J Am Chem Soc 116:8733–8740
86. Taylor WS, Campbell AS, Barnas DF, Babcock LM, Linder CB (1997) J Phys Chem A 101:2654
87. Heinemann C, Wesendrup R, Schwarz H (1995) Chem Phys Lett 239:75
88. Wesendrup R, Schroder D, Schwarz H (1994) Angew Chem Int Ed 33:1174
89. Magnera TF, David DE, Michl J (1987) J Am Chem Soc 109:936
90. Jackson GS, White FM, Hammill CL, Clark RJ, Marshall AG (1997) J Am Chem Soc 119:7567
91. Becke AD (1993) J Chem Phys 98:5648
92. Lee C, Yang W, Parr RG (1988) Phys Rev B 37:785
93. Becke AD (1998) Phys Rev A 38:3098
94. Perdew JP, Chevary JA, Vosko S, Jackson KA, Pederson MR, Singh DJ, Fiolhais C (1992) Phys Rev B 46:6671
95. Frisch MJ, Trucks GW, Schlegel HB, Scuseria GE, Robb MA, Cheeseman JR, Zakrzewski VG, Montgomery JA Jr, Stratmann RE, Burant JC, Dapprich S, Millam JM, Daniels AD, Kudin KN, Strain MC, Farkas O, Tomasi J, Barone V, Cossi M, Cammi R, Mennucci B, Pomelli C, Adamo C, Clifford S, Ochterski J, Petersson GA, Ayala PY, Cui Q, Morokuma K, Malick DK, Rabuck AD, Raghavachari K, Foresman JB, Cioslowski J, Ortiz JV, Stefanov BB, Liu G, Liashenko A, Piskorz P, Komaromi I, Gomperts R, Martin RL, Fox DJ, Keith T,

Al-Laham MA, Peng CY, Nanayakkara A, Gonzalez C, Challacombe M, Gill PMW, Johnson BG, Chen W, Wong MW, Andres JL, Head-Gordon M, Replogle ES, Pople JA (2001) Gaussian 98, Revision A. 11, Gaussian, Inc., Pittsburgh PA
96. Amsterdam Density Functional (ADF) (2004) SCM, Theoretical Chemistry, Vrije Universiteit, Amsterdam, Netherlands (www.scm.com)
97. Baerends EJ, Ellis DE, Ros P (1973) Chem Phys 2:41
98. Boerrigter PM, te Velde G, Baerends EJ (1988) J Int Quantum Chem 33:87
99. Te Velde G, Baerends EJ (1992) J Chem Phys 99:84
100. Hay PJ, Wadt WR (1985) J Chem Phys 82:270
101. Hay PJ, Wadt WR (1985) J Chem Phys 82:299
102. Wadt WR, Hay PJ (1985) J Chem Phys 82:284
103. Ehlers AW, Bohme M, Sapprich S, Gobbi A, Hollwarth A, Jonas V, Kohler KF, Stegmann R, Veldkamp A, Grenking G (1993) Chem Phys Lett 208:111
104. Dai D, Balasubramanian K (1994) J Chem Phys 100:4401
105. Cui Q, Djamaladdin G, Morokuma K (1998) J Chem Phys 108:8414
106. Lenthe EV, Baerends EJ, Snijders JG (1993) J Chem Phys 99:4597
107. Lenthe EV, Baerends EJ, Snijders JG (1994) J Chem Phys 101:9783
108. Minori A, Sayaka M, Takahito N, Kimihiko H (2005) Chem Phys 311:129
109. Spain EM, Morse MD (1992) J Chem Phys 97:4605
110. Perdew JP (1986) Phys Rev B 33:8822
111. Airola MB, Morse MD (2002) J Chem Phys 116:1313
112. Taylor S, Lemire GW, Hamrick Y, Fu ZW, Morse MD (1988) J Chem Phys 89:5517
113. Bishea GA, Marak N, Morse MD (1991) J Chem Phys 95:5618
114. Bishea GA, Morse MD (1990) Chem Phys Lett 171:430
115. Balasubramanian K (1987) J Chem Phys 87:6573
116. Wang H, Carter EA (1992) J Phys Chem 96:1197
117. Dediu A (2000) Chem Res 100:543
118. Yanagisawa S, Tsuneda T, Hirao K (2001) J Comput Chem 22:1995
119. Fortunelli A (1999) J Mol Struct (Theochem) 493:233
120. Schwarz H (2004) Int J Mass Spectrom 237:75
121. Basch H, Musaev DG, Morokuma K (2002) J Mol Struct (Theochem) 586:35
122. Harada M, Dexpert H (1996) J Chem Phys 100:565
123. Yuan D, Wang Y, Zeng Z (2005) J Chem Phys 122:114310
124. Ranasinghe YA, MacMahou TJ, Freiser BS (1991) J Phys Chem 95:7721
125. Fukui K (1970) J Phys Chem 74:4161
126. Fukui K (1981) Acc Chem Res 14:363
127. Dewar MJS (1951) Bull Soc Chem Fr 18:C71
128. Chatt J, Duncanson LA (1953) J Am Chem Soc 2939
129. Schroder D, Shaik S, Schwarz H (2000) Acc Chem Res 33:139
130. Shaik S, Danovich D, Fiedler A, Schröder D, Schwarz H (1995) Helv Chim Acta 78:1393
131. Danovich D, Shaik S (1997) J Am Chem Soc 119:1773
132. Litorija M, Ruscic B (1997) J Chem Phys 107:9852
133. Wittborn C, Wahlgren U (1995) Chem Phys 201:357
134. Yoshizawa K, Shiota Y, Yamabe T (1999) J Chem Phys 111:538
135. Yoshizawa K, Kagawa Y (2000) J Phys Chem A 104:9347

Cobalt-Catalyzed Hydroformylation and Cobalt Carbonyl Clusters: Recent Computational Studies

Chunfang Huo, Matthias Beller, and Haijun Jiao

Abstract Recent density functional theory computations of cobalt-catalyzed hydroformylation of propene, *N*-vinyl acetamide, 1,3-butadiene, acetylene, propyne, and allene and the urea formation from methyl amine as well as Pauson–Khand reaction have been reviewed. The detailed catalytic mechanism and regioselectivity have been discussed and compared with the available experimental data. It shows that modern computational chemistry provides not only qualitative but also quantitative aspects of catalytic reactions.

1 Introduction

Homogeneous catalysis is of great importance in industrial and synthetic processes [1–3]. In contrast to heterogeneous catalysis, homogeneous catalysis has mild reaction condition, high activity, and selectivity. With the increased efficiency and economics of catalyst recovery processes [4–8], and the increased demand for highly selective processes in industry, the application of homogeneous catalysis on an industrial scale is expected to grow more rapidly in the near future [9].

C. Huo
State Key Laboratory of Coal Conversion, Institute of Coal Chemistry, Chinese Academy of Sciences, Taiyuan 030001, People's Republic of China

M. Beller
Leibniz-Institut für Katalyse e.V. an der Universität Rostock, Albert-Einstein-Strasse 29a, 18059 Rostock, Germany

H. Jiao (✉)
State Key Laboratory of Coal Conversion, Institute of Coal Chemistry, Chinese Academy of Sciences, Taiyuan 030001, People's Republic of China

Leibniz-Institut für Katalyse e.V. an der Universität Rostock, Albert-Einstein-Strasse 29a, 18059 Rostock, Germany
e-mail: haijun.jiao@catalysis.de

O. Wiest and Y. Wu (eds.), *Computational Organometallic Chemistry*,
DOI 10.1007/978-3-642-25258-7_8,

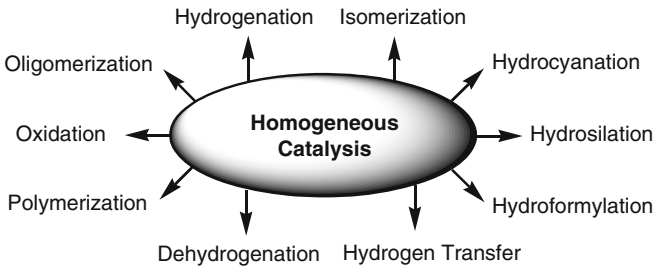

Fig. 1 Applications of homogeneous catalysis

Most of the major applications of homogeneous catalysis are shown in Fig. 1 [3]. For homogeneous catalysis, transition-metal complexes are usually considered as the most versatile catalysts arising from their unique properties [2]: (a) coordinating with a wide variety of ligands forming a series of complexes, which exhibit diverse properties, (b) moderate strength of metal–ligand bonds (30–80 kcal/mol), which allows bonds to form or break easily, and this is vital to sustaining a catalytic cycle, (c) achieving a variety of oxidative states, (d) the geometry flexibility of transition-metal complexes is crucial in homogeneous catalysis, because it not only can provide the free site for reactant coordination, but also can bring the different reactant molecules in close position to facilitate the reaction proceeding, (e) transition-metal complexes possess the proper reactivity, i.e., change the metal or ligands can make sure that the complex is reactive enough to continue the catalytic cycle, but not so reactive that undesirable side reactions occur. Furthermore, it has been verified that the catalytic activity and selectivity (including chemio-, regio-, and stereoselectivity) highly depend on the metal and the number as well as type of ligands.

Although transition-metal catalysts are quite versatile and there are many kinds of homogeneous catalysis containing dozens of reaction steps, only a handful of elementary reactions are involved in the typical catalytic cycles. These elementary reactions can be briefly classified into substitution, migratory insertion, oxidative addition, reductive elimination, hydrogen exchange, β-hydrogen transfer, α-bond metathesis, and nucleophilic addition [3, 10]. However, due to the complexity of homogeneous catalysis and the instability of key intermediates, it is difficult to achieve the complete knowledge about these catalytic cycles only by means of the experimental methods. However, recent progress in computational chemistry has shown that many important chemical and physical properties of the species involved in the transition-metal catalytic reactions can be obtained from first principles by various computational techniques [10, 11]. The increased importance and acceptance of computational chemistry have been shown in the recently published reviews [10, 11] and book chapters [12–14].

Hydroformylation is the largest-scale industrial process of homogeneous catalysis, and should be the most representative example for studies ([1, 3], selected recent examples: [15–20]). More importantly, hydroformylation covers the very important elemental reactions, e.g., coordination, migratory insertion, oxidative

addition, reductive elimination, and hydrogen transfer. Therefore, investigation of hydroformylation will throw light on comprehending of homogeneous catalysis. In addition to hydroformylation, which uses monometallic carbonyl complex as catalyst, Pauson–Khand (PK) reaction uses bimetallic carbonyl complex as catalyst. Based on the above consideration, we will devote this chapter to the theoretical study of the mechanism of hydroformylation and PK reaction as well as the properties of the corresponding cobalt-based catalyst.

2 Synopsis of Hydroformylation

Hydroformylation was discovered by Otto Roelen in 1938 during an investigation of the origin of oxygenated products occurring in cobalt-catalyzed Fischer–Tropsch reactions [21, 22]. The observation of Roelen that ethylene, H_2, and CO were converted into propanal marked the beginning of hydroformylation catalysis (Fig. 2).

As an efficient route for converting alkenes and synthesis gas (CO + H_2) into the corresponding aldehydes, hydroformylation has developed into an extremely important industrial process [1, 3, 15–20]. In the latest decades, over 6 million tons per year of oxo products are obtained accordingly. Because alkene insertion into the M–H bond can occur in two ways, i.e., the *anti*-Markovnikov and Markovnikov addition (Fig. 3) [23], the product of terminal alkene hydroformylation is usually a mixture of linear (normal) and branched (iso) isomers (Fig. 2) [24–26]. Therefore, controlling the addition direction is vital in many commercial hydroformylation reactions.

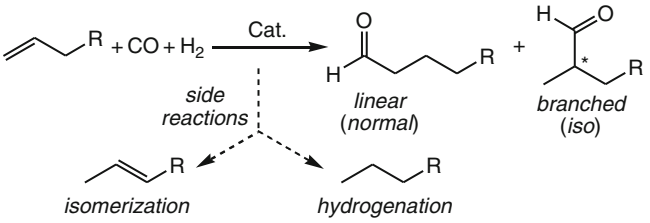

Fig. 2 The general reaction for hydroformylation

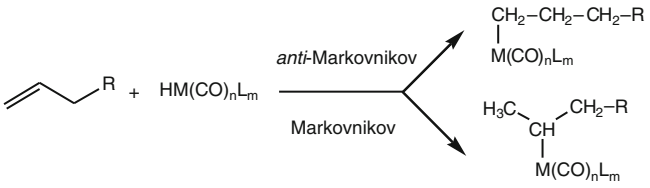

Fig. 3 Two ways for alkene insertion into the M–H bond

For conventional applications, *anti*-Markovnikov orientation leading to linear aldehydes is preferred [3]. These linear aldehydes are then hydrogenated to alcohols or oxidized to carboxylic acids. Esterification of the alcohols with phthalic anhydride producing dialkyl phthalate plasticizers for polyvinyl chloride plastics is the largest end use. Detergents and surfactants make up the next largest category, followed by solvents, lubricants, and chemical intermediates. The latest research revealed that hydroformylation is also one of the most versatile methods for the functionalization of C=C bonds, and consequently is regarded as a very powerful synthetic tool for the preparation of fine chemicals [27]. In this field, Markovnikov orientation forming branched optical pure aldehydes is desired. As the valuable precursors for producing sophisticated pharmaceutically active molecules and agrochemicals, the demand for branched optical pure aldehydes is rapidly increasing in recent years [28]. For example, branched aldehydes resulting from hydroformylation of vinyl aromatics are the intermediates for optically active nonsteroidal anti-inflammatory agents (functionalized 2-arylpropanoic acids). Several chiral aldehydes prepared by hydroformylation of simple alkenes can be converted to optically active α-amino acids. (For a general review article on asymmetric hydroformylation, see: [29].) Due to its industrial importance, hydroformylation of alkenes has received considerable attention both experimentally (there are huge numbers of publications about hydroformylation, for some reviews [30–36]; see also the annual survey: [37–41]) and theoretically [11–14, 42, 43].

3 Hydroformylation Catalysts

Hydroformylation catalysts typically consist of a transition-metal atom (M) to form metal carbonyl hydride species. In some cases, these complexes are modified by additional ligands (L). The general structure is $H_xM_y(CO)_zL_n$. This type of active hydroformylation species may be generated by precursors of different composition. Since the catalytic activity and selectivity are closely related to the metal atom and ligands, the improvement of catalyst performance can mainly be achieved by the variation of the center atom or the modification of the ligands [44, 45].

Although several metal-based catalysts (Ru, Pt, Pd, Ir, or Os) are utilized on laboratory scale, e.g., in asymmetric hydroformylation [27], the main interest in industry and academic research focuses on Co- and Rh-based catalysts [15–20]. Co-based catalysts completely dominated industrial hydroformylation until the early 1970s. With the technology development of Rh-based processes, in the situation of industrial hydroformylation emerges a remarkable change in 1990s. On the commercial scale, Rh-based catalysts have become the main choice for hydroformylation of small alkenes (C3–C6), whereas a significant number of higher aldehydes are produced via cobalt catalysis. Especially for hydroformylation of the C8/C9 range (diisobutene, propene trimer) alkenes, the conventional precatalyst $Co_2(CO)_8$ is still in the predominant position.

The exclusively used cobalt catalysts in commercial hydroformylation plants are $HCo(CO)_4$ and $HCo(CO)_3(PR_3)$ [30–36]. Two factors are responsible for them in

charge of producing higher aldehydes. First, in Co-based systems, distillation is often feasible for the separation of products and catalysts, even though it is highly energy consuming in some cases. However, for the Rh-based catalytic processes, the high boiling points of aldehydes beyond C_7 make such an operation impractical even under reduced pressure due to thermal stability considerations of the catalysts. The second reason can be attributed to Co-based catalyst ability for isomerization of alkenes. In practice, industrial feedstocks are often the mixture of terminal and internal alkenes. Under the Co-catalyzed hydroformylation conditions, internal alkenes are isomerized to terminal alkenes prior to hydroformylation, leading to the higher selectivity for linear aldehyde.

4 Mechanism of Co-catalyzed Hydroformylation

The widely accepted mechanism for Co-catalyzed hydroformylation was proposed by Heck and Breslow [46] in 1961 (Fig. 4). The first step is the dissociation of a carbonyl from $HCo(CO)_4$ to open up a coordination site for alkene. Then, alkene coordination and insertion into the Co–H bond occur forming the alkyl species.

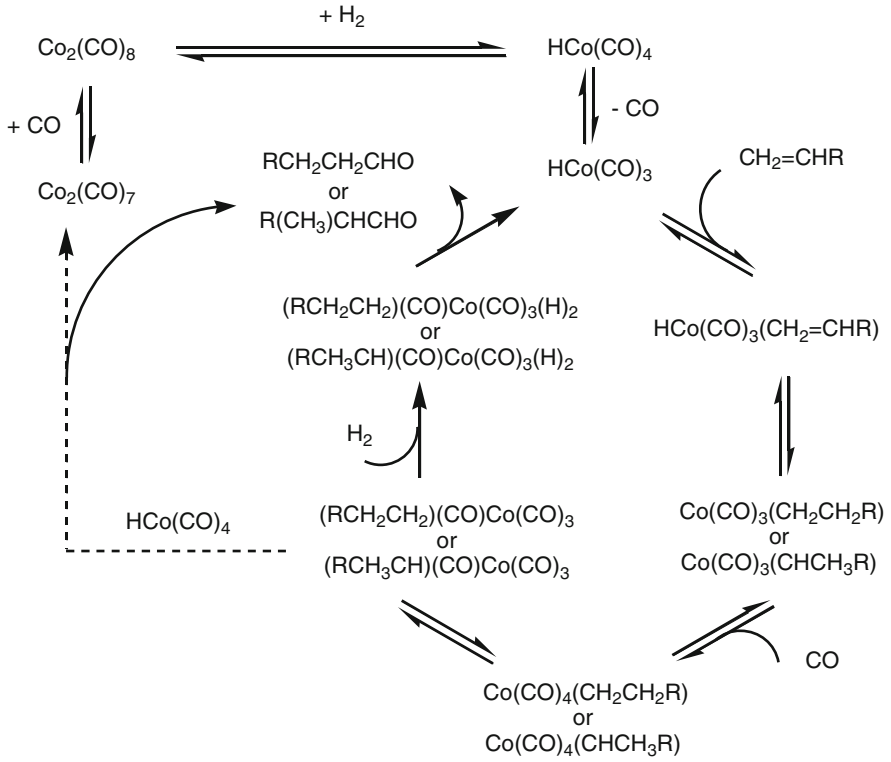

Fig. 4 Heck–Breslow hydroformylation mechanism

After that, the acyl species are produced via CO addition and insertion reactions. Sequentially, H_2 oxidative addition takes place leading to the dihydride complexes. Finally, aldehydes are reductively eliminated, and the active catalyst species $HCo(CO)_3$ is regenerated. The experimental evidence suggested that H_2 oxidative addition can be the rate-determining step [25, 47]. In addition, Heck and Breslow also suggested a bimetallic pathway. In this case, $HCo(CO)_4$ reacts with the acyl intermediates via an intermolecular hydride transfer, followed by reductive elimination of aldehydes producing $Co_2(CO)_8$. They asserted that this pathway is not favored due to the low concentration of the bimetallic catalyst species presenting to the eliminated aldehyde products. However, stoichiometric hydroformylation studies have shown that the bimetallic hydride transfer mechanism is operational, and is proposed to be a possibility for slower catalytic hydroformylation of internal alkenes [48]. Furthermore, the monometallic pathway has been repeatedly verified to be the dominant mechanism for 1-alkenes and cyclohexane [49]. The spectroscopic studies under normal hydroformylation conditions also strongly supported the monometallic mechanism [50].

Apart from the experimental works, hydroformylation of alkenes has attracted broad interests of computational chemists. Theoretical works mainly explored the structures and energies of the possible intermediates and transition states involved in the catalytic cycle, and determined the reaction paths connecting reactants and products. The objectives are establishing the well-understood hydroformylation mechanism, and further revealing the relationships among structure and reactivity and selectivity. The first review of theoretical study on hydroformylation was done by Ziegler and Versluis in 1992 [51]. These intensive theoretical studies prior to 2000 have been compiled by Frenking et al. [11] into a detailed and comprehensive paper in chemical reviews. Recently, the theoretical studies of hydroformylation by rhodium catalysts have been reviewed by Maseras et al. in book chapters in 2002 and 2004 [13, 14]. Here, we wish to report some recent new developments in Co-catalyzed hydroformylation on the respect of theoretical studies, and some important aspects from earlier investigations have been emphasized for comparison.

5 Recent Theoretical Studies on Hydroformylation

5.1 Active Catalyst $HCo(CO)_3$

The possible structure of $HCo(CO)_3$ catalyst [52] has been discussed controversially in the literature, and this controversy has also reflected the historical development of computational chemistry, as summarized in the review paper by Frenking et al. [11]. The previous discussions were performed mainly on four possible structures, as shown in Scheme 1.

In 1993, Ziegler et al. [52] reported the first comprehensive density functional theory investigation based on full optimization. They found that $HCo(CO)_3$ adopts

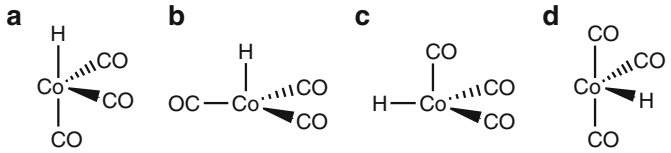

Scheme 1 Proposed structures for $HCo(CO)_3$

a singlet ground state with a butterfly geometry in C_s symmetry (**a**), which derives from dissociation of one equatorial CO in $HCo(CO)_4$. The second singlet structure in C_{3v} symmetry (**b**) with the removal of the axial CO from $HCo(CO)_4$ is 35 kJ/mol higher in energy, and all possible triplet states are also about 100 kJ/mol higher in energy than the C_s singlet state (**a**). Furthermore, Ziegler et al. analyzed the IR spectra of $HCo(CO)_3$, and assigned the experimentally detected two C–O stretch frequencies at 2,018 and 2,025 cm^{-1} as a possible combination of C_s and C_{3v} structures.

A systematic study on the structure and energy of $HCo(CO)_n$ ($n = 1$–4) was reported by Huo et al. in 2002 at the B3LYP/6-311 + G* density functional level of theory [53]. In agreement with the results of Ziegler, the B3LYP study also showed that $HCo(CO)_3$ has two singlet ground states, one from equatorial CO dissociation, and the other from axial CO dissociation. However, B3LYP calculations suggested that the most stable $HCo(CO)_3$ has a planar C_{2v} structure with hydrogen atom along the C_2 axis, and the Co center has planar tetra-coordination (**a′**), which is very close to the C_s butterfly form (**a**) by Ziegler. Starting from **a**, the structure optimization results in **a′**. The computed C–O stretching frequencies (2,023 and 2,031 cm^{-1}) agree with the experimental values (2,108 and 2,025 cm^{-1}).

In addition to the electronic structure and energy of $HCo(CO)_3$, it is also interesting to compare to CO dissociation energy from trigonal bipyramid $HCo(CO)_4$ (C_{3v}) to form $HCo(CO)_3$ on the singlet potential energy surface. The B3LYP calculations showed that the dissociation of an equatorial CO to form the planar $HCo(CO)_3$ (**a′**) is more favored than that of axial CO to form the C_{3v} structure (**b**) by 44.4 kJ/mol. In addition, Co–H homolysis needs much higher energy than both CO dissociations (229.7 vs. 107.5 and 151.9 kJ/mol). On the basis of the fact that there is no spin change during the dissociation of $HCo(CO)_4$ and no Co–H dissociation, as well as **a′** is more stable than **b**, equatorial CO dissociation should be the only energetically favored pathway, and the formation **b** can be ruled out. In addition, the most stable triplet state (like structure **c** in Scheme 1) is higher in energy than **a′** by 37.7 kJ/mol, but slightly more stable than **b** by 5.9 kJ/mol, respectively.

5.2 *Hydroformylation of Propene*

For studying the regioselectivity, Grima et al. [54] investigated the propene complexes (**1b-1, 1b-2** in Scheme 2) with the CNDO/2 method and at low ab initio

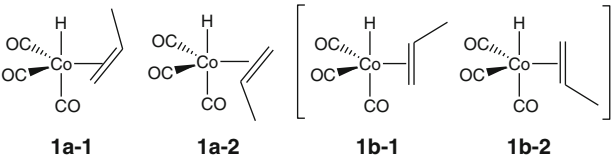

Scheme 2 Possible structures for $HCo(CO)_3(\eta^2\text{-}C_2H_4)$ and $HCo(CO)_3(\eta^2\text{-}C_3H_6)$

level of theory in 1977. They found that structure **1b-1** to be slightly more stable than **1b-2**. This important energetic difference explained the observed regioselectivity in favor of the linear product.

The subsequent step is the propene insertion process. Grima et al. [54] analyzed the [2 + 2] addition process for the propene insertion into the Co–H bond by means of CNDO/2 method. They proposed that the origin of the regioselectivity was due to the electrostatic dipole–dipole interaction between Co–H and C=C favoring the linear product, and the disfavored branched product was due to the higher energy required to inverse the olefinic dipole for the proper interaction. However, this interpretation is not supported by the high-level calculations as indicated below.

A systematic study on the propene hydroformylation with $HCo(CO)_3$ as catalyst was reported by Huo et al. [55] in 2003 at the B3LYP/6-311 + G* density functional level of theory (the relative energies are based on $HCo(CO)_3$, propene, CO, and H_2, and the relative free energies are scaled at 403 K and 200 atm.). They found two most stable structures (**1a-1** and **1a-2**) with the coordinated propene perpendicular to the H–Co axis. In agreement with the results of Grima, both **1b-1** and **1b-2** are two local energy minimum structures, and **1b-1** is only slightly more stable than **1b-2** by 0.5 kJ/mol in free energy. In addition, they found two transition states (**TS-1** and **TS-2**) for the rotation of the coordinated propene, and their barriers differ only 1.9 kJ/mol in free energy. No transition states between **1b-1** and **1a-2** as well as **1b-2** and **1a-1** could be located. Such small barriers and energy differences indicate the flat potential energy surface and the free rotation of propene under real reaction condition (Scheme 3).

B3LYP calculations showed that the insertion processes, which can lead to both the linear propyl (**1L**) and branched isopropyl (**1B**) complexes, have nearly the same activation free energies (25.8 and 26.5 kJ/mol) and reaction free energies (−4.5 and −4.1 kJ/mol). These results indicated that the insertion process does not determine the regioselectivity, in contrast with the proposal by Grima et al. [54]. On the other hand, the rather low activation barriers and much less exergonic properties suggested that the insertion processes are reversible. This explains the observed isomerization between internal and terminal olefins in experiment reasonably.

The next step is CO addition. The energy difference between the formed propyl (**2La**) and isopropyl (**2Ba**) tetracarbonyl complexes ($C_3H_7Co(CO)_4$) determines the regioselectivity. At the B3LYP /6-311 + G* level, **2La** is computed to be more stable than **2Ba** by 11.4 kJ/mol in free energy, while **1L** is only 0.4 kJ/mol more stable than **1B** in free energy. The free energy difference of 11.4 kJ/mol is originated from the repulsive interaction between the equatorial CO ligands and

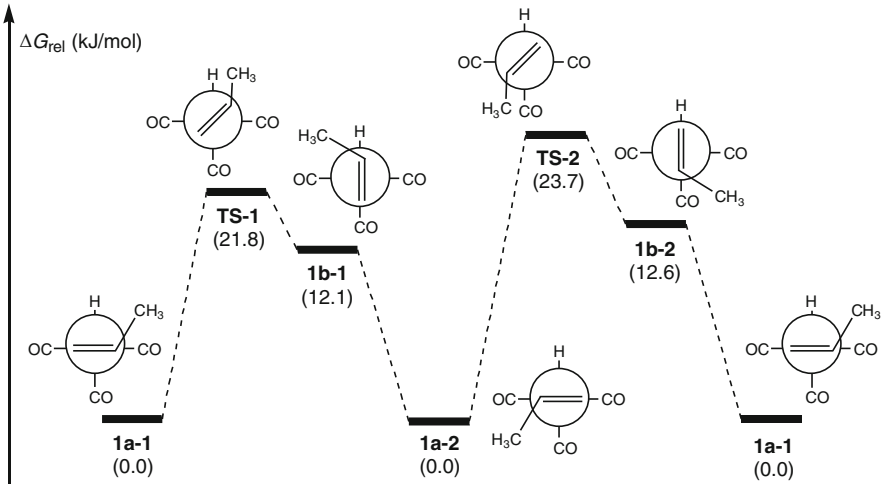

Scheme 3 Potential free energy profile (kJ/mol) for propene rotation in $HCo(CO)_3(\eta^2\text{-}C_3H_6)$

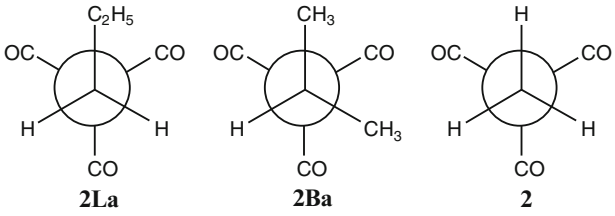

Scheme 4 Newman projection of **2La** and **2Ba**

the propyl or isopropyl groups, as shown by their Newman projection in Scheme 4. In **2La**, there are two CO and C_2H_5 gauche interactions, while there are four CO and CH_3 gauche interactions in **2Ba**. As a consequence, the Co–C_{alkyl} distance in **2La** (2.111 Å) is shorter than that in **2Ba** (2.154 Å), and the Co–CH_3 distance in **2** is only 2.080 Å. In addition, CO addition to form **2La** and **2Ba** is highly exergonic by −37.5 and −26.5 kJ/mol, respectively. The corresponding transition states for **1L** to **2La** and **1B** to **2Ba** are located, and the computed activation free energies are 29.3 and 37.4 kJ/mol, respectively. Thus, the linear CO addition is more favored both thermodynamically and kinetically.

The next important step is CO insertion. With $CH_3Co(CO)_4$ (**2**) as a model compound, a systematic investigation of CO insertion process was carried out at the B3LYP level without any constraints by Goh and Marynick [42]. The entire sequence is presented in Scheme 5. It was verified that the CO insertion reaction does not occur on a C_s symmetry potential energy surface as proposed by previous calculations. The interesting feature of this reaction is that methyl migration involves a simultaneous migration and twisting of the axial methyl group into the equatorial plane of the original trigonal bipyramid (**TS(2a/2b)**). The subsequent

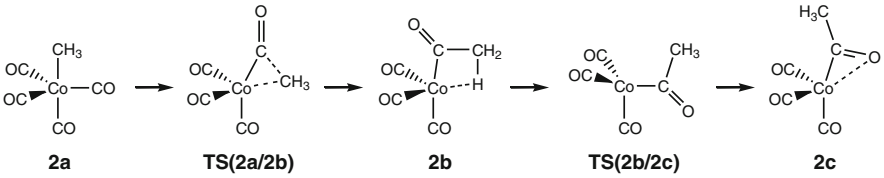

Scheme 5 Goh and Marynick proposed the mechanism for CO insertion [42]

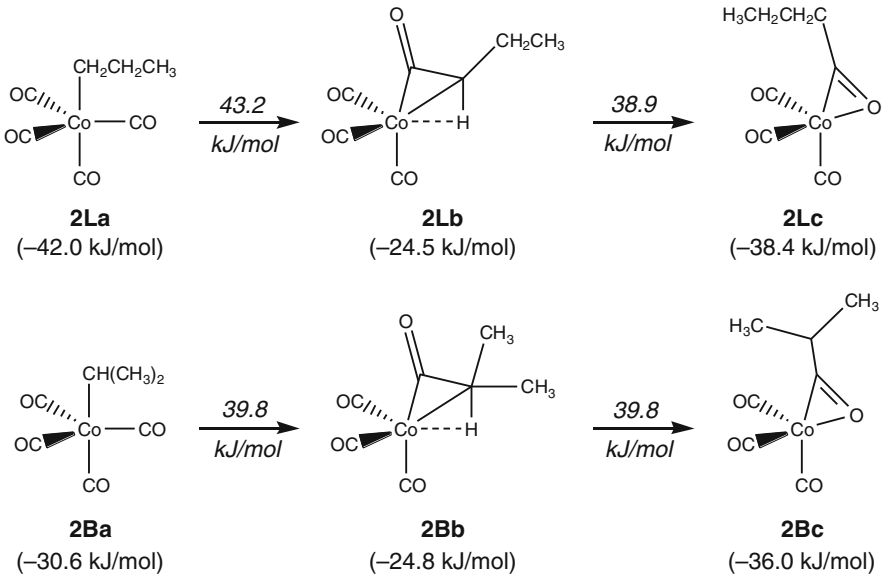

Scheme 6 B3LYP mechanism for CO insertion in **2La** and **2Ba**

relaxation leads to an intermediate best described as an axially substituted $(CH_3CO)Co(CO)_3$ species, with an agostic bond occupying the formally vacant equatorial site (**2b**), which can be converted into the more stable intermediate (**2c**) by the further rotation of the acetyl group via the transition state (**TS(2b/2c)**).

This unusual migration/twist mechanism is originated from the frontier molecular orbitals, and their efficient mixing can only be achieved by twisting the CH_3 group. The first step from **2a** to **2b** is endothermic by 27.2 kJ/mol and the corresponding barrier is 50.2 kJ/mol. The second step from **2b** to **2c** has a barrier of 39.3 kJ/mol, and is exothermic by −15.9 kJ/mol. The overall process from **2a** to **2c** is slightly exothermic by −11.3 kJ/mol.

Indeed, this CO insertion mechanism was also found for propyl (**2La**) and isopropyl (**2Ba**) complexes ($C_3H_7Co(CO)_4$) [55]. The related B3LYP structures and free energies are shown in Scheme 6. It is clear that they have the same structural patterns as well as comparable barriers and reaction energies. For CO insertion, the activation free energies for propyl and isopropyl species are 43.2 and

39.8 kJ/mol, which are somewhat lower than that for methyl. The CO insertion step for propyl and isopropyl species is also predicted to be endergonic by 17.5 and 5.8 kJ/mol, respectively. Furthermore, the overall process from **2La** to **2Lc** is slightly endergonic by 3.6 kJ/mol, while that from **2Ba** to **2Bc** is exergonic by −5.4 kJ/mol.

The last step of the hydroformylation catalytic cycle is hydrogen oxidative addition and aldehyde reductive elimination. The first systematic theoretical study on this step was carried out by Ziegler and coworkers [56, 57], and two conceived reaction paths are depicted in Scheme 7. At the HFS level [56], it was found that H_2 coordination to **2c** forming the most stable hydrogen complex **3a** is nearly thermoneutral with a calculated reaction enthalpy of −2 kJ/mol. The isomer **3a′** with H–H bond perpendicular to the basal plane is less stable than **3a** by 19 kJ/mol, which is rather small for their conversion. Furthermore, it was concluded that both the oxidative addition/reductive elimination sequence (path A) and the process involving the four-center intermediate (path B) are likely candidates for the formation of aldehyde, indicated by the close energy barrier of 77 and 85 kJ/mol. However, the subsequent BP86 results [57] showed that the corresponding H_2 coordination reaction is an exothermic process that releases 10.5 kJ/mol, and the energy barrier for the oxidative addition/reductive elimination process is predicted to be only 36.3 kJ/mol, which is kinetically favored over path B involving a four-center transition state with an energy barrier of 70.4 kJ/mol.

Recently, the H_2 oxidative addition and aldehyde reductive elimination process (path A) of acyl complexes ($C_3H_7COCo(CO)_3$), **2 L** and **2B**, was studied by Huo et al. at the B3LYP level [55]. The corresponding B3LYP structures and free energies for both linear and branched paths are shown in Scheme 8. The first step

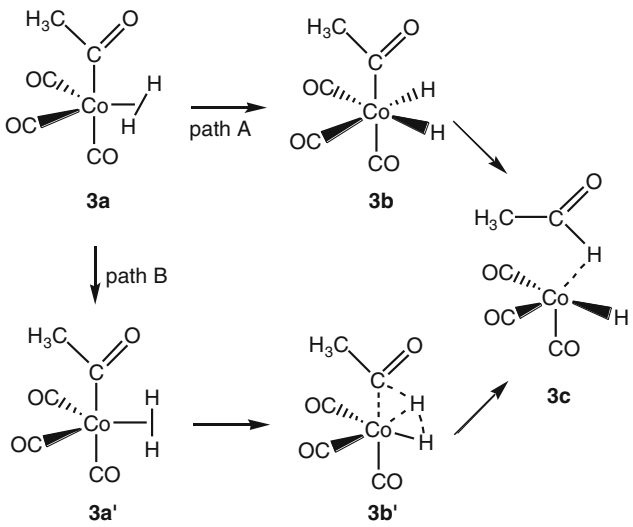

Scheme 7 Possible reaction paths for H_2-induced aldehyde formation

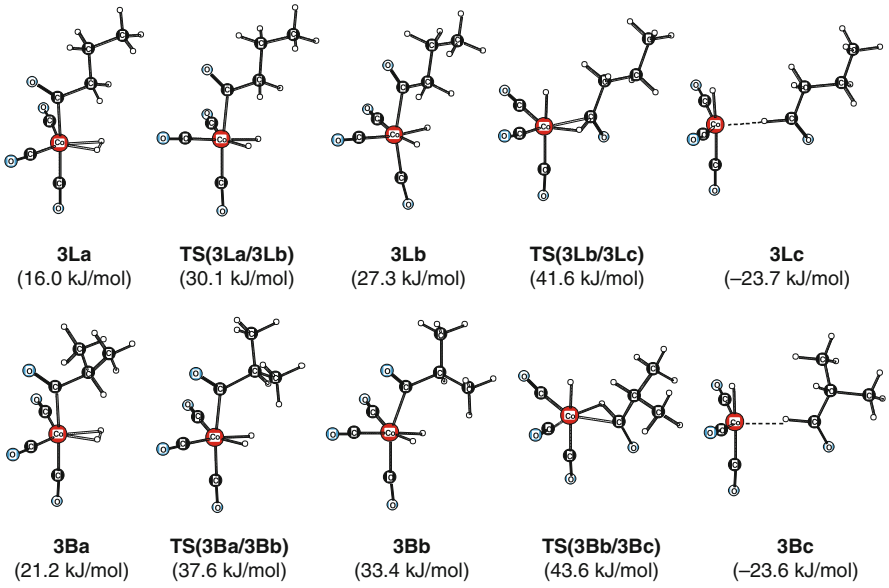

Scheme 8 H_2 oxidative addition and aldehyde reductive elimination

of this process is H_2 coordination to the formal coordinatively unsaturated intermediates **2Lb**/**2Lc** and **2Bb**/**2Bc** forming the corresponding hydrogen adducts (**3La** and **3Ba**), which are the precursors for H_2 oxidative addition with the formation of the dihydrido intermediates (**3Lb** and **3Bb**). It was found that the oxidative addition step for linear and branched paths is endergonic by 11.3 and 12.2 kJ/mol, with the activation free energies of 14.1 and 16.4 kJ/mol, respectively. The subsequent reductive elimination leads to the formation of the aldehyde adducts (**3Lc** and **3Bc**), which is exergonic by −51.0 and −57.0 kJ/mol, and has the activation free energies of 14.3 and 10.2 kJ/mol, respectively. As shown in Scheme 8, there are no significant differences between the elementary steps for linear and branched processes. The most important finding at B3LYP is that H_2 coordination has a rather higher free energy barrier (37.0 and 40.4 kJ/mol from **2Lb** and **2Lc** to **3La**, as well as 48.8 and 52.8 kJ/mol from **2Bb** and **2Bc** to **3Ba**) than the corresponding H_2 oxidative addition (14.1 and 16.4 kJ/mol).

The B3LYP calculations depicted the complete catalytic cycle of $HCo(CO)_3$-catalyzed propene hydroformylation. The most important findings are (1) the propene insertion step is a thermal neutral process with rather small activation barriers, and this explains the observed isomerization from internal olefin to terminal olefin by using cobalt-based catalysts; (2) CO addition to $RCo(CO)_3$ is a highly exergonic and irreversible process, and the yielded $RCo(CO)_4$ determines the regioselectivity in favor of the linear product. This originated from the energetic difference of the linear and branched $RCo(CO)_4$ isomers, caused by the steric effect of the alkyl group with the equatorial CO ligands; and (3) H_2 coordination has a

rather higher barrier than the corresponding H_2 oxidative addition, and could be the rate-determining step.

5.3 *Hydroformylation and Hydromethoxycarbonylation of* N-*Vinyl Acetamide*

In 2004, a comprehensive experimental and theoretical study on the hydroformylation and hydromethoxycarbonylation of *N*-vinyl acetamide was reported by Klaus et al. [58]. The goal of this study is to get insight into the observed regioselectivity in favor of the branched (*iso*) product (Fig. 5). Both hydroformylation and hydroalkoxycarbonylation have the same reaction mechanism, and they differ only in the step of oxidative addition with hydrogen (H_2) leading to aldehydes or alcohol (ROH) yielding amino acid esters.

Due to the functional groups, *N*-vinyl acetamide ($CH_3CONHCH{=}CH_2$) can coordinate to $HCo(CO)_3$ via the C=C double bond (**4**), the nitrogen lone pair (**4a**), or the oxygen lone pair (**4b**). At the B3LYP level (the relative free energies are based on complex (**4**), *N*-vinyl acetamide, H_2, and CO or methanol, scaled at 298 K), both **4** and **4b** are close in free energy (−2.9 kJ/mol), while **4a** is very higher in free energy (33.9 kJ/mol). This indicates that both **4** and **4b** can be in equilibrium, and the formation of **4a** is unlikely. On the basis of these energetic differences and the expected products, only **4** was considered as starting point for the catalytic cycle of hydroformylation and hydromethoxycarbonylation.

The C=C insertion, which leads to the formation of linear (**L**) and branched (**B**) alkyl complexes (Scheme 9), is similar to that of propene. It was found that both paths have nearly the same activation free energies (18.0 and 18.4 kJ/mol, respectively). There is therefore no kinetic control over the regioselectivity, in agreement with the findings for the olefin insertion process of the propene complex [55]. Apart from the alkyl complexes stabilized by the Co···H–C agostic interaction (**4La** and **4Ba**), the nitrogen (**4Lb** and **4Bb**) or oxygen (**4Lc** and **4Bc**) lone pairs can also stabilize the alkyl complexes. **4Lc** and **4Bc** are more stable than **4La/4Ba** and **4Lb/4Bb**. The most stable complex is **4Bc**, and **4Lc** is 13.8 kJ/mol higher in free energy. Based on these calculations and also on the fact that there is no difference in activation free energies in the insertion process, the formation of **4Lc** is unlikely, and **4Bc** is the only insertion product. Therefore, the regioselectivity with *N*-vinyl acetamide as the substrate in hydroformylation and carboxylation is determined by

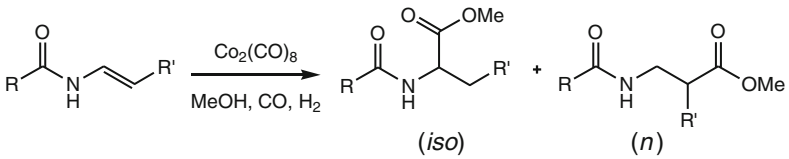

Fig. 5 Hydroalkoxycarbonylation of enamide to amino acid ester

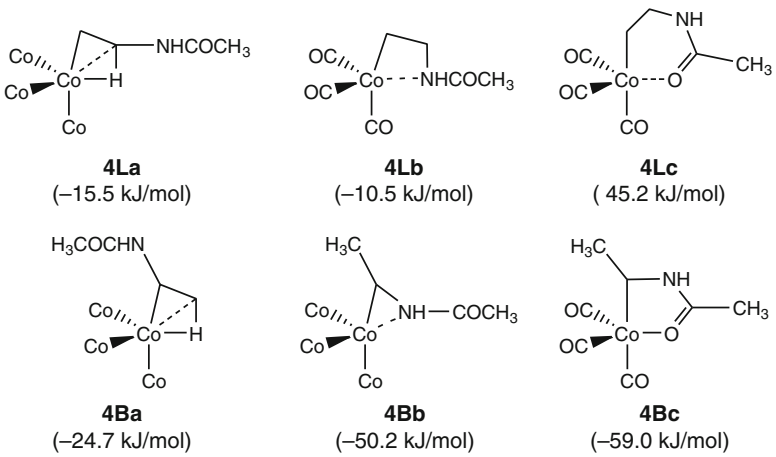

Scheme 9 C=C insertion mechanism of *N*-vinyl acetamide

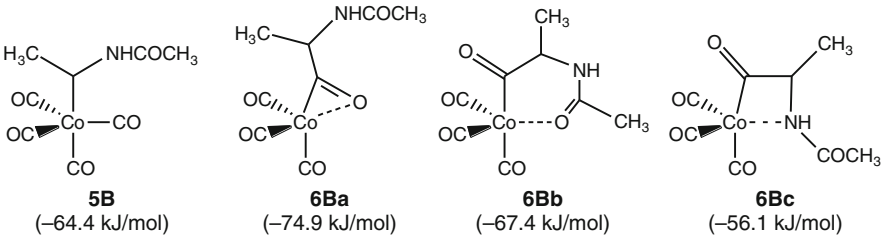

Scheme 10 B3LYP mechanism for CO insertion in **5B**

the stability of the branched alkyl product (**4Bc**). This agrees perfectly with the experimental observations (Scheme 9).

Due to the very strong similarity, here, only the results of CO addition to **4Bc** and insertion to the branched alkyl complex (**5B**) are summarized, and the same is also for the subsequent formation of aldehyde and amino acid ester. As found for CO insertion in **2** ($CH_3Co(CO)_4$) [42] and in **2La** and **2Ba** ($C_3H_7Co(CO)_4$) [55], similar reaction path was also found for **5B**. As shown in Scheme 10, the most stable insertion product is **6Ba**, while the other two isomers **6Bb** and **6Bc** are higher in free energy by 7.5 and 18.8 kJ/mol. This indicates that functional groups, like nitrogen and oxygen lone pairs, do not alter the CO insertion mechanism, neither the relative energies nor the structures.

As shown in Scheme 11, the next step includes H_2 coordination, oxidative addition, and aldehyde reductive elimination. As compared to propene, there are no significant effects from functional groups. Starting from the most stable acyl complex **6Ba**, H_2 coordination with the formation of **7B** is endergonic by 62.3 kJ/mol. The subsequent oxidative addition from **7B** to **8B** is also endergonic by 28.1 kJ/mol with the activation free energy of 34.8 kJ/mol. The reductive elimination from **8B** to

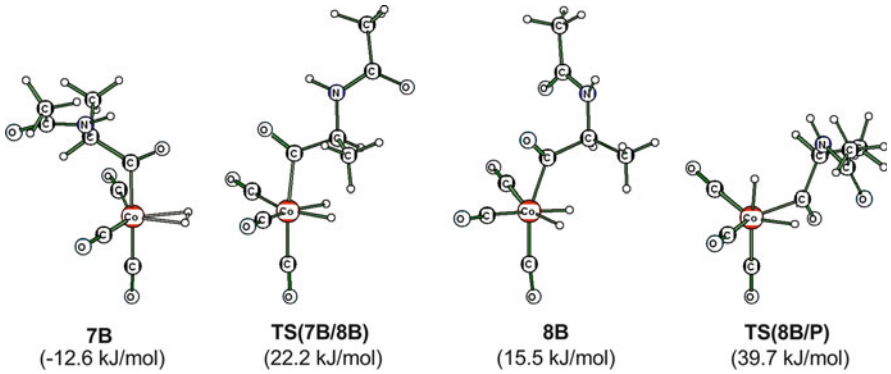

Scheme 11 H_2 oxidative addition and aldehyde reductive elimination

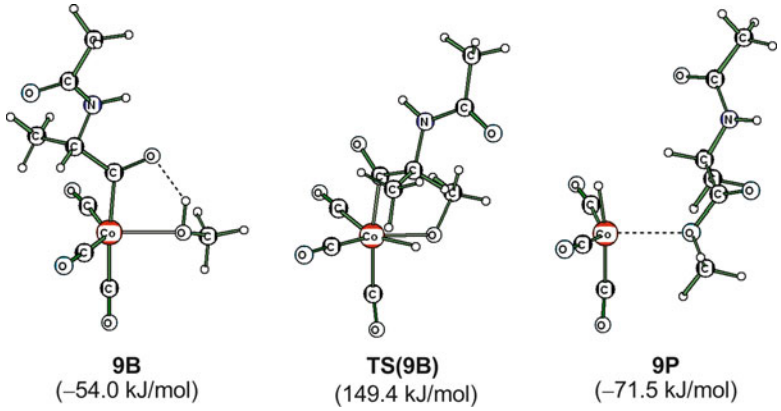

Scheme 12 Methanol oxidative addition and ester reductive elimination

aldehyde and the active catalyst is a highly exergonic process, and has the activation free energy of 24.2 kJ/mol.

In addition to H_2 oxidative addition forming aldehyde, methanol oxidative addition yielding amino acid ester was also considered. The corresponding methanol complex (**9B**) was located (Scheme 12). Due to the attractive electrostatic interaction, the O–H group of methanol toward the acyl C=O bond forms a formal five-membered ring. This is in contrast to the corresponding H_2 complex (**7B**), in which the H–H bond is perpendicular to the Co–C_{acyl} bond.

For methanol oxidative addition, only the transition state (**TS(9B)**) was located, and attempts to locate the hydride and methoxo intermediate failed. Further optimization following the imaginary vibration mode of **TS(9B)** led to the direct formation of the final product (**E**) without any barrier (also without the corresponding reductive elimination transition state), indicating the flat potential energy surface. The driving force for the simplified reaction should be the attractive electrostatic interaction between the negatively charged oxygen center of the CH_3O

ligand and the positively charged carbon center of the acyl ligand in **TS(9B)**. Both ligands have the appropriate orientation, which can facilitate further reaction. Also in contrast to H_2 oxidative addition, methanol oxidative addition has a much higher activation free energy barrier of 203.3 kJ/mol, and this explains the rather relatively low yield.

In addition to hydroformylation and hydromethoxycarbonylation, the hydrogenation of *N*-vinyl acetamide was also computed. It clearly showed that hydrogenation is not favored energetically and this is because the CO coordination to **4Bc** leading to **5B** is exergonic by −5.4 kJ/mol, while the corresponding competitive H_2 coordination is endergonic by 69.5 kJ/mol. Therefore, hydrogenation of *N*-vinyl acetamide is not competitive to hydroformylation.

The B3LYP calculations presented the complete catalytic cycle of *N*-vinyl acetamide hydroformylation using $HCo(CO)_3$ as catalyst. The computed free energy profiles for hydroformylation (solid line) and hydroalkoxycarbonylation (dotted line) for the branched products are shown in Scheme 13. The most important findings are (1) the C=C coordination is equally populated as that of the oxygen lone pair, while that of nitrogen lone pair is not competitive; (2) in contrast to propene insertion, the C=C insertion of *N*-vinyl acetamide is a highly exergonic and irreversible process with small free energy barriers, and thus the relative

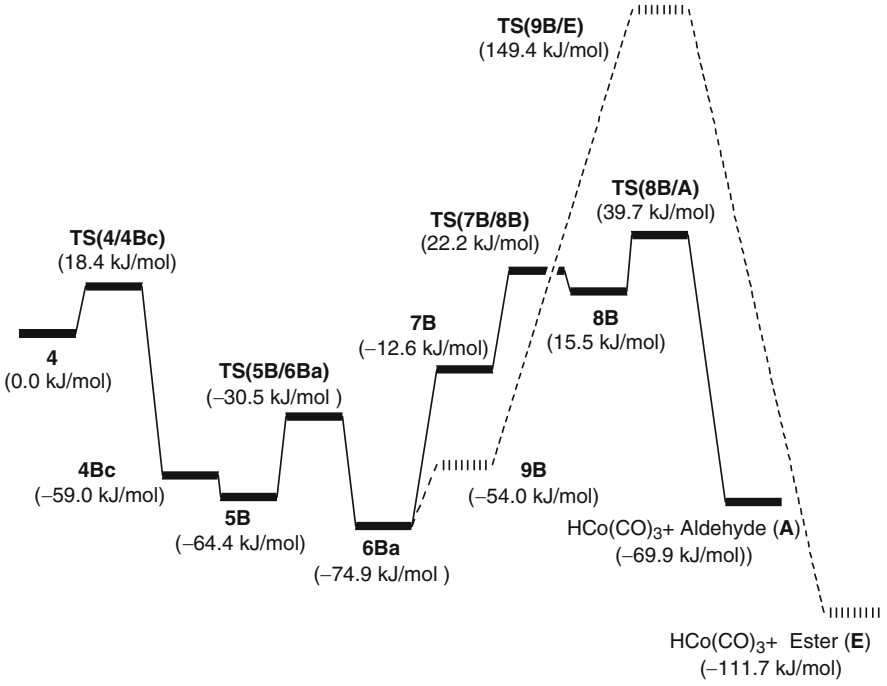

Scheme 13 Free energy profiles for hydroformylation (*solid line*) and hydroalkoxycarbonylation (*dotted line*) for the branched products

stability of the O=C stabilized alkyl complexes determines the regioselectivity in favor of the branched product; and (3) methanol has much higher oxidative addition barrier than H_2 on the one hand and on the other hand, H_2-induced aldehyde formation is a two-step process (oxidative addition/reductive elimination), while methanol induced ester formation is a single-step process (oxidative addition).

5.4 Hydroformylation of 1,3-Butadiene

The interest in 1,3-butadiene hydroformylation is the atom-efficient green route for producing β,γ-unsaturated aldehyde and 1,6-hexanedial (adipaldehyde), which is a valuable precursor for producing ε-caprolactam and adipic acid/hexamethylene-1, 6-diamine (HMDA) as key monomers in nylon-6 and nylon-6,6 manufacture.

In 1952, Adkins and Williams recognized that the hydroformylation of butadiene might lead to interesting products such as adipic aldehyde or pentenals [59]. In 1974, BASF patented a two-step process using a rhodium and a cobalt catalyst to yield adipic aldehyde (resp. alcohol) with about 60% selectivity [60]. Systematic studies on the Rh-catalyzed hydroformylation of butadiene were performed by Fell et al., [61–63] and they found that both steric and electronic factors of phosphine ligands influence the product distribution. Depending on the catalysts used, various amounts of saturated monoaldehydes and dialdehydes were formed. Secondary phosphines led to an almost complete 1,4-addition product in the primary step of the hydroformylation of butadiene. In 1985, van Leeuwen and Roobeek [64] successfully hydroformylated butadiene by 1,2-bis(diphenylphosphino)ethane-Rh (I) complex to give pentanal in over 90% selectivity. It was suggested that the β,γ-unsaturated aldehyde is formed as the initial product [65, 66], which can further isomerize to the thermodynamically more stable α,β-unsaturated aldehyde. Since the intermediate α,β-unsaturated aldehyde is much more facile to hydrogenation than hydroformylation [67], the saturated aldehyde is formed. In 1995, Bertozzi et al. [68] reported that the hydroformylation of butadiene promoted by rhodium–mesitylene cocondensate has the unusual high chemoselectivity and regioselectivity in the β,γ-unsaturated aldehyde (96%). In 1997, Horiuchi et al. [69] presented a highly selective asymmetric hydroformylation catalyzed by (*R*,*S*)-BINAPHOS-Rh(I) complex under mild conditions to give optically active β,γ-unsaturated aldehyde (up to 95%). On the other hand, some attempts at preparing adipaldehyde by butadiene hydroformylation have been made mainly on patent literatures [70–74]. In most cases, the selectivity to the desired adipaldehyde is low. Recently, Ohgomori et al. [75] developed a catalyst composed of rhodium and DIOP, with a higher selectivity about 37% for the formation of adipaldehyde. Furthermore, they deduced that the ratio of 1,2-addition to 1,4-addition may be determined by the equilibrium of $\{\eta^4$-(EE)-butadiene$\}\{$(AE)-diphospine$\}$(H)Rh and $\{\eta^4$-(AE)-butadiene$\}\{$(EE)-diphospine$\}$(H)Rh.

Despite many experimental works, very little basic work was done on the mechanistic aspects. Using online high-pressure IR technique, Mirbach [76]

explored the cobalt-carbonyl-catalyzed hydroformylation of 1,3-butadiene. The formation of the intermediates, η^3-$C_4H_7Co(CO)_3$ and σ-$C_4H_7Co(CO)_4$, were observed. In the recent online IR and NMR study on the pyridine-modified cobalt-catalyzed hydromethoxycarbonylation of butadiene [77], the existence of the above intermediates was verified, and $C_4H_7Co(CO)_4$ was further characterized having the 1,4-addition structure $(H_3CHC{=}CHCH_2)Co(CO)_4$. In addition, the deuterioformylation experiment [68] also suggested that the η^3-butenyl complexes are likely to be the key intermediates.

The first systematic B3LYP DFT investigation into the complete catalytic cycle of 1,3-butadiene hydroformylation using $HCo(CO)_3$ as active catalyst was reported by Huo et al. [78]. It was found that the coordination mode of 1,3-butadiene to $HCo(CO)_3$ is similar to that of propene [55]. The most stable structure has the C=C bond perpendicular to the H–Co bond (**10**), and butadiene moiety can rotate freely with the rotation barrier of 23.8 kJ/mol in free energy, while the structures with the C=C bond parallel to the H–Co bond facilitate the subsequent insertion reaction leading to Markovnikov alkyl complex (**11a**) or *anti*-Markovnikov alkyl complex (**11b**), as shown in Scheme 14 (the relative free energies are based on $HCo(CO)_3$, butadiene, CO, and H_2, scaled at 403 K and 200 atm.).

The calculated large thermodynamic stability of **11a** over **11b** by 83.3 kJ/mol in free energy indicates that the *anti*-Markovnikov insertion path is unlikely. In addition, the Markovnikov path is also more favored kinetically by 7.1 kJ/mol in free energy. The higher stability of **11a** derives from the *syn*-η^3-allyl coordination. Thus, the formation of the linear 1,2-addition product, pent-4-enal, can be ruled out.

According to the *syn*-η^3-allyl structure in **11a**, there are two possibilities for CO addition, one leads to the linear 1,4-addition $(CH_3CH{=}CHCH_2)Co(CO)_4$ complex (**12a**), and the other leads to the branched 1,2-addition $(CH_2{=}CHCH(CH_3))Co(CO)_4$ complex (**12b**). As shown in Scheme 15, the linear intermediate (**12a**) is more stable than the branched one (**12b**) by 27.6 kJ/mol in free energy. In addition,

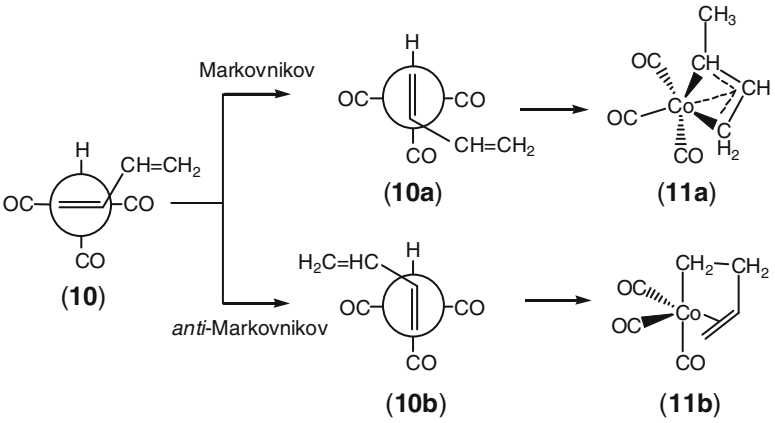

Scheme 14 Butadiene insertion: Markovnikov and *anti*-Markovnikov mechanism

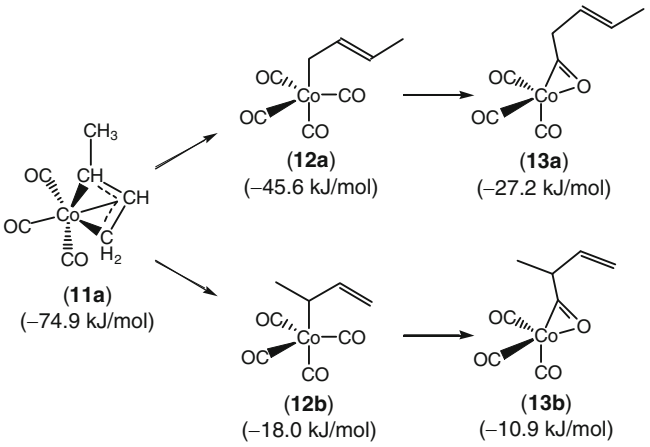

Scheme 15 CO addition and insertion of **11a**

the CO addition leading to **12a** has a lower activation free energy than that leading to **12b** (98.3 vs. 119.2 kJ/mol). Therefore, the formation of **12a** is more favored both thermodynamically and kinetically, which leads to the linear 1,4-addition product as the only product. This is in agreement with the recent study of online high-pressure IR technique by Tuba et al. [77], and they found that both **11a** and **12a** are the stable intermediates in the hydroformylation of 1,3-butadiene. In addition, they attributed the slow hydroformylation rates to the catalytic inertness of the π-allyl complex η^3-$C_4H_7Co(CO)_3$, in line with the B3LYP theoretical results. Further calculations showed that the linear CO insertion product (**13a**) is more stable than the branched one (**13b**) by 16.3 kJ/mol in free energy. Indeed, the insertion process from **12a** to **13a** has lower activation free energies and more stable intermediates than that from **12b** to **13b**. These energetic differences are also observed in the subsequent H_2 oxidative addition and aldehyde reductive elimination. Due to the very strong similarity of these processes to those for propene hydroformylation [55], it is not necessary to repeat all the details here. As a consequence, the linear 1,4-addition product, penta-3-enal, is the only principal product; neither the linear 1,4-addition product nor the branched 1,2-addition product can be observed kinetically and thermodynamically. For 1,4-addition path, the CO addition has the largest free energy barrier, and should be the rate-determining step.

On the basis of the computed kinetic and thermodynamic data, it is very interesting to have a comparison with the recent experimental observation of the most stable intermediates. Using online IR and NMR techniques in the cobalt-catalyzed hydromethoxycarbonylation of butadiene, Tuba et al. [77] observed several key intermediates and found that (1) the allyl complex (η^3-C_4H_7)$Co(CO)_3$ (**11a**) is quite stable at 100°C, and no further reactions could be detected after the formation for several hours under 75 bar of CO at 100°C in MeOH; (2) the but-2-enyl complex ($CH_3CH{=}CHCH_2$)$Co(CO)_4$ (**12a**) is very unstable, and can be easily converted to the acyl complex ($CH_3CH{=}CHCH_2CO$)$Co(CO)_4$ with CO

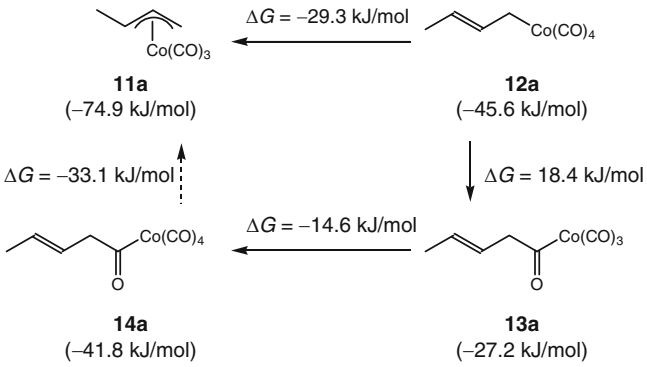

Scheme 16 Relationship of relative free energies among various key intermediates

(**14a**, quantitative formation at −40°C under 70 bar of CO); (3) **12a** can be very easily converted to **11a** by losing CO by raising the reaction temperature from −40°C to room temperature; (4) the acyl complex (**14a**) is stable at 0°C under 70 bar of CO, but can be easily converted to **11a** at higher temperature (>40°C) by decarbonylation reaction.

Although there are no quantitative kinetic and thermodynamic data available for direct comparison, these experimental results agree qualitatively with the B3LYP computations. The free energy changes (scaled at 130°C) are shown in Scheme 16. For example, **12a** by losing CO resulting in **11a** has a negative free energy change of −29.3 kJ/mol due to the large entropy effect. This is why **12a** to **11a** can be conducted by raising temperature (from −40°C to room temperature). The same explanation is also found for the formal change from the acyl complex (**14a**) by losing two CO molecules to **11a** at even higher temperature (140°C), since this formal process is exergonic by −33.1 kJ/mol due to the large entropy contribution. In addition, the endergonic property from **12a** to **14a** by 3.8 kJ/mol explains the facial reaction at low temperature (−40°C). All these energetic changes agree with the experimentally observed stability and reactivity of the involving intermediates.

In addition to the calculated kinetic and thermodynamic data in gas phase, Huo et al. also examined the influence of methanol as polar solvent. It was found that the free energies of activation and reaction in methanol are comparable with the data in gas phase, and no disorders of the stationary points on the energy profiles due to solvation can be found. This indicates that the polar solvent like methanol can stabilize species involved in the catalytic cycle to some extent, but cannot change their relative values in activation and reaction. In addition to methanol as solvent, methanol as reactant is also not competitive to CO coordination, and therefore, the rate-determining step will not be affected.

However, methanol as reactant has large effect on H_2 addition in both gas phase and solution, hinders the H_2 coordination and also the subsequent formation of aldehyde, and results in the formation of ester from methanol oxidative addition (hydromethoxycarbonylation). However, methanol oxidative addition has much

higher activation free energy (ca 205 kJ/mol [58]) than H_2 oxidative addition (ca. 25 kJ/mol), and this indicates that direct methanol oxidative addition is unlikely as compared to H_2 oxidative addition. On this basis, it is easily to understand the accelerating effect of the hydromethoxycarbonylation of 1,3-butadiene by pyridine, since pyridine as base deprotonates methanol to form pyridinium ion and methoxide (CH_3O^-), and CH_3O^- will react with the acyl complex to yield ester via nucleophilic substitution, as proposed by Tuba et al. [77]. This will reduce the rather high methanol oxidative addition barrier.

In summary, butadiene hydroformylation or hydromethoxycarbonylation favors the formal 1,4-addition product in high regioselectivity. The enhanced stability of the *syn*-η^3-allyl complex ((η^3-$CH_2CHCH(CH_3)$)$Co(CO)_3$) presents a distinctly thermodynamic preference for the Markovnikov insertion. Therefore, the formation of linear 1,2-addition product via the *anti*-Markovnikov path is almost suppressed. The CO addition to the *syn*-η^3-allyl complex favors the formation of 1,4-addition intermediate over the branched intermediate both kinetically and thermodynamically. Accordingly, the 1,4-addition unsaturated aldehyde $H_3CHC{=}CHCH_2CHO$ should be the principal product, in agreement with the experimental findings. The CO addition is the rate-determining step. Methanol as solvent and ligand does not change the potential energy surface compared to that found in gas phase.

5.5 *Hydroformylation of Alkyne and Allene*

The interest of alkyne and allene hydroformylation is the formation of α,β-unsaturated aldehydes, which are valuable intermediates in fine chemical and pharmacy. In contrast to alkenes, the studies on the hydroformylation of alkynes are relatively scant. The first case of acetylene hydroformylation was reported by Natta and Pino in 1951 [79]. It was found that in the presence of metallic cobalt at 120–150°C and 200–300 atm, acetylene reacted with synthesis gas yielding a mixture of high-boiling, unidentified products. During the following 40 years, hydroformylation of alkynes to α,β-unsaturated aldehydes had little success [80–85]. The early investigations usually resulted in low selectivity and/or low yield of unsaturated aldehydes, primarily because the formation of the corresponding saturated aldehydes and non-carbonylated olefins could hardly be suppressed.

The breakthrough in the hydroformylation of alkynes to α,β-unsaturated aldehydes emerged in the mid-1990s. Several effective catalysts such as the catalyst system of $Rh(CO)_2(acac)$ and a sophisticated bisphosphite ligand [86], the heterobimetallic catalyst $PdCl_2(PCy_3)_2/Co_2(CO)_8$ [87], and the zwitterionic rhodium complex with triphenyl phosphite as ligand [88, 89] were successively developed. These exciting achievements revealed that the hydroformylation of acetylenic species to α,β-unsaturated aldehydes with high activity and selectivity is accessible.

The other potential resource for producing α,β-unsaturated aldehydes is allenes. With the cumulated diene structural unit, allenes exhibit some unique reaction behaviors and serve as potential precursors in the synthesis of highly complex

and strained target molecules of biological and industrial importance [90]. However, the information about the allenes' hydroformylation is relatively scant. One experimental study was carried out by Fell and Beutler in 1976 [91], and they found that hydroformylation of 1,2-dienes gave mixtures of mono- and dialdehydes.

The first systematic B3LYP DFT investigation into the hydroformylation of alkynes and allene was carried out by Huo et al. [92, 93]. It was found that acetylene hydroformylation has very similar catalytic mechanism as that of propene, therefore only the differences are emphasized, and no general comparison is made. Scheme 17 shows the activation and reaction free energies.

The acetylene coordination to the active catalyst $HCo(CO)_3$ forms the most stable π-complex (**15a**) with the C≡C bond in the equatorial plane. The following step of acetylene insertion into Co–H bond leads to the stable vinyl complex $(H_2C{=}CH)Co(CO)_3$ (**15b**), which has a butterfly geometry with vinyl group in the axial site. In addition, acetylene insertion has an activation free energy of 28.5 kJ/mol, and is an exergonic (−84.9 kJ/mol) and irreversible process, in contrast to the thermal neutral process of alkenes. Therefore, it is expected that the regioselectivity of terminal alkynes RC≡CH with $HCo(CO)_3$ leading to linear or branched product should be controlled by this irreversible step.

The subsequent CO addition to **15b** leads to the formation of the vinyl tetracarbonyl cobalt complex $(H_2C{=}CH)Co(CO)_4$ (**15c**). The CO addition does not have any barrier and is exergonic by −33.9 kJ/mol. The successive carbonylation of (**15c**) leading to the most stable acyl complex $(\eta^3\text{-}H_2C{=}CHCO)Co(CO)_3$

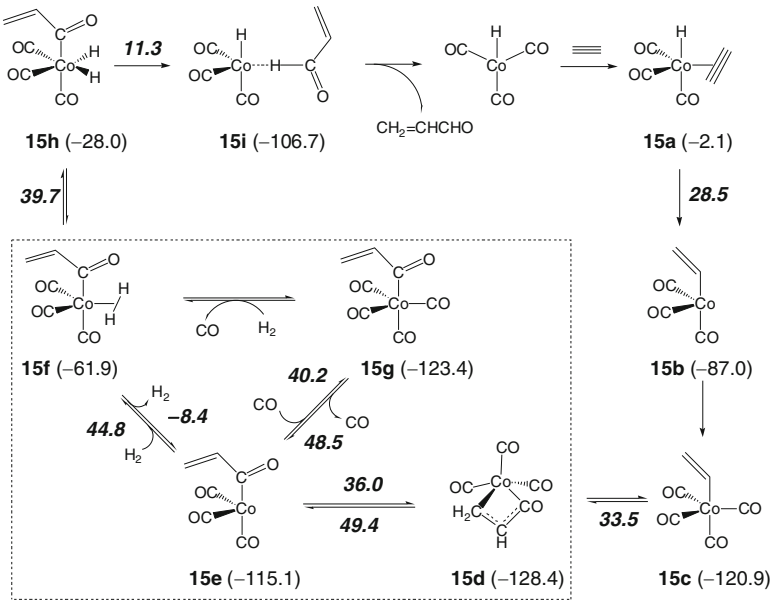

Scheme 17 Activation (*bold* and *italics*) and reaction free energies (kJ/mol, based on $HCo(CO)_3$, acetylene, CO, and H_2, scaled at 403 K and 200 atm.) of acetylene hydroformylation

(**15d**) has an activation free energy of 33.5 kJ/mol and is slightly exergonic by −7.5 kJ/mol. **15d** further arranges into **15e** for H_2 addition (**15f**) and subsequent oxidative addition (**15h**) as well as acrolein reductive elimination (**15i**).

The H_2 coordination and oxidative addition to **15e** are computed to be endergonic processes (53.2 and 33.9 kJ/mol), and the competitive CO coordination for the formation of $(H_2C{=}CHCO)Co(CO)_4$ (**15g**) is exergonic by −8.3 kJ/mol. Thus, the formation of **15g** is more favored thermodynamically, and also dominant in the possible equilibrium between $(H_2C{=}CHCO)Co(CO)_4$ (**15g**) and $(H_2C{=}CHCO)Co(CO)_3(\eta^2\text{-}H_2)$ (**15f**). As shown in Scheme 17, the isomerization from **15d** to **15e** and the CO dissociation from **15g** to **15e** as well as H_2 coordination from **15e** to **15f** have very close activation free energies (44.8–49.4 kJ/mol). Therefore, each of them around **15e** can be the rate-determining step under the variation of the reaction condition (temperature, pressure, and solvent).

It is also interesting to note that the possible hydrogenation reaction of acetylene is not competitive to hydroformylation; this is because that CO addition to **15b** forming **15c** is energetically much more favored than the corresponding H_2 addition (−120.9 vs. −55.2 kJ/mol, respectively). Therefore, the formation of saturated aldehyde is due to the further hydrogenation of the unsaturated aldehyde from hydroformylation.

The unsaturated aldehyde contains two functional groups, C=C and C=O. Hydrogenation of C=C bond will lead to saturated aldehyde, while hydrogenation of C=O bond will yield allyl alcohol. The B3LYP calculations by Huo et al. suggested that the chemoselectivity of acrolein ($CH_2{=}CH{-}CH{=}O$) hydrogenation is mainly determined by the higher stability of the C=C coordination over the C=O coordination by 14.6 kJ/mol in free energy [94]. Furthermore, the free energy barriers for C=O hydrogenation are higher than those of C=C hydrogenation by more than 75 kJ/mol. Thus, propanal (CH_3CH_2CHO) is the principal hydrogenation product, while the formation of allyl alcohol ($CH_2{=}CHCH_2OH$) is almost suppressed, in line with the experimental observations.

For terminal alkynes instead of acetylene as substrates, the alkynes insertion into the Co–H bond can occur in two ways, e.g., *anti*-Markovnikov for linear isomers (PL) and Markovnikov for branched isomers (AB), as shown in Scheme 18. The same case also can be found for allenes (AL and AB). In addition, it is possible for mutual isomerization between alkynes and allenes. This may also result in the diversification of products. Therefore, the key problem of terminal alkynes or

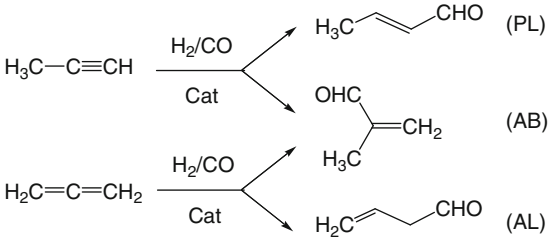

Scheme 18 Hydroformylation products of propyne and allene

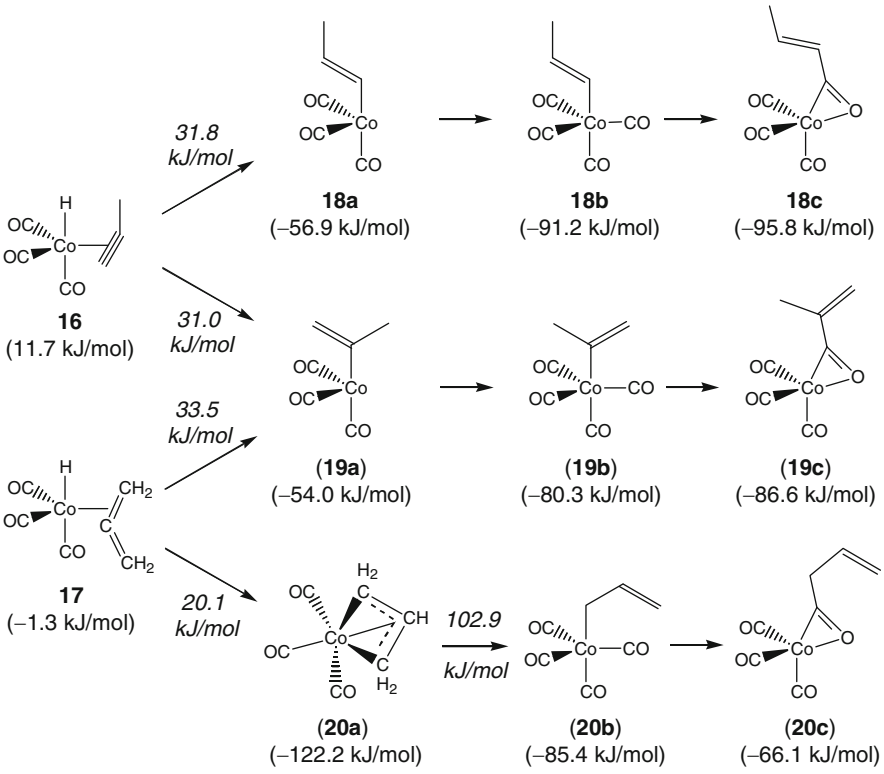

Scheme 19 Activation (*italics*) and reaction free energies of propyne and allene hydroformylation

allenes' hydroformylation is the control of the regioselectivity to get the desired α,β-unsaturated aldehydes.

The B3LYP/6-311 + G* computed activation and reaction free energies for propyne and allene hydroformylation are shown in Scheme 19 (based on $HCo(CO)_3$, allene, CO, and H_2, scaled at 403 K and 200 atm.). Similar to acetylene, propyne insertion reaction is a one-step and irreversible process, and thus should determine the observed regioselectivity. However, the *anti*-Markovnikov insertion forming **18a** and the Markovnikov insertion forming **19a** have nearly the same reaction free energies (−68.6 and −65.7 kJ/mol), and the comparable activation free energies (31.8 and 31.0 kJ/mol). As a consequence, no regioselectivity can be expected both thermodynamically and kinetically.

In contrast to propyne, allene hydroformylation presents a kinetic and thermodynamic preference for the *anti*-Markovnikov insertion, as indicated by the lower activation free energy (20.1 vs. 33.5 kJ/mol) and the higher stability of the insertion product (−122.2 vs. –54.0 kJ/mol) for *anti*-Markovnikov path with respect to Markovnikov path. In terms of these energy differences, a ratio of 98:2 for *anti*-Markovnikov to Markovnikov products is predicted kinetically. Furthermore, from

thermodynamic point of view, the predicted product ratio would be quantitatively. Therefore, the irreversible allene insertion step determines the observed regioselectivity, and the linear unsaturated aldehyde should be the principal product. In addition, no subsequent H_2 coordination and oxidative addition, as well as aldehyde reductive elimination, will affect the regioselectivity.

In summary, allene hydroformylation favors the linear *anti*-Markovnikov product (but-3-enal) in high regioselectivity both kinetically and thermodynamically. This regioselectivity mainly comes from the enhanced stability of the η^3-allylic intermediate ($(\eta^3\text{-}CH_2CHCH_2)Co(CO)_3$). In contrast, propyne does not show any regioselectivity in producing but-2-enal and methacrylaldehyde.

5.6 *Urea Formation from Primary Amine with Dicobalt Octacarbonyl*

In addition to hydroformylation with H_2 to activate $Co_2(CO)_8$ into $HCo(CO)_4$ and H_2 oxidative addition leading to aldehyde formation, primary amine (RNH_2) either can activate $Co_2(CO)_8$ into $HCo(CO)_4$ and $(RNH)Co(CO)_4$, or has oxidative addition to the $(RNHCO)Co(CO)_3$ complex leading to the formation of urea-like molecule, $(RNH)_2C{=}O$. Hong et al. carried out not only the experimental investigation [95], but also the corresponding B3LYP DFT calculations to explain the reaction mechanism [96]. They proposed two reaction routes, route 1 is the insertion-addition pathway (Scheme 20, top), and route 2 is the addition-insertion pathway (Scheme 20, bottom). The relative free energies are scaled at 298 K. Using methyl amine (CH_3NH_2) as model primary amine, the elementary steps for both routes including the amino group migration to the Co–CO bond, additional (CH_3NH_2) association, N–H oxidative addition of the coordinated amine to the cobalt center, and reductive elimination of $(CH_3NH)C{=}O$ were computed.

As shown in Scheme 20, the insertion step from **21** to **22a** in route 1 is more favored both kinetically and thermodynamically than the addition step from **21** to **23a** in route 2 (9.6 and −37.2 vs. 24.7 and −18.8 kJ/mol, respectively). In addition, route 2 (**23b** to **23c**) has much higher N–H oxidative addition barrier than that of route 1 (**22c** to **22d**) (237.7 vs. 205.9 kJ/mol, respectively), and such high barriers are responsible for the dramatic reaction conditions. Direct comparison indicates that route 1 is more favored and less complicated than route 2. Therefore, the insertion-addition route 1 should be the most likely catalytic mechanism.

6 Polynuclear Cobalt Carbonyl Complexes

$Co_2(CO)_8$: Cobalt carbonyl complexes play an important role in organometallic synthesis and catalysis. $Co_2(CO)_8$ (**24**), the first binuclear metal carbonyl, was originally prepared by Mond et al. [97] in 1908 via the reaction of finely divided

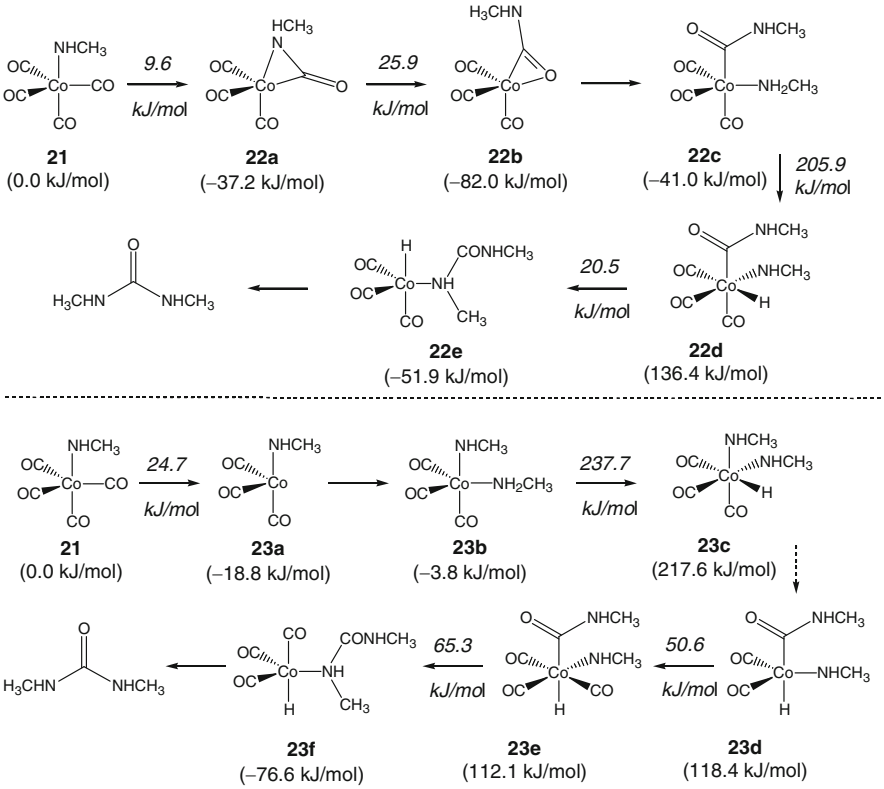

Scheme 20 Computed activation (*italics*) and reaction free energies for the proposed insertion-addition pathway (*top*) and addition-insertion pathway (*bottom*) for urea formation

cobalt metal with carbon monoxide at 150°C and 30 atm. Based on the early study of the carbonyl region of its infrared spectrum, Bor and Noack [98–100] proposed that $Co_2(CO)_8$ has at least two isomeric forms: the first one (**24a**) has two bridging and six terminal carbonyl groups in idealized C_{2v} symmetry as detected in solid state, and the second one (**24c**) with eight terminal carbonyls in D_{3d} symmetry is analogous to that found for the isoelectronic $[Fe_2(CO)_8]^{2-}$ anion. Later, the existence of a third isomer (**24b**) with eight terminal ligands in D_{2d} symmetry was detected by infrared spectroscopy [101–103]. Raman spectroscopy also showed the presence of three forms in solution [104] (Scheme 21).

At the B3LYP/LANL2DZ level, the structures and interconversion process of $M_2(CO)_8$ (M = Co, Rh, Ir) isomers were investigated by Aullón and Alvarez in 2001 [105]. Three isomers were calculated and suggested as the stationary points on the corresponding energy surfaces, with the D_{2d} isomer as the most stable one for M = Co and Ir, and the C_{2v} isomer as the most stable for M = Rh. The optimized structural parameters of the bridged form of $Co_2(CO)_8$ are very similar to those reported by Ziegler [106], and are also in good agreement with the experimental

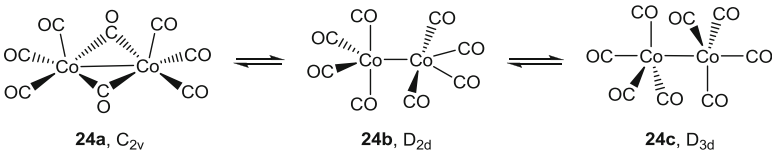

Scheme 21 Structural isomers of $Co_2(CO)_8$ (**24**)

data [107, 108], such as the Co–Co distance (2.545 Å calculated, 2.536 and 2.539 Å experimental). These data are consistent with the description of the coordination sphere of the metal atom as a square pyramid. In two non-bridged forms, the Co–Co bond length is significantly longer than that in the bridged one. In the D_{2d} isomer, the axial ligands form angles of less than 90° with the equatorial plane, indicating the presence of a weak semi-bridging interaction ($Co\cdots C = 2.83$ Å and $Co–Co–C_{ax} = 77.1°$), similar to that observed in the optimized isoelectronic anion $[Fe_2(CO)_8]^{2-}$ anion (2.87 Å and 76° for the same parameters) [109], and in $Mn_2(CO)_8$ (2.74 Å and 82°) [110]. The D_{3d} isomer has trigonal bipyramidal coordination around the metal atoms. Such a structure was found in isoelectronic compound of $Co_2(CO)_6(ER_3)_2$ [111, 112]. The Co–Co distance in the optimized structure of 2.671 Å agrees well with the experimental data (2.639–2.671 Å). The equatorial carbonyls are bent toward the second metal atom with the $Co–Co–C_{eq}$ angle of less than 90°.

Furthermore, the B3LYP results [105] indicated that the interconversion of $C_{2v} \leftrightarrow D_{2d}$ structures can take place via the rearrangement of the terminal and bridging and CO ligands of the C_{2v} structure. The process, D_{2d} to C_{2v}, was calculated to be endothermic by 6.2 kJ/mol, with a tiny energy barrier of 12.4 kJ/mol. This is consistent with the experimental observation that $Co_2(CO)_8$ is fluxional at room temperature, even in the solid state, as seen by the equivalence of all carbonyl ligands in the ^{13}C NMR spectrum [113]. The $D_{2d} \leftrightarrow D_{3d}$ conversion was slightly more endothermic by 24.3 kJ/mol and had energy barrier of 35.2 kJ/mol. However, no transition state could be located between C_{2v} and D_{3d} isomers, indicating that their interconversion must proceed through a D_{2d} intermediate.

$Co_4(CO)_{12}$: In 1932, the thermal decomposition of $Co_2(CO)_8$ was reported to give a black substance of the stoichiometry $[Co(CO)_3]_n$ [114]. It was confirmed as the tetramer $Co_4(CO)_{12}$ by X-ray diffraction first in 1959 in a two-dimensional study [115] and later in 1966 in a full three-dimensional study [116]. Using DFT methods with the B3LYP, BLYP, and BP86 functionals, the equilibrium geometries, thermochemistry, and vibrational frequencies of $Co_4(CO)_{12}$ (**25**) were characterized by Xie et al. [117]. The B3LYP predicted that the global minimum has C_{3v} symmetry with three bridging and nine terminal carbonyls, which is close to an experimentally realized structure. A more symmetrical structure with T_d symmetry, analogous to that observed in the valence isoelectronic $Ir_4(CO)_{12}$ molecule, lies 117.2 kJ/mol higher in energy and has a small imaginary vibrational frequency (40i). In addition, the Co–Co distances were calculated to be 2.51 and 2.47 Å for the

C_{3v} and T_d structures, respectively. These suggest the single bond required for an 18-electron configuration for the metal atoms.

$Co_6(CO)_{16}$: Synthesis of $Co_6(CO)_{16}$ came from the analogy between cobalt carbonyl chemistry and rhodium carbonyl chemistry. Early work on reductive carbonylation of rhodium trichloride in the presence of silver or copper powder under various conditions led to a red substance that lost CO on heating to give a black substance [118]. By means of X-ray diffraction, Dahl and coworkers [119–121] found the red rhodium carbonyl to be the tetranuclear $Rh_4(CO)_{12}$ and the black rhodium carbonyl to be the hexanuclear $Rh_6(CO)_{16}$. Subsequently, $Co_6(CO)_{16}$ was achieved by Chini [122, 123] via the reduction of the tetrahedral $Co_4(CO)_{12}$ with sodium amalgam followed by oxidation of the resulting octahedral $Co_6(CO)_{15}^-$ anion with ferric chloride. It is the simplest homoleptic metal carbonyl structure having carbonyl groups bridging three metal atoms on a face of the metal octahedron. The theoretical work by Xie et al. [117] also showed that the $Co_6(CO)_{16}$ (**26**) structure has T_d symmetry and satisfies the Wade–Mingos rules for an octahedral cluster. The predicted bond distances are 2.56, 1.77/2.02, and 1.66/1.20 Å for Co–Co, Co–C, and C–O, respectively.

$[Co_6C(CO)_n]^{2-}$ (n = 12, 13, 14, 15, 16): The chemistry of metal carbonyl carbide clusters dates back to the discovery in 1962 of the iron carbonyl carbide $Fe_5C(CO)_{15}$ cluster as an unexpected stable side product isolated in trace quantities (<0.5%) after careful chromatographic separation from certain reactions of iron carbonyls with alkynes [124]. After that, a variety of ionic metal carbonyl carbide clusters were discovered such as octahedral $[Co_6C(CO)_{13}]^{2-}$, trigonal prismatic $[Co_6C(CO)_{15}]^{2-}$, and square anti-prismatic $[Co_8C(CO)^{18}]^{2-}$ [125, 126]. Interestingly, the stoichiometries, $[Co_6C(CO)_{15}]^{2-}$ and $[Co_6C(CO)_{13}]^{2-}$, differ only by two carbonyl groups, but their Co_6 skeletons are based on totally different polyhedrons. Using DFT method, the interplay between octahedral and trigonal prismatic structures of $[Co_6C(CO)_n]^{2-}$ with an interstitial carbon atom has been studied by Zhao et al. [127]. It was found that the experimentally known structure of $[Co_6C(CO)_{15}]^{2-}$ consisting of a Co_6 trigonal prism with each of its edges bridged by carbonyl groups is a particularly stable structure lying more than 83 kJ/mol below any other isomers. Addition of a CO group to this $[Co_6C(CO)_{15}]^{2-}$ structure gives the lowest energy $[Co_6C(CO)_{16}]^{2-}$ structure, and also a Co_6 trigonal prism with one of the vertical edges bridged by two CO groups and the remaining eight edges each bridged by a single CO group. However, this $[Co_6C(CO)_{16}]^{2-}$ structure is thermodynamically unstable with respect to CO loss reverting to the stable trigonal prismatic $[Co_6C(CO)_{15}]^{2-}$. This suggested that 15 carbonyl groups is the maximum that can be attached to a Co_6C skeleton in a stable compound. The lowest energy structure of $[Co_6C(CO)_{14}]^{2-}$ has a highly distorted octahedral Co_6 skeleton and is thermodynamically unstable with respect to disproportionation to $[Co_6C(CO)_{15}]^{2-}$ and $[Co_6C(CO)_{13}]^{2-}$. The lowest energy $[Co_6C(CO)_{13}]^{2-}$ structure is very similar to a known stable structure with an octahedral Co_6 skeleton. The lowest energy $[Co_6C(CO)_{12}]^{2-}$ structure is a relatively symmetrical D_{3d} structure containing a carbon-centered Co_6 puckered hexagon in the chair form.

6.1 *Pauson–Khand (PK) Reaction*

Apart from cobalt carbonyl catylyzed hydroformylation, Pauson–Khand (PK) reaction is another type of reaction catalyzed with bimetallic carbonyl complex. Formally Pauson–Khand (PK) is a [2 + 2 + 1] cycloaddition of an alkyne, an alkene, and a CO group into cyclopentenone [128–130]. This process was initially discovered in 1973 [131], and early studies focused on using dicobalt octacarbonyl as both reaction mediator and the source of the carbonyl functional group. Since several variants of the original thermal protocol were introduced, PK reaction has received more and more fundamental and organic synthesis interests [132, 133].

The widely accepted mechanism was proposed by Magnus in 1985 (Fig. 6) [134, 135]. It starts from the formation of the well-characterized (μ-alkyne) hexacarbonyldicobalt tetrahedral complex, followed by the ligand substitution of losing a CO group and incorporating an alkene moiety. After that, coupling of the alkyne and alkene occurs to form the cobaltacycle. The final product of cyclopentenone is produced by the subsequent CO insertion and reductive elimination steps; at the same time the active catalyst of hexacarbonyldicobalt is regenerated. In this catalytic cycle, it was suggested that ligand substitution leading to coordination of the reacting alkene is probably the rate-determining step, while cobaltacycle formation is the product-determining step, since (with adequately substituted substrates) both the regiochemistry and the stereochemistry of the product cyclopentenone are fixed in it.

Although the above mechanism has been universally accepted, apart from the initially formed (μ-alkyne)hexacarbonyldicobalt, only one of the proposed intermediates along this pathway has been synthesized and characterized as stable entities. In 2009, Brusey et al. [136] reported the syntheses, X-ray crystallographic structural characterizations, and a variable temperature NMR investigation of a series of (η^2-alkene)-(μ-alkyne)pentacarbonyldicobalt complexes, which represented the first isolated examples of the first step in the proposed mechanism of the PK reaction. Fortunately, density functional methods now can make accurate predictions of structures and energetics in organometallic systems. Therefore, a series of density

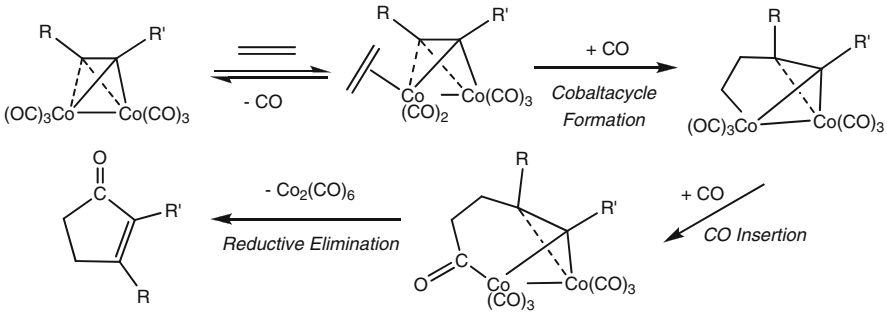

Fig. 6 Magnus proposed mechanism of the PK reaction [134, 135]

functional studies have been reported on the structures and energetics of the polynuclear cobalt carbonyl complexes and catalytically active intermediates, in order to give guidance for the potential applications of these species and a deeper understanding of the reaction mechanisms.

Using acetylene and ethylene as model compounds, the systematic DFT studies on the mechanisms of $Co_2(CO)_8$-mediated PK reaction were performed by Vázquez in 1999 at VWN/PW91xc level [137] and by Yamanaka and Nakamura in 2001 at B3LYP/631LAN level [138]. Along the Magnus proposed reaction path, all intermediates and transition states were located, and the energy profiles were mapped. In successive work by Pericàs et al. [139] and Robert et al. [140], much attention has been paid to the steps relevant to the enantioselectivity and regioselectivity.

As shown in Scheme 22 [139], (μ-HCCH)$Co_2(CO)_6$ (**27**) dissociative loss of CO is strongly endothermic by 140.2 kJ/mol and should be the rate-determining step of the reaction. The subsequent ethylene coordination can stabilize this coordinatively unsaturated species by 90.0 kJ/mol, and thus completes the ligand substitution stage. The next stage, cobaltacycle formation, has some interesting characteristics. The olefin insertion step has moderate activation energy of 69.0 kJ/mol and is slightly endothermic by 8.8 kJ/mol. However, the following CO coordination to cobalt is strongly exothermic by −118.0 kJ/mol. These suggested that the overall cobaltacycle formation is irreversible when the reaction is performed in a CO-rich environment, and determines the stereo- and regiochemistry of the overall reaction.

According to these results, practical rate increase in PK reaction can be achieved through acceleration of the initial CO dissociation step. The loss of a CO ligand normally proceeds thermally or upon treatment with a mild oxidant such as an amine N-oxide [132, 133]. Pericàs et al. have studied the different possibilities of dissociative loss of CO from the dicobalt hexacarbonyl complexes of

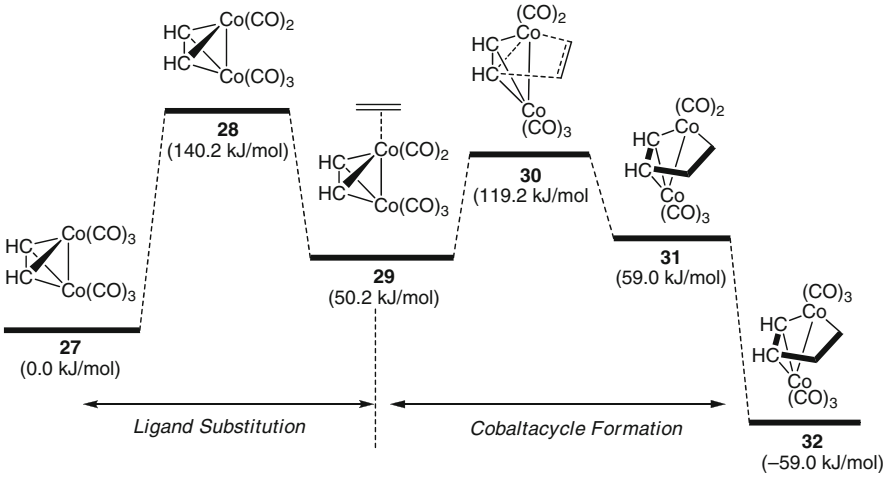

Scheme 22 Energy profiles for $Co_2(CO)_8$-mediated PK reaction

dimethylaminoacetylene, propyne, and ynamines [139]. It was found that the strongly electron-donating substituents on alkyne molecule could exert a positive effect on dissociation of the initial hexacarbonyl complex through the combined effect of anomeric and trans effects. The dissociation of the dimethylaminoacetylene complex was predicted to be much easier than that of propyne (36.8 vs. 77.8 kJ/mol). On the other hand, the ynamine complexes are extremely reactive toward strained olefins, but cannot react with cyclohexene, indicating that the easy dissociation of the initial complex is not sufficient for the observation of PK reactivity. For giving a good explanation on this behaviour, they further performed a combined semiempirical [PM3(tm)] and DFT [VWN/PW91xc] calculation on the cobaltacycle formation step for a variety of cyclic olefins covering different degrees of strain. A clear correlation between exothermicity of the cobaltacycle formation step and olefin strain was observed, thus providing an answer to the question of why strained olefins are more reactive in PK reaction.

How to control the enantioselectivity of the PK reaction is a fundamental topic. Among the different methodologies implemented to this end, the use of chiral ligands on cobalt, introduced by Pauson and Brunner in 1988 [141, 142], has the advantage of starting from immediately available precursors and that the adducts do not require further elaboration aimed at the removal of chiral auxiliaries. Based on this consideration, Pericàs et al. [139] choose a series of semi-labile ligands to play the role of the chelating auxiliaries for exploring ligand-enantiocontrolled PK reaction. It was found that the reacting olefin has coordinated to the cobalt atom not bearing the phosphine ligand, and the reaction has taken place at that precise cobalt atom. To understand the effect of a phosphine ligand on a cobalt carbonyl cluster, they also carried out a combined PM3(tm)/DFT calculation on these species. It showed that axial substitution is most favorable ($\Delta E_{eq/ax} = 18.8$ kJ/mol). The substitution leads to a decrease in reactivity, and the further CO dissociation (and, hence, PK reactivity) is directed toward the unsubstituted $Co(CO)_3$ moiety. These theoretical results have helped in the development of efficient chelating (P,N) and bridging (P,S) ligands for the stereochemical control of the reaction and in the understanding of their action modes.

How to control the regioselectivity of the PKR is another topic of fundamental and practical importance. For a long time, it was supposed that the steric effects of the acetylenic substituents are mainly responsible for the observed regioselectivity [140]. In the intermolecular PK reaction with the larger acetylenic substituent, olefin coordinates adjacently to the less bulky acetylenic substituent and that the subsequent C–C bond formation occurs between an olefinic carbon and this closer acetylenic carbon eventually leading to the α-substituted cyclopentenone. Indeed, ethyl propiolate under PK conditions yields mainly an α-carbethoxy-substituted cyclopentenone [143]. However, ethyl butynoate under similar conditions reacts to form only a *β*-carbethoxy-substituted derivative ([144]; for other reactions with 2-alkynoates, see [145]). To rationalize this, a detailed DFT B3LYP study has been carried out by Robert et al. [140] in 2001 on alkynedicobalt hexacarbonyl complexes (**33** in Scheme 23) to probe for the first time whether electronic

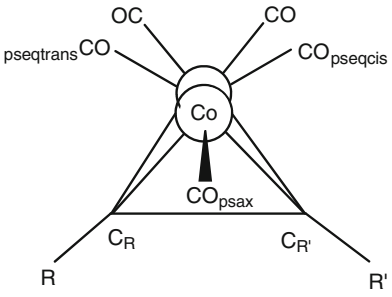

33a R = H; R' = CH_3
33b R = H; R' = CO_2CH_3
33c R = CH_3; R' = CO_2CH_3

Scheme 23 Structures of the complexes **33**

differences in the acetylenic substituents could impact on the regiochemistry of the PK reaction.

In complex **33a**, the C_R–$C_{R'}$ bond is strongly polarized, and the larger charge density focuses on C_R ($q(C_R) = -0.31$e vs. $q(C_{R'}) = -0.18$e). The longer Co–CO bond length is calculated for CO at trans-positioned with respect to R′. Therefore, it is reasonable to expect this CO ligand to dissociate more easily, as supported by the calculated bond dissociation energy of 101.3 kJ/mol. The olefin then occupies the vacant coordination site, which leads to the observed α-methylcyclopentenone.

In complex **33b**, where the C_R–$C_{R'}$ bond lacks obvious polarization ($q(C_R) = -0.36$e and $q(C_{R'}) = -0.33$e), the Co–CO_{pseq} bond dissociation energies are nearly identical (110.5 and 111.7 kJ/mol, respectively). In this case, the steric effects, as opposed to electronic ones, should play the decisive role. Therefore, the CO_{pseq} ligands should dissociate with equal facility and ultimately lead to the larger substituent of acetylene at the α position in the cyclopentenone.

In complex **33c**, in which the R and R′ substituents are sterically similar, the C_R–$C_{R'}$ bond should again be strongly polarized, but with $C_{R'}$ having the higher electron density ($q(C_R) = -0.14$e and $q(C_{R'}) = -0.34$e). Thus the $CO_{pseqcis}$ ligand is easy to dissociate, as indicated by the calculated bond dissociation energies (158.6 kJ/mol for CO_{psax} and 102.5 kJ/mol for $CO_{pseqcis}$). Subsequently, norbornene will coordinate to cobalt at a cis pseudoequatorial coordination site, and then lead to the ester function at the β position in cyclopentenone.

These results showed that when acetylene has sterically similar substituents, the regiochemistry is entirely governed by electronic differences in the acetylenic substituents, which translate, through discriminant carbon monoxide loss, into regioselective cyclopentenone formation. On the other hand, when acetylenic substituents are likely in electronic nature, the regioselectivity of the products determines by the steric effects. This insight has given guidance for controlling the regioselectivity of PK reaction by introducing various substituents to acetylene.

7 Final Remarks

The recent density functional theory computations on the detailed catalytic mechanism and regioselectivity of cobalt-mediated hydroformylation of propene, *N*-vinyl acetamide, 1,3-butadiene, acetylene, propyne, and allene and the urea formation from methyl amine as well as Pauson–Khand (PK) reaction have been discussed and compared. It shows clearly that the step, which determines the regioselectivity of hydroformylation, depends on the nature of substrates, and no general conclusion can be made. For PK reaction, the regioselectivity appears to be determined by the electronic nature and steric effects of acetylenic substituents. Despite the intensive studies performed both experimentally and theoretically, there are still many works to be done for getting better understanding of hydroformylation and PK reaction. The most important feature in future work is the computational screening of novel tailored ligands in favor of the desired reaction product under the consideration of economy, ecology, and environment.

References

1. Cornils B, Herrmann WA (2002) Applied homogeneous catalysis with organometallic compounds, vol 1. Wiley, Weinheim
2. Spessard GO, Miessler GL (1997) Organometallic chemistry. Prentice-Hall, Upper Saddle River, NJ
3. Parshall GW, Ittel SD (1992) Homogeneous catalysis. Wiley-Interscience, New York
4. Kaupp G (1994) Angew Chem Int Ed Engl 33:1452–1455
5. Savage PE, Gopalan S, Mizan TI, Martino CJ, Brock EE (1995) AIChE J 41:1723–1778
6. Rathke JW, Klingler RJ, Krause TR (1991) Organometallics 10:1350–1355
7. Guo Y, Akgerman A (1997) Ind Eng Chem Res 36:4581–4585
8. Ke J, Han B, George MW, Yan H, Poliakoff M (2001) J Am Chem Soc 123:3661–3670
9. Stinson SC (1999) Chem Eng News 77:65
10. Niu S, Hall MB (2000) Chem Rev 100:353–406 and references cited therein
11. Torrent M, Solà M, Frenking G (2000) Chem Rev 100:439–493 and references cited therein
12. van Leeuwen PWNM, Morokuma K, van Lenthe JH (1995) Theoretical aspects of homogeneous catalysis, application of ab initio molecular orbital theory. Kluwer Academic, Dordrecht
13. Carbo JJ, Maseras F, Bo C (2002) In: Maseras F, Lledos A (eds) Computational modeling of homogeneous catalysis, Kluwer Academic, Dordrecht
14. Ujaque G, Maseras F (2004) Application of hybrid DFT/molecular mechanics to homogeneous catalysis. Struct. Bond. 112:117–149
15. Gual A, Godard C, Claver C, Castillon S (2009) Eur J Org Chem 1191–1201
16. Vautravers NR, Cole-Hamilton DJ (2009) Chem Commun 92–94
17. Selent D, Baumann W, Wiese K-D, Börner A (2008) Chem Commun 6203–6205
18. Watkins AL, Hashiguchi BG, Landis CR (2008) Org Lett 10:4553–4556
19. Goudriaan PE, Jang X-B, Kuil M, Lemmens R, van Leeuwem PWNM, Reek JNH (2008) Eur J Org Chem 6079–6092
20. Piras I, Jennerjahn R, Jackstell R, Baumann W, Spannenberg A, Franke R, Wiese K-D, Beller M (2010) J Organomet Chem 695:479–486
21. Roelen O (1938) (Ruhrchemie AG). D. B. P. 849:458

22. Roelen O (1953) (Ruhrchemie AG). Chem. Zentr. 927
23. Beller M, Seayad J, Tillack A, Jiao H (2004) Angew Chem Int Ed 43:3368–3398
24. Crabtree RH (1988) The organometallic chemistry of the transition metals. Wiley, New York
25. Feng J, Garland M (1999) Organometallics 18:417–427
26. Paciello R, Siggel L, Röper M (1999) Angew Chem Int Ed Engl 38:1920–1923
27. Agbossou F, Carpentier J-F, Mortreux A (1995) Chem Rev 95:2485–2506
28. Collins AN, Sheldrake GN, Crosby J (1992) Chirality in industry. Wiley, Chichester
29. Consiglio G (1993) In: Ojima I (ed) Catalysis in asymmetric synthesis. VCH Publishers Inc., New York
30. Dwyer C, Assumption H, Coetzee J, Crause C, Damoense L, Kirk M (2004) Coord Chem Rev 248:653–669
31. Damoense L, Datt M, Green M, Steenkamp C (2004) Coord Chem Rev 248:2393–2407
32. Kamer PCJ, van Rooy A, Schoemaker GC, van Leeuwen PWNM (2004) Coord Chem Rev 248:2409–2424
33. Freixa Z, van Leeuwen PWNM (2003) Dalton Trans 1890–1901
34. Breit B (2003) Acc Chem Res 36:264–275
35. Bohnen H-W, Cornils B (2002) Adv Catal 47:1–64
36. van Leeuwen PWNM, Claver C (2000) Rhodium catalyzed hydroformylation. Kluwer Academic, Dordrecht
37. Ungváry F (2007) Coord Chem Rev 251:2072–2086
38. Ungváry F (2007) Coord Chem Rev 251:2087–2102
39. Ungváry F (2004) Coord Chem Rev 248:867–880
40. Ungváry F (2003) Coord Chem Rev 241:295–312
41. Ungváry F (2002) Coord Chem Rev 228:61–82
42. Goh SK, Marynick DS (2002) Organometallics 21:2262–2267
43. Gleich D, Hutter J (2004) Chem Eur J 10:2435–2444
44. Bourissou D, Guerret O, Gabbaï FP, Bertrand G (2000) Chem Rev 100:39–92
45. Tillack A, Jiao H, Castro IG, Hartung CG, Beller M (2004) Chem Eur J 10:2409–2420
46. Heck RF, Breslow DS (1961) J Am Chem Soc 83:4023–4027
47. Dombeck D (1983) Adv Catal 32:325–416
48. Whyman R (1974) J Organomet Chem 66:C23–C25
49. Mirbach MF (1984) J Organomet Chem 265:205–213
50. Pino P, Major A, Spindler F, Tannenbaum R, Bor G, Horváth IT (1991) J Organomet Chem 417:65–76
51. Ziegler T, Versluis L (1992) Adv Chem Ser 230:75–93
52. Ziegler T, Cavallo L, Bérces A (1993) Organometallics 12:3586–3593
53. Huo C-F, Li Y-W, Wu G-S, Beller M, Jiao H (2002) J Phys Chem A 106:12161–12169
54. Grima JPh, Choplin F, Kaufmann G (1977) J Organomet Chem 129:221–237
55. Huo C-F, Li Y-W, Beller M, Jiao H (2003) Organometallics 22:4665–4677
56. Versluis L, Ziegler T (1990) Organometallics 9:2985–2992
57. Solà M, Ziegler T (1996) Organometallics 15:2611–2618
58. Klaus S, Neumann H, Jiao H, Jacobi von Wangelin A, Gördes D, Strübing D, Hübner S, Hateley M, Weckbecker C, Riermeier T, Beller M (2004) J Organomet Chem 689:3685–3700
59. Adkins H, Williams JR (1952) J Org Chem 17:980–987
60. BASF (Kummer, R.) (1974) German Patent (OLS) 24,14,253
61. Fell B, Rupilius W (1969) Tetrahedron Lett 10:2721–2723
62. Fell B, Bahrmann H (1977) J Mol Catal 2:211–218
63. Bahrmann H, Fell B (1980) J Mol Catal 8:329–337
64. van Leeuwen PWNM, Roobeek CF (1985) J Mol Catal 31:345–353
65. Botteghi C, Branca M, Saba A (1980) J Organomet Chem 184:C17–C19
66. Wilkinson G, Brown CK, Mowat W, Yagupsky G (1971) J Chem Soc A 850–859
67. Botteghi C, Salomon Ch (1974) Tetrahedron Lett 15:4285–4288

68. Bertozzi S, Campigli N, Vitulli G, Lazzaroni R, Salvadori P (1995) J Organomet Chem 487:41–45
69. Horiuchi T, Ohta T, Shirakawa E, Nozaki K, Takaya H (1997) Tetrahedron 53:7795–7804
70. Kummer R, Weiss FJ (1978) Symp Rhodium Homogeneous Catal 87
71. Packett DL (1993) European Patent Application EP 577,042
72. Packett DL (1994) Chem Abstr 120:298075j
73. DL Packett (1994) US Patent 5,312,996, 1994
74. Packett DL (1995) Chem Abstr 123:82828w
75. Ohgomori Y, Suzuki N, Sumitani N (1998) J Mol Catal A 133:289–291
76. Mirbach MF (1984) Transition Metal Chem 9:465–468
77. Tuba R, Mika LT, Bodor A, Pusztai Z, Tóth I, Horváth IT (2003) Organometallics 22:1582–1584
78. Huo C-F, Li Y-W, Beller M, Jiao H (2005) Organometallics 24:3634–3643
79. Natta G, Pino P (1951) The 12th international congress of pure and applied chemistry, New York, September 1951
80. Greenfield H, Wotiz JH, Wender I (1957) J Org Chem 22:542–546
81. Fell B, Beutler M (1972) Tetrahedron Lett 13:3455–3456
82. Doyama K, Joh T, Shiohara T, Takahashi S (1988) Bull Chem Soc Jpn 61:4353–4360
83. Wuts PGM, Ritter AR (1989) J Org Chem 54:5180–5182
84. Campi EM, Jackson WR, Nilsson Y (1991) Tetrahedron Lett 32:1093–1094
85. Nombel P, Lugan N, Mulla F, Lavigne G (1994) Organometallics 13:4673–4675
86. Johnson JR, Cuny GD, Buchwald SL (1995) Angew Chem Int Ed Engl 34:1760–1761
87. Ishii Y, Miyashita K, Kamita K, Hidai M (1997) J Am Chem Soc 119:6448–6449
88. Van den Hoven BG, Alper H (1999) J Org Chem 64:3964–3968
89. Van den Hoven BG, Alper H (1999) J Org Chem 64:9640–9645
90. Zimmer R, Dinesh CU, Nandanan E, Khan FA (2000) Chem Rev 100:3067–3125
91. Fell B, Beutler M (1976) Erdöl & Kohle, Erdgas, Petrochemie 29:149–153
92. Huo C-F, Li Y-W, Beller M, Jiao H (2004) Organometallics 23:765–773
93. Huo C-F, Li Y-W, Beller M, Jiao H (2005) Chem Eur J 11:889–902
94. Huo C-F, Li Y-W, Beller M, Jiao H (2004) Organometallics 23:2168–2178
95. Hong F-E, Tsai Y-T, Chang Y-C, Ko B-T (2001) Inorg Chem 40:5487–5488
96. Hong F-E, Chang Y-C (2004) Organometallics 23:718–729
97. Mond L, Hirtz H, Cowap DM (1908) Chem News 98:165
98. Noack K (1963) Spectrochim Acta 19:1925
99. Bor G (1963) Spectrochim Acta 19:2065
100. Noack K (1964) Helv Chim Acta 47:1064
101. Bor G, Noack K (1974) J Organomet Chem 64:367–372
102. Bor G, Dietler UK, Noack K (1976) J Chem Soc, Chem Commun 914
103. Sweany RL, Brown TL (1977) Inorg Chem 16:415–421
104. Onaka S, Shriver DF (1976) Inorg Chem 15:915–918
105. Aullón G, Alvarez S (2001) Eur J Inorg Chem 3031–3038
106. Folga E, Ziegler T (1993) J Am Chem Soc 113:5169–5176
107. Sumner GG, Klug HP, Alexander LE (1964) Acta Crystallogr 17:732
108. Leung P, Coppens P (1983) Acta Crystallogr, Sect B 39:535
109. Aullón G, Alvarez S (2001) Organometallics 20:818–826
110. Barckholtz TA, Bursten BE (1998) J Am Chem Soc 120:1926–1927
111. Macchi P, Garlaschelli L, Martinengo S, Sironi A (1998) Inorg Chem 37:6263–6268
112. Jones RA, Seeberger MH, Stuart AL, Whittlesey BR, Wright TC (1986) Acta Crystallogr, Sect C 42:399
113. Hanson BE, Sullivan MJ, Davis RJ (1984) J Am Chem Soc 106:251–253
114. Hieber W, Mühlbauer F, Ehman EA (1932) Chem Ber 65:1090
115. Corradini P (1959) J Chem Phys 31:1676
116. Wei CH, Dahl LF (1966) J Am Chem Soc 88:1821–1822

117. Xie Y, King RB, Schaefer HF III (2005) Spectrochim Acta Part A 61:1693–1699
118. Hieber W, Lagally H (1943) Z Anorg, Allgem Chem 251:96
119. Wei CH, Wilkes GR, Dahl LF (1967) J Am Chem Soc 89:4792–4793
120. Wei CH (1969) Inorg Chem 8:2384–2397
121. Corey ER, Dahl LF, Beck W (1963) J Am Chem Soc 85:1202–1203
122. Chini P (1967) Chem Commun 440
123. Albano V, Chini P, Scatturin V (1968) Chem Commun 163
124. Braye EH, Dahl LF, Hübel W, Wampler DL (1962) J Am Chem Soc 84:4633–4639
125. Albano VG, Braga D, Martinengo S (1986) J Chem Soc, Dalton Trans 981
126. Martinengo S, Strumolo D, Chini P, Albano VG, Braga D (1985) J Chem Soc, Dalton Trans 35
127. Zhao J, Xu J, King RB (2008) Inorg Chem 47:9314–9320
128. Geis O, Schmalz HG (1998) Angew Chem Int Ed 37:911–914
129. Jeong N (1998) Trans Met Org Synth 1:560–577
130. Chung YK (1999) Coord Chem Rev 188:297–341
131. Khand IU, Knox GR, Pauson PL, Watts WE, Foreman MI (1973) J Chem Soc, Perkin Trans 1:977–981
132. Shambayti S, Crowe WE, Schreiber SL (1990) Tetrahedron Lett 31:5289–5292
133. Jeong N, Chung YK, Lee BY, Lee SH, Yoo S-E (1991) Synlett 204–206
134. Magnus PC, Exon C, Albaugh-Robertson P (1985) Tetrahedron 41:5861–5869
135. Magnus PC, Principe LM (1985) Tetrahedron Lett 26:4851–4854
136. Brusey SA, Banide EV, Dörrich S, O'Donohue P, Ortin Y, Müller-Bunz H, Long C, Evans P, McGlinchey MJ (2009) Organometallics 28:6308–6319
137. Vázquez J (1999) Ph. D. Thesis, University of Barcelona
138. Yamanaka M, Nakamura E (2001) J Am Chem Soc 123:1703–1708
139. Pericàs MA, Balsells J, Castro J, Marchueta I, Moyano A, Riera A, Vázquez J, Verdaguer X (2002) Pure Appl Chem 74:167–174
140. Robert F, Milet A, Gimbert Y, Konya D, Greene AE (2001) J Am Chem Soc 123:5396–5400
141. Bladon P, Pauson PL, Brunner H, Eder J (1988) J Organomet Chem 353:449–454
142. Derdau V, Laschat S, Dix I, Jones PG (1999) Organometallics 18:3859–3864
143. Krafft ME, Romero RH, Scott IL (1995) Synlett 677–678
144. Krafft ME, Romero RH, Scott IL (1992) J Org Chem 57:5277–5278
145. Fonquerna S, Moyano A, Pericàs MA, Riera A (1995) Tetrahedron 51:4239–4254